Copernicus assisted environmental monitoring across the Black Sea Basin - PONTOS

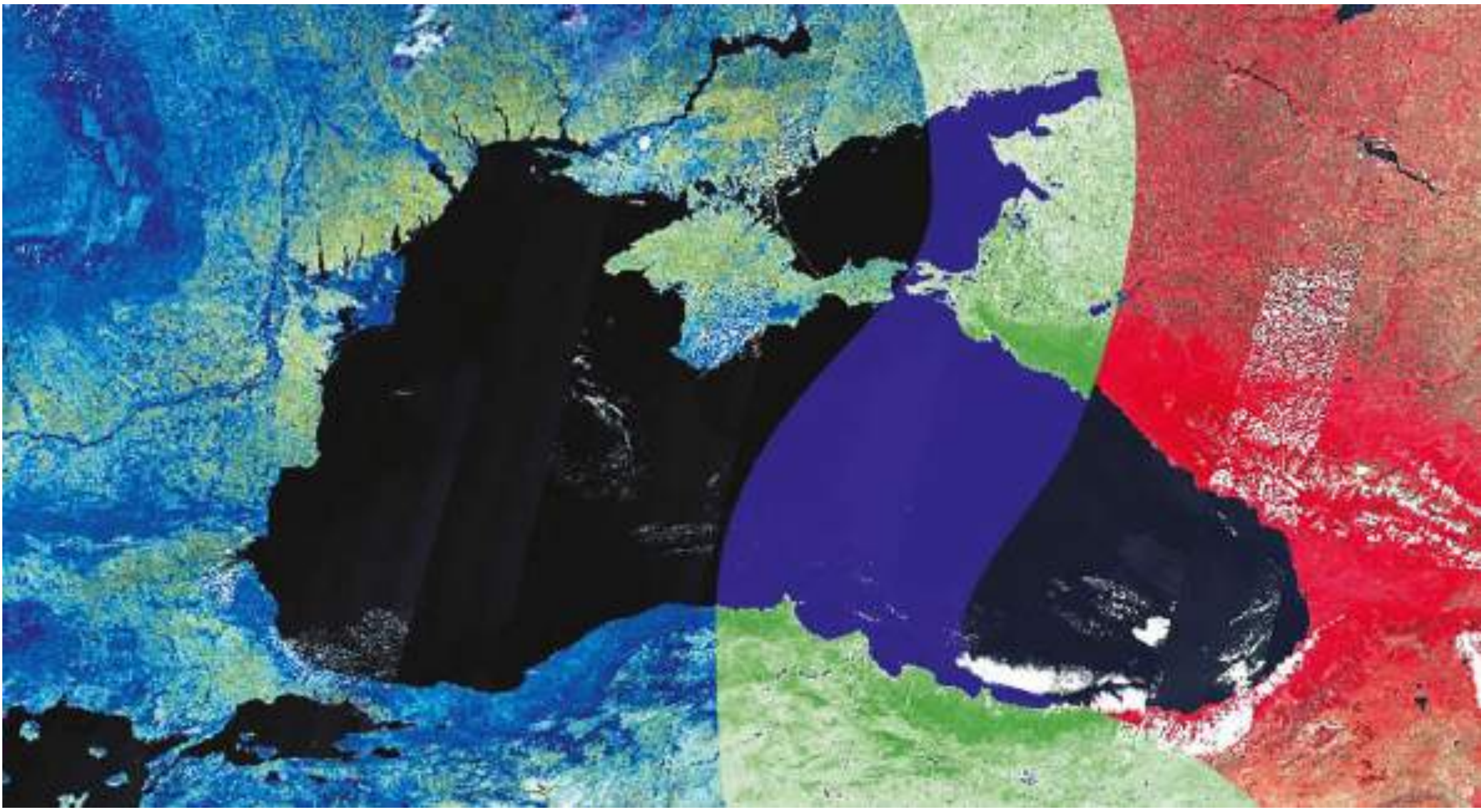

Integrated assessment on chlorophyll concentration and eutrophication dynamics

Deliverable D.T1.2.5

PONTOS-GR (Greece)

Table of Contents

1 Introduction

Coastal lagoons are considered unique, complex ecosystems with significant environmental and socioeconomic value (Jimeno-Sáez et al., 2020; Sylaios and Theocharis, 2002). They form shallow coastal water bodies, mostly situated in river deltaic zones, being isolated from the sea by a sand barrier, land spit or other similar geomorphic feature, originating from the sediment outflux of the adjacent river. Lagoons are connected to the sea by one or more tidal inlets, through which the lagoon basin communicates with the open sea (Kjerfve, 1994). The geometric characteristics of these inlets (length, width, depth) govern the exchange dynamics and fluxes of water, salt, nutrient and SPM between the lagoon's basin and the open sea, classifying them into flood- or ebb-dominated systems. In flood-dominated systems, flood prevails over ebb within a typical tidal cycle, meaning that influx is stronger than outflux. These are relatively deep entrance inlets with high inlet cross-sectional (A_C) to lagoon basin (A_b) areas ratio. On the contrary, in ebb-dominated lagoons, ebb prevails over flood, meaning that outflux is stronger than influx. The distortion of the tidal signal through the inlet necessarily impacts the water flow between the ocean and the lagoon, and a strong asymmetry of the current velocity occurs, known as residual circulation capable to carry pollutants and sediments.

Lagoons are considered of high ecological value, as recognized by European legislation through the application of the Habitats Directive and the Natura 2000 network, providing a series of ecosystem services, including fish production, biodiversity conservation, nutrient cycling, pollutants removal such as heavy metals (Costanza et al., 1997; Zanchettin et al., 2007). They act as transitional buffer zones for the transfer of freshwater and substances from the terrestrial to the coastal zones. A portion of the chemical compounds entering the lagoon environment from the land or the sea is deposited into the lagoonal sediments, making the systems extremely delicate to retain their ecological balance. Environmental degradation caused by alterations in watershed hydrology, pollution and human activities affects the capacity of the lagoon to deliver the above ecosystem services (Kjerfve, 1994).

The great variety of anthropogenic pressures alters the balance of the coastal lagoon ecosystem, making crucial the need for consistent monitoring and management of these territories. One of the major threats these systems face is eutrophication, defined as the accelerated primary production and the occurrence of increased biomass of primary producers, such as phytoplankton, due to nutrient over-enrichment (Devlin et al., 2011). Eutrophication problems associated with human activities have been identified as one of the main causes of water quality deterioration of coastal ecosystems (Kadiri et al., 2021). Several negative impacts are associated with eutrophication: the accelerated phytoplankton production limits sunlight availability to benthic aquatic plants; depletes dissolved oxygen in the water column, and especially at the bottom, due to decomposition of accumulated biomass resulting in hypoxic or anoxic conditions; and decreases species diversity and abundance.

This could give rise to shifts in invertebrate communities and permanent changes in aquatic habitats, with negative implications for pelagic and benthic fauna, including fish stocks. For example, a high fish mortality rate was reported in Ismarida lake in August 2013

(Koutrakis et al., 2016) and in Vistonida lagoon in July 2014. Eutrophication could also lead to algal toxin production, with a wider range of toxic species reported in estuarine environments, compared to freshwater environments, which could significantly affect the edibility of local seafood (Shumway, 1990). Such adverse effects may trigger negative socio-economic consequences, becoming significant over time.

The phytoplankton biomass, represented by chlorophyll-a (Chl-a), is an important indicator to evaluate the state of eutrophication in water bodies, thus helpful in coastal ecosystem monitoring and management. Systematic monitoring in coastal ecosystems is essential, but in-situ monitoring (e.g., water sample collection and analysis in the laboratory) is a time and money consuming method and is laborious to adequately assess the entire system on a regular basis. Satellite remote sensing is a feasible way to monitor water bodies when water quality over large regions has to be monitored with regular frequency. There is also the possibility to estimate water quality in non-accessible water bodies. However, passive satellite monitoring is heavily dependent upon weather, air mass temperature changes and sunlight conditions, which directly affect the quality and quantity of useful data.

The objective of this study is to map and assess Chl-a concentration in the coastal lagoons of Northern Greece. Those coastal lagoons have cultural, environmental and economic importance, therefor monitoring is needed to address the water quality changes. We focus on the study of the temporal and spatial evolution of Chl-a for the period 2013-2021. Landsat 8 satellite images were retrieved and processed for the time period 2013-2015 and Sentinel-2 images for the period 2015-2021.

Chl-a values were initially assessed using the well-known C2RCC algorithm. This algorithm has been validated in the open sea environment of Case 1 (in which their inherent optical properties are dominated by phytoplankton, e.g., most open ocean waters) and Case 2 waters (containing colored dissolved organic matter (CDOM) and inorganic mineral particles in addition to phytoplankton. However, the interference of (a) the shallow sea bottom reflection, (b) the sun glint and (c) the presence of non-algal particles on the optical signal (spectral reflectances) measured by satellites has not been adequately evaluated. In this report, we attempted to recalibrate the C2RCC processor using in-situ Chl-a concentration data and the respective spectral reflectance values for the appropriate training of a Takagi-Sugeno neuro-fuzzy algorithm to correct the satellite-derived Chl-a values.

Figure 1 explains graphically the steps to be followed for this analysis.

Figure 1. Methodological steps followed in present study.

1.1 Satellite Remote Sensing and Chlorophyll-a Algorithms

The Water Framework Directive (WFD, 2000/60/EC) obligates all European Union (EU) member states to implement water management and estimate the ecological status of water bodies, through systematic monitoring and classification. The measurement of Chl-a in water is commonly used (a) as an indicator to monitor water quality in coastal and inland waters, (b) in the surveillance of harmful algal blooms (HABs), (c) and in ecological studies of phytoplankton biomass and productivity (Jordan et al., 1991; Morrow et al., 2000). Deriving the chlorophyll concentration associated with algal blooms is an important metric which provides quantitative algal biomass measures useful in documenting the severity of blooms and their long-term trends, especially in relation to nutrient targets and water quality guidelines. Moreover, Chl-a has also been used as an indicator of cyanobacteria (Ogashawara and Moreno-Madriñán, 2014). Other water quality indicators like total suspended matter (TSM), turbidity, Secchi depth and colored dissolved organic matter (CDOM) can also be measured using remote sensing techniques (Toming et al., 2016).

Remote sensing has been used for decades to estimate Chl-a concentration, most notably with operational applications in the oceans (Hu et al., 2012; Mobley, 1995; O'Reilly et al., 1998; Schalles, 2006). However, significant progress has been made in applying remote sensing in inland water bodies with positive outcomes, as described in Palmer et al. (2015) and Bukata (2013). The main challenge to use remote sensing is to isolate the Chl-a signal from other cell components and other optically active compounds and the effects of the vertical distribution variation of chlorophyll in the water column.

The first satellite sensor developed to evaluate Chl-a concentration was the Coastal Zone Color Scanner (CZCS) onboard Nimbus 7 which was launched in late 1978. A two-band ratio of 443–550 nm was calibrated and routinely used for Chl-a estimation (O'Reilly et al., 1998). Two more operational sensors were also developed for the monitoring of Chl-a concentration using bands in the blue and the green regions (Sea-viewing Field of view sensor—SeaWIFS-and Moderate resolution Imaging Spectroradiometer — MODIS) (O'Reilly et al., 1998; Schalles, 2006).

The Chl-a algorithms in ocean waters are based on a simple interaction of phytoplankton density with water, in which usually blue to green band ratios have a robust and sensitive relation to Chl-a during low concentration levels (1–30 mg/m^3). This relationship becomes less sensitive at higher Chl-a concentration (above 30 mg/m^3) and is highly compromised by the effects of colored dissolved organic matter (CDOM) in turbid and optically complex waters (Schalles, 2006). Indeed, chlorophyll retrieval algorithms adopting blue to green band ratios have been shown to be robust for offshore waters, but are known to be sensitive to interference from non-algal constituents (particularly CDOM), as well as uncertainties brought about by atmospheric correction failure over highly turbid waters.

The distinct scattering/absorption features of Chl-a are the strong absorption between 400–500 nm (blue) and 680 nm (red), and the reflectance maximums at 550 nm (green) and 700nm (near-infrared-NIR) (Han, 1997). Wavelength range for characterizing Chl-a is between 400 nm and 900 nm (Han and Jordan, 2005). Therefore, the four bands mostly associated with Chl-a are the blue, green, red and NIR bands (Han, 1997; Yew-Hoong Gin et al., 2002).

According to Schalles (2006), low Chl-a concentration (<2 mg/m^3) shows higher reflectance in the blue part of the spectrum (400–500 nm) and reflectance decreases as wavelength increases, with extremely low reflectance values, near 0, in the near infrared spectrum (NIR, 700–800 nm); Chl-a concentrations between 2 and 30 mg/m^3 show higher reflectance in the green (500–600 nm) and red bands (600–700 nm), with peak reflectance in the green part of the spectrum; and Chl-a concentrations over 300 mg/m^3, show peak reflectance in the NIR and minimum high in the green part of the spectrum, the blue and red bands show low reflectance.

These principles are used to select bands and develop algorithms to retrieve Chl-a from satellite images since it is evident that spectral signature changes depending on the content of Chl-a in water. Usually, local-based algorithms are needed for inland water bodies, and they vary significantly from one site to another since their development is based on the specific optical constituents of a water body.

These operational algorithms are based on comparing blue to green ratios and have been generated for oceanic waters in which color is dominated by phytoplankton. The largest value of the ratios is used in a fourth-order polynomial regression equation, as the exponential term in a power function equation. These exponential equations best represent the sigmoidal relationship between Chl-a and the band ratio calculations (O'Reilly et al., 1998). The good performance of blue and green ratios in oceanic waters is due to the general tendency that as the phytoplankton concentration increases, reflectance decreases in the blue (400–515 nm) and increases in the green (515–600 nm) (Kirk, 1994). Ocean color and meteorological instruments have a coarse spatial resolution which precludes their applications to small inland lakes (Cao et al., 2020).

Some efforts have been made to find suitable sensors, but none were specifically designed for inland waters. Many lake Chl-a estimations were performed using ocean satellites color sensors including the Coastal Zone Color Scanner (Antoine et al., 1996), SeaWiFS (Dall'Olmo et al., 2005) and Earth Observation Systems, e.g., Moderate Resolution Imaging Spectroradiometer (Gitelson et al., 2008), Medium Resolution Imaging Spectrometer (MERIS) (Gitelson et al., 2008; Gurlin et al., 2011), meteorological satellite, like Advanced Very High Resolution Radiometer (Ibelings et al., 2003), and medium to high resolution land resources satellite, such as Landsat Operational Land Imager (OLI) (Liu et al., 2020) and Sentinel Multispectral Imager (MSI) (Toming et al., 2016).

The launch of Multispectral Imager's (MSI) onboard Copernicus Sentinel-2 mission in 2015 opened a great new potential in small water bodies remote sensing. The derived imagery comes with a spatial resolution of 10 m, 20 m and 60 m, depending on the band, exposing the monitoring of small waterbodies with more sophisticated algorithms based on neural networks, like the Case-2 Regional CoastColour (C2RCC) developed by ESA CoastColour project.

The Sentinel 3A satellite sensor OLCI (Ocean and Land Colour Instrument) launched in February 2016 by the European Space Agency (ESA) is particularly useful for chlorophyll retrievals due to their waveband selection in the red and near-infra-red (R-NIR) portion of the spectrum.

Algorithm approaches exploiting the R-NIR perform well in turbid eutrophic waters and line-height algorithms, such as the Maximum Chlorophyll Index (MCI), the Cyanobacteria Index (CI) and the Maximum Peak Height (MPH), are particularly favorable due to their relative insensitivity to uncertainties in atmospheric correction. Indeed, the application of line-height algorithms to uncorrected or partially atmospherically-corrected (using the bottom of Rayleigh reflectance) aquatic colored satellite data has become increasingly popular. The MCI, CI and MPH indices are well validated for the detection of dense surface algal blooms and have been calibrated for quantitative mapping of chlorophyll concentrations in a range of coastal and inland waters. Similarly, phycocyanin (PC) is a frequently used cyanobacteria marker pigment and forms the basis of many proposed remote sensing algorithms for detecting cyanobacteria.

2 Materials and Methods

2.1 In situ data collection

Field measurements were carried out during the period 2015-2018, from the shallow parts of the lagoons under study. Water samples from the surface of the lagoons were collected and Chl-a concentration was determined. A database of 130 Chl-a values is created. Those in-situ Chl-a concentration values were used to evaluate and calibrate the remote sensing algorithms using the Takagi-Sugeno neurofuzzy model.

2.2 Remote sensing images

2.2.1 Copernicus Sentinel-2 Mission

The Copernicus Sentinel-2 mission comprises a constellation of two polar-orbiting satellites placed in the same sun-synchronous orbit, phased at 180° to each other. It aims at monitoring the variability in land surface conditions, and its wide swath width (290 km) and high revisit time (10 days at the equator with one satellite, and 5 days with 2 satellites under cloud-free conditions, which results in 2-3 days at mid-latitudes) will support monitoring of Earth's surface changes. Sentinel-2 satellites are on track from 2015 to today and image data files consist of twelve spectral bands with a maximum resolution of 10 m (Table 1).

Table 1. Spectral bands, central wavelengths (nm) and corresponding spatial resolutions (m) of Sentinel-2 MSI sensor.

Bands		Central wavelength (nm)	Spatial Resolution (m)
Band 1	**Coastal aerosol**	443	60
Band 2	**Blue**	490	10
Band 3	**Green**	560	10
Band 4	**Red**	665	10
Band 5	**Red Edge-1**	705	20
Band 6	**Red Edge-2**	740	20
Band 7	**Red Edge-3**	783	20
Band 8	**NIR**	842	10
Band 8A	**NIR Vapor**	865	20
Band 9	**Water Vapor**	945	60
Band 10	**SWIR-Cirrus**	1375	60
Band 11	**SWIR-1**	1.610	20
Band 12	**SWIR-2**	2190	20

2.2.1.1 Sentinel- 2 Data

Sentinel-2 (2A and 2B) imagery was retrieved from Sentinel Scientific Data Hub (https://scihub.copernicus.eu/) and Earth Explorer (https://earthexplorer.usgs.gov/) databases. Sentinel-2 products are a compilation of elementary granules of fixed size, along with a single orbit. A granule is the minimum indivisible partition of a product (containing all possible spectral bands). For Level-1C and Level-2A (Figure 2), the granules, also called tiles, are 100 × 100 km ortho-images in UTM/WGS84 projection that divides the Earth's surface into 60 zones. Each UTM zone has a vertical width of 6° of longitude and horizontal width of 8° of latitude.

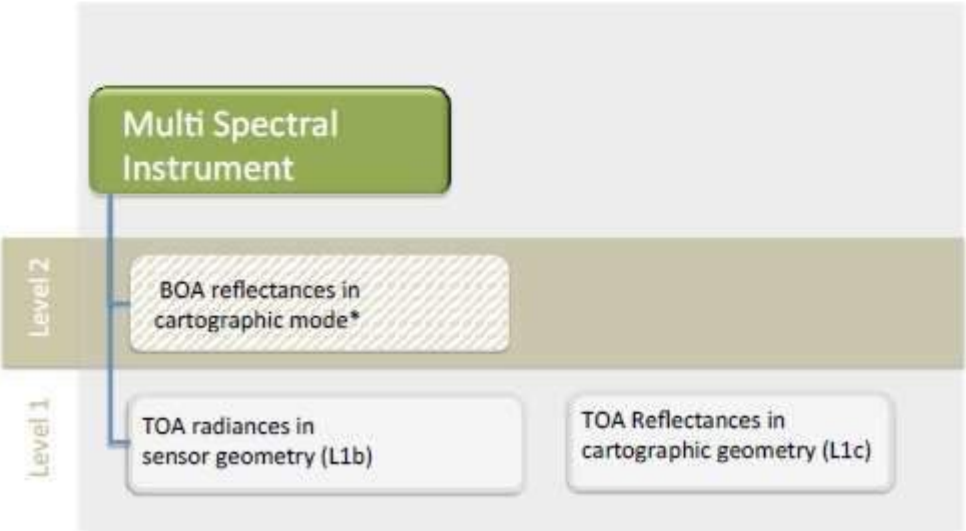

Figure 2. Graphical Representation of Sentinel-2 Core Products.

In this study the historical satellite images were retrieved for the tiles T34TGL, T35TKF and T35TLF in order to cover the entire area of the Greek Pilot area and the period from the early 2015 to 2021 (Figure 3).

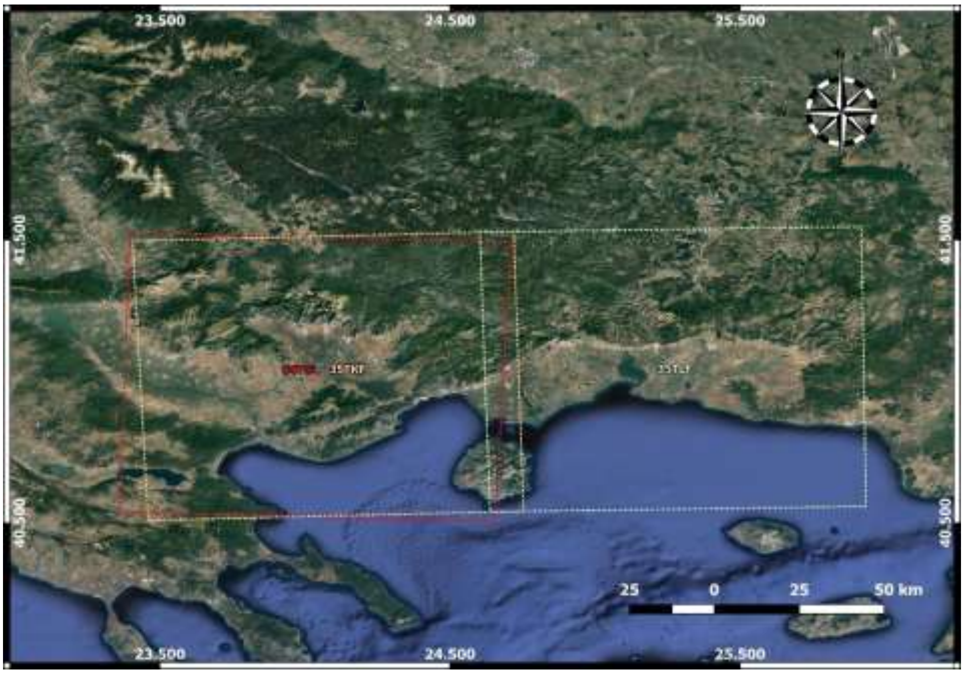

Figure 3. Sentinel-2 tiles over study area of Greek Pilot site (Nestos delta zone).

The satellite images with clouds over the study sites were not used for the Chl-a determination analysis. All images were retrieved in L1C product in order to use the same atmospheric correction for all of them. The number of retrieved images appear in Table 2.

Table 2. Retrieved images from Sentinel-2 mission for each lagoon through years 2015-2021.

Year	Tile	Vassova	Eratino	Agiasma	Porto Lagos	Xirolimni	Ptelea
2015	**T34TGL**	8	8	8			
	T35TKF	1	1	1			
	T35TLF				8	8	8
2016	**T34TGL**	3	3	3			
	T35TKF	1	1	1			
	T35TLF				6	6	6
2017	**T34TGL**	17	17	17			
	T35TKF	3	3	3			
	T35TLF				22	22	22
2018	**T34TGL**	31	31	31			
	T35TKF	1	1	1			
	T35TLF				31	31	31
2019	**T34TGL**	21	21	21			
	T35TKF	12	12	12			
	T35TLF				28	28	28
2020	**T34TGL**	44	44	44			
	T35TKF	1	1	1			
	T35TLF				47	47	47
2021	**T34TGL**	14	14	14			
	T35TLF				13	13	13
Sum		157	157	157	155	155	155

2.2.2 Landsat 4-5 Thematic Mapper (TM)

The Landsat sensors have been widely used for the estimation of optically-related water quality parameters, such as total Chl-a, suspended matter, turbidity, Secchi disk depth, total phosphorus, dissolved oxygen, chemical oxygen demand (COD), and biochemical oxygen demand (BOD) (Gholizadeh et al., 2016; Ouma et al., 2020). The 30-m spatial resolution of their images allows measurements even on small water systems (~ 0.08 km^2) (Brezonik et al., 2005).

Landsat 4-5 was on board from July 1982 to May 2012. It carries the Landsat Thematic Mapper (TM) sensor and has a 16-day repeat cycle. Their image data files consist of seven spectral bands (Table 3) and the resolution is 30 m for bands 1 to 7 (thermal infrared band 6 was collected at 120 m, but was resampled to 30 meters). The approximate scene size is 170 km north-south by 183 km east-west.

Table 3. Spectral bands, wavelengths (nm) and corresponding spatial resolutions (m) of Landsat 4-5.

Band		**Wavelength (μm)**	**Resolution (m)**
B1	**Blue**	0.45-0.52	30
B2	**Green**	0.52-0.60	30
B3	**Red**	0.63-0.69	30
B4	**NIR**	0.76-0.90	30
B5	**SWIR-1**	1.55-1.75	30
B6	**TIR**	10.4-012.50	120 (30)
B7	**SWIR-2**	2.08-2.35	30

2.2.3 Landsat 7 Enhanced Thematic Mapper Plus (ETM+)

Landsat 7 was launched in April 1999 carrying the Enhanced Thematic Mapper Plus (ETM+) sensor. This instrument is an improved version of the Thematic Mapper instruments that were onboard Landsat 4 and Landsat 5. Landsat 7 orbits the Earth at 705 km in a sun-synchronous, near-polar orbit (98.2 degrees inclination) and has a 16-day repeat cycle with an equatorial crossing time: 10:00 a.m.

Landsat 7 images consist of eight spectral bands (Table 4) with a spatial resolution of 30 m for Bands 1 to 7. The resolution for Band 8 (panchromatic) is 15 m. Approximate scene size is 170 km north-south by 183 km east-west.

2.2.4 Landsat 8

The Landsat 8 mission launched in February 2013 and orbits the Earth in a sun-synchronous, near-polar orbit (98.2 degrees inclination) and has a 16-day repeat cycle with an equatorial crossing time of 10:00 a.m. +/- 15 minutes.

Landsat 8 mission carries the Operational Land Imager (OLI) and the Thermal Infrared Sensor (TIRS) instruments. The OLI comprises 9 bands, measuring in the visible, near infrared, and shortwave infrared portions (VNIR, NIR, and SWIR) of the spectrum. The TIRS includes 2 bands and measures land surface temperature in two thermal bands with a new technology that applies quantum physics to detect heat. These two sensors provide seasonal coverage of the global landmass at a spatial resolution of 30 meters (visible, NIR, SWIR); 100 meters (thermal); and 15 meters (panchromatic).

Table 4. Spectral bands, wavelengths (nm) and corresponding spatial resolutions (m) of Landsat 7 and 8.

Landsat 7				**Landsat 8**			
Band		**Wavelength (μm)**	**Spatial Resolution (m)**	**Band**		**Wavelength (μm)**	**Spatial Resolution (m)**
				B1	**Coastal/Aerosol**	0.435-0.451	30
B1	**Blue**	0.441-0.514	30	**B2**	**Blue**	0.452-0.512	30
B2	**Green**	0.519-0.601	30	**B3**	**Green**	0.533-0.590	30
B3	**Red**	0.631-0.692	30	**B4**	**Red**	0.636-0.673	30
B4	**NIR**	0.772-0.898	30	**B5**	**NIR**	0.851-0.879	30
B5	**SWIR-1**	1.547-1.749	30	**B6**	**SWIR-1**	1.566-1.651	30
B7	**SWIR-2**	2.064-2.345	30	**B7**	**SWIR-2**	2.107-2.294	30
B8	**Panchromatic**	0.515-0.896	15	**B8**	**Panchromatic**	0.503-0.676	15
				B9	**Cirrus**	1.363-1.384	30
B6	**TIR**	10.31-12.36	60	**B10**	**TIR-1**	10.60-11.19	100
				B11	**TIR-2**	11.500-12.510	100

The OLI sensor is compatible with the earlier Landsat sensors and presents improved measurement capabilities. It provides two new spectral bands, one tailored especially for detecting cirrus clouds and the other for coastal zone observations. TIRS collects data for two more narrow spectral bands in the thermal region formerly covered by one wide spectral band on Landsats 4–7. The 100 m TIRS data is registered to the OLI data to create radiometrically, geometrically, and terrain-corrected 12-bit data products.

2.2.4.1 Landsat 8 Data

Landsat 8 imagery was retrieved from Earth Explorer database (https://earthexplorer.usgs.gov/). The scene size is approximately 170 km north-south by 183 km east-west.

In this study the historical satellite images with path and row (183,31), (183,32) and (182,32) were retrieved in order to cover the Greek Pilot area for the period 2013-2015.

All images were retrieved in L1C product in order to use the same atmospheric correction for all of them. The number of retrieved images appear in Table 5.

Table 5. Retrieved images from Landsat 8 for each lagoon through years 2015-2021.

Year	Path	Row	Greek Pilot area
2013	**183**	**32**	11
	183	**31**	10
	182	**32**	10
2014	**183**	**32**	7
	183	**31**	6
	182	**32**	10
2015	**183**	**32**	13
	183	**31**	12
	182	**32**	14
Sum			**93**

2.3 Satellite Data Processing

2.3.1 C2RCC Processor

The C2RCC outputs results for Chl-a and TSM concentration, however algorithm execution demands additional background information, such as water surface salinity, elevation, ozone, water surface temperature, and air pressure. To increase the accuracy of the processor, salinity and temperature values were used from previous in situ measurements. Values for the surface ozone layer and air pressure were retrieved from the ERA5 model, a fifth generation ECMWF atmospheric reanalysis dataset of the global climate, covering the period from January 1950 to present and providing hourly estimates in a large number of atmospheric, land and oceanic climate variables, with 30km spatial resolution.

2.3.2 The Takagi-Sugeno neuro-fuzzy model

A fuzzy model is a non-linear method aiming to create a quantitative model utilizing data collected from complex phenomena. A series of "IF-THEN" rules help to define the mapping of inputs to outputs. A rule is made up of input and output variables and adjectives such as “low” and “high” that identify those variables. Before constructing a Takagi–Sugeno-rule-based fuzzy inference system, all the terms should be defined together with the adjectives that describe them.

In this study, a Takagi-Sugeno neuro-fuzzy model was developed aiming to inter-calibrate the Chl-a concentration values. A database of 130 in-situ Chl-a concentration values were associated with the respective reflectance values from bands 4 to 7 of Sentinel 2 and bands 1 to 5 of Landsat 8. 60% of data from the database were used for training the Takagi-Sugeno neuro-fuzzy model, 20% for model validation and 20% for model testing. The model was implemented in Matlab 2018, utilizing the standard Adaptive Neural Fuzzy Inference System (ANFIS) algorithm. Initially, the fuzzification of input values (4 antecedents: reflectances at each band; 1 output: log(Chl-a)) through the general bell-shaped membership function and the grid partition method, led to the definition of membership values in the three fuzzy sets ("low", "medium", "high"). Then, a series of multiple-input–single output fuzzy rules were applied of the form: if band1 is "LOW" AND band2 is "MEDIUM" AND band3 is "LOW" and band4 is "HIGH" then log(Chl-a) = f(band1, band2, band3, band4). Finally, the evaluation and weighting of the basis functions and the final evaluation of the output Chl-a value were followed in the defuzzification step.

Model testing error analysis exhibited the following metrics: Mean Squared Error = 0.000018; Root Mean Squared Error = 0.00418; r2 = 0.996 for Sentinel 2 and Mean Squared Error = 0.000043; Root Mean Squared Error = 0.00659; r2 = 0.925 for Landsat 8.

Figure 4 presents the distribution of the three fuzzy sets per Sentinel 2 band.

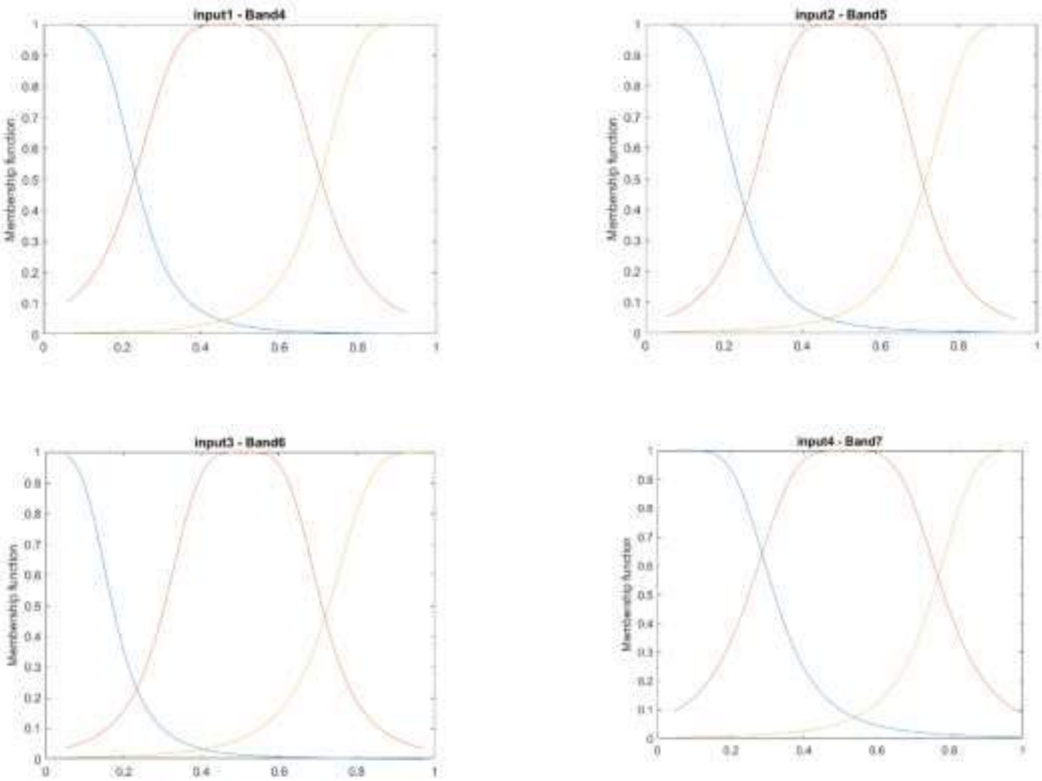

Figure 4. The fuzzy sets per Sentinel 2 band.

All input data, along the x-axis of the following diagrams, were normalized prior the neuro-fuzzy implementation. The y-axis represents the degree of membership of each input value into a specific fuzzy set.

Figure 5 illustrates the variation in the training and testing errors, between the observed and modelled values throughout the model iterations. It occurs that after a certain number of iterations the training error remains stable at very low levels (0.001 0.004 mg/m^3) while the testing error converges towards 0.004 mg/m^3. Figure 6 depicts the change of the prediction error over the iterations performed by the TS neuro-fuzzy model.

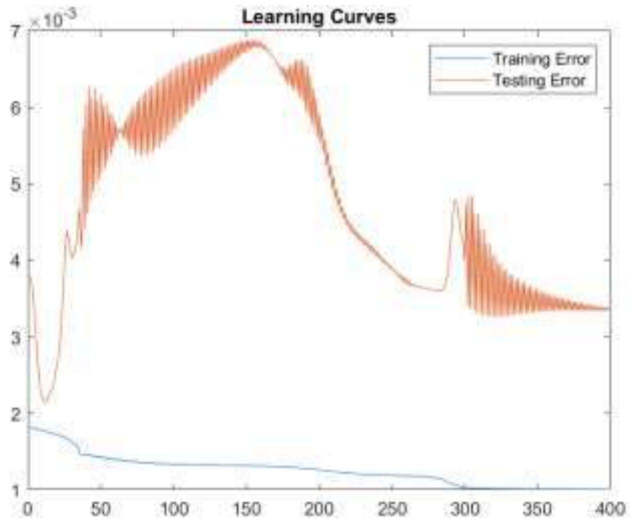

Figure 5. The variation of the training prediction error with the number of model iterations.

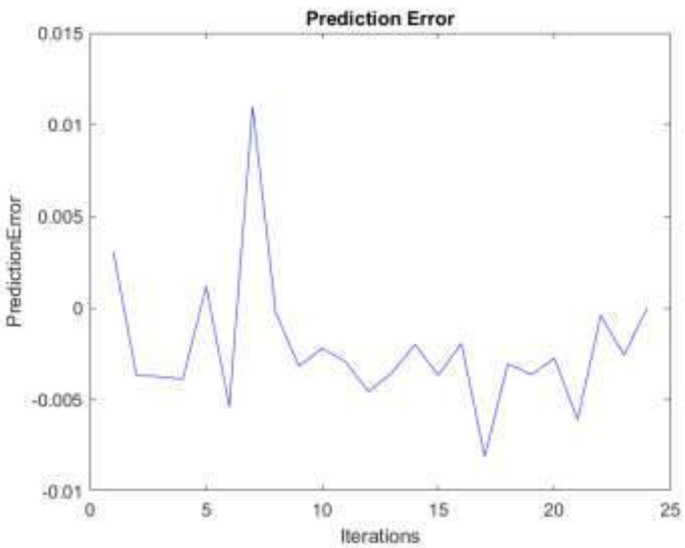

Figure 6. The variation of the prediction error with the number of model iterations.

2.3.3 The PONTOS Methodological Framework

Figure 7 describes the methodological framework of PONTOS eutrophication assessment and monitoring. Sentinel 2 and Landsat 8 satellite images were collected for the study area and period. All images were stored on the local DUTH server purchased from PONTOS project for that purpose. Satellite images were imposed on subsetting, atmospheric correction and resampling. Chl-a data were derived using the Takagi-Sugeno neuro-fuzzy model and maps of surface Chl-a concentration distribution were created. Furthermore, data were statistically analyzed, frequency distributions per lagoon were examined and threshold Chl-a levels for the identification and warning of extreme eutrophic events and blooms were established. Probability density functions and cumulative density functions were fitted on the histograms and the probability of threshold exceedance per lagoon and per lagoon's specific zone were assessed. Maps of probability for threshold exceedance were created illustrating areas vulnerable and prone to eutrophication.

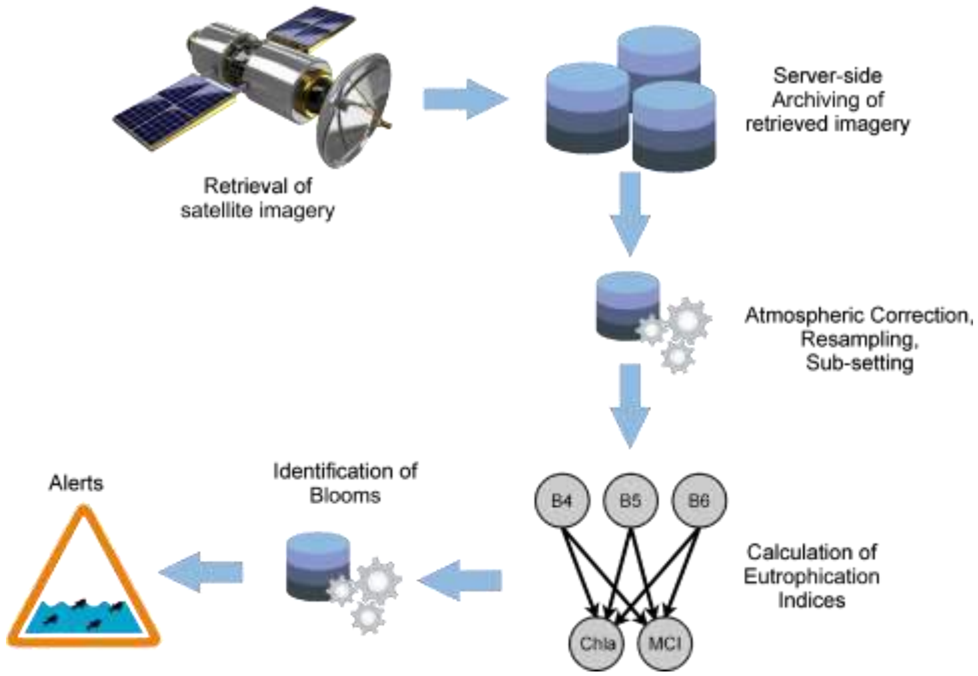

Figure 7. The PONTOS methodological framework for eutrophication assessment.

2.4 Eutrophication Assessment

Several trophic conditions classification schemes have been proposed in the literature to assess the environmental state of aquatic systems in terms of nutrients recycling. More complete trophic classification schemes are based on nutrients (phosphates, nitrates, ammonium), chlorophyll-a and total number of phytoplankton cells. Aquatic systems are classified into oligotrophic, lower mesotrophic, higher mesotrophic and eutrophic and ranges are given per parameter. Nutrient concentrations are given in µM, phytoplankton cells number in cells/l and chlorophyll in µg/l.

Table 6. Classification of aquatic systems according to their trophic conditions.

Parameter	Oligotrophic	Lower mesotrophic	Higher mesotrophic	Eutrophic
Phosphates (PO4) (µM)	<0.07	0.07-0.14	0.14-0.68	>0.68
Nitrates (NO3) (µM)	<0.62	0.62-0.65	0.65-1.19	>1.19
Ammonium (NH4) (µM)	<0.55	0.55-1.05	1.05-2.20	>2.20
Phytoplankton (cells/l)	$<6.0\times10^3$	6.0×10^3-1.5×10^5	1.5×10^5-9.6×10^5	$>9.6\times10^5$
Chlorophyll-a (µg/l)	<0.10	0.10-0.60	0.60-2.21	>2.21

The scheme above introduces a scale with four levels of eutrophication: eutrophic, higher mesotrophic, lower mesotrophic and oligotrophic, though 5 classes are required for WFD.

To achieve this harmonization, a new eutrophication scale was proposed by Karydis (1996) and Simboura et al. (2005), to comply with the ecological status levels described in WFD.

To process the satellite-derived Chl-a data, a chlorophyll multimetric is proposed to incorporate compliance assessment of five statistics in chlorophyll biomass:

- mean
- median
- percentage compliance over a threshold (10 µg/l Chl)
- percentage compliance over a threshold (20 µg/l Chl)
- percentage exceedance over a maximum threshold (50 µg/l Chl).

Estimates for the chlorophyll-a multimetric are proposed to delineated into two salinity zones, inner (salinity 1 - 25) and outer (salinity > 25), with thresholds for assessing compliance of the statistics, for each specific salinity zone.

To assess the percentages exceeding a certain threshold value, historic Chl-a data derived from satellite images were collected at specific sites, representing diverse conditions within each lagoon. These data were used to assess the probability of exceedance of a certain Chl-a level. Several probability density functions are available in the literature to be fitted on these Chl-a distributions. Therefore, on the Chl-a frequency histogram the best theoretical probability density function was fitted. The AIC and BIC minimization served as the criteria to select the most appropriate fitting model and assess the probability of Chl-a eutrophication threshold exceedance, set at 2 mg/m^3.

2.5 Study Site Description

2.5.1 The Greek Pilot area (PONTOS-GR)

The Greek Pilot area consists of 3 lagoons that belong to the Nestos complex (Vassova, Eratino and Agiasma lagoon), one located in Xanthi Prefecture (Porto-Lagos lagoon) and two in Rodopi Prefecture (Xirolimni and Ptelea lagoon) (Figure 8). All these lagoons are ecologically important sites, part of the East Macedonia and Thrace National Park and protected by the Convection on Wetlands of International Importance (Ramsar Convention) (Tsihrintzis et al., 2007).

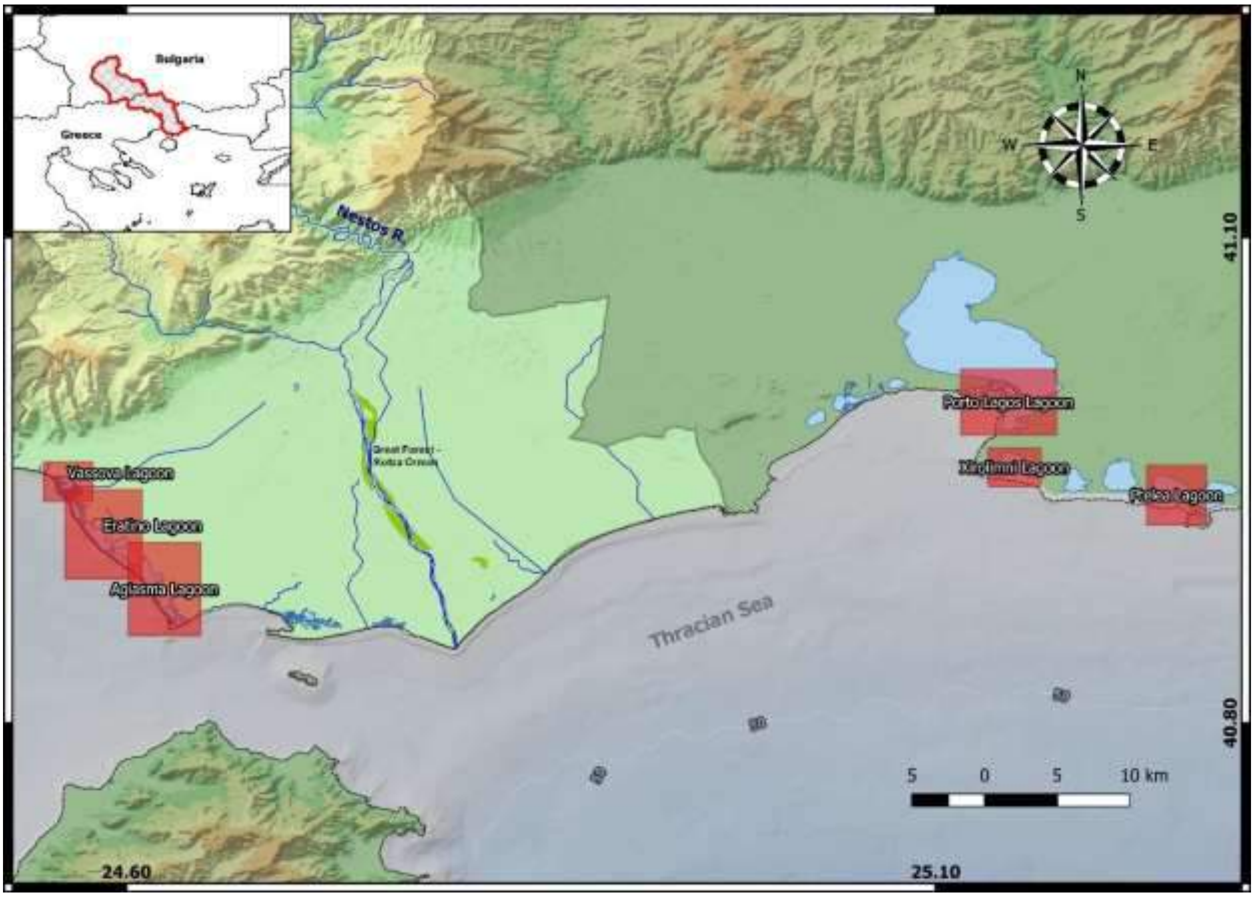

Figure 8. Lagoons under study.

2.5.1.1 Vassova lagoon

Vassova lagoon is a small in size (2.7 km^2) and shallow (mean depth: 0.8 m) coastal lagoon located at the western bank of river Nestos (Figure 9). The lagoon consists of a central main basin used for extensive aquaculture, and 16 dredged wintering canals, ranging from 30 to 50 m long and 0.5 m deep each. Vassova lagoon may be considered as a closed system, i.e., there is no freshwater input except directly from rainfall and through seepage from the adjoining agricultural lands. The lagoon is connected to the open sea (Kavala Gulf, North Aegean Sea) with an inlet channel approximately 15 m wide, 200 m long and 0.7 – 0.8 m deep at mean sea level. This lagoon is ecologically important providing water-fowl habitat, and is also exploited for fish production (30 tn/year) (Sylaios et al., 2006).

Figure 9. Vassova lagoon.

2.5.1.2 Eratino lagoon

Eratino Lagoon is approximately 2.9 km^2, with a length of about 5.9 km, average width of 0.7 km (maximum width of 1.5 km) and a perimeter of 43 km (Figure 10). The mean depth of the lagoon is 0.8 m and the maximum depth 3.4 m. The lagoon is connected to the open sea (Kavala Gulf) with two inlet channels and it communicates with Vassova lagoon through a narrow, shallow channel (Tsihrintzis et al., 2007). Eratino receives fresh water by a natural channel in the northern part of the basin and agricultural runoff by direct drainage (Sylaios and Theocharis, 2002).

Figure 10. Eratino lagoon.

2.5.1.3 Agiasma lagoon

Agiasma, a shallow lagoon with a mean depth of 0.5 m, covers an area of 3.3 km^2, with a length of about 7 km, a mean width of 0.8 km and a perimeter of 24.3 km. It is connected with the sea with two narrow outlets (Figure 11). The outlet in the middle of the basin remains open during stocking, from mid-February to May, while the outlet in the south part of the lagoon is always open. Agiasma is considered to be one of the less affected by eutrophication system of the Nestos Delta complex (Orfanidis et al., 2008).

Figure 11. Agiasma lagoon.

2.5.1.4 Porto Lagos lagoon

Porto Lagos is a shallow coastal lagoon, with a mean depth of about 0.5 m and covers an area of 3.75 km^2 (Figure 12). It is connected to Vistonis Lake through three short channels (50 m long and 25 m wide) and to Vistonikos Gulf (Thracian Sea, Northern Aegean Sea) through a channel 60 m wide and 600 m long. It is a micro-tidal environment with tidal range less than 0.30 m during spring tides. Wave action is negligible and water circulation allows for the sufficient oxygenation of the lagoon. Water is generally turbid; highest turbidity was observed during the warmest months. The lagoon bottom is regular, covered by soft mud and sand on the periphery. Salt marshes, mudflats and sandflats border the lagoon. Seagrasses constitute the majority of submerged aquatic vegetation (Koutrakis et al., 2005).

Figure 12. Porto-Lagos lagoon.

2.5.1.5 Xirolimni lagoon

Xirolimni lagoon has an average depth of 0.6 m covering an area of 1.8 km^2 and is located on the western side of the Fanari settlement (Figure 13). It connects to the sea with a narrow, 320 m long outlet. Xirolimni receives fresh water from precipitation and direct runoff.

Figure 13. Xirolimni lagoon.

2.5.1.6 *Ptelea lagoon*

Ptelea is a shallow system with an area of 3.6 km^2. It communicates with Elos lagoon from the East and with the Thracian Sea through a narrow inlet (Figure 14). Both Xirolimni and Ptelea are located within an agricultural watershed and they receive fresh water from precipitation or direct drainage.

Figure 14. Ptelea lagoon.

All six lagoons are surrounded by permanent cultivated areas (mostly cotton, maize, alfalfa), which leads to receiving agricultural runoff especially during flash flood events. Lagoons are forced by similar tidal influence (spring tidal range 0.4 m and neap tidal range 0.2 m) at their mouths and they belong to the same Koppen climatic zone (Csb, warm summer Mediterranean climate). Mean annual precipitation is around 320 mm ranging between 420 – 430 mm and air temperature between -5-38 °C with mean temperature around 15 °C. In North Aegean Sea, winds blowing from the north and northeast dominate, while south-southwestern winds prevail in spring and summer. The geometric and hydrologic parameters for the six lagoons are summarized in at **Table 7**.

Table 7. Study sites and their Geometric and hydrologic characteristics.

Lagoon	Geographical boundaries	A (km^2)	h (m)	V (km^3)	Perimeter (km)
Vassova	24.552° A, 40.929° B : 24.569° A, 40.957° B	2.70	0.80	3.00×10^{-3}	5.25
Eratino	24.566° A, 40.894° B : 24.605° A, 40.938° B	2.88	0.77	2.23×10^{-3}	42.50
Agiasma	24.612° A, 40.853° B : 24.625° A, 40.913° B	3.33	0.50	1.66×10^{-3}	24.30
Porto-Lagos	25.133° A, 40.979° B : 25.168° A, 41.011° B	4.91	1.00	3.16×10^{-3}	40.00
Xirolimni	24.608° A, 40.861° B : 24.637° A, 40.903° B	1.76	0.52	0.90×10^{-3}	6.42
Ptelea	25.232° A, 40.923° B : 25.264° A, 40.964° B	3.60	0.80	2.90×10^{-3}	6.93

where A = lagoon surface area, h = mean lagoon water depth, V = lagoon water volume

3 Results

3.1 Spatial Chlorophyll analysis

By applying the Takagi-Sugeno neuro-fuzzy model, the spatio-temporal distribution of Chl-a concentration data were obtained and mapped. Satellite images for the period 2013-2021 were processed. Period 2013-2015 was covered by Landsat 8 images and period 2015-2021 by Sentinel 2 images. Indicatively, a series of images throughout the years are presented, to show the seasonal evolution of Chl-a for each of the lagoons under study.

3.1.1 Vassova lagoon

Figures 12-21 show the spatial distribution of Chl-a in Vassova lagoon for the year 2013-2021. During 2013 (Figure 15), the highest Chl-a concentration values were reached in August. The increase started from the upper part of the basin and in the following summer months it moved to the central basin. In the autumn and winter months, the Chl-a values are decreased.

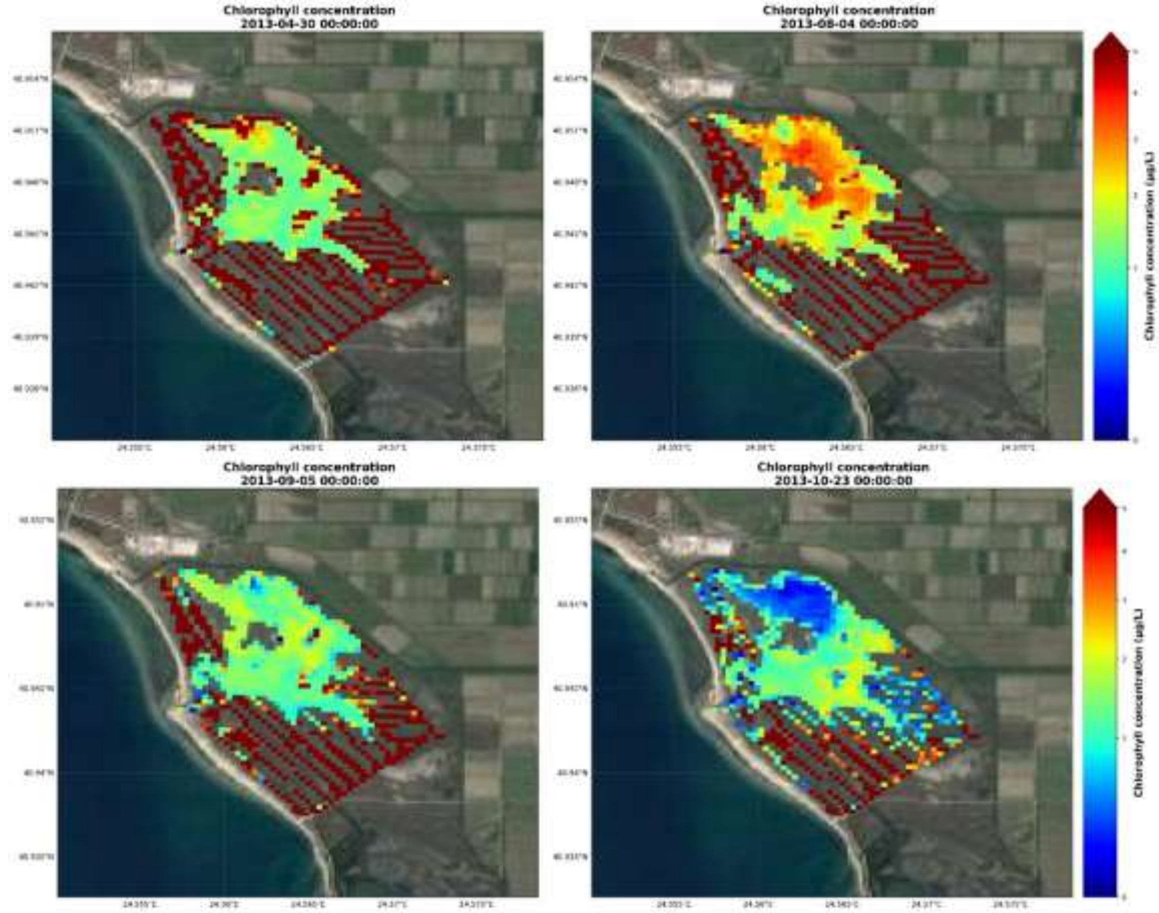

Figure 15. Seasonal evolution of Chl-a concentration in Vassova lagoon for the year 2013, based on Landsat 8 satellite images.

During 2014 (Figure 16), the Chl-a values were low from January to early July. Then they showed an increase at the northern part of the basin. The Chl-a values started to decrease in the following months.

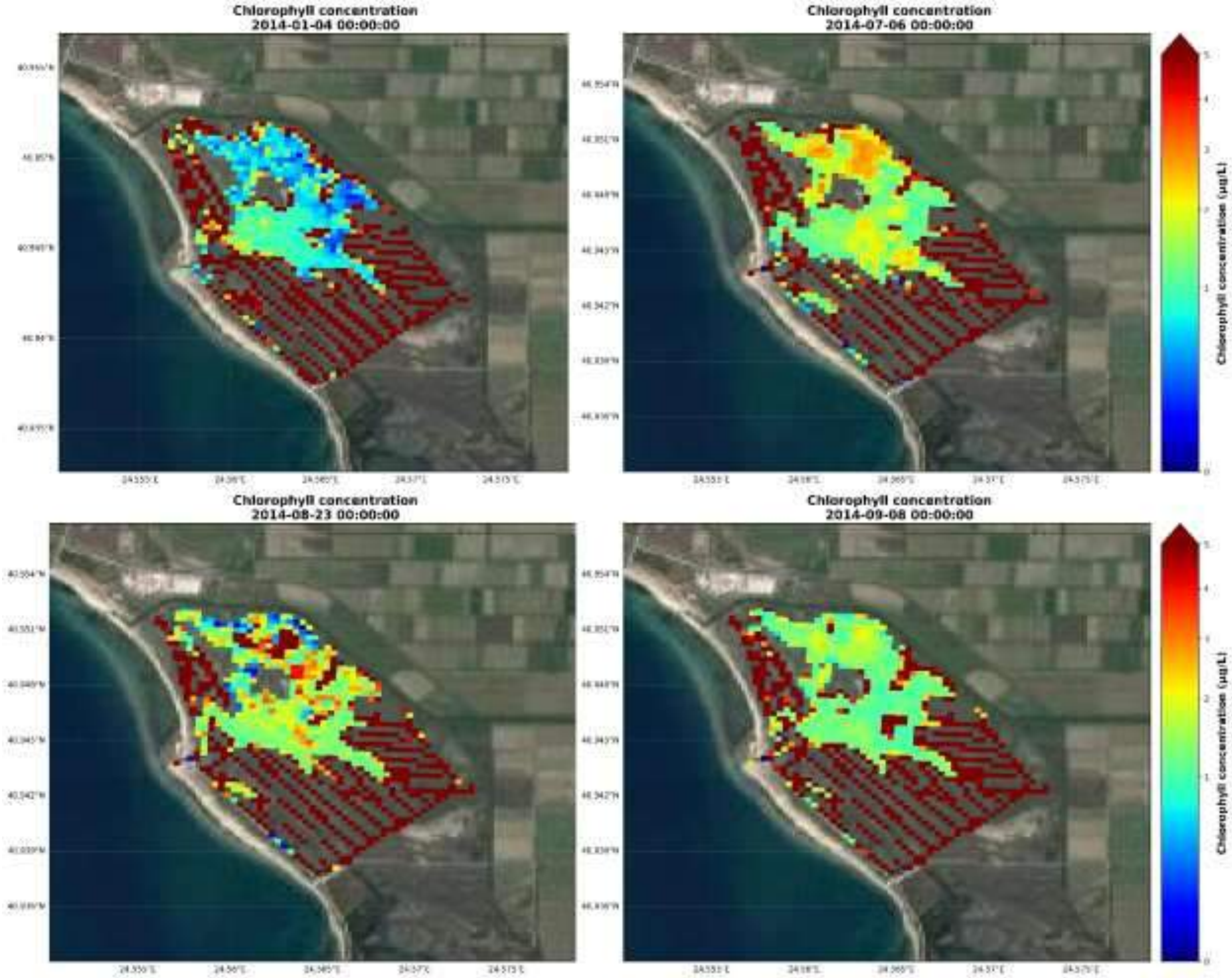

Figure 16. Seasonal evolution of Chl-a concentration in Vassova lagoon for the year 2014, based on Landsat 8 satellite images.

The first half of 2015 is presented in Figure 17 covered by Landsat 8 and the second half is presented in Figure 18 covered by Sentinel 2. During the first half of the year, Chl-a values decreased from January to February and then started increasing again until April.

Higher values are observed in the summer. At the end of the summer, Chl-a decreased until the end of the year, starting from the center of the basin and then spreading towards the coast.

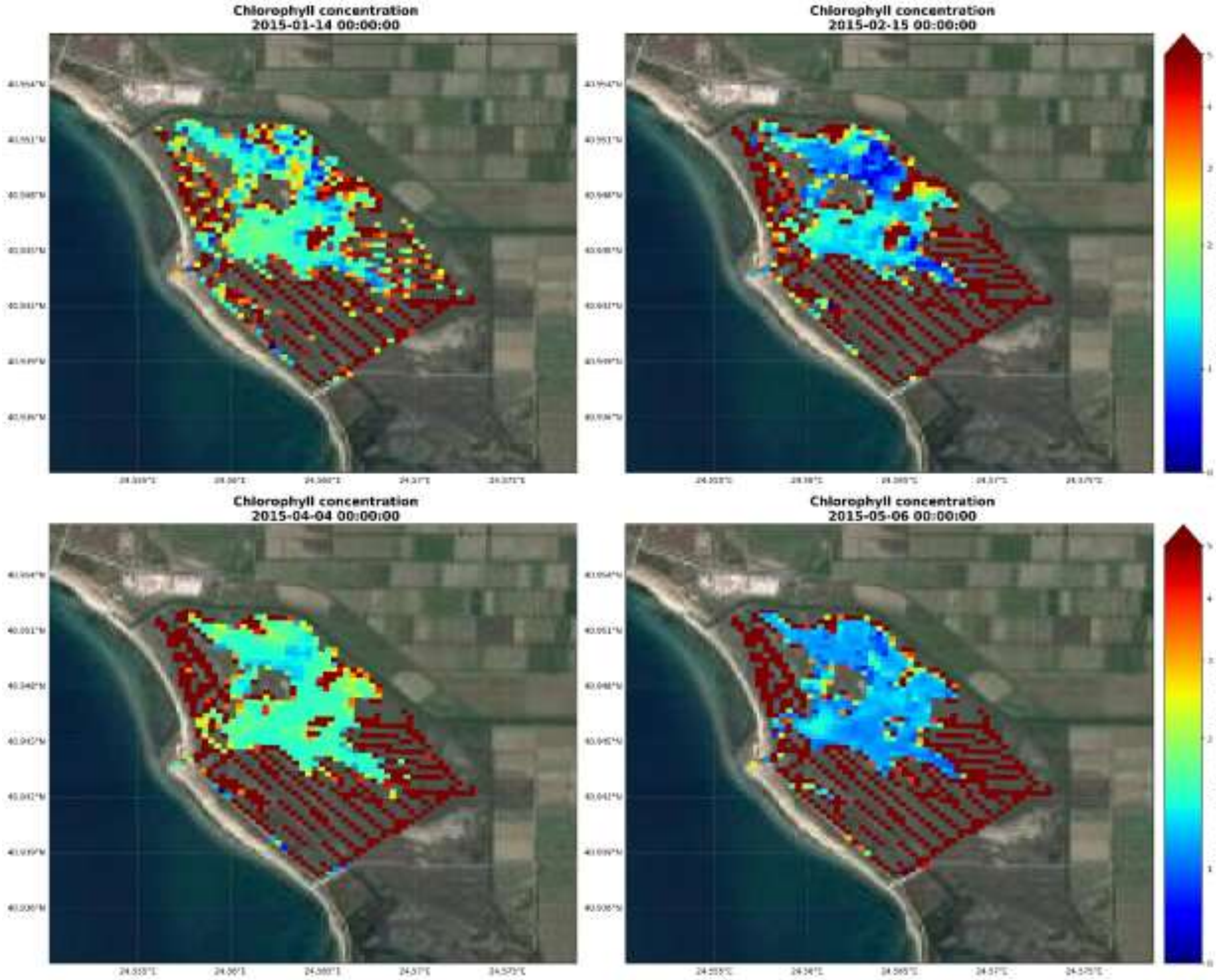

Figure 17. Seasonal evolution of Chl-a concentration in Vassova lagoon for the year 2015, based on Landsat 8 satellite images.

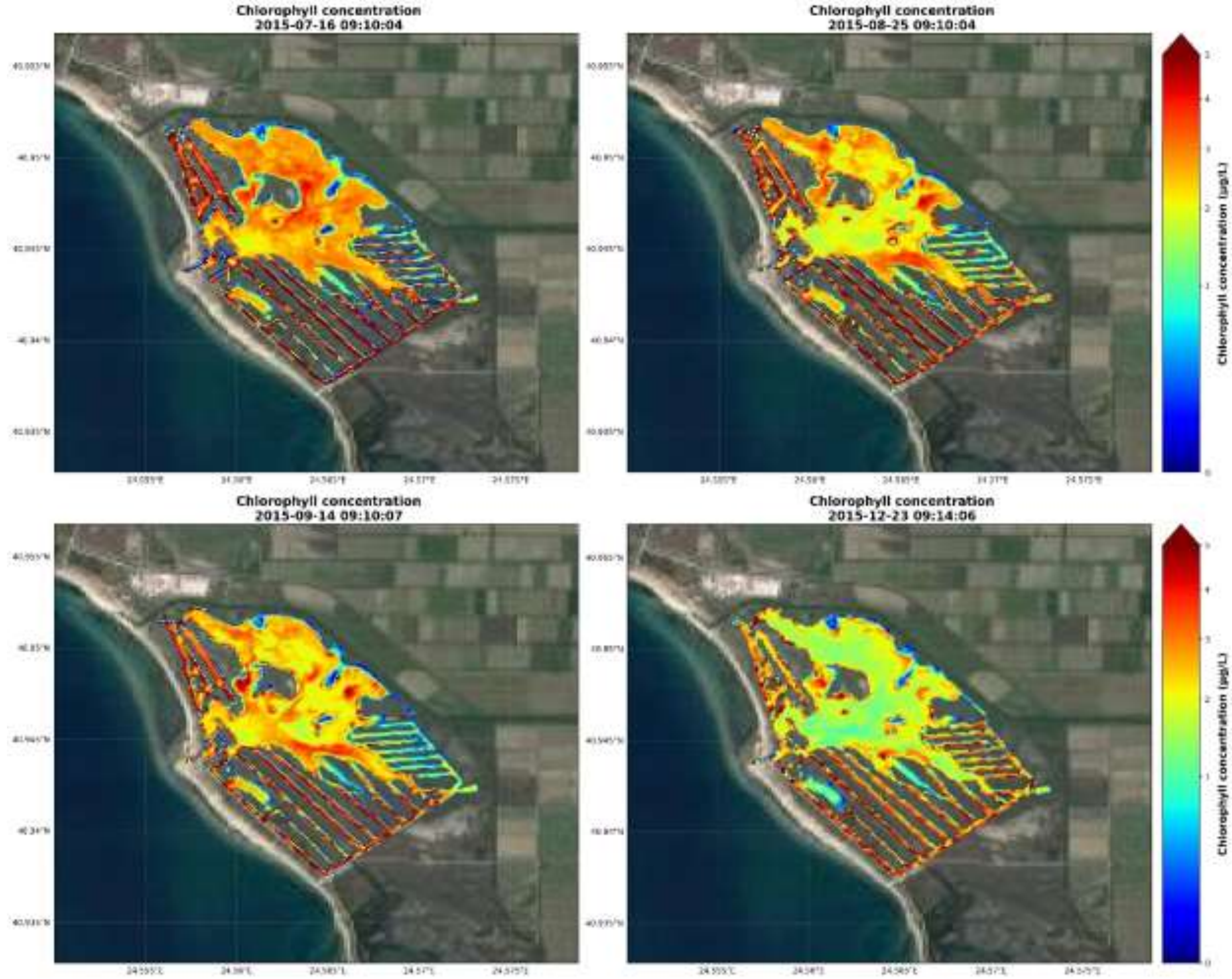

Figure 18. Seasonal evolution of Chl-a concentration in Vassova lagoon for the year 2015, based on Sentinel 2 satellite images.

The same pattern in Chl-a evolution is observed in 2016 (Figure 19), where the higher values are observed in the summer months and the decrease as we move on to the autumn and winter. The Chl-a values in the wintering canals increased in the summer and reached their highest values in September 2016.

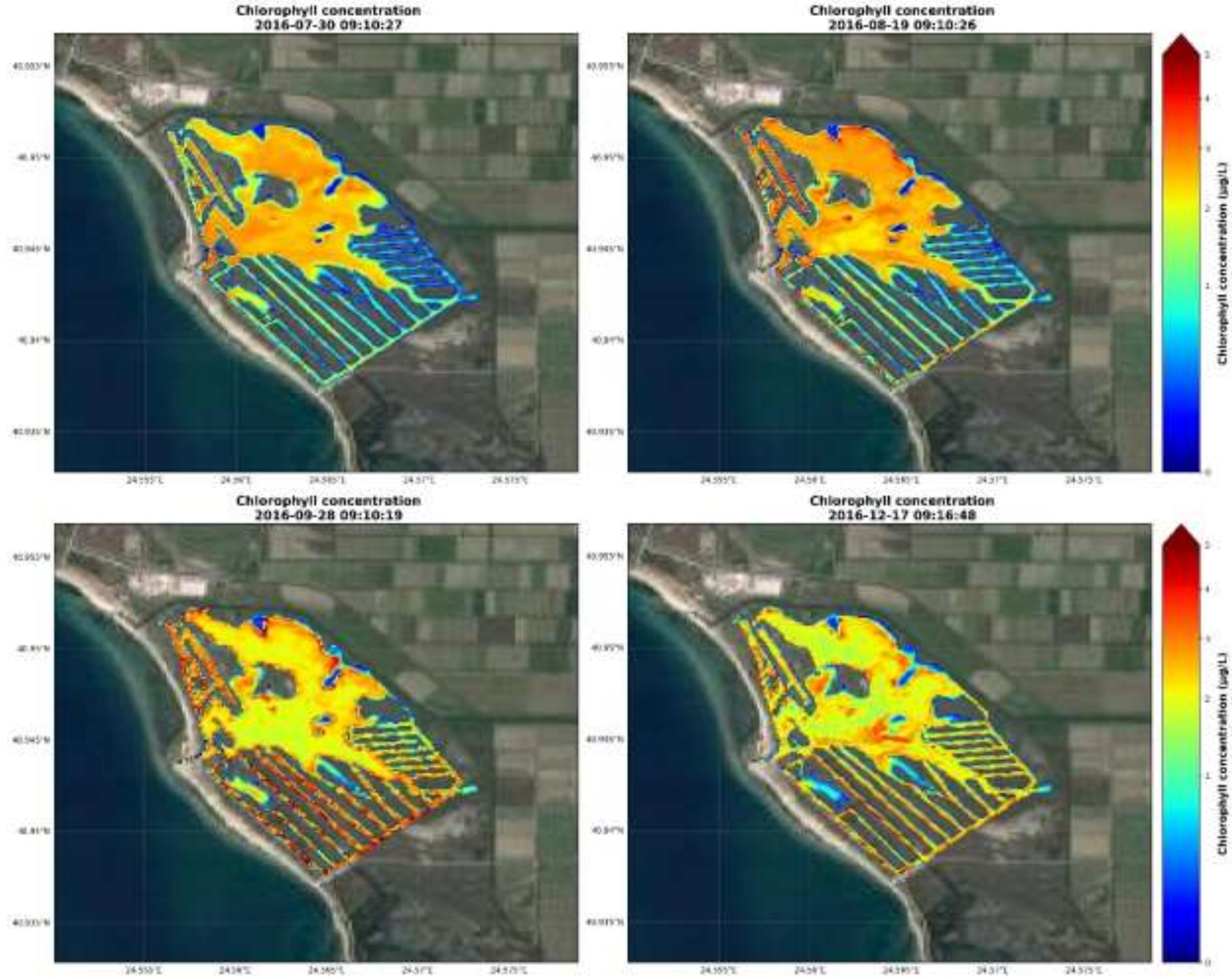

Figure 19. Seasonal evolution of Chl-a concentration in Vassova lagoon for the year 2016, based on Sentinel 2 satellite images.

Figure 20 shows the increase, from the low concentrations from the beginning of the year to the highest in June. The increase begins from the north and then expands to the rest of the basin. In the following months, Chl-a values decreased and then increased again, reaching their highest values in August. In the following months, Chl-a decreases until the end of the year.

The selected images for 2018 (Figure 21) show the increase of Chl-a values, from low concentrations at the beginning of the year until the summer, where the highest values occur in August. The highest values are observed at the center of the basin. In the following months, Chl-a values decrease until December.

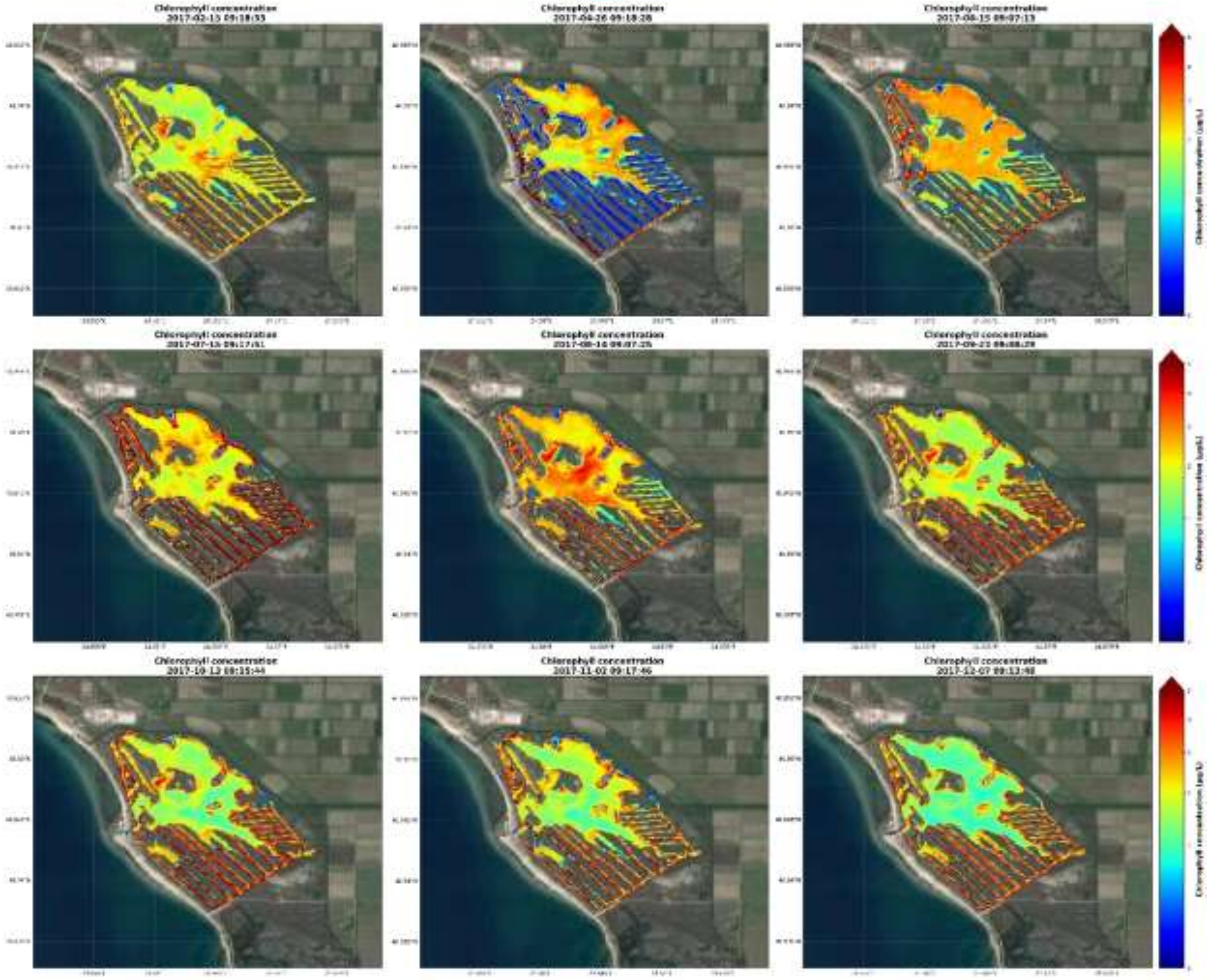

Figure 20. Seasonal evolution of Chl-a concentration in Vassova lagoon for the year 2017, based on Sentinel 2 satellite images.

Years 2019-2021 show a similar pattern in Chl-a values evolution (Figures 19-21). Initially, there is an increase of Chl-a values from January until August and after August, a decrease starts until the end of the year. The Chl-a increase starts from the north shore, then spreads to the center of the basin and ultimately to the wintering canals.

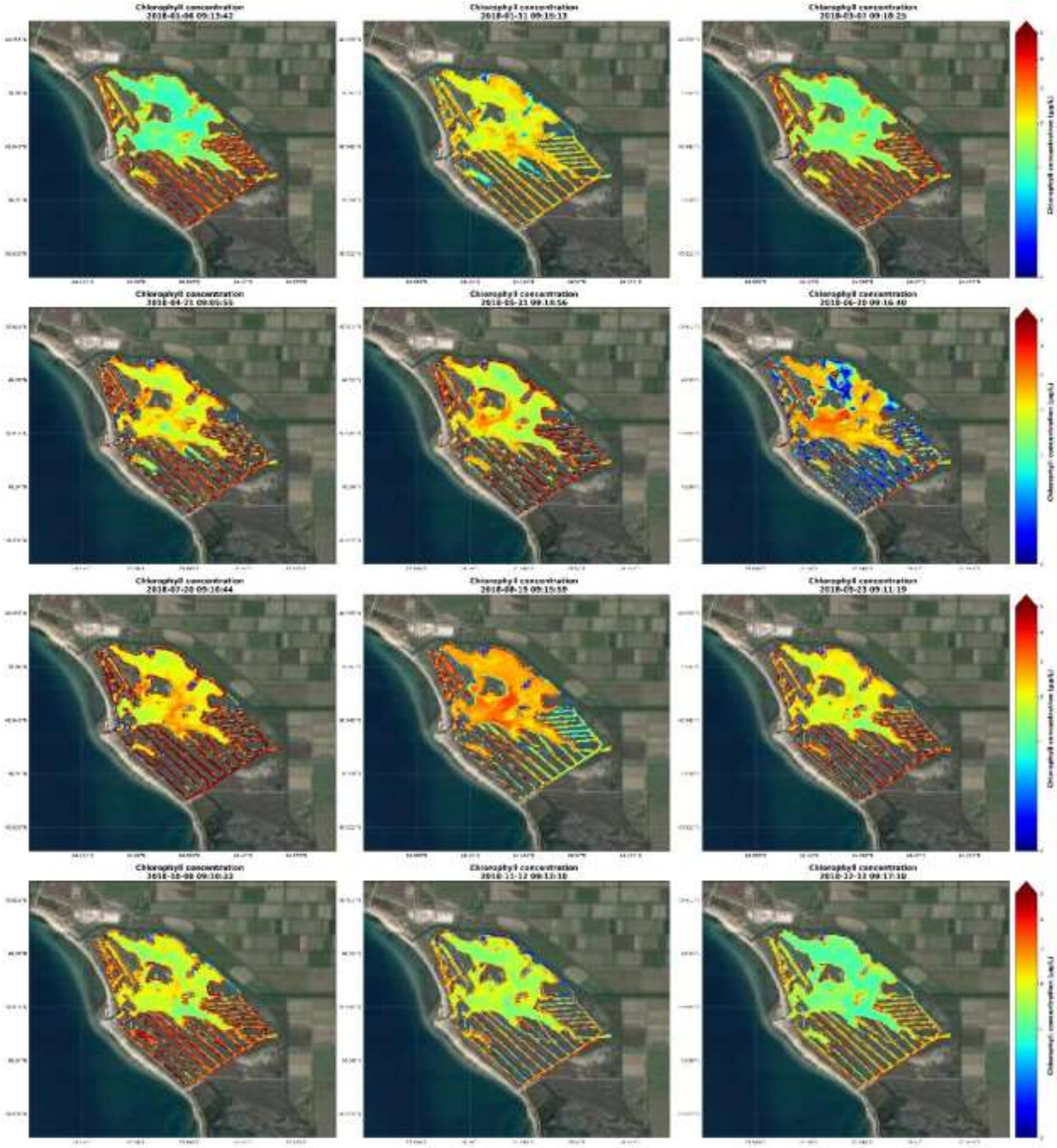

Figure 21. Seasonal evolution of Chl-a concentration in Vassova lagoon for the year 2018, based on Sentinel 2 satellite images.

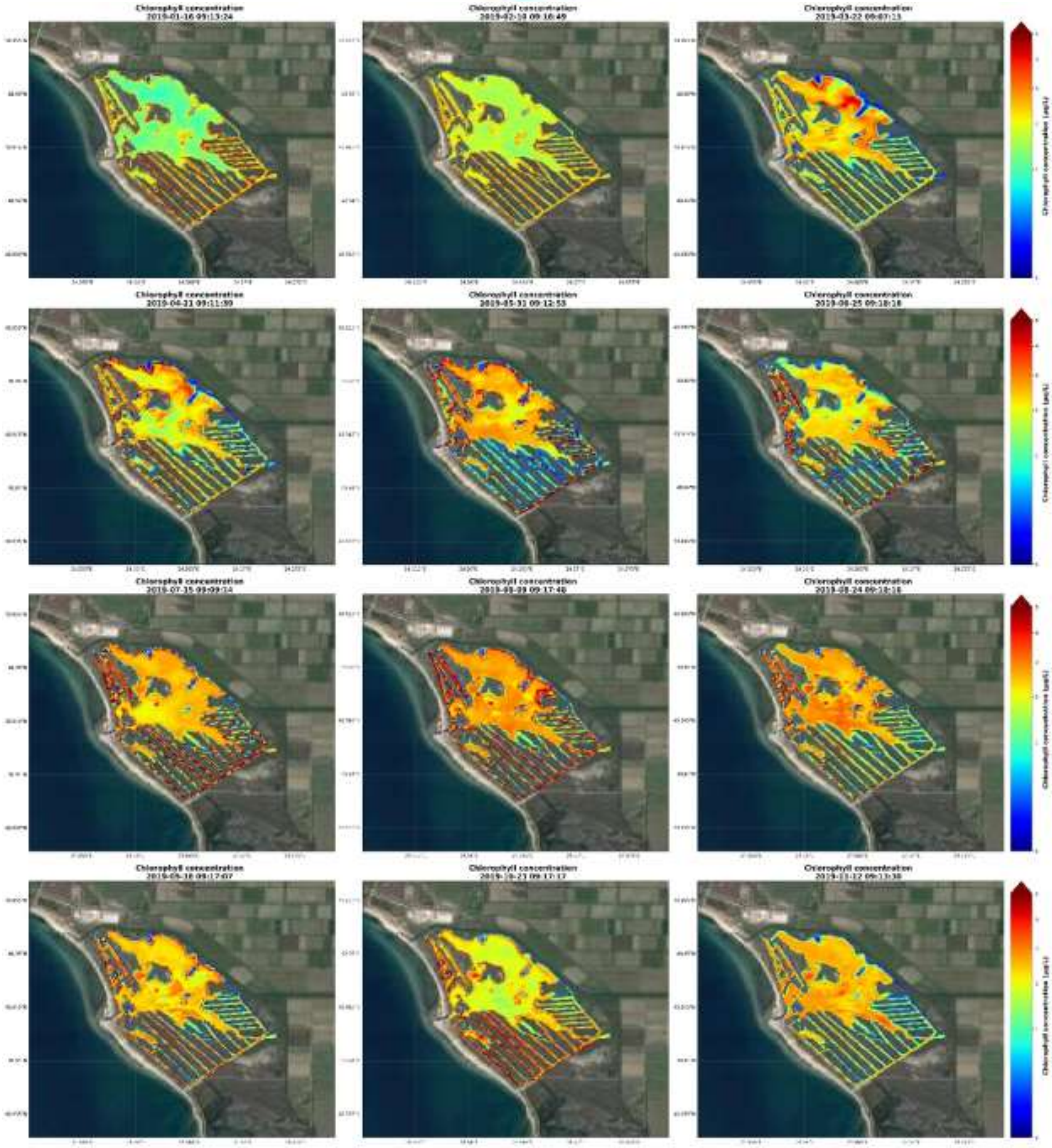

Figure 22. Seasonal evolution of Chl-a concentration in Vassova lagoon for the year 2019, based on Sentinel 2 satellite images.

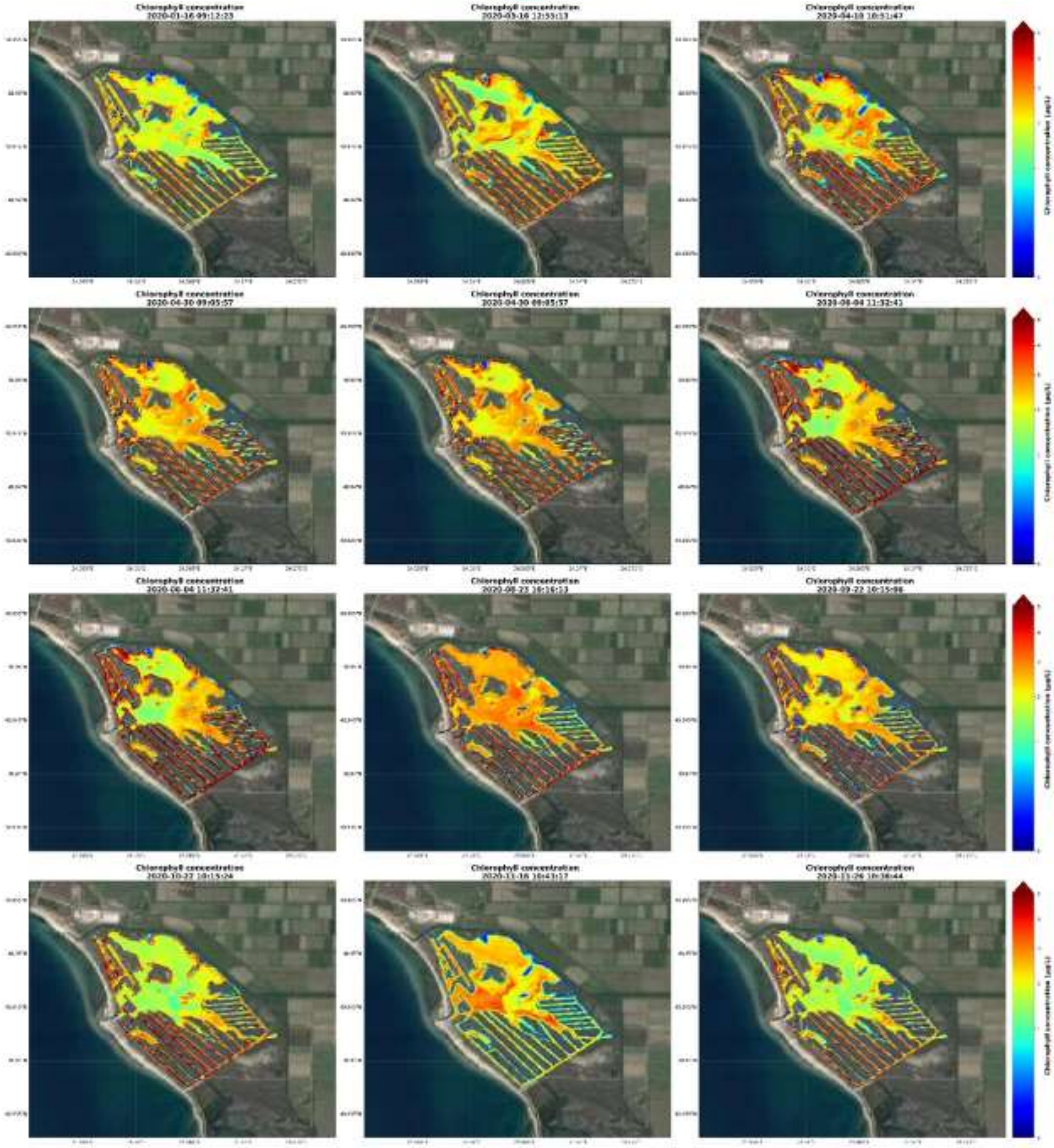

Figure 23. Seasonal evolution of Chl-a concentration in Vassova lagoon for the year 2020, based on Sentinel 2 satellite images.

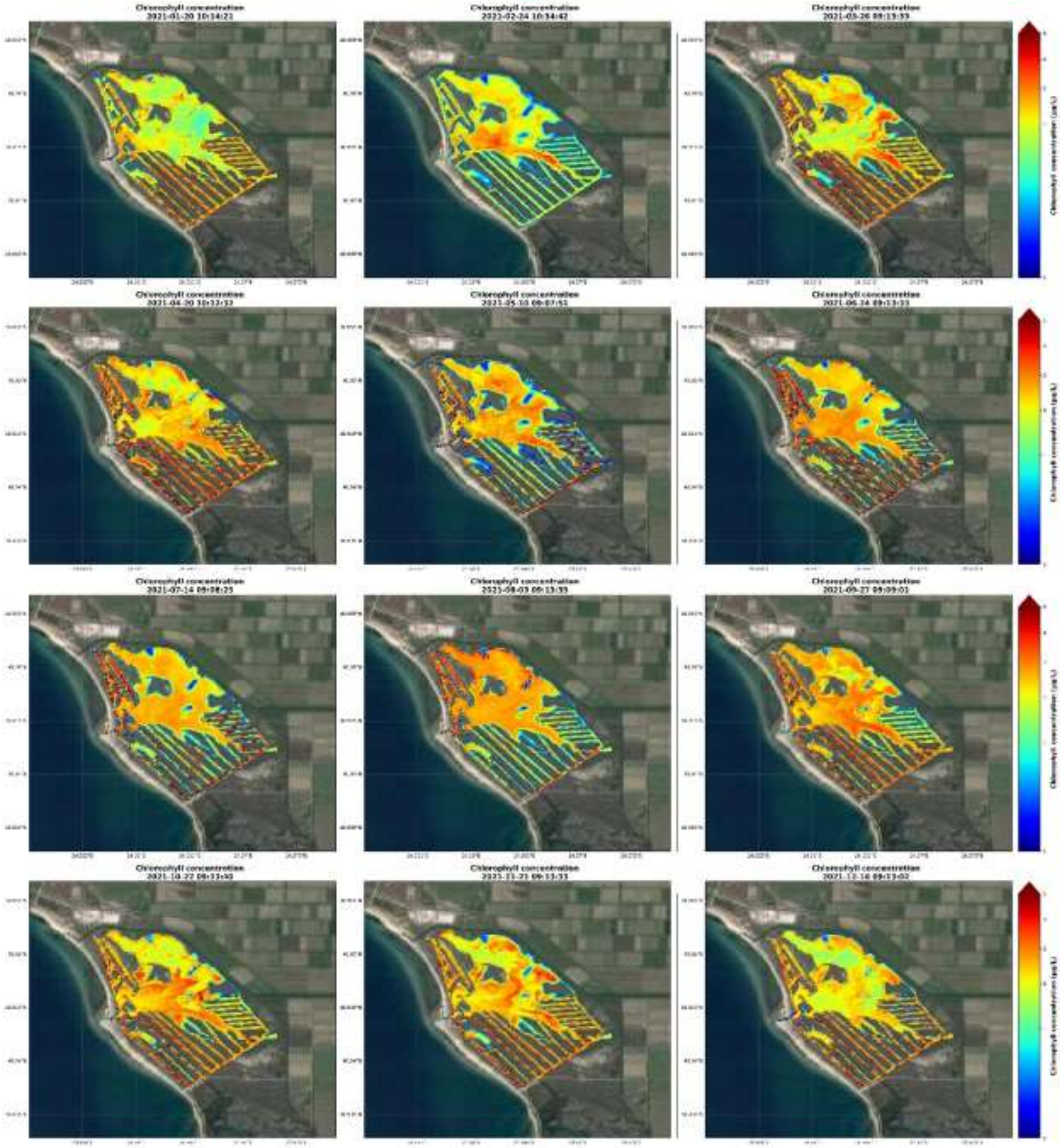

Figure 24. Seasonal evolution of Chl-a concentration in Vassova lagoon for the year 2021, based on Sentinel 2 satellite images.

3.1.2 Eratino lagoon

Figures 22-31 show the spatial distribution of Chl-a in Eratino lagoon for the years 2013-2021. During 2013 (Figure 25), the highest Chl-a concentration values were reached in July (up to 4.0 µg/l). The increase in Chl-a concentration started from the center of the basin and in the following summer months moved to the eastern and the southern parts of the lagoon.

In autumn and winter months, the Chl-a values decreased, with the northern and the southern parts having higher values than the center of the basin.

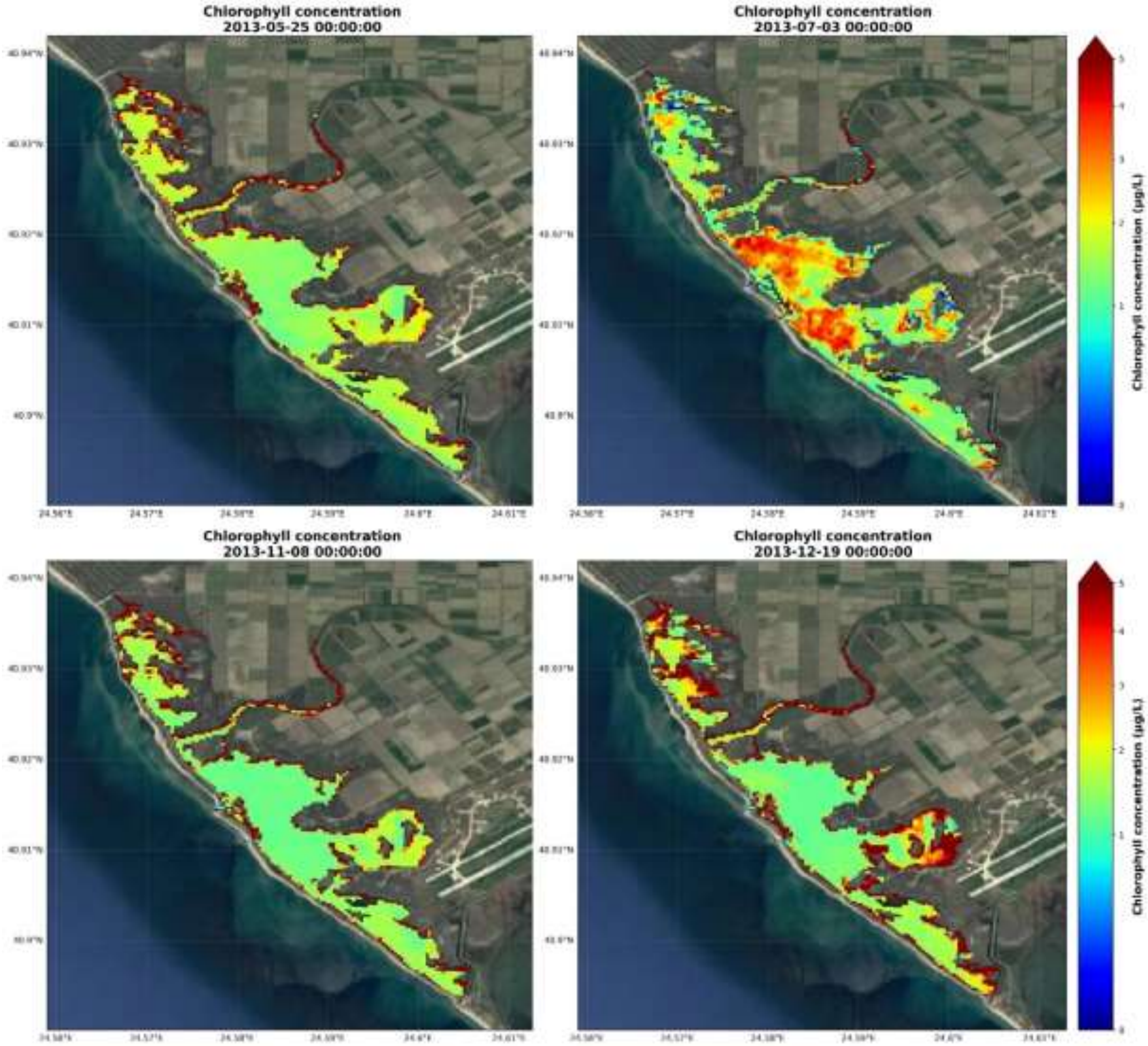

Figure 25. Seasonal evolution of Chl-a concentration in Eratino lagoon for the year 2013, based on Landsat 8 satellite images.

During 2014 (Figure 26), the Chl-a values were low from January to early July when they showed an increase at the northern part of the basin. The Chl-a values continued to increase and they reached the highest values in December 2014 (2.2 μg/l).

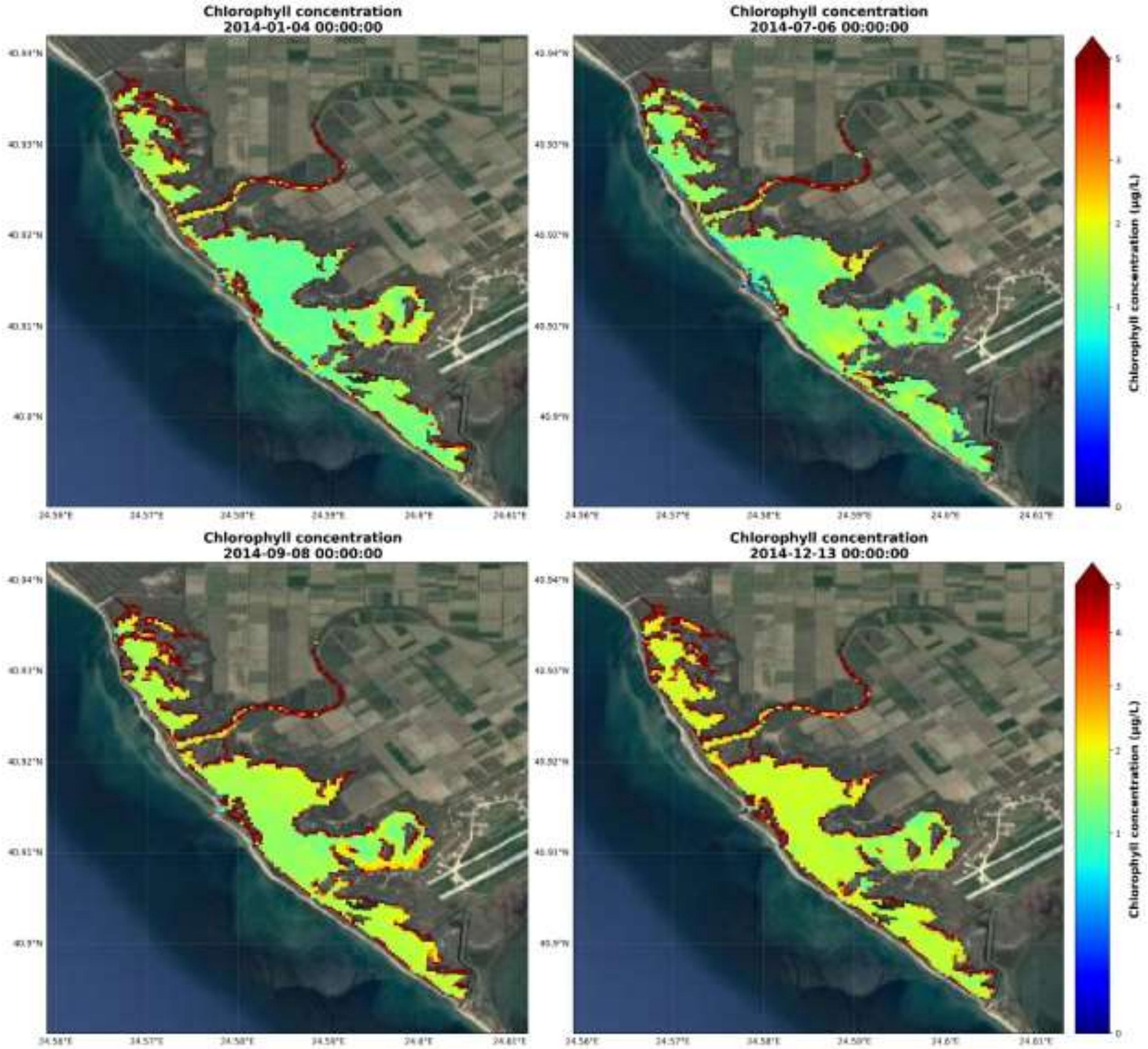

Figure 26. Seasonal evolution of Chl-a concentration in Eratino lagoon for the year 2014, based on Landsat 8 satellite images.

The first half of 2015 is presented in Figure 27 covered by Landsat 8 and the second half is presented in Figure 28 covered by Sentinel 2. The highest values were detected in December 2014, led to similarly high values in January 2015 (Figure 27). Chl-a values decreased from January to February and then started increasing again until April. In April the bottom part of the lagoon shows lower concentrations (1.0-2.0 μg/l).

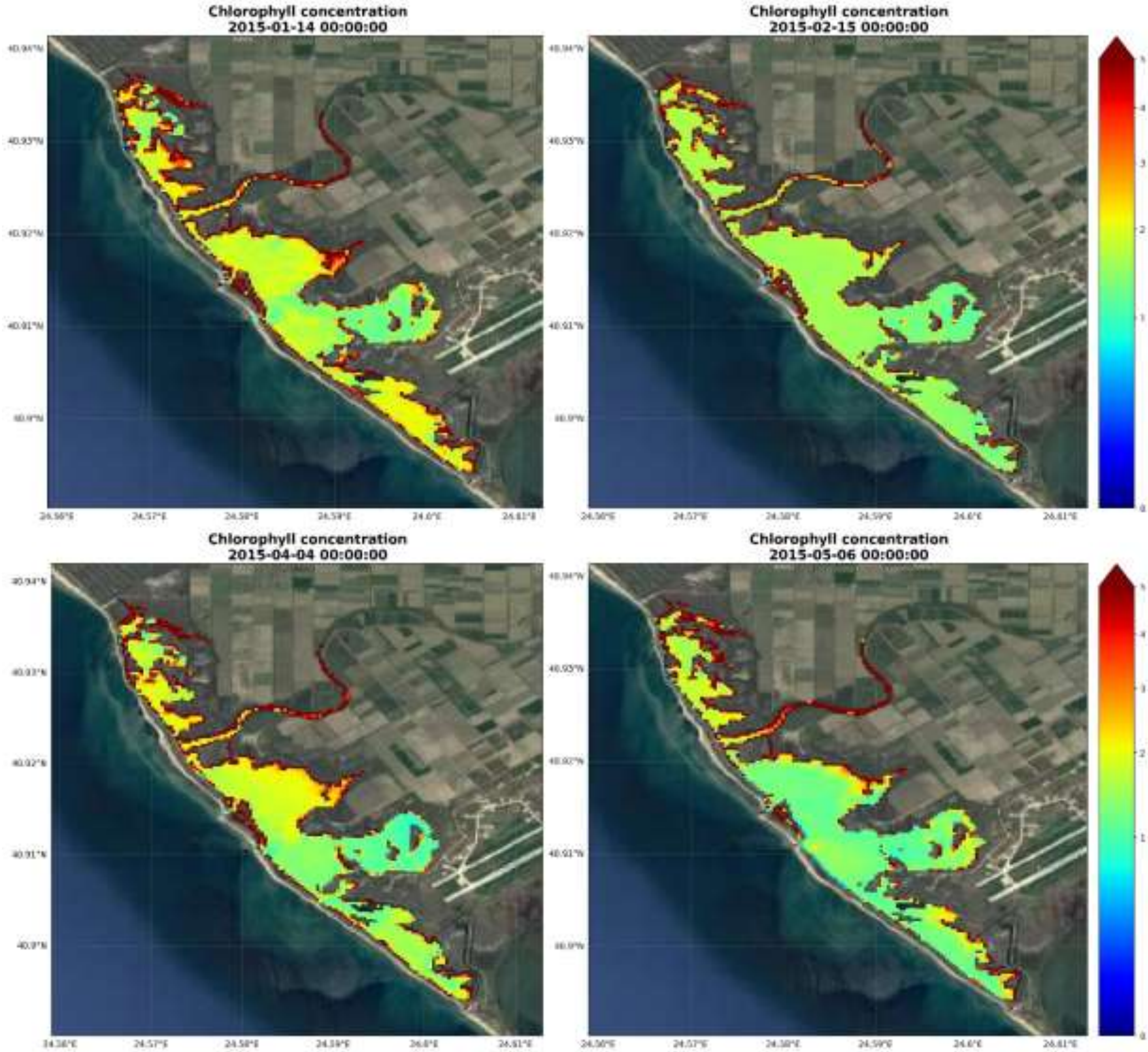

Figure 27. Seasonal evolution of Chl-a concentration in Eratino lagoon for the year 2015, based on Landsat 8 satellite images.

Figure 28 shows that the higher values are observed during the summer. At the end of the summer Chl-a deceased until the end of the year, with the exception of the southeast part, which seems to retain higher values compared to the rest of the basin.

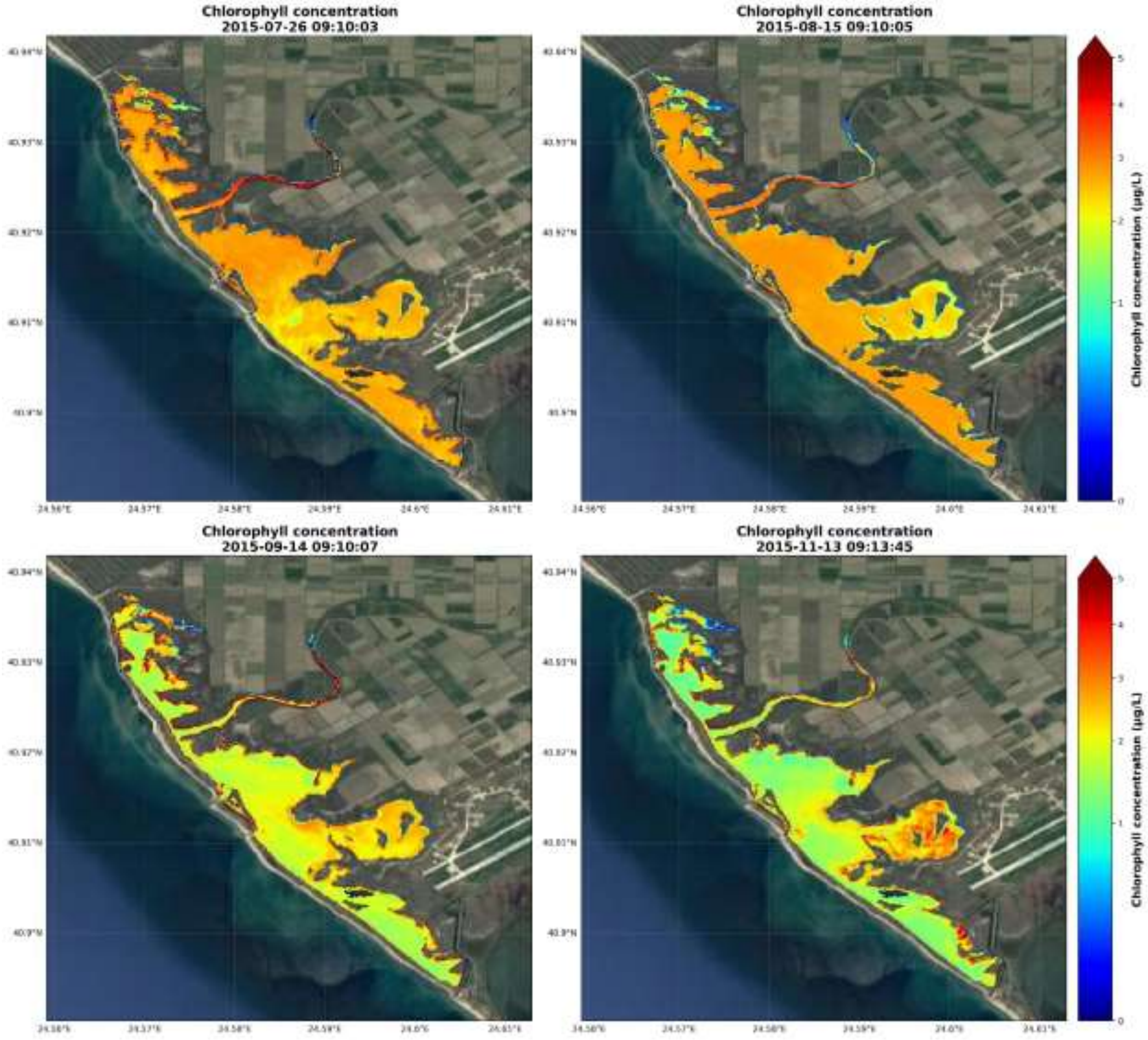

Figure 28. Seasonal evolution of Chl-a concentration in Eratino lagoon for the year 2015, based on Sentinel 2 satellite images.

The same pattern in Chl-a evolution is observed in 2016, where the higher values are observed in the summer months and they decrease as we move on to the autumn and winter. The higher values at the eastern parts in the autumn and winter months are also observed in 2016 (Figure 29).

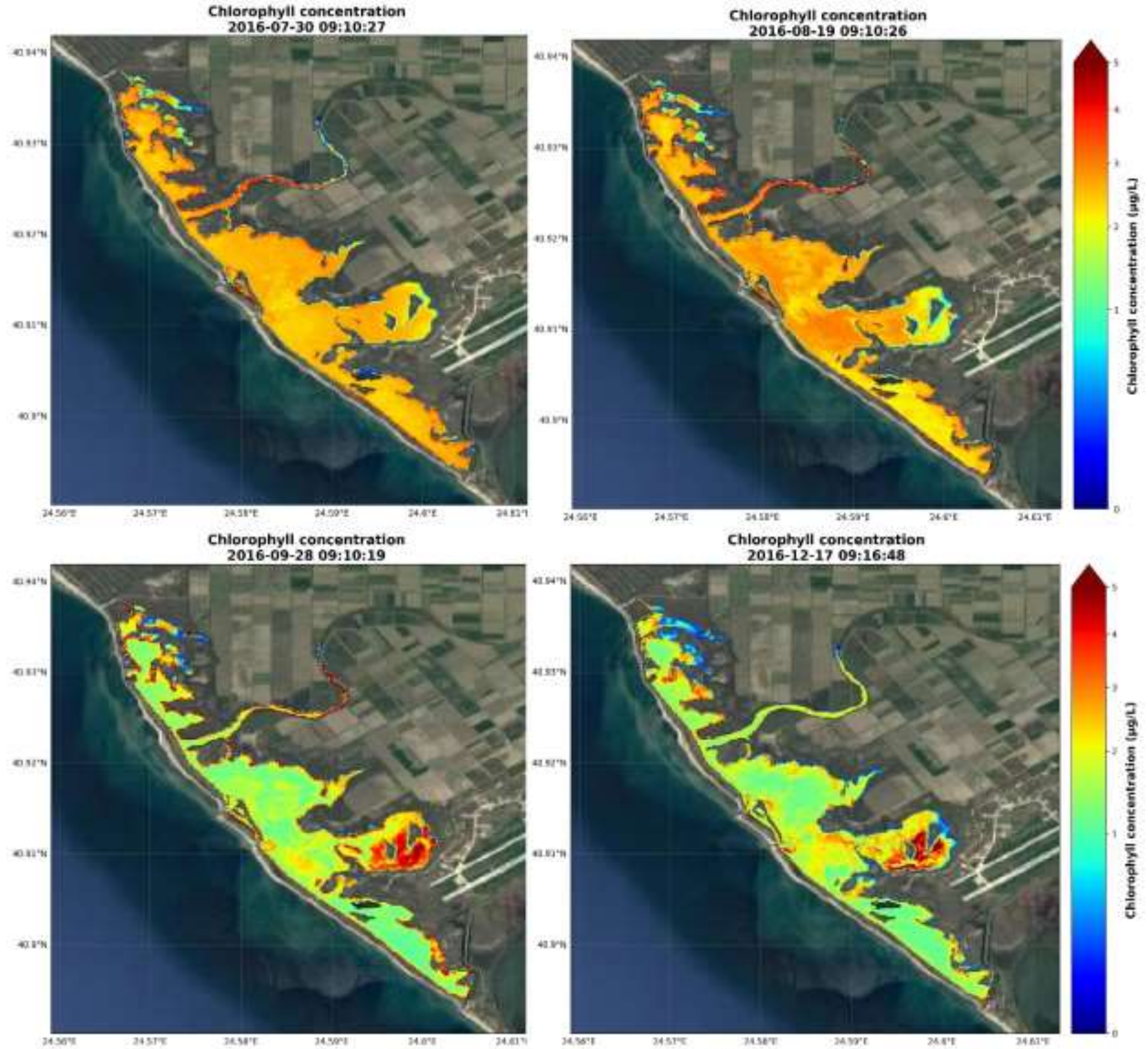

Figure 29. Seasonal evolution of Chl-a concentration in Eratino lagoon for the year 2016, based on Sentinel 2 satellite images.

Figure 30 shows the increase, from the low concentrations from the beginning of the year to the highest in June. The increase begins from the south and then expands to the rest of the basin. In the following months, Chl-a values decreased until the lowest level was reached at the end of autumn. At the end of December, a small increase in Chl-a is observed. The southeast part keeps showing higher values compared to the rest of the lagoon.

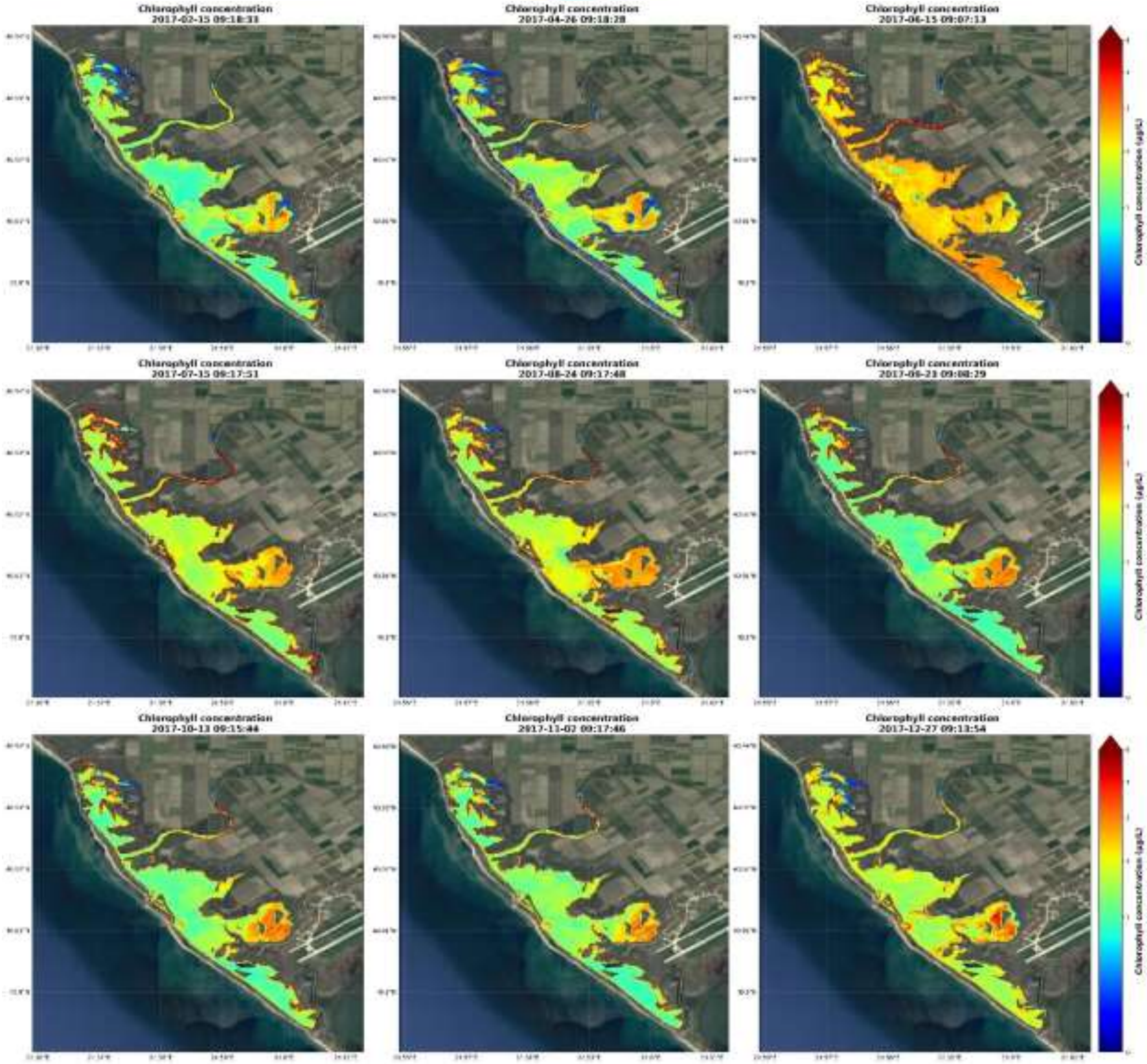

Figure 30. Seasonal evolution of Chl-a concentration in Eratino lagoon for the year 2017, based on Sentinel 2 satellite images.

Figure 31 shows the temporal and spatial evolution during 2018. Chl-a values are low at the beginning of the year and increase gradually until late May. The highest values are observed at the center of the basin. In the following months, Chl-a values decrease and then increase again until they reach the highest values at the end of the summer. Another peak is observed in November.

In 2019 (Figure 32), the first increase in Chl-a starts in late March and remains until late June. Then the Chl-a values slightly decrease in July and increase again in late August. The last maximum in Chl-a values is observed in November.

The slightly higher values detected in December 2019 led to high values in January 2020 (Figure 33). The first Chl-a peak is observed in March 2020 and concentration remains high until the end of the summer. The highest Chl-a values are reached in May 2020. Then Chl-a decreases until November. In mid-November, another maximum is reached (2.5-3.5 µg/l).

During 2021 (Figure 34), maximum Chl-a values are reached in February (2.5-3.5 µg/l) and then in May (2.5-4.5 µg/l). Higher values localize at the center part of the lagoon. In the following months, the Chl-a values decrease until the end of the year.

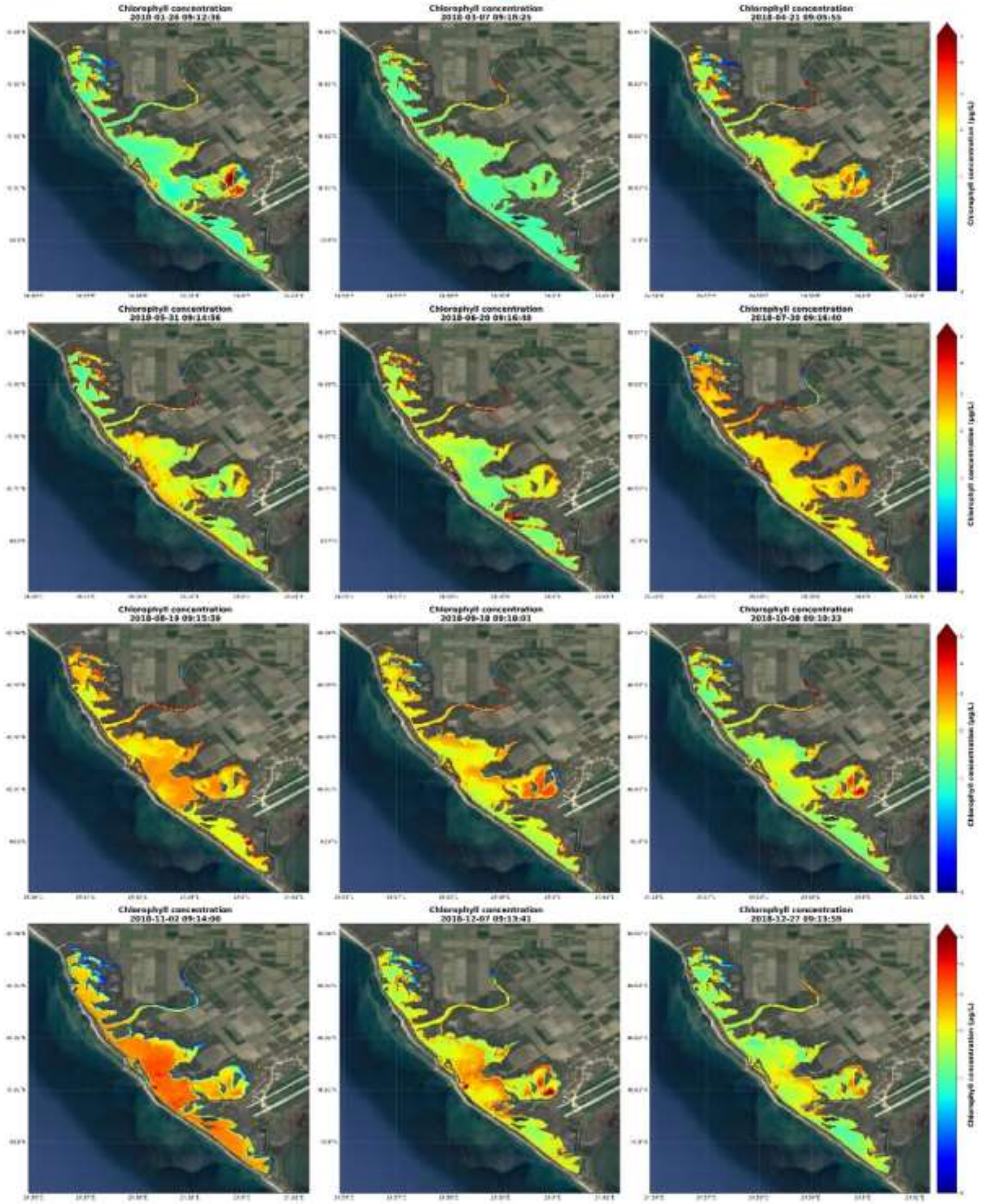

Figure 31. Seasonal evolution of Chl-a concentration in Eratino lagoon for the year 2018, based on Sentinel 2 satellite images.

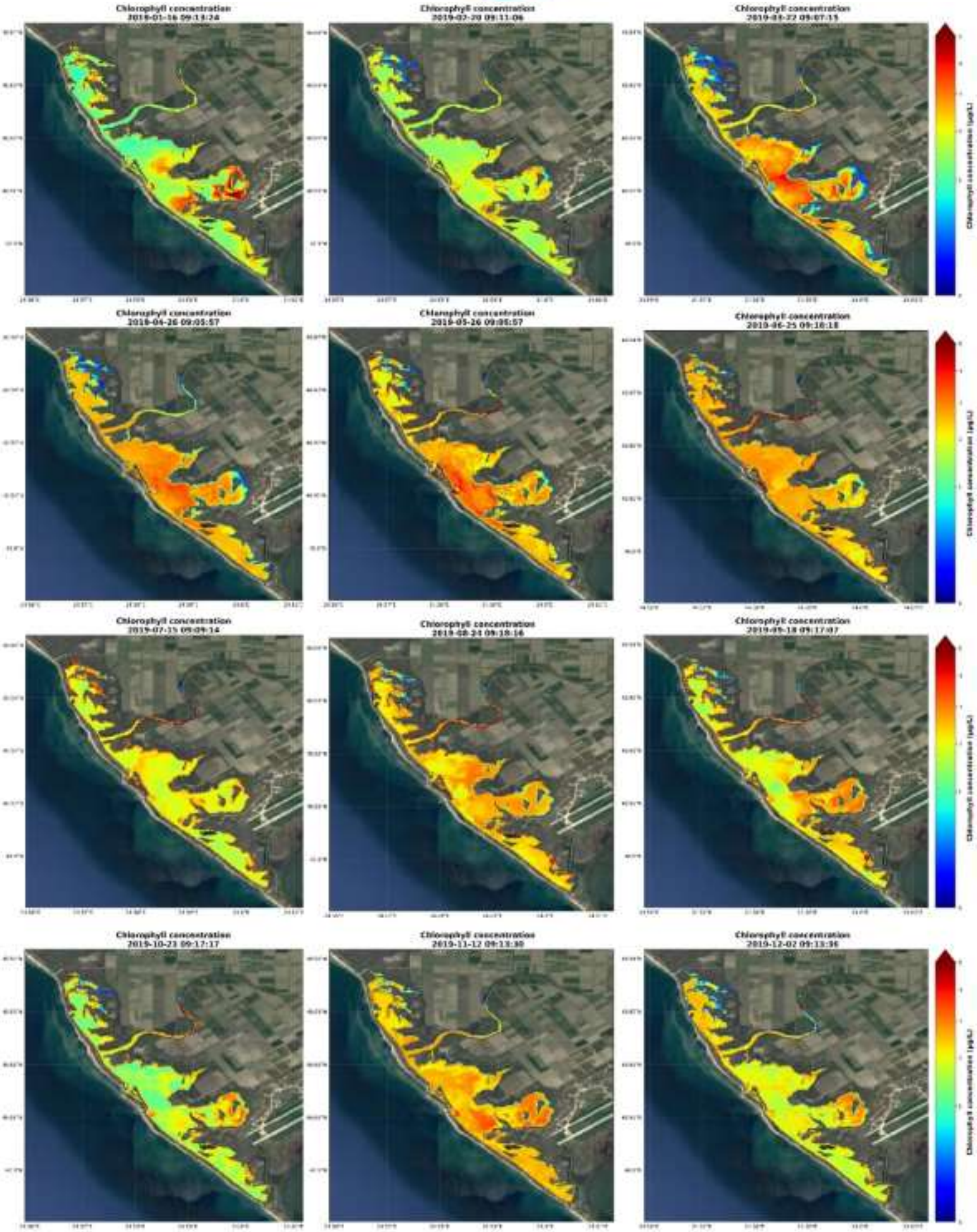

Figure 32. Seasonal evolution of Chl-a concentration in Eratino lagoon for the year 2019, based on Sentinel 2 satellite images.

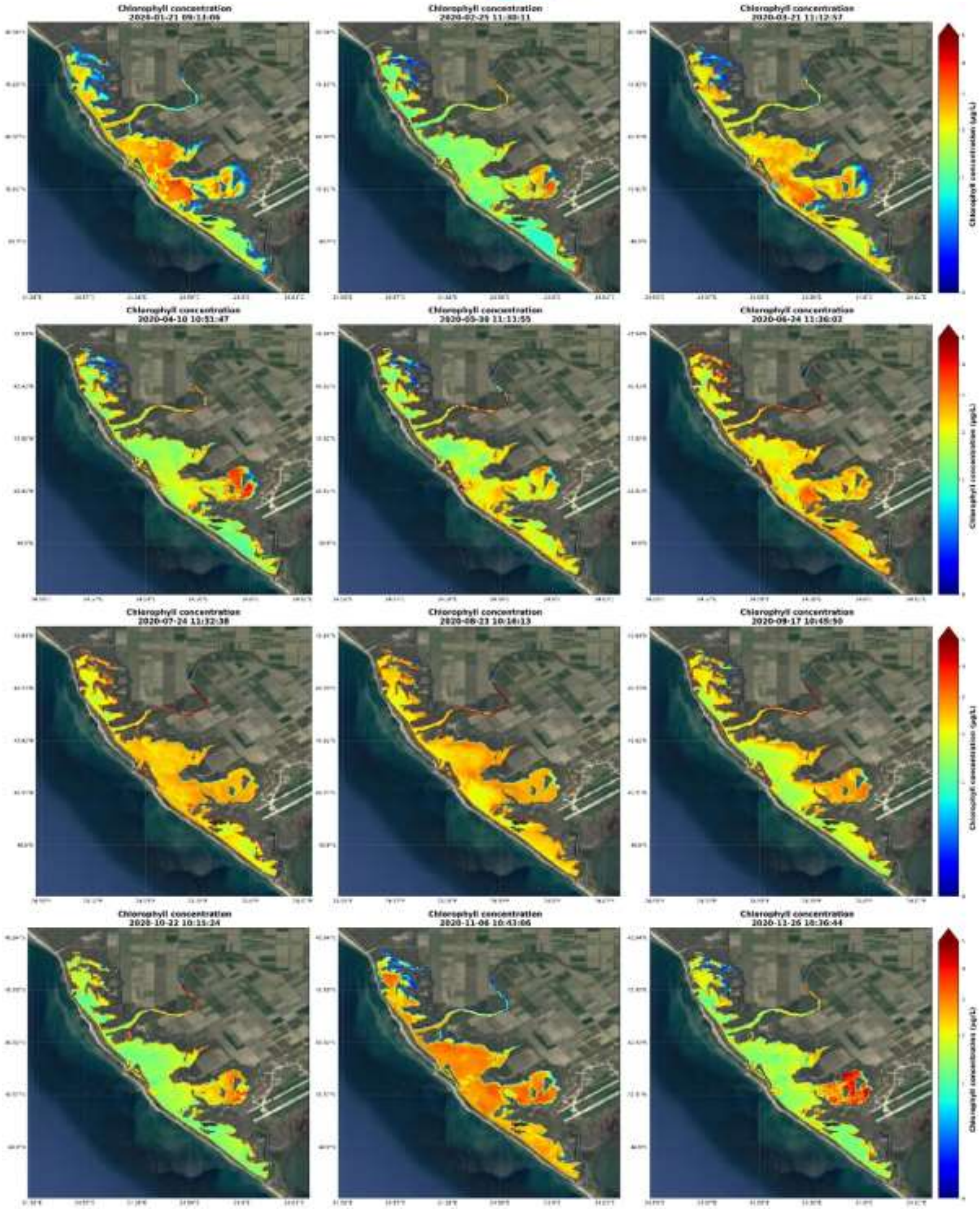

Figure 33. Seasonal evolution of Chl-a concentration in Eratino lagoon for the year 2020, based on Sentinel 2 satellite images.

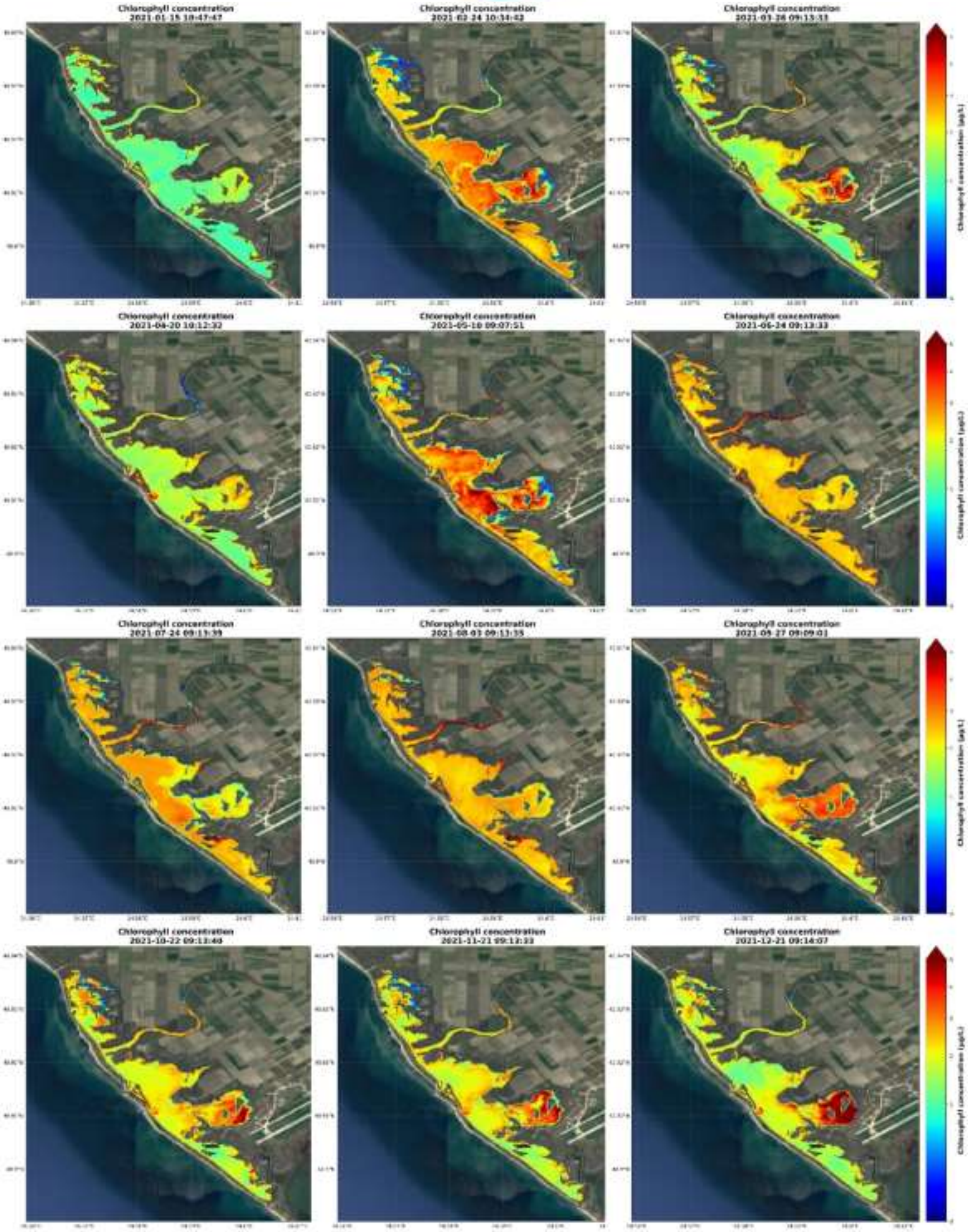

Figure 34. Seasonal evolution of Chl-a concentration in Eratino lagoon for the year 2021, based on Sentinel 2 satellite images.

3.1.3 Agiasma lagoon

Figures 32-41 show the spatial distribution of Chl-a in Agiasma lagoon for the years 2013-2021. In April 2013, high Chl-a values are determined at the western part of the lagoon (up to 45 μg/l), however low values are detected in the rest basin (around 1.5 μg/l). In July Chl-a increases, starting from the center of the lagoon. In the following months, Chl-a values decrease.

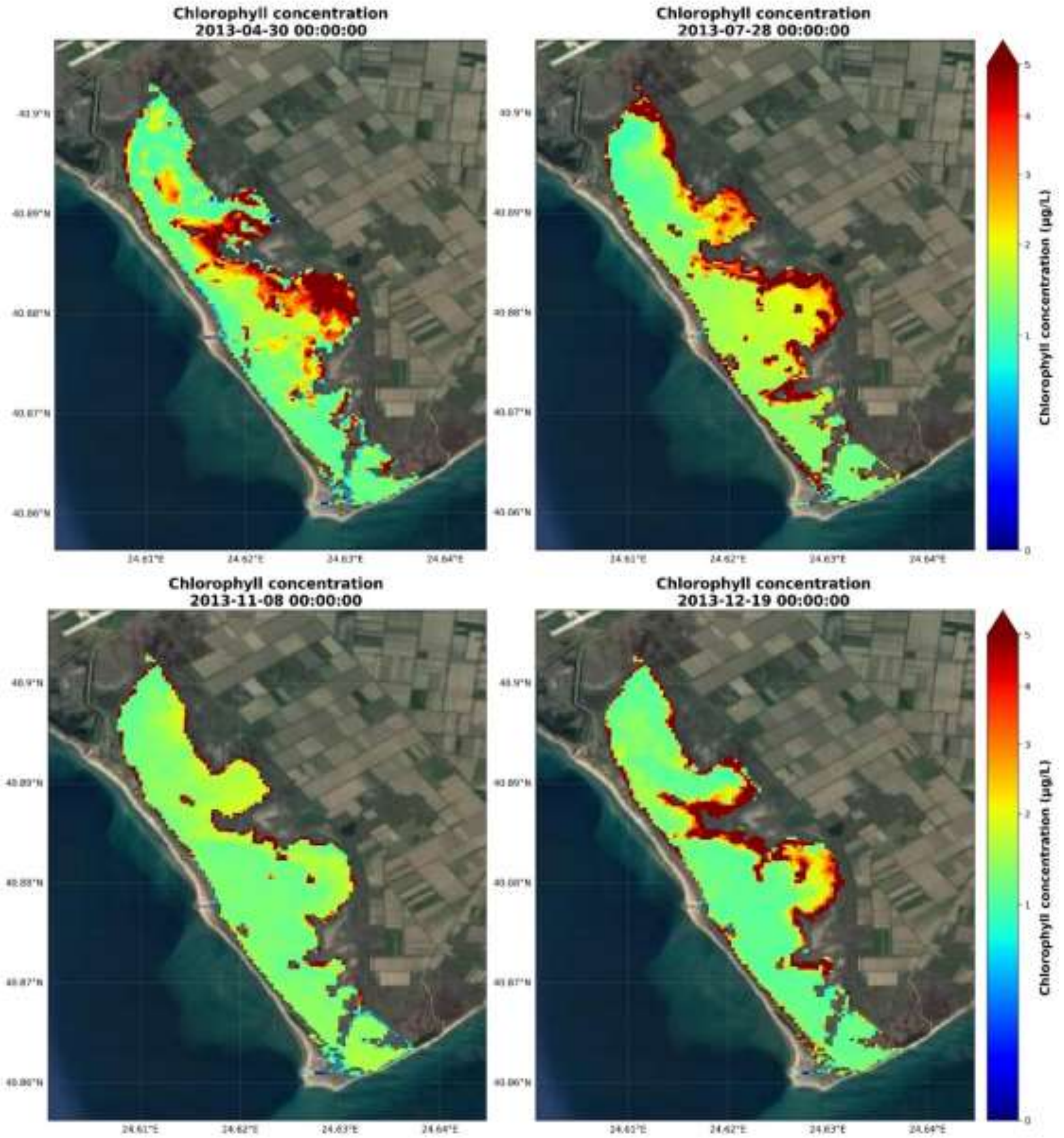

Figure 35. Seasonal evolution of Chl-a concentration in Agiasma lagoon for the year 2013, based on Landsat 8 satellite images.

The available images for 2014 (Figure 36) show an increase from May to the highest values in August. Higher values are detected in the northern and western parts of the lagoon (2.5-5.0 µg/l) and lower at the southern parts (1.0-1.8 µg/l). In the following months, Chl-a values decreased until the end of the year.

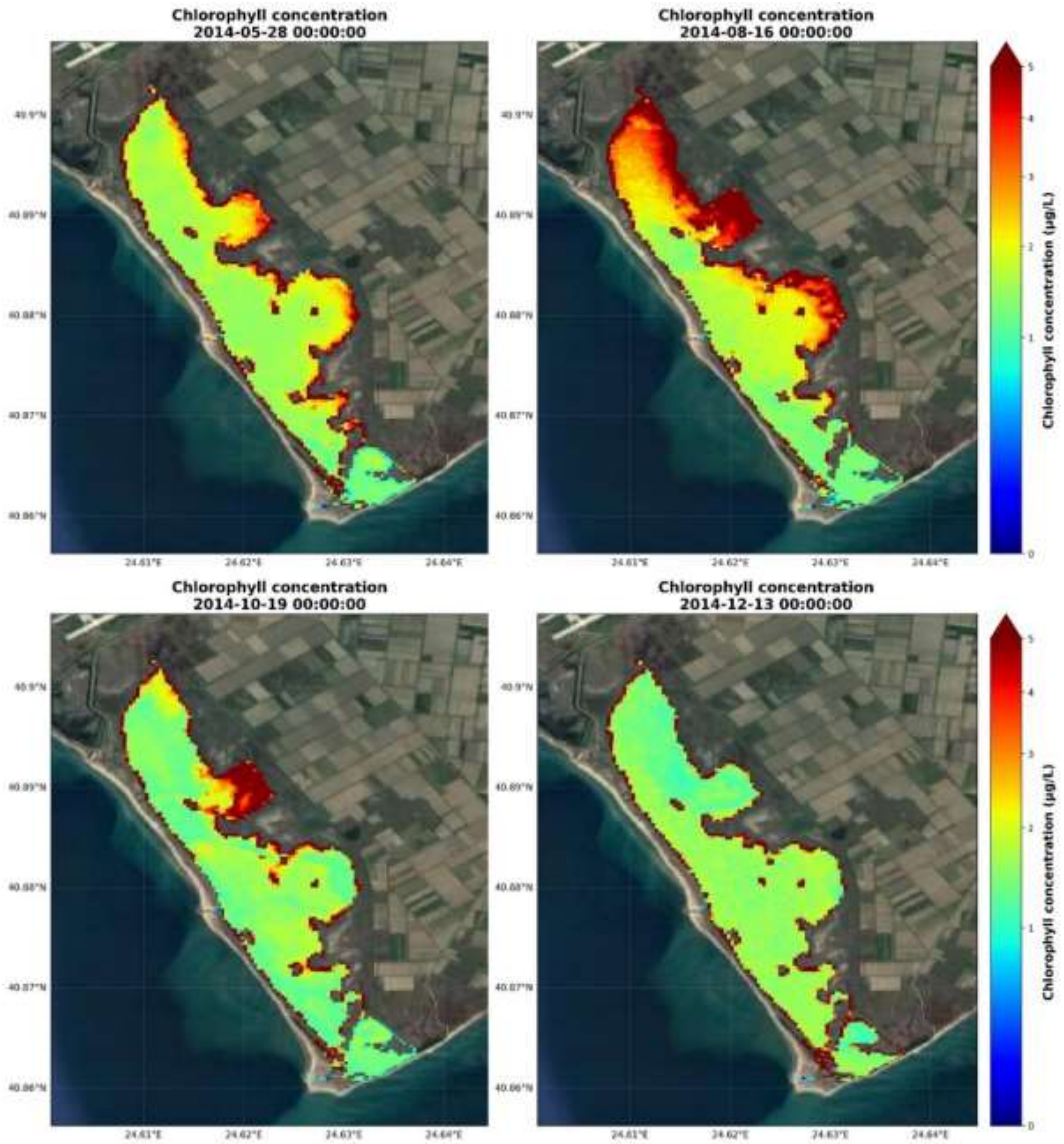

Figure 36. Seasonal evolution of Chl-a concentration in Agiasma lagoon for the year 2014, based on Landsat 8 satellite images.

The first half of 2015 is presented in Figure 37 covered by Landsat 8 and the second half is presented in Figure 38 covered by Sentinel 2. During the first half of the year, Chl-a values decrease from January to February and then started increasing again until late May. In May the south-eastern parts of the lagoon shows lower concentrations (1.2 μg/l), compared to the rest of the basin (2.0-5.0 μg/l)

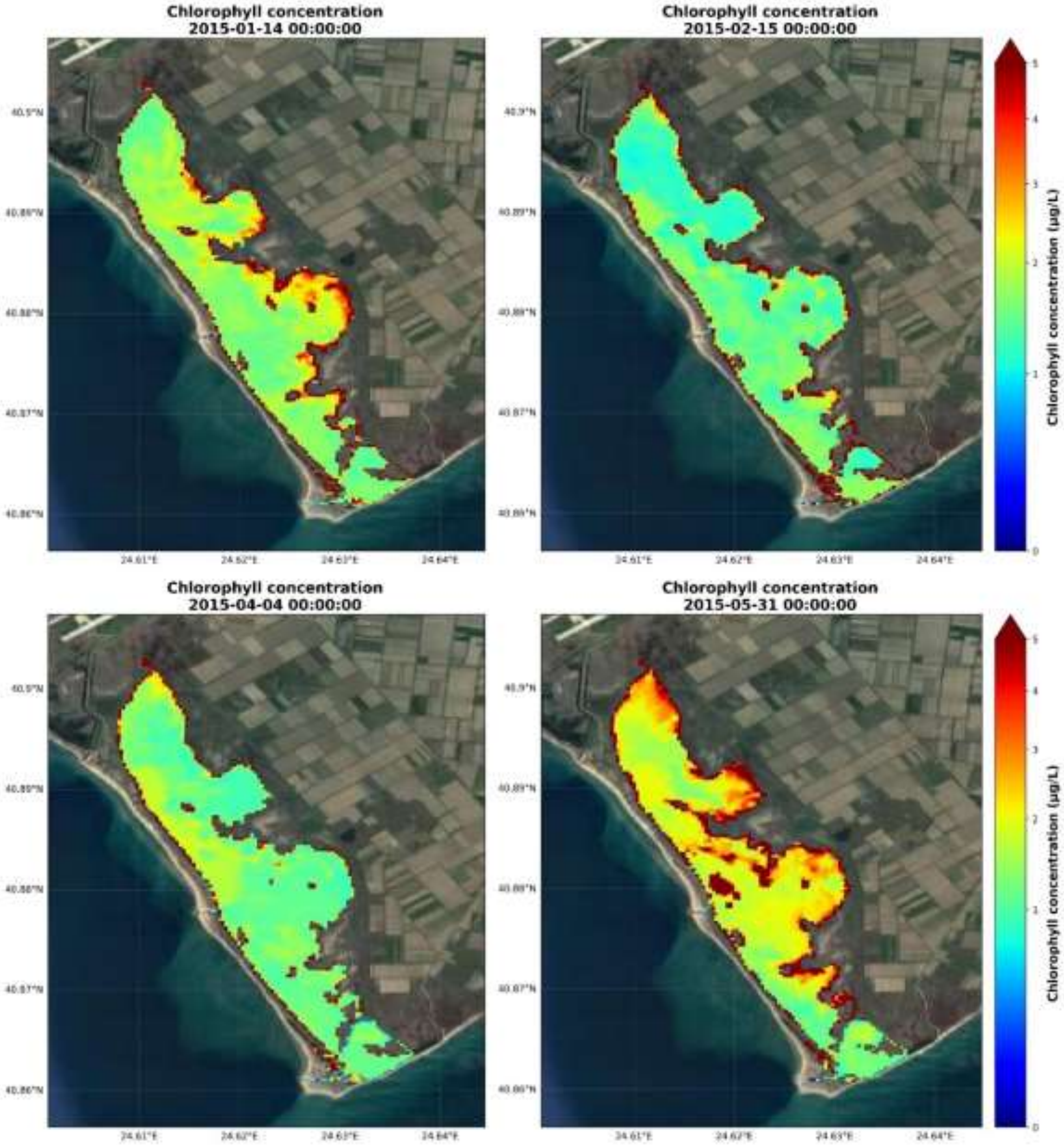

Figure 37. Seasonal evolution of Chl-a concentration in Agiasma lagoon for the year 2015, based on Landsat 8 satellite images.

For the second half of 2015 (Figure 38), higher Chl-a values are observed during the summer. At the end of the summer, Chl-a deceased until the end of the year, with the exception of the northern part, which seems to retain higher values compared to the rest of the basin (3.5 μg/l).

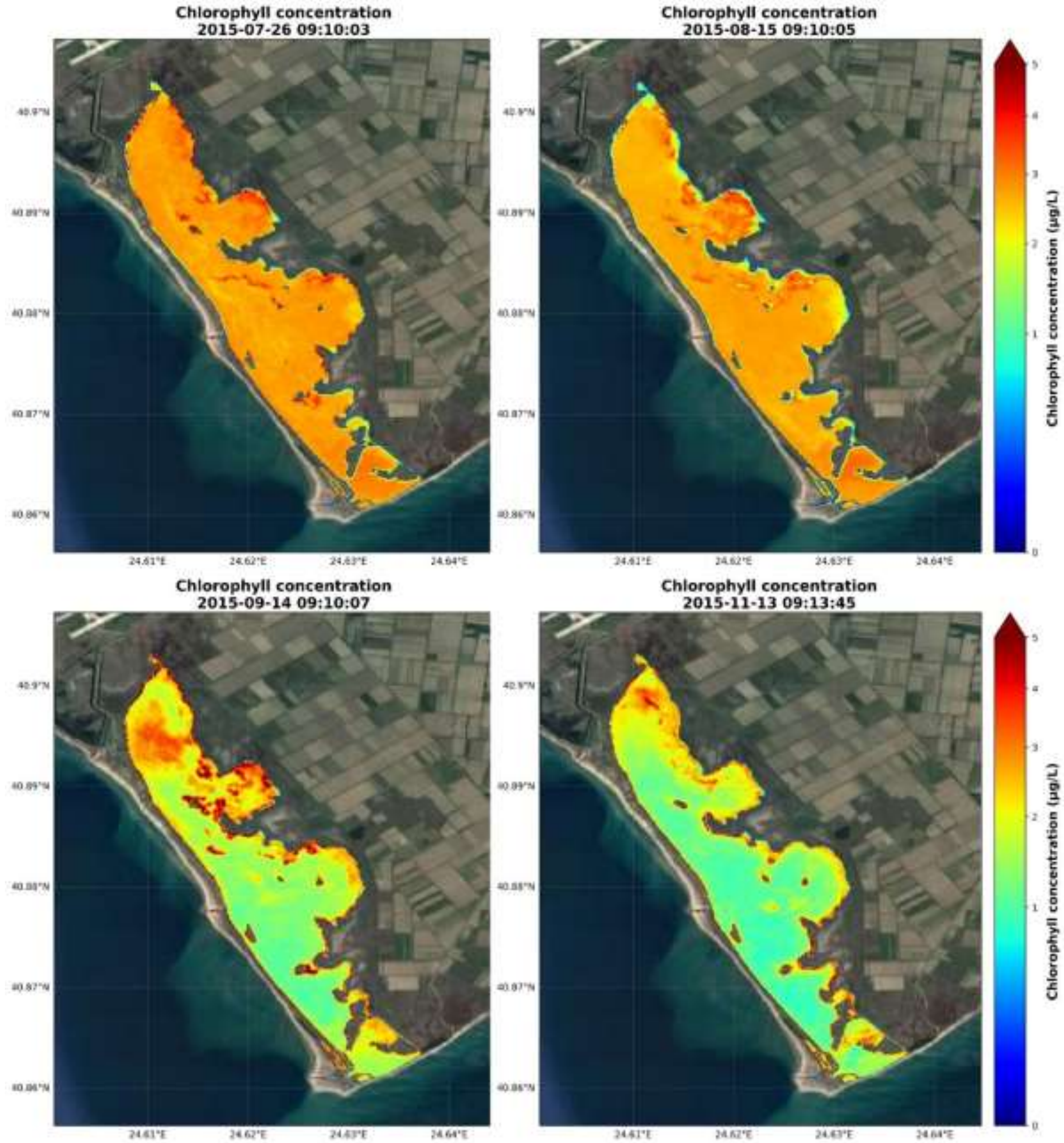

Figure 38. Seasonal evolution of Chl-a concentration in Agiasma lagoon for the year 2015, based on Sentinel 2 satellite images.

The same pattern in Chl-a evolution is observed in 2016 (Figure 39), where higher values are observed in the summer months and then decrease as we move towards autumn and winter. Higher values at the northern part in the autumn and winter months are also observed in 2016.

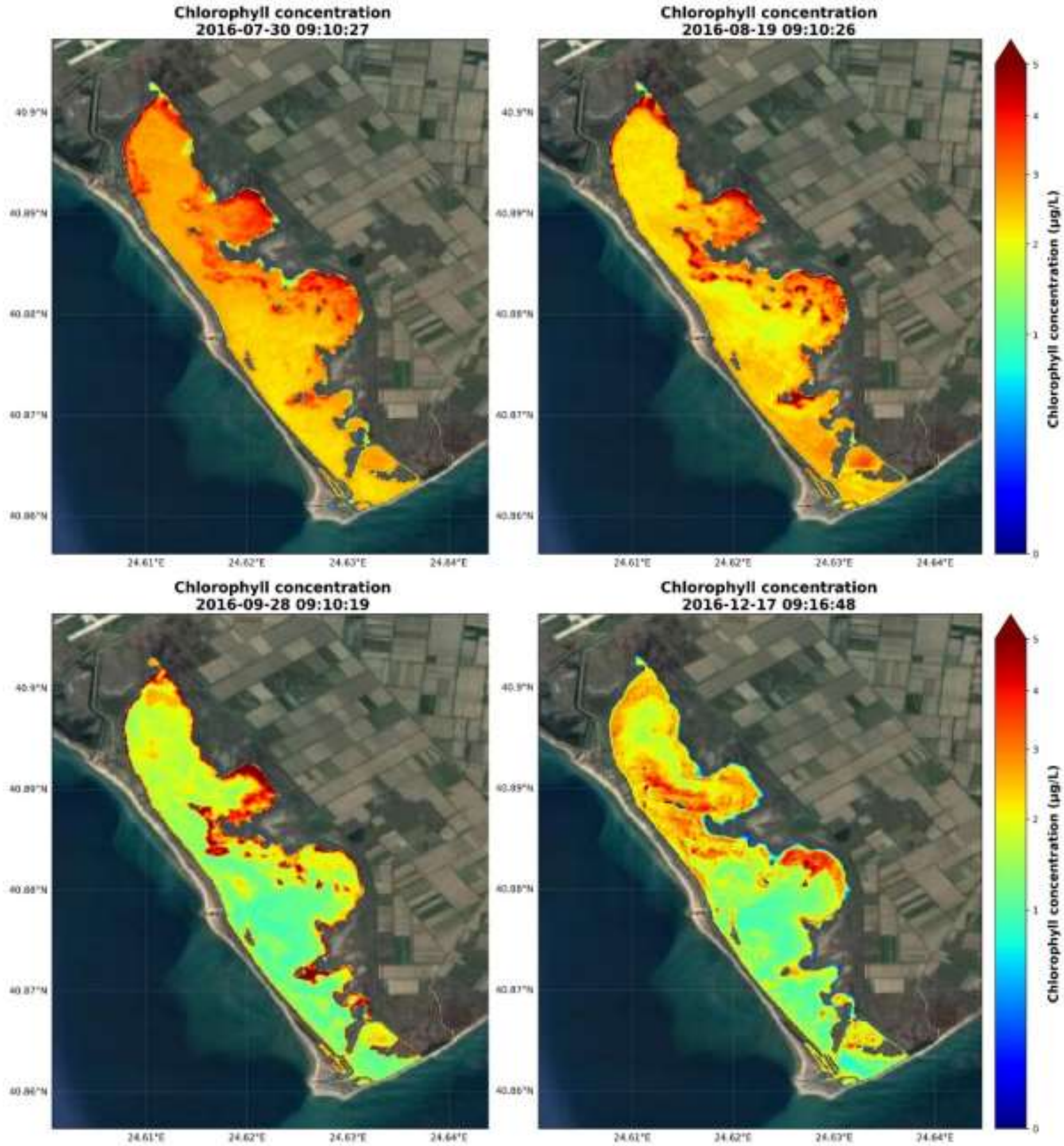

Figure 39. Seasonal evolution of Chl-a concentration in Agiasma lagoon for the year 2016, based on Sentinel 2 satellite images.

At the beginning of 2017, higher Chl-a values at the upper part of the lagoon are detected in February. There is a decreasing trend as we move towards April. Chl-a values increase in the whole basin in late June. In the following months, a decrease is detected, except for the northern part of the lagoon, which seems to retain high values compared to the rest of the basin.

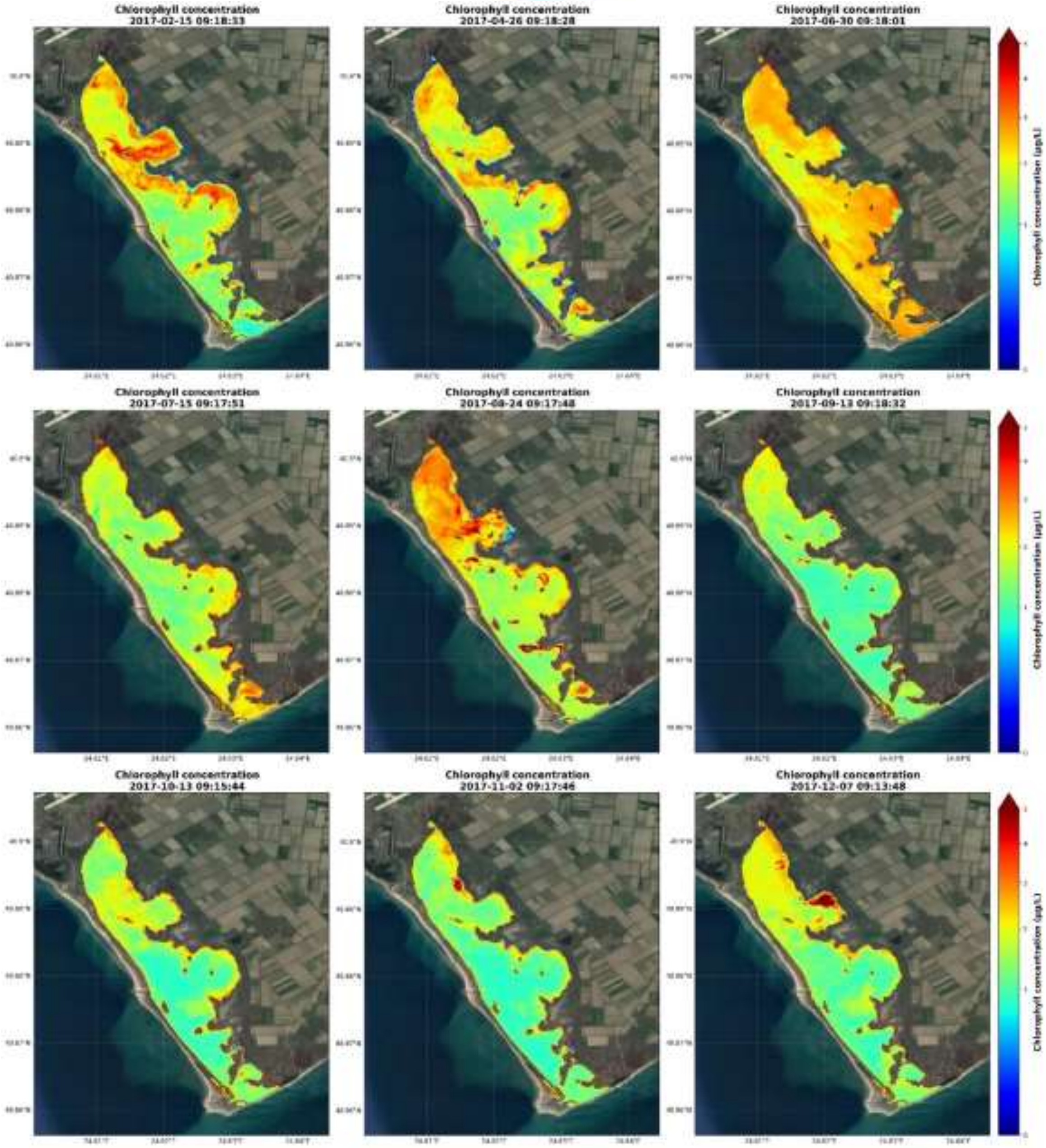

Figure 40. Seasonal evolution of Chl-a concentration in Agiasma lagoon for the year 2017, based on Sentinel 2 satellite images.

Figure 41 show an increase in Chl-a values, from low concentrations in January to higher in May (2.5-3.0 μg/l), starting from the northern parts (late April) and then spreading to the rest of the basin. In the following months, Chl-a decreases until July and then increases again and remains high until the mid of September. Another peak is observed in November.

In 2019 (Figure 42), higher Chl-a values are observed in January compared to previous years (up to 4.5 μg/l). Then there is an increase from February until May, starting from the north-western parts and expanding to the rest basin. After a decrease in the following months, the highest values are observed in late summer. Then a decrease starting from the southern part of the lagoon is observed and in November the autumn maximum is reached.

In 2020 (Figure 43), the first increase in Chl-a values is observed in March, with the north-western parts showing higher values (2.0-4.0 μg/l) than the rest of the lagoon. In the following months, Chl-a evolution follows the same pattern as in 2019.

During 2021 (Figure 44), a maximum in Chl-a values is reached in May, with the higher values localized at the northern and central parts of the lagoon. In the following months, a decrease is observed and the Chl-a distributes more uniformly across the basin. A peak is observed at the beginning of October. A decrease is observed from late October starting from the southern part and spreading to the center of the lagoon.

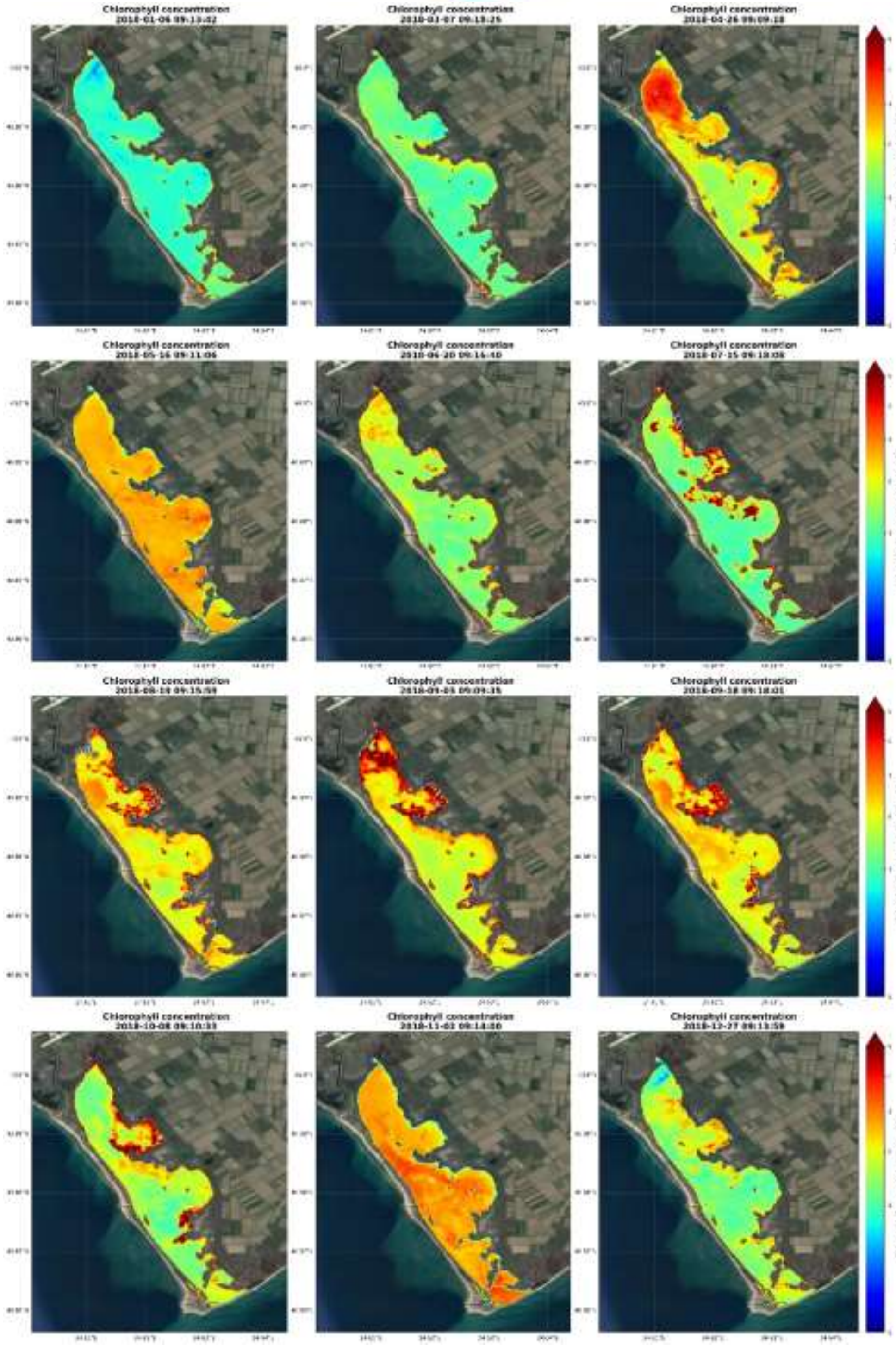

Figure 41. Seasonal evolution of Chl-a concentration in Agiasma lagoon for the year 2018, based on Sentinel 2 satellite images.

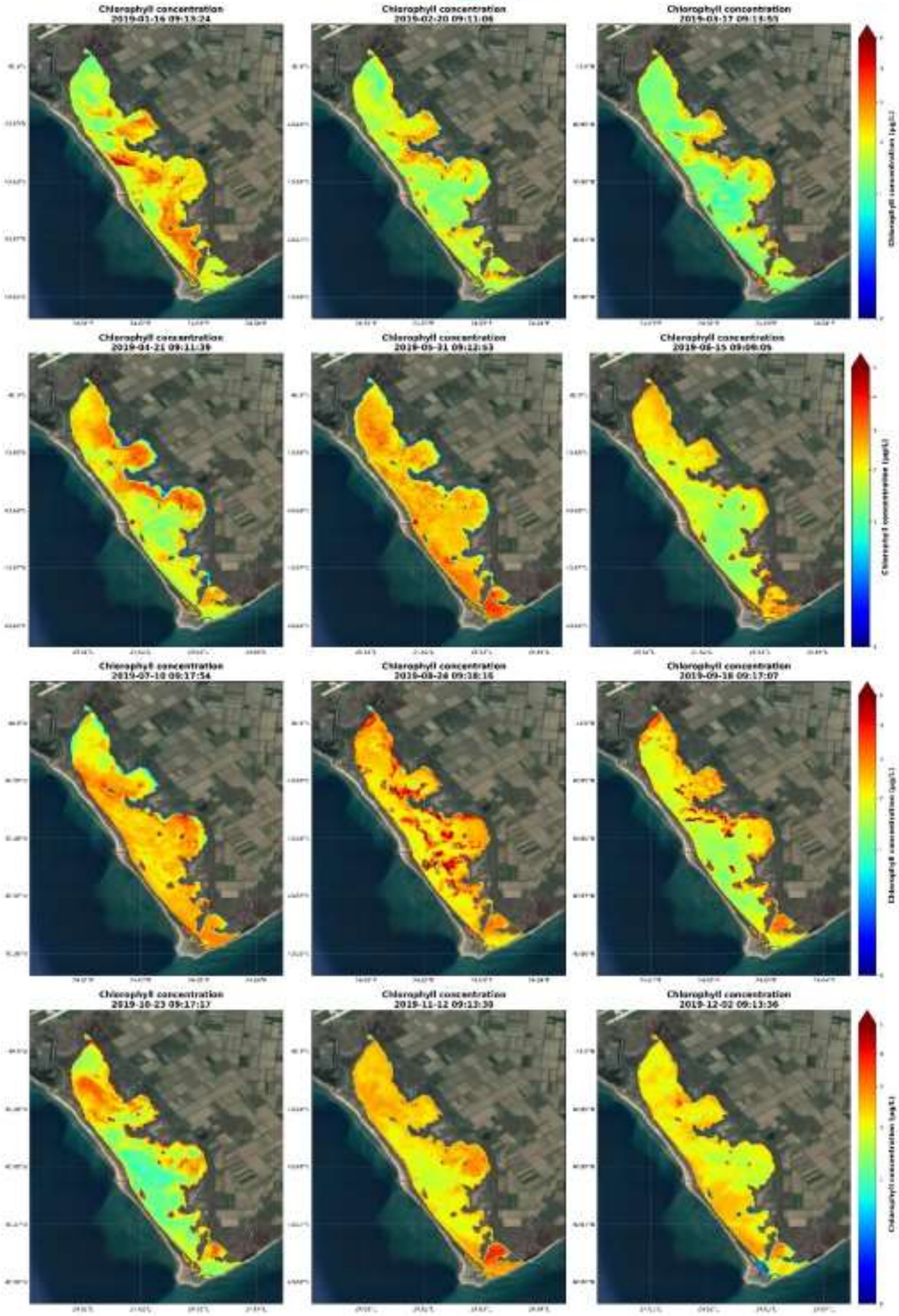

Figure 42. Seasonal evolution of Chl-a concentration in Agiasma lagoon for the year 2019, based on Sentinel 2 satellite images.

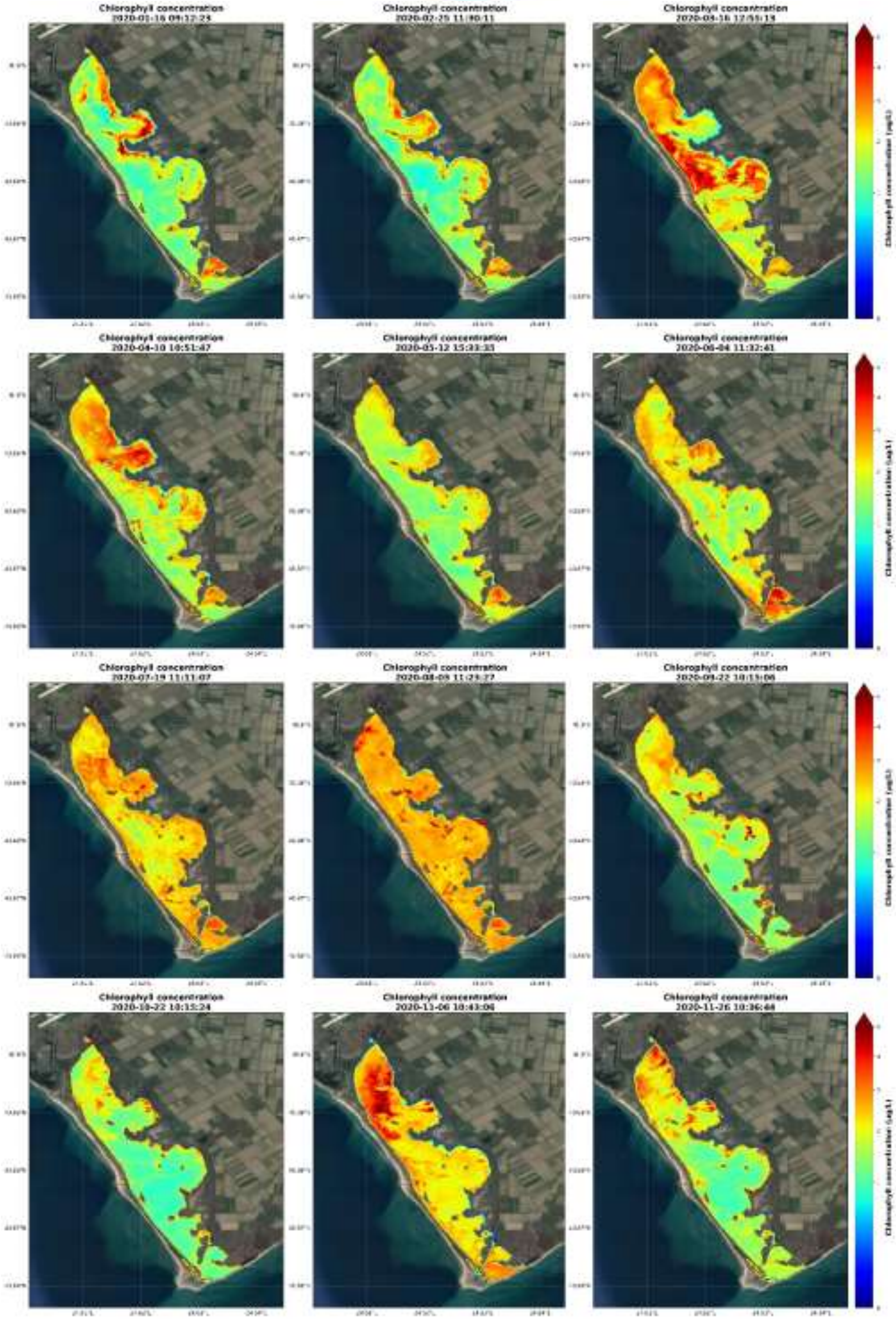

Figure 43. Seasonal evolution of Chl-a concentration in Agiasma lagoon for the year 2020, based on Sentinel 2 satellite images.

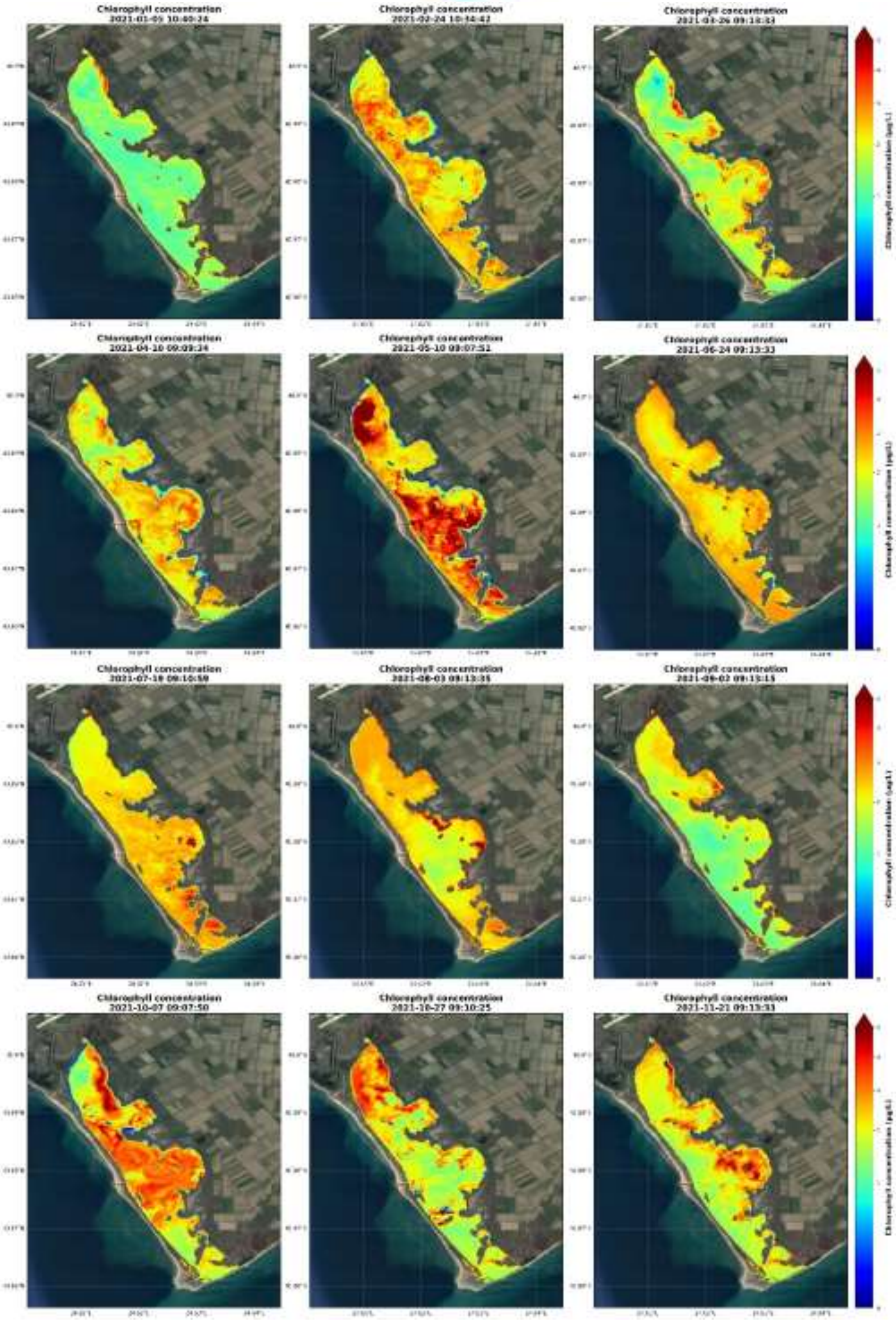

Figure 44. Seasonal evolution of Chl-a concentration in Agiasma lagoon for the year 2021, based on Sentinel 2 satellite images.

3.1.4 Porto Lagos lagoon

Figures 42-51 show the spatial distribution of Chl-a in Porto Lagos lagoon for the years 2013-2021. During 2013 (Figure 45), the highest Chl-a concentration values were reached in late summer. These high values are found at the northeastern part (3.0-5.0 μg/l). On the contrary, the Chl-a values at the southeastern part of the lagoon are lower probably due to the entry of seawater from the eastern lagoon mouth. In the following months, Chl-a values decrease, except from the northern part, where Chl-a values increase, probably due to the water outflown from Vistonis lagoon.

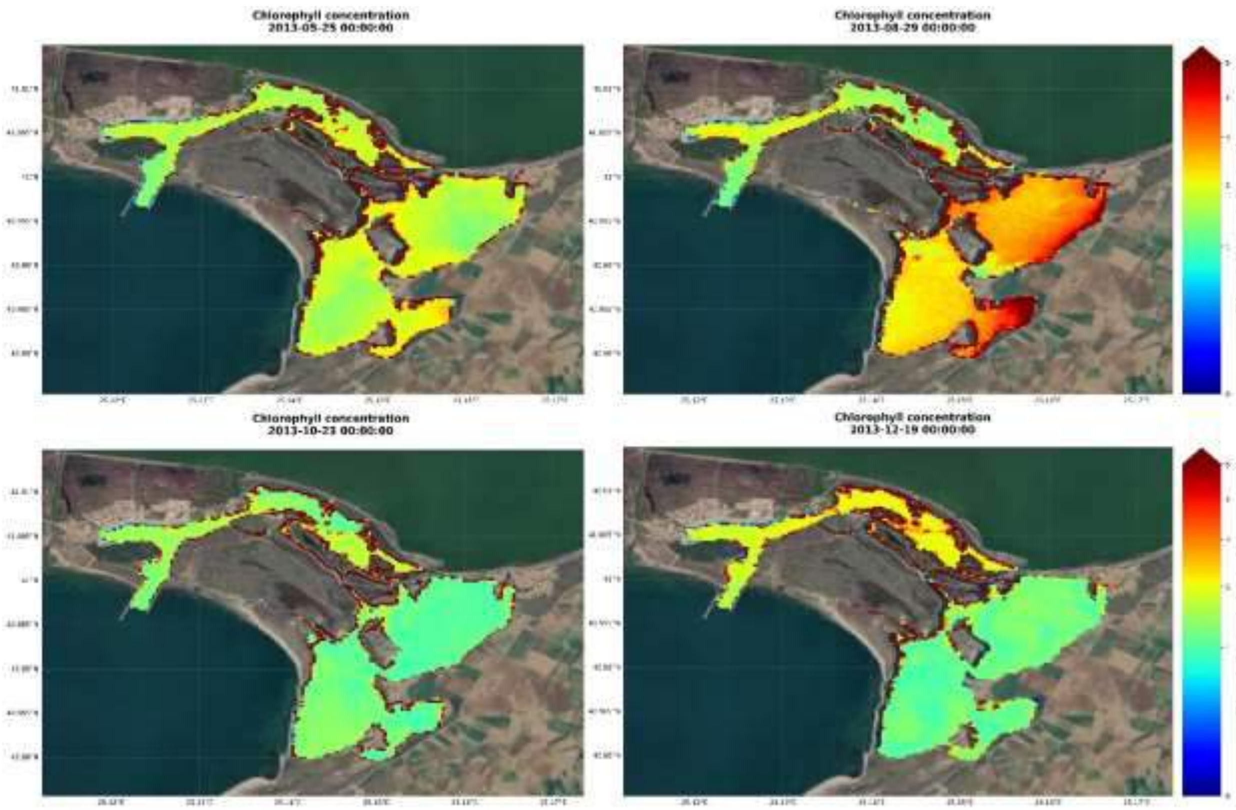

Figure 45. Seasonal evolution of Chl-a concentration in Porto Lagos lagoon for the year 2013, based on Landsat 8 satellite images.

Figure 46 shows the increase of Chl-a from the beginning of January until the summer 2014. Chl-a values in August range from 1.5 to 30 μg/l, with the highest values being shown at the eastern parts of the lagoon. In the following months, Chl-a values decrease (1.0-1.5 μg/l).

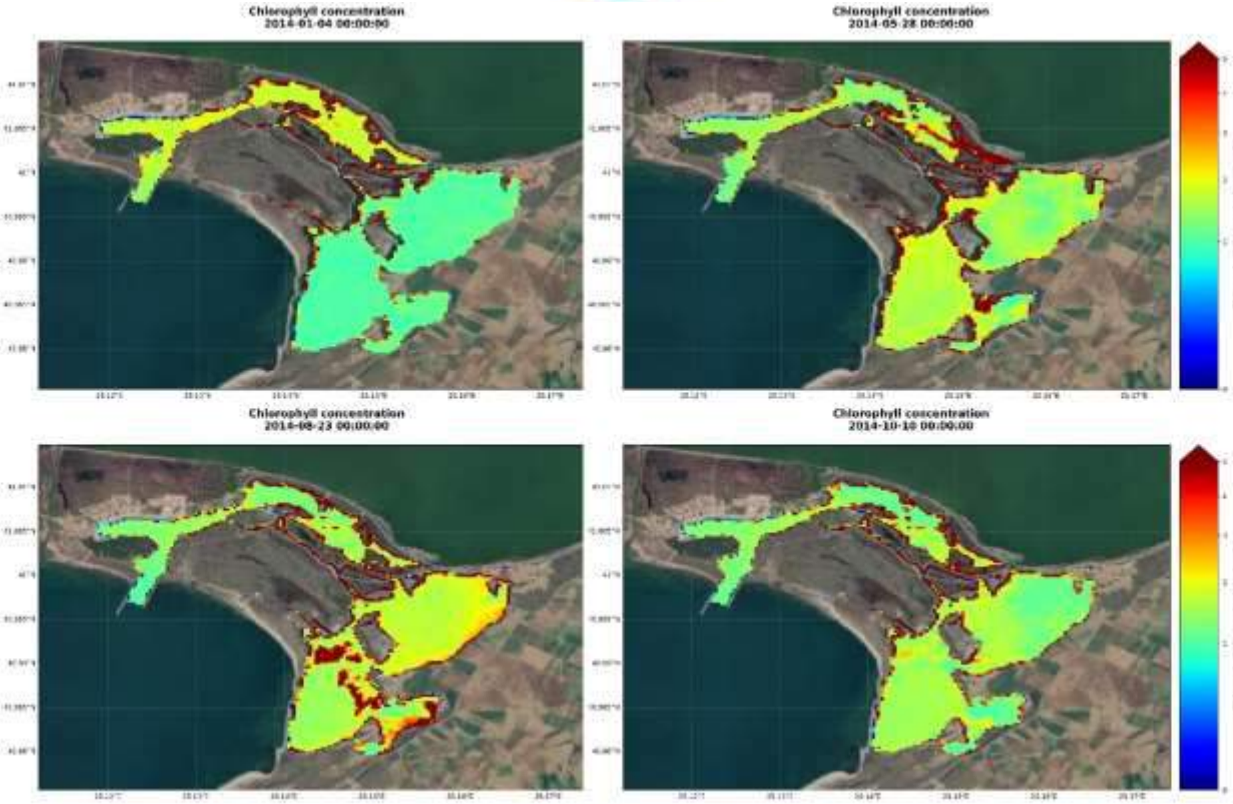

Figure 46. Seasonal evolution of Chl-a concentration in Porto Lagos lagoon for the year 2014, based on Landsat 8 satellite images.

The first half of 2015 is presented in Figure 47 covered by Landsat 8 and the second half is presented in Figure 48 covered by Sentinel 2. The images selected for the first half of 2015 show the gradual increase from low Chl-a in February to higher values in May. The higher values in May are up to 3 μg/l, and they are uniformly distributed across the basin. In June 2015 the values slightly decrease, especially at the northwestern and the northeastern parts.

Project funded by EUROPEAN UNION

PONTOS

Black Sea CROSS BORDER COOPERATION

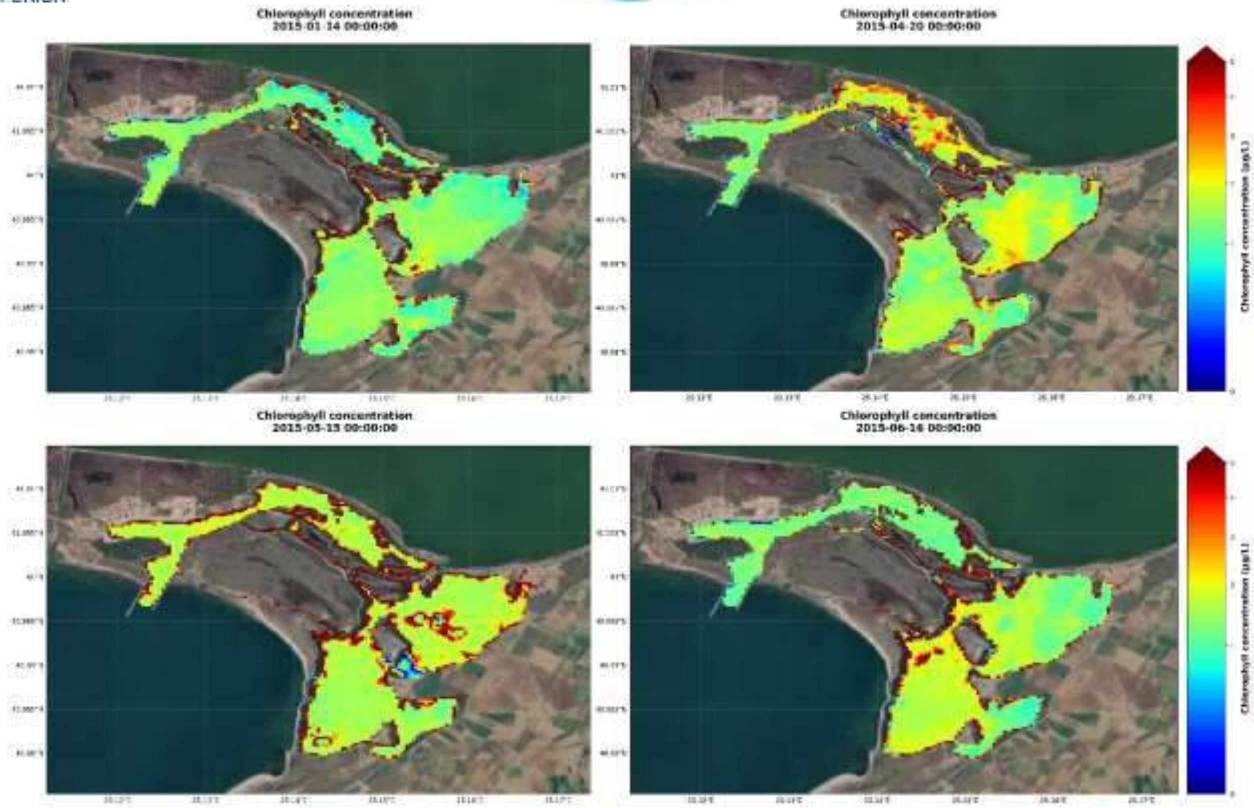

Figure 47. Seasonal evolution of Chl-a concentration in Porto Lagos lagoon for the year 2015, based on Landsat 8 satellite images.

In July and August (Figure 48), Chl-a is almost uniformly distributed across the basin (up to 3.8 μg/l). The highest values are found at the northern part of the basin. In the following months, the Chl-a values decrease considerably.

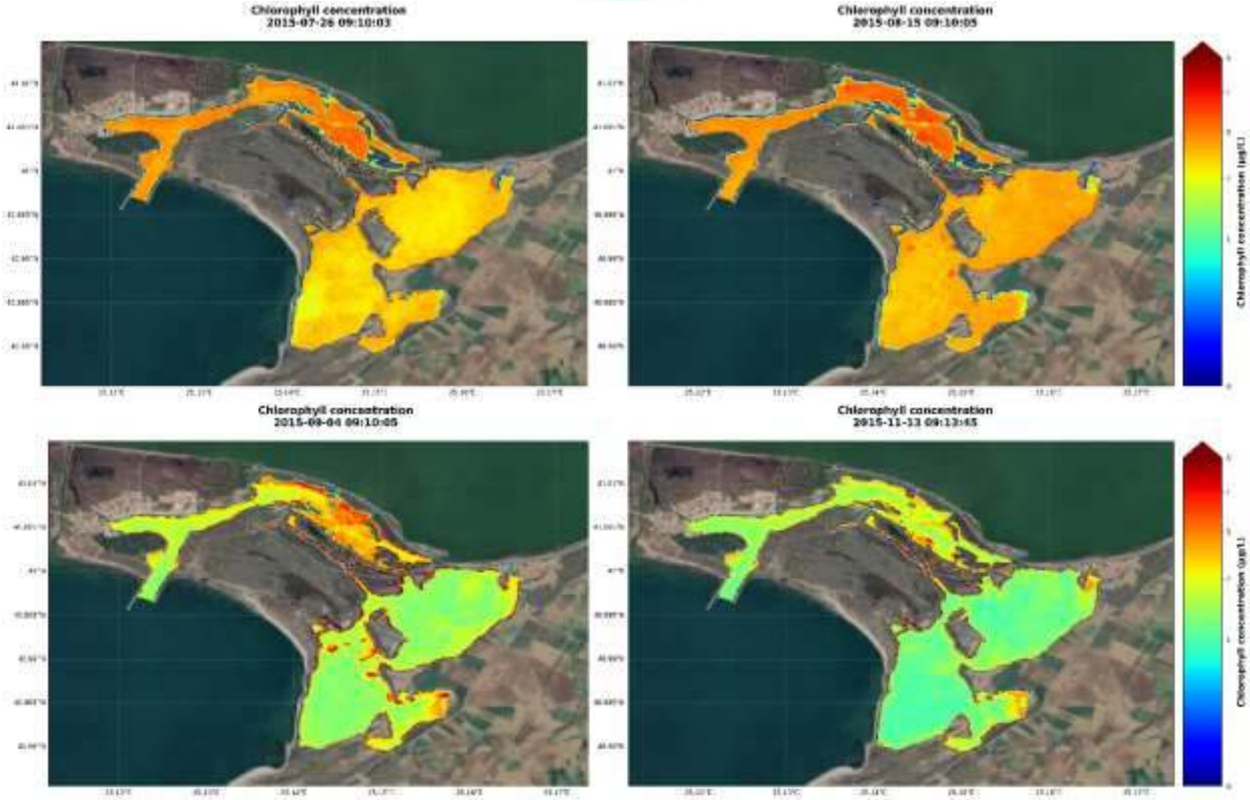

Figure 48. Seasonal evolution of Chl-a concentration in Porto Lagos lagoon for the year 2015, based on Sentinel 2 satellite images.

For 2016 two images during summer and one in winter are presented as due to cloud coverage limited images were available to cover the seasonal cycle of Chl-a (Figure 49). The higher values are observed in July (2.0-3.5 μg/l). The lower values are found at the southern parts of the lagoon. The Chl-a values decrease as we move towards the end of the year.

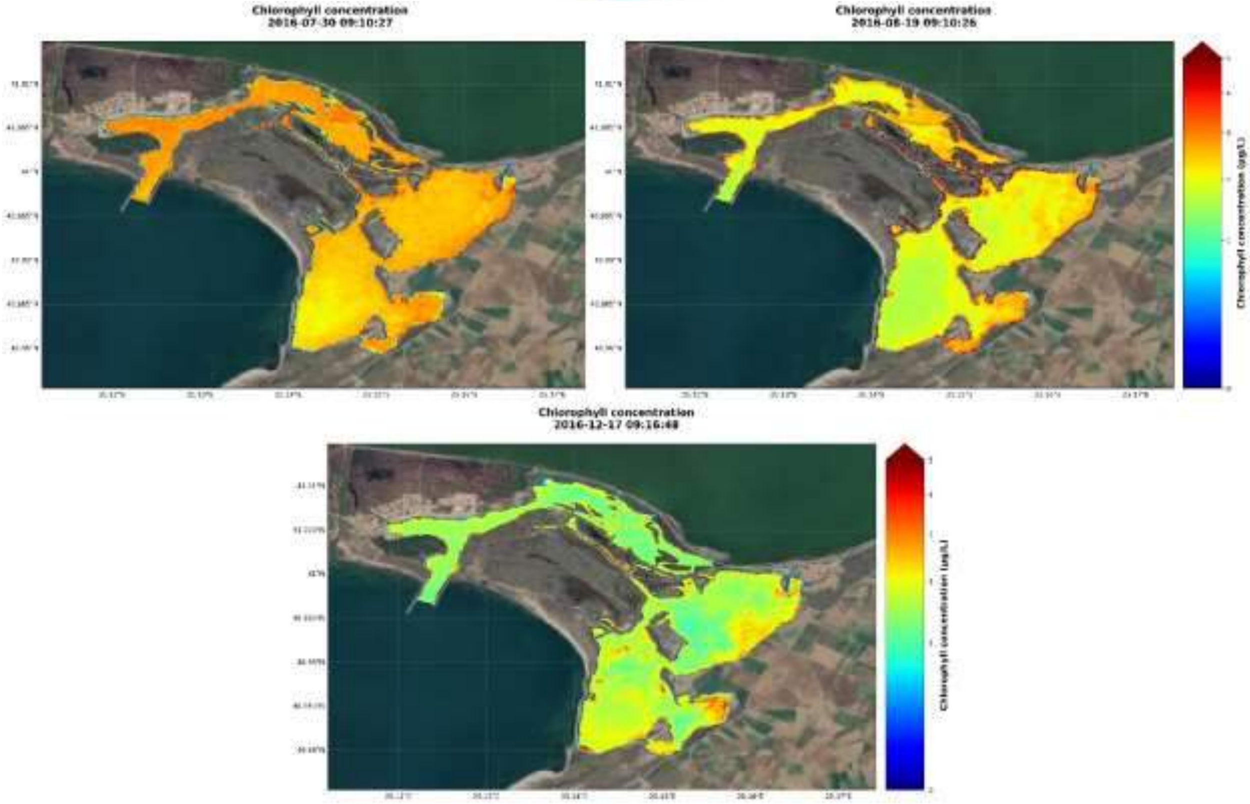

Figure 49. Seasonal evolution of Chl-a concentration in Porto Lagos lagoon for the year 2016, based on Sentinel 2 satellite images.

Figure 50 shows the increase of Chl-a values, from low concentrations in February 2017 to higher at the beginning of August 2017. The increase starts from the south and southeastern parts (April), then to the northern part (June) and then expands to the northeastern sub-basin (August). In the following months, Chl-a decreases reaching its lowest value in November. A slight increase is observed in December, covering the whole basin.

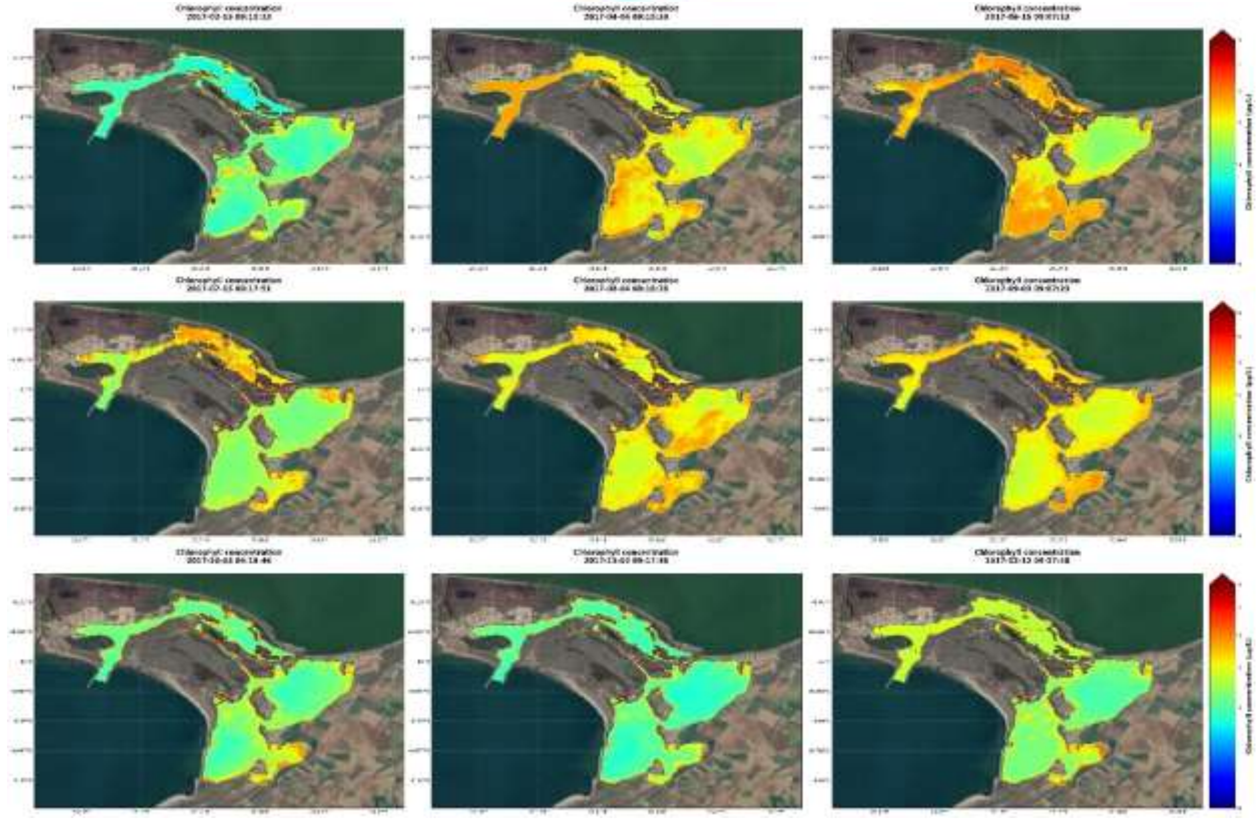

Figure 50. Seasonal evolution of Chl-a concentration in Porto Lagos lagoon for the year 2017, based on Sentinel 2 satellite images.

Figure 51 shows the increase in Chl-a values, from low concentrations in January to higher in May. These values vary from 3.0 to 3.5 µg/l. Chl-a decreases in July but increases again in August. A peak is observed in November, where Chl-a ranges from 2.5 to 4.5 µg/l. The lowest values are reached in December (around 1.0 µg/l).

During 2019 (Figure 52), Chl-a starts to increase until late June, reaching the first peak. The highest values are localized at the southern and southeastern parts (up to 3.5 µg/l). In the following months, Chl-a values decrease. The decrease starts from the northern part, spreading towards the south. In November, a maximum is reached which remains stable until December.

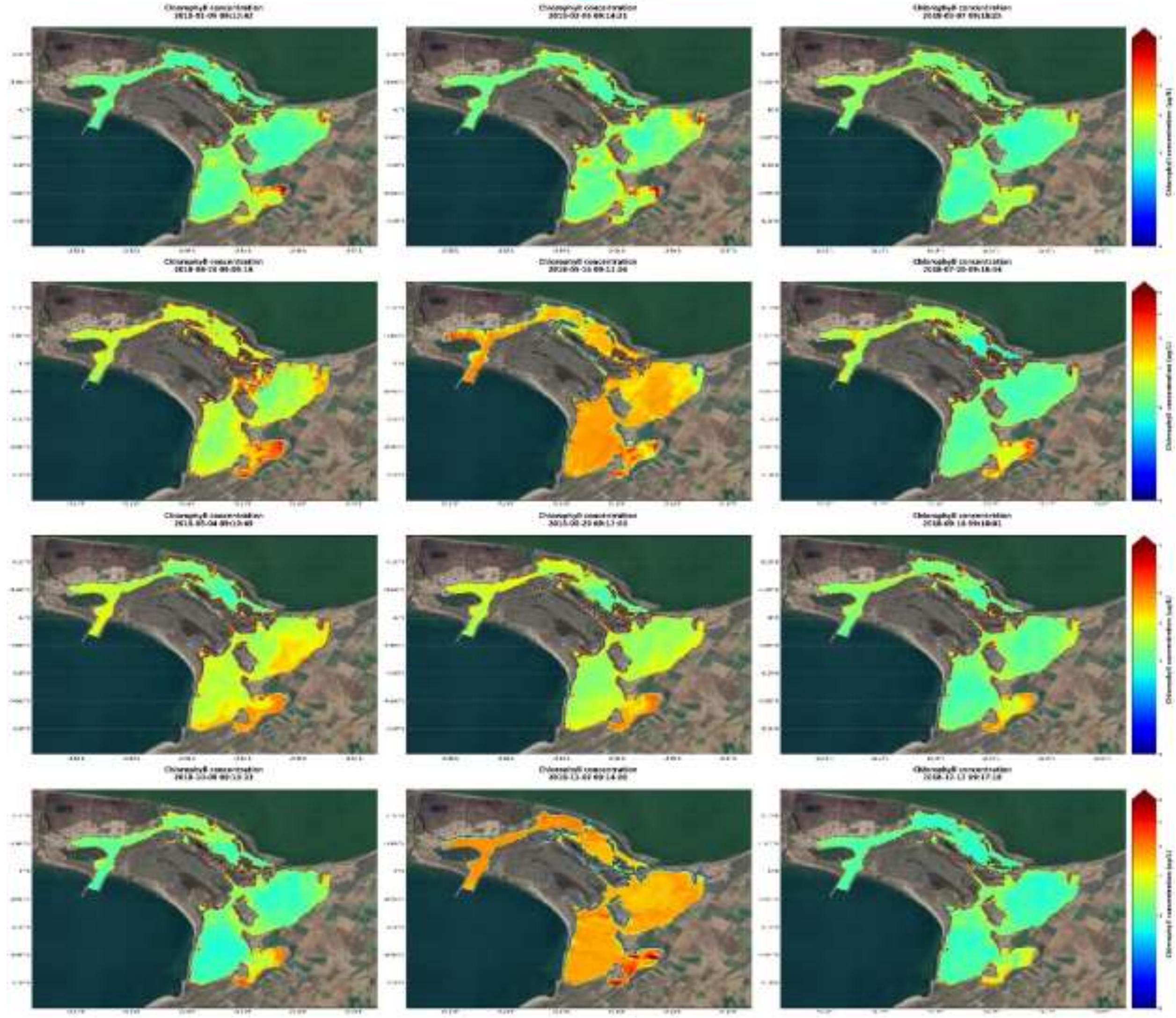

Figure 51. Seasonal evolution of Chl-a concentration in Porto Lagos lagoon for the year 2018, based on Sentinel 2 satellite images.

A decrease from December 2019 to January 2020 was observed, however higher values remained in the lower part of the basin (Figure 53). Those high values spread at the southern parts during February. The first Chl-a peak is observed in July. Chl-a values increase from February and reach their highest values in July. Then, Chl-a decreases until the end of the year.

During 2021 (Figure 54), a maximum in Chl-a values is reached in July with the higher values being confined at the northern parts. In the following months, a decrease is observed as we move towards the autumn and winter months. High Chl-a values are observed in February, especially at the western part and the center of the northeast basin (up to 5.0 μg/l).

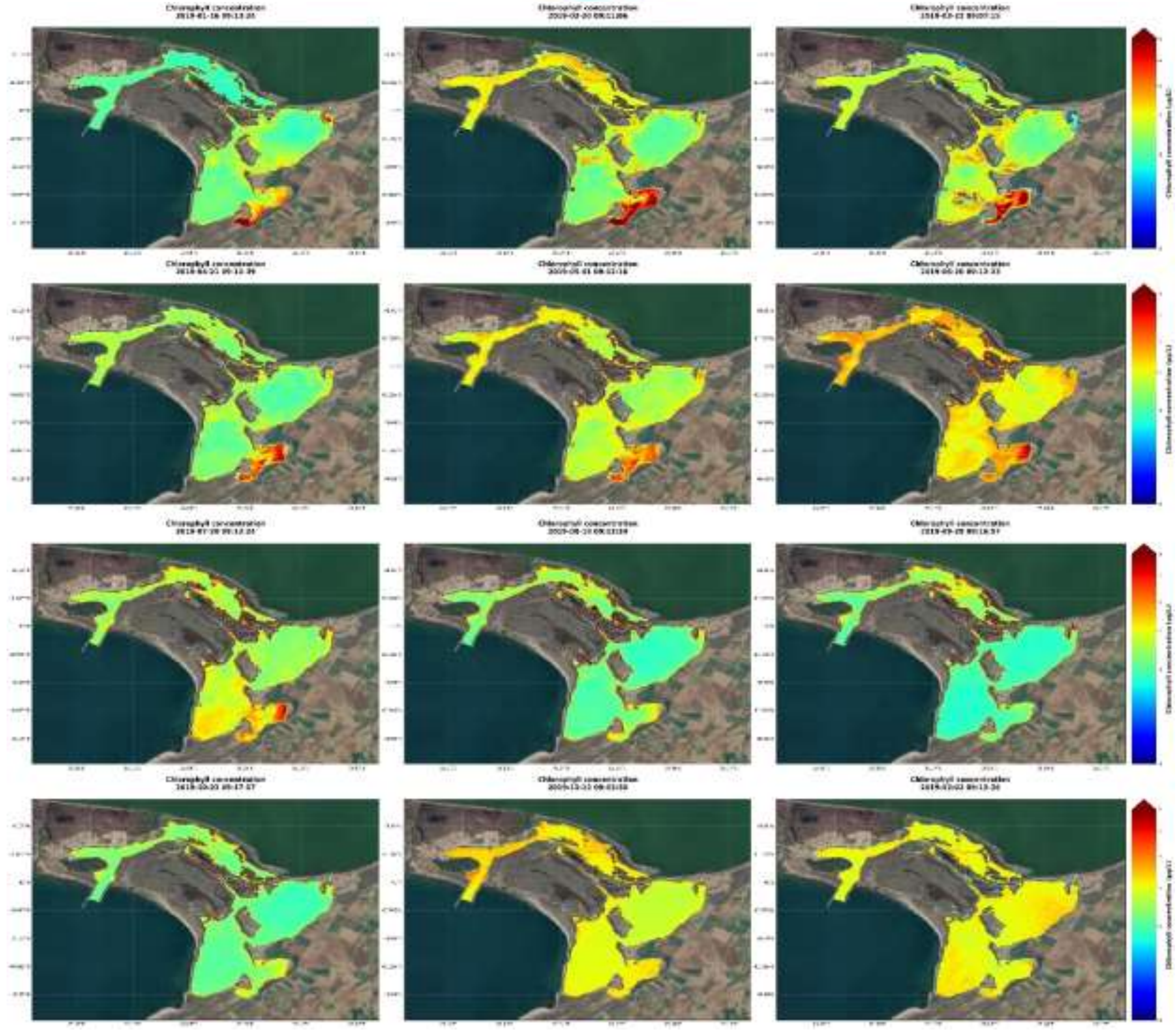

Figure 52. Seasonal evolution of Chl-a concentration in Porto Lagos lagoon for the year 2019, based on Sentinel 2 satellite images.

Project funded by EUROPEAN UNION

PONTOS

Black Sea CROSS BORDER COOPERATION

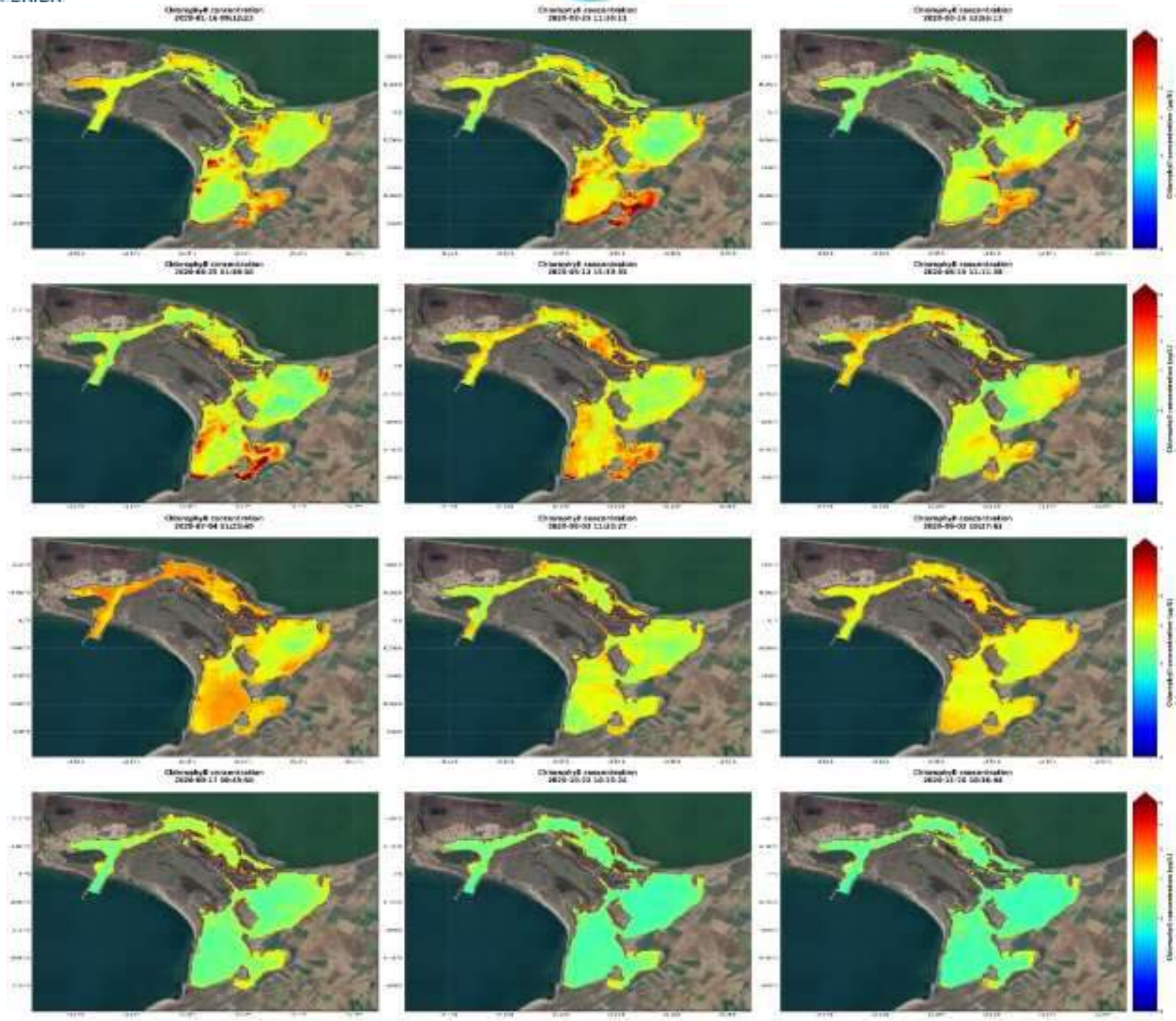

Figure 53. Seasonal evolution of Chl-a concentration in Porto Lagos lagoon for the year 2020, based on Sentinel 2 satellite images.

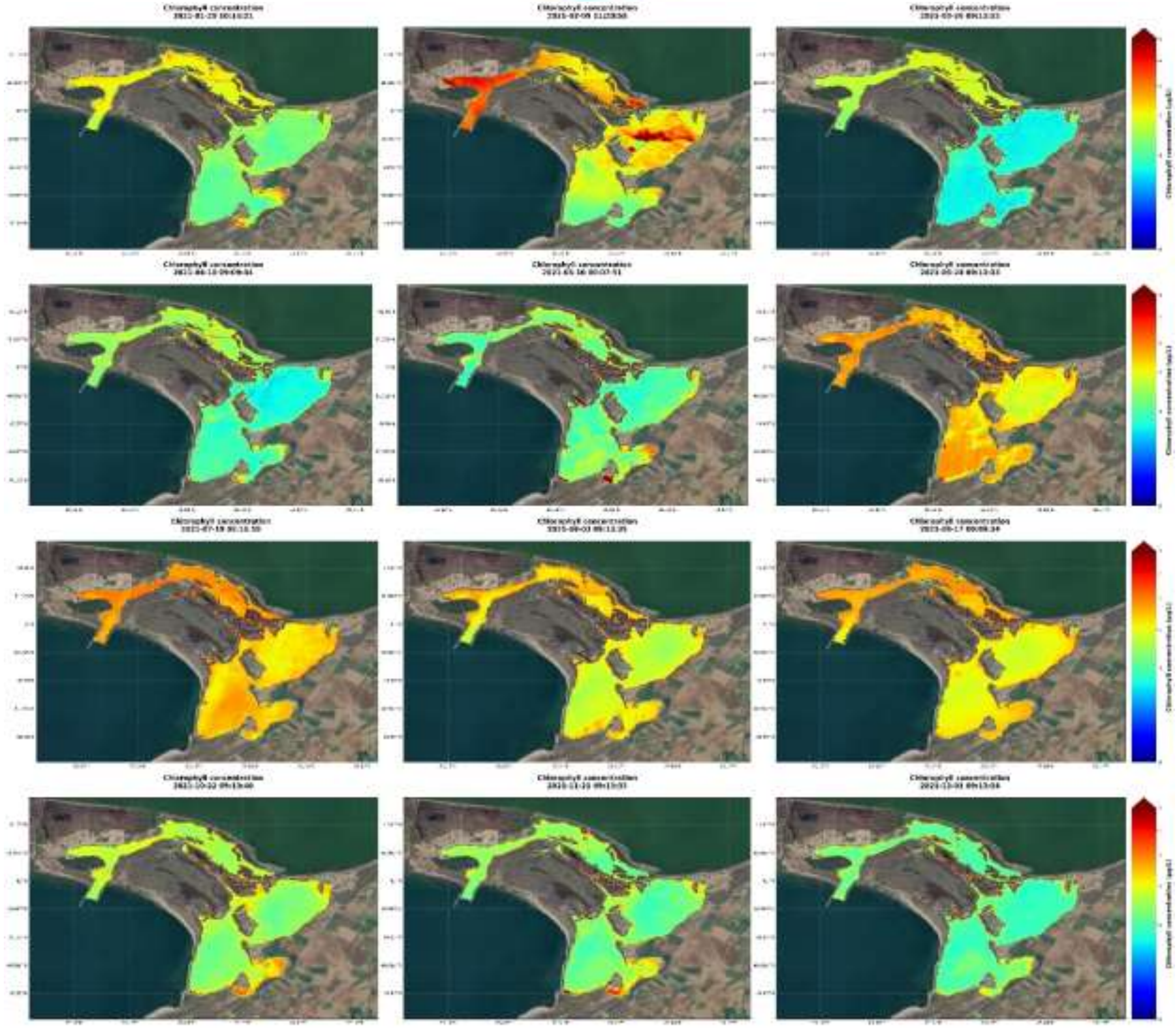

Figure 54. Seasonal evolution of Chl-a concentration in Porto Lagos lagoon for the year 2021, based on Sentinel 2 satellite images.

3.1.5 Xirolimni lagoon

Figures 52-61 show the spatial distribution of Chl-a in Xirolimni lagoon for the years 2013-2021. During 2013 (Figure 55), the first peak is reached in May. The highest values are found at the center of the basin and the southern shores (1.5-2.0 μg/l). In summer, the northern part exhibits higher values, compared to the rest of the lagoon (up to 3.5 μg/l). The third peak is reached in November, where higher values are confined at the shores. Then, Chl-a decrease as winter approaches.

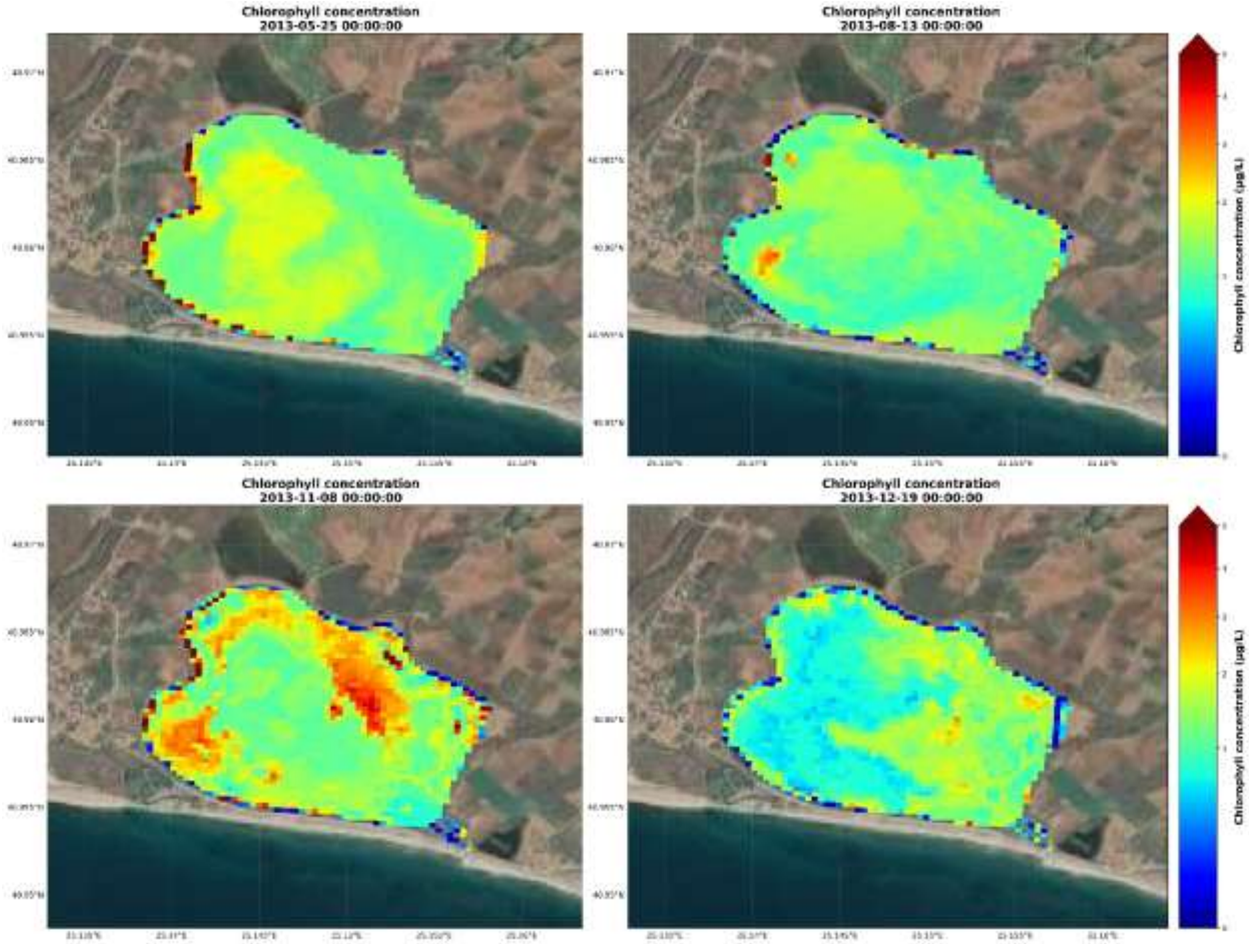

Figure 55. Seasonal evolution of Chl-a concentration in Xirolimni lagoon for the year 2013, based on Landsat 8 satellite images.

Figure 56 illustrates the increase of Chl-a from the beginning of January until the end of summer. Chl-a values in August range from 1.0 to 10 μg/l, with the highest values restricted at the eastern part of the lagoon. In the following months, Chl-a values decrease (1.0-4.0 μg/l).

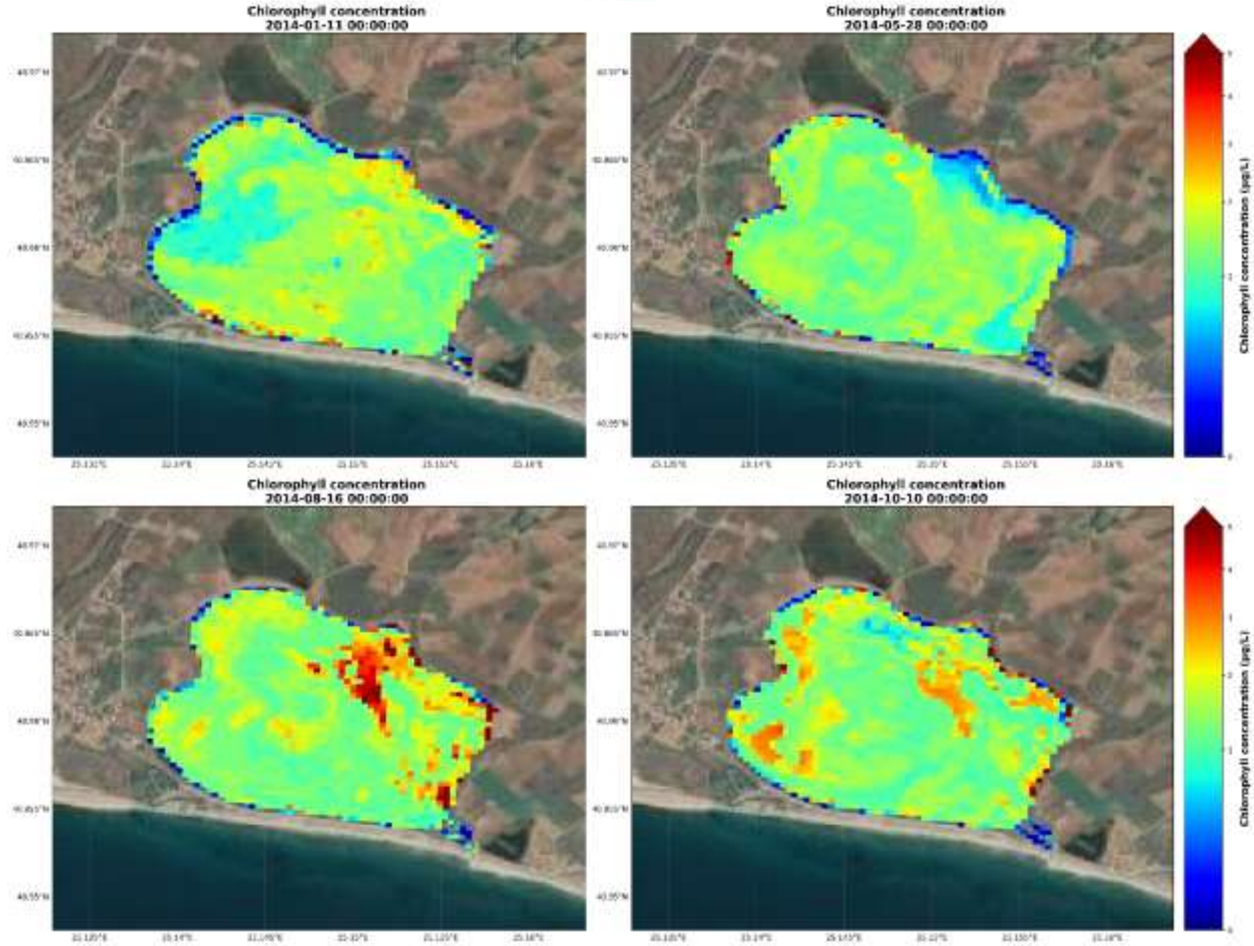

Figure 56. Seasonal evolution of Chl-a concentration in Xirolimni lagoon for the year 2014, based on Landsat 8 satellite images.

The first half of 2015 is presented in Figure 57 covered by Landsat 8 and the second half is presented in Figure 58 covered by Sentinel 2. The images selected for the first half of 2015 show the increase from low Chl-a in February to higher values in June. These higher values in June reach up to 5 μg/l, mostly restricted at the northern and western shores.

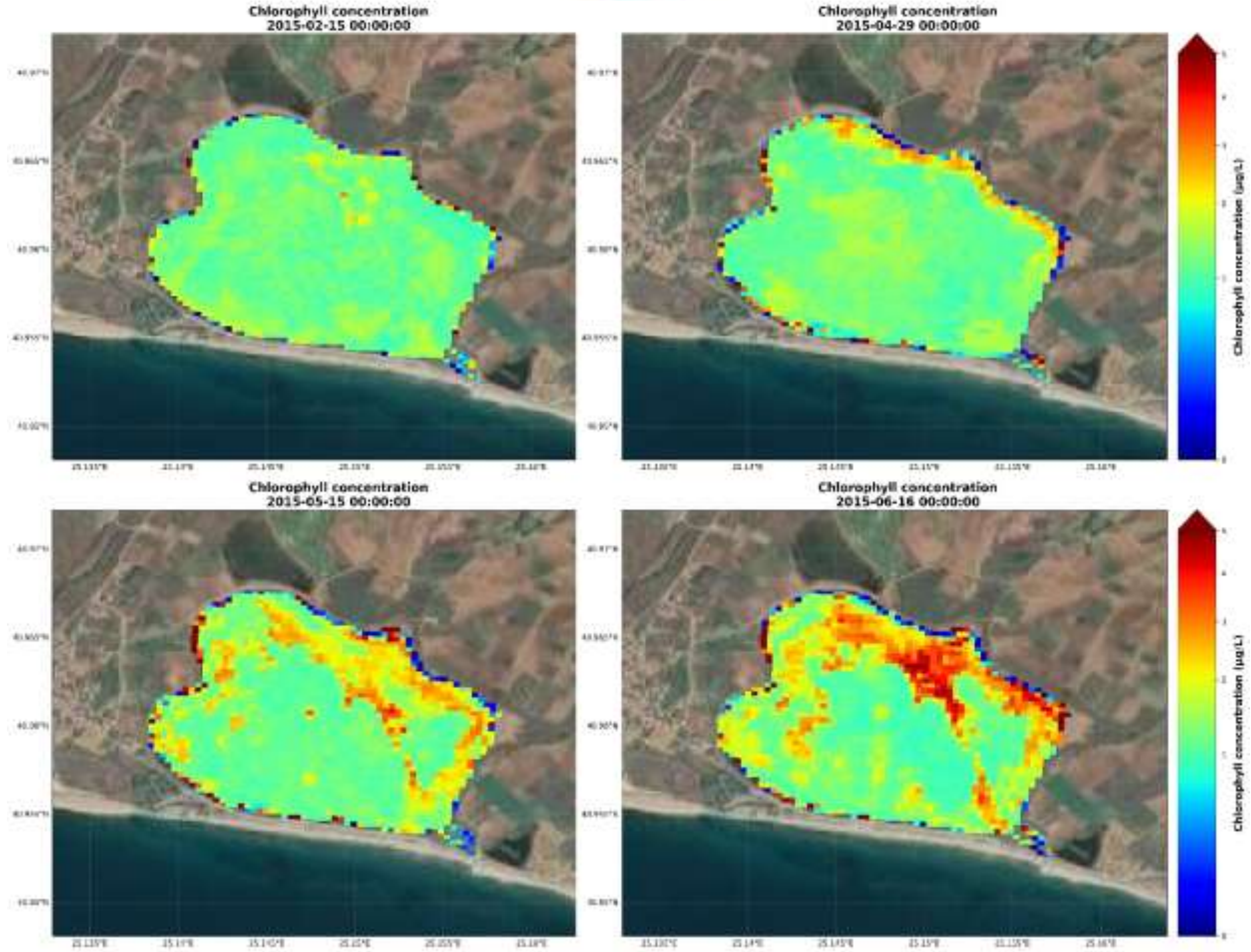

Figure 57. Seasonal evolution of Chl-a concentration in Xirolimni lagoon for the year 2015, based on Landsat 8 satellite images.

In July (Figure 58), Chl-a is almost uniformly distributed across the basin (3.0-5.0 μg/l). From August to November, Chl-a is almost stable, with the higher values concentrated close to the shores.

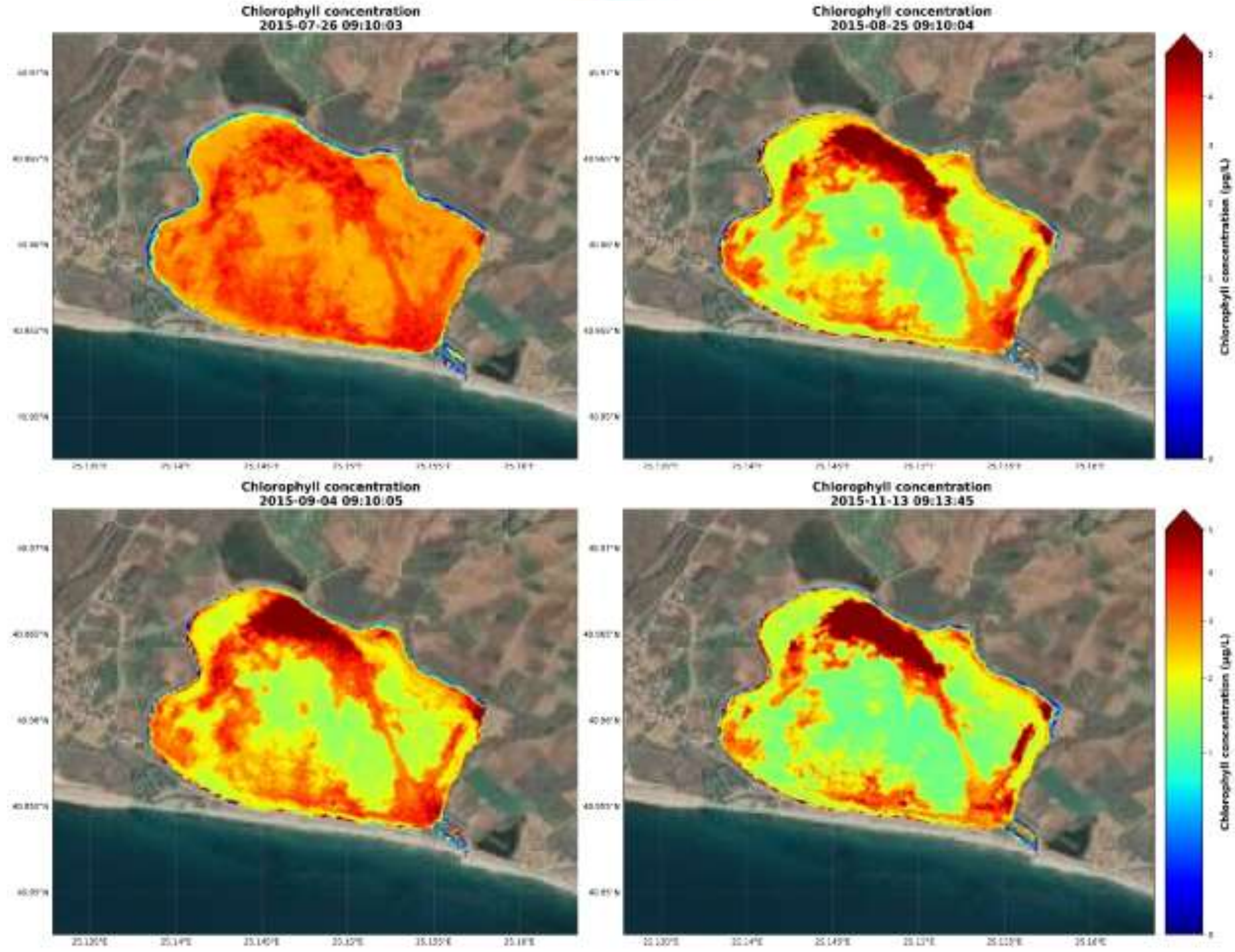

Figure 58. Seasonal evolution of Chl-a concentration in Xirolimni lagoon for the year 2015, based on Sentinel 2 satellite images.

For 2016 three images during summer are presented as due to cloudiness limited images were available covering the seasonal Chl-a cycle (Figure 59). In the first image of July, lower Chl-a values are observed in the center of the basin (1.5 μg/l) and the higher values close to the shores (up to 7.0 μg/l). In the second image of July, Chl-a values increase and they are evenly distributed across the basin. In August, Chl-a decreases but remains evenly distributed.

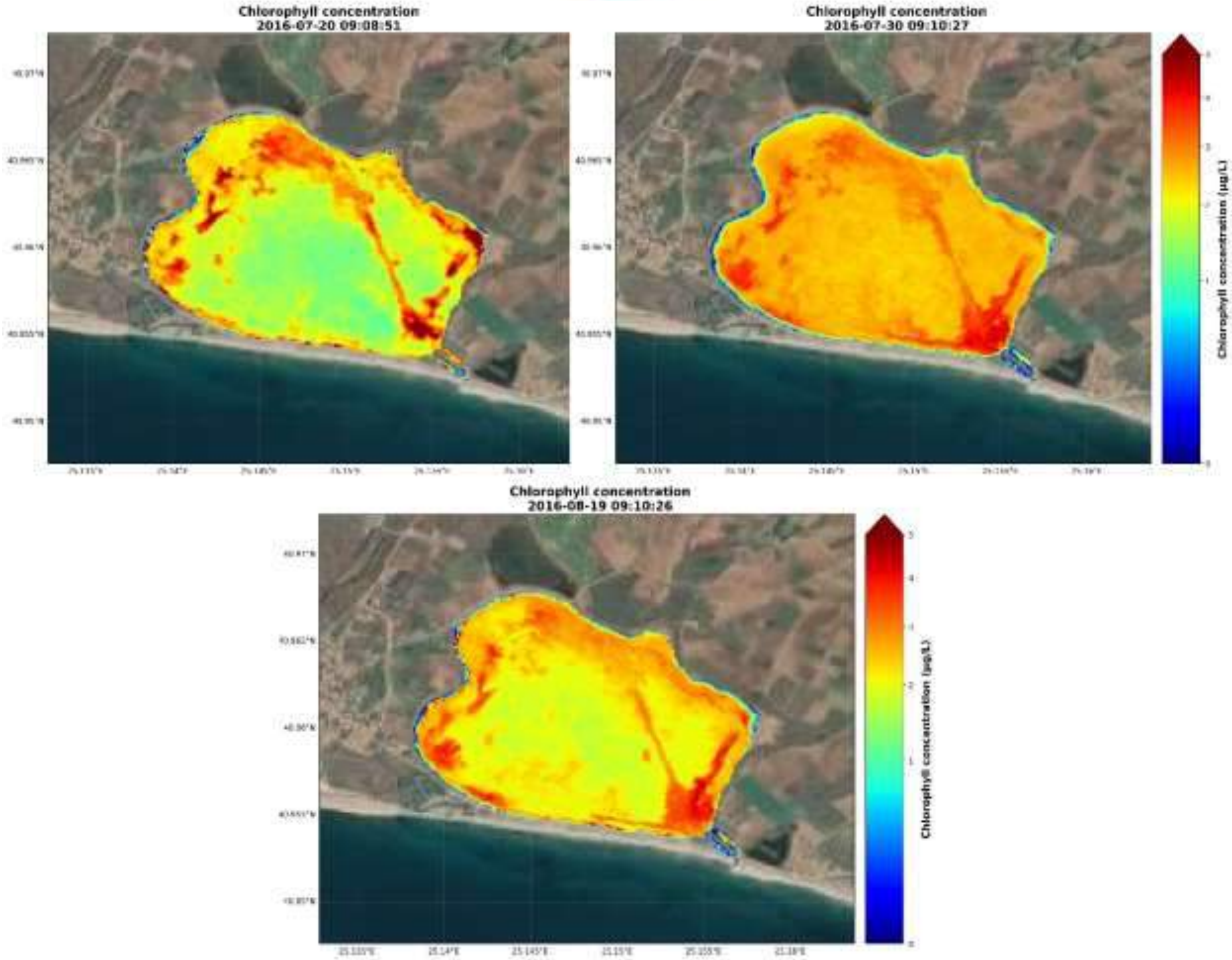

Figure 59. Seasonal evolution of Chl-a concentration in Xirolimni lagoon for the year 2016, based on Sentinel 2 satellite images.

During 2017 (Figure 60), higher Chl-a values are observed close to the shores of the lagoon. These increased values move towards the central part in April and then expand to the whole basin in May. The highest Chl-a reaches 55 μg/l in May. In the following months, Chl-a decreases to its lowest values in December (1.3-4.0 μg/l).

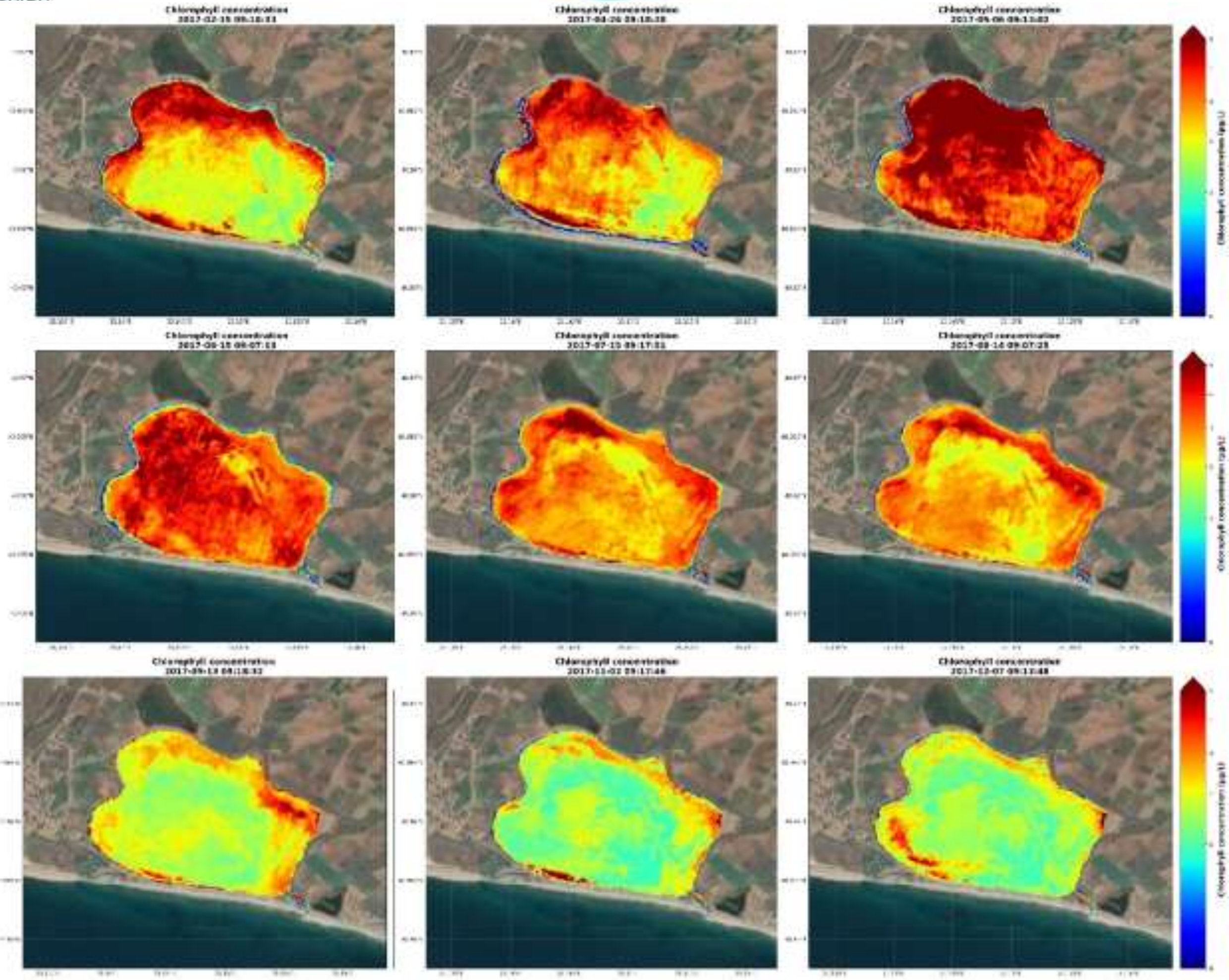

Figure 60. Seasonal evolution of Chl-a concentration in Xirolimni lagoon for the year 2017, based on Sentinel 2 satellite images.

Figure 61 shows the increase of Chl-a values, from low concentrations in January to higher in May. Almost the whole basin shows high Chl-a values that range from 2.5 to 8.0 µg/l. In June, Chl-a values decrease at the northern part (lower than 1.5 µg/l), but increase at the southern and eastern shores. In the following months, Chl-a decreases until its lowest values, by the end of July. A peak is observed in mid-August, with higher values concentrating in the center and close to the shores of the lagoon. Another peak is observed in November, where Chl-a ranges from 2.5 to 7 µg/l.

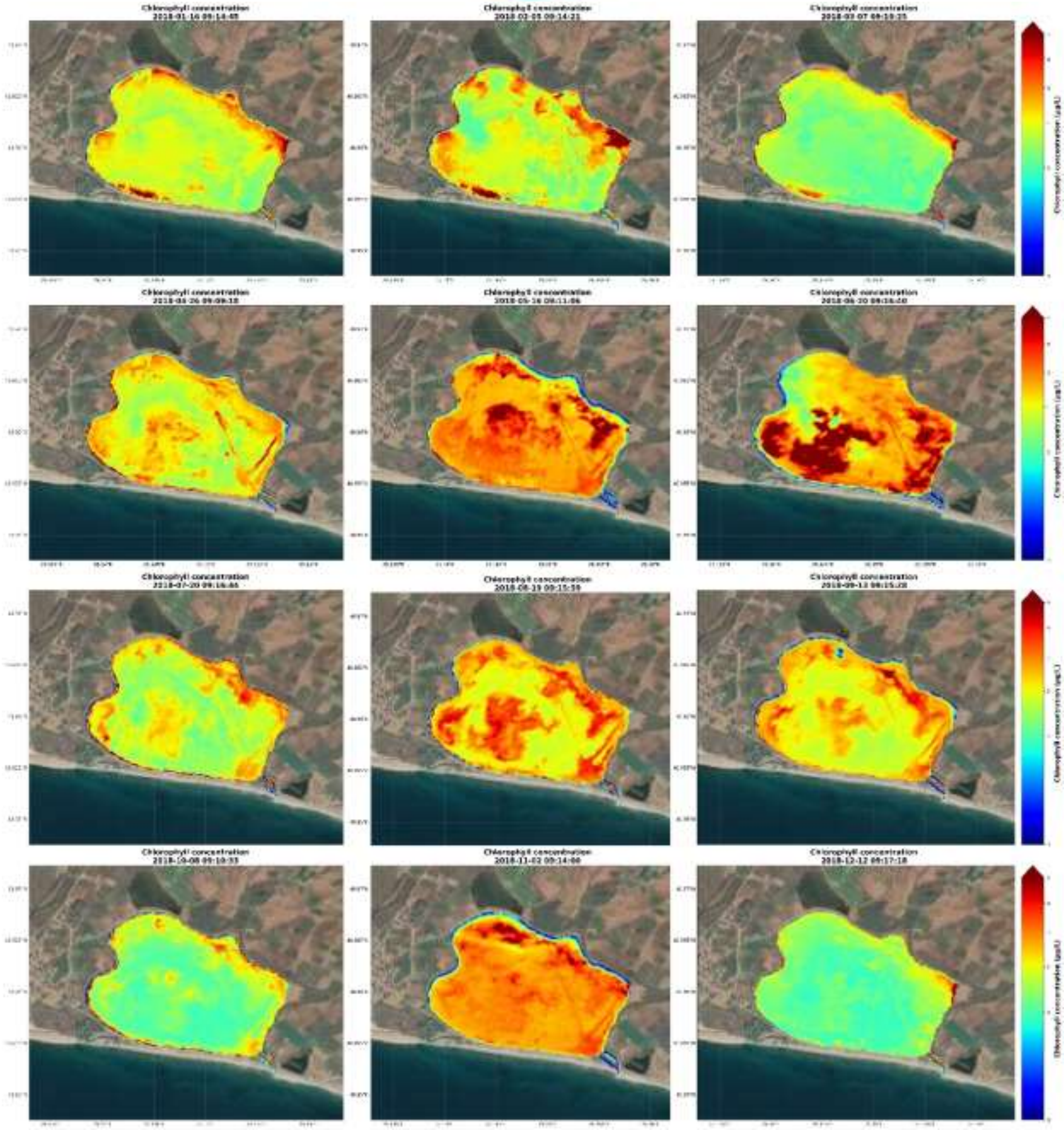

Figure 61. Seasonal evolution of Chl-a concentration in Xirolimni lagoon for the year 2018, based on Sentinel 2 satellite images.

During 2019 (Figure 62), Chl-a starts to increase until late April, reaching the first peak. Chl-a appears evenly distributed across the basin, ranging from 2.5 to 3.5 μg/l. In the following months, Chl-a values decrease, with the higher values moving towards the shores. In November, a maximum is reached which remains stable until December.

The high values detected in December 2019 led to high values in January 2020 (Figure 63). Higher values are met across the shores (up to 5.0 μg/l) and lower at the central parts of the basin (1.5 μg/l). The first Chl-a peak is observed in May. Chl-a values increase from February and reach the highest values in May. Then Chl-a decreases until November. In mid-November, a maximum is reached (2.5-3.5 μg/l).

During 2021 (Figure 64), a maximum in Chl-a values is reached in July with the higher values are mostly found at the northern and southern parts. The increase spreads from the northern shores to the central basin (March to June 2021). In the following months, a decrease is observed in the autumn and winter months.

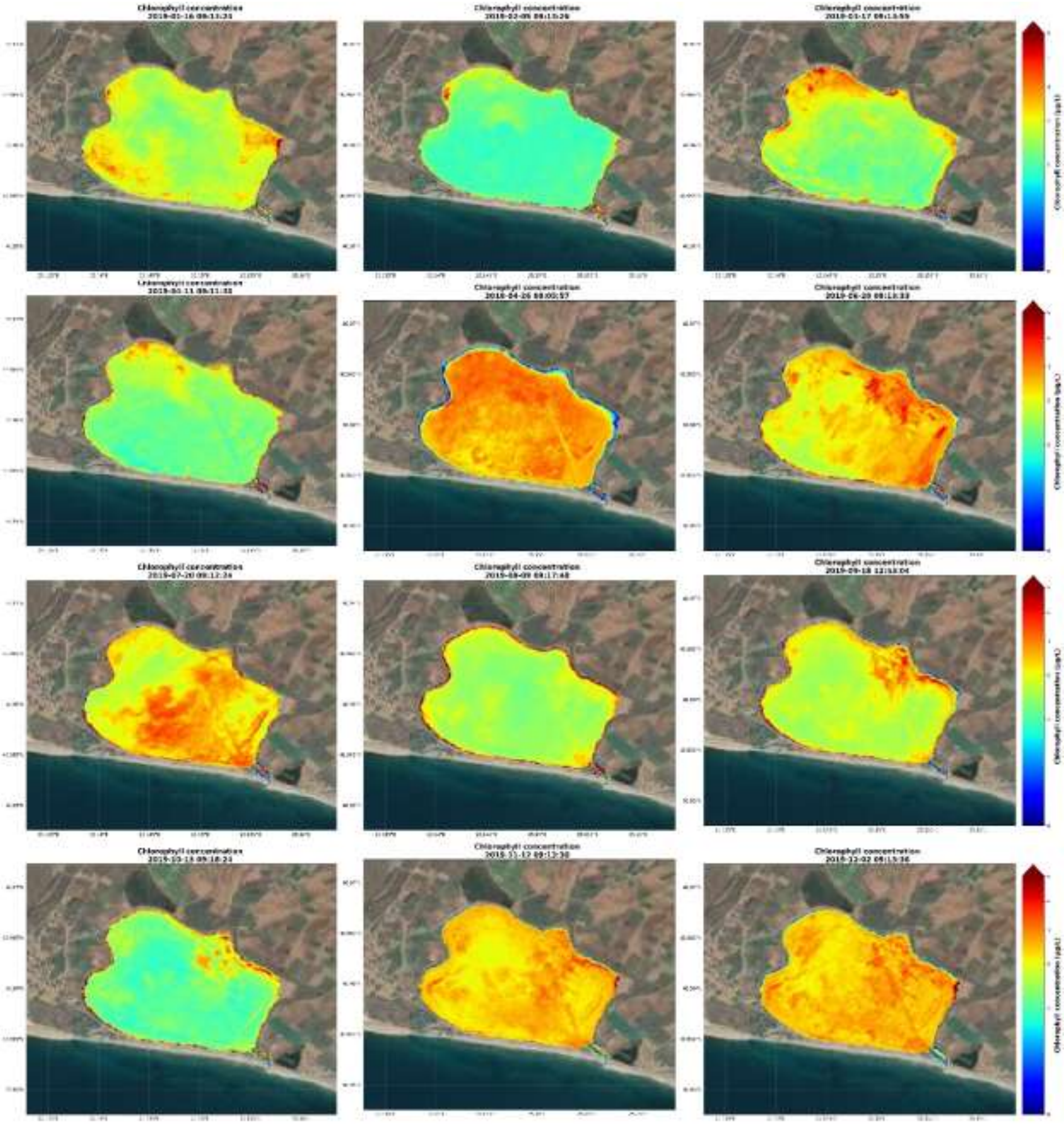

Figure 62. Seasonal evolution of Chl-a concentration in Xirolimni lagoon for the year 2019, based on Sentinel 2 satellite images.

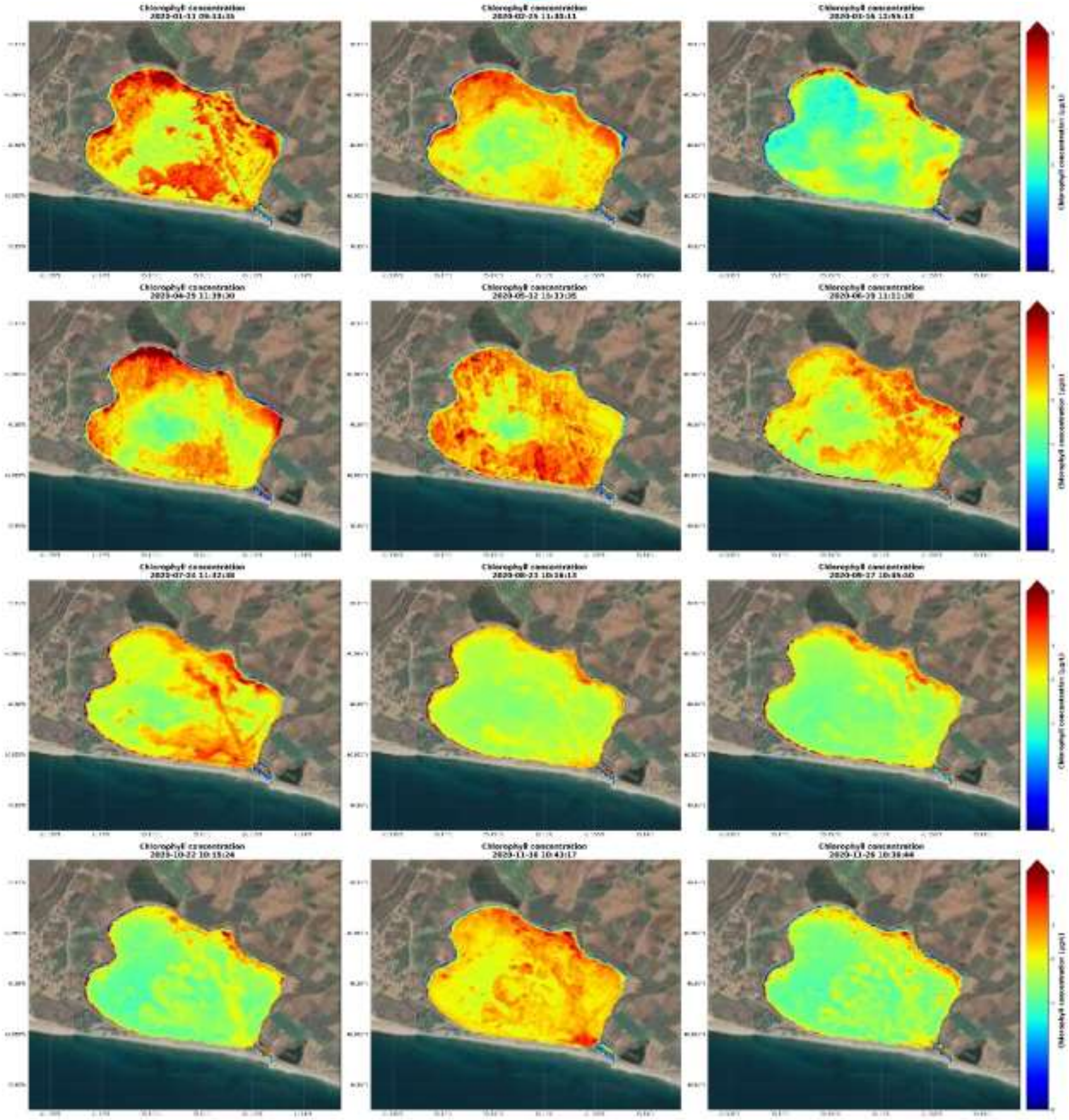

Figure 63. Seasonal evolution of Chl-a concentration in Xirolimni lagoon for the year 2020, based on Sentinel 2 satellite images.

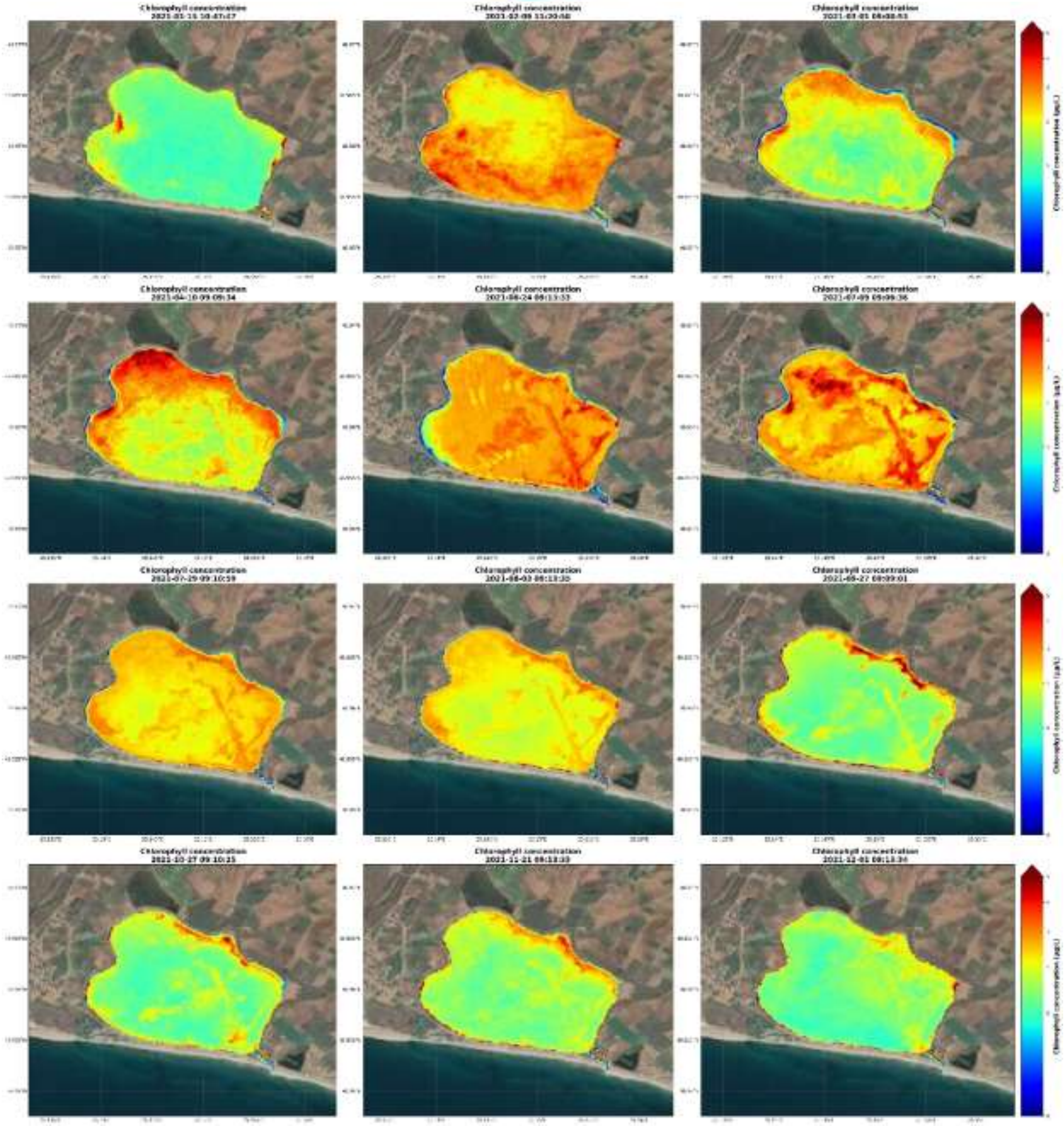

Figure 64. Seasonal evolution of Chl-a concentration in Xirolimni lagoon for the year 2021, based on Sentinel 2 satellite images.

3.1.6 Ptelea lagoon

Figures 62-71 present the spatial distribution of Chl-a in Ptelea lagoon for the years 2013-2021. During 2013 (Figure 65), the first peak is reached in May. The highest values are mostly concentrated at the eastern shores (up to 30 μg/l) and the northern part of the basin (3.0-3.5 μg/l). In the following months, Chl-a decreases until July, when it starts to increase again until late summer. This concentration rise starts from the northern part (July, 2.5-3.0 μg/l) and eventually is transferred at the center of the basin (late August). In summer, the eastern and western shores show high values, ranging from 4.0 to 30 μg/l. The third peak is reached in November and then Chl-a decrease as we move towards the winter.

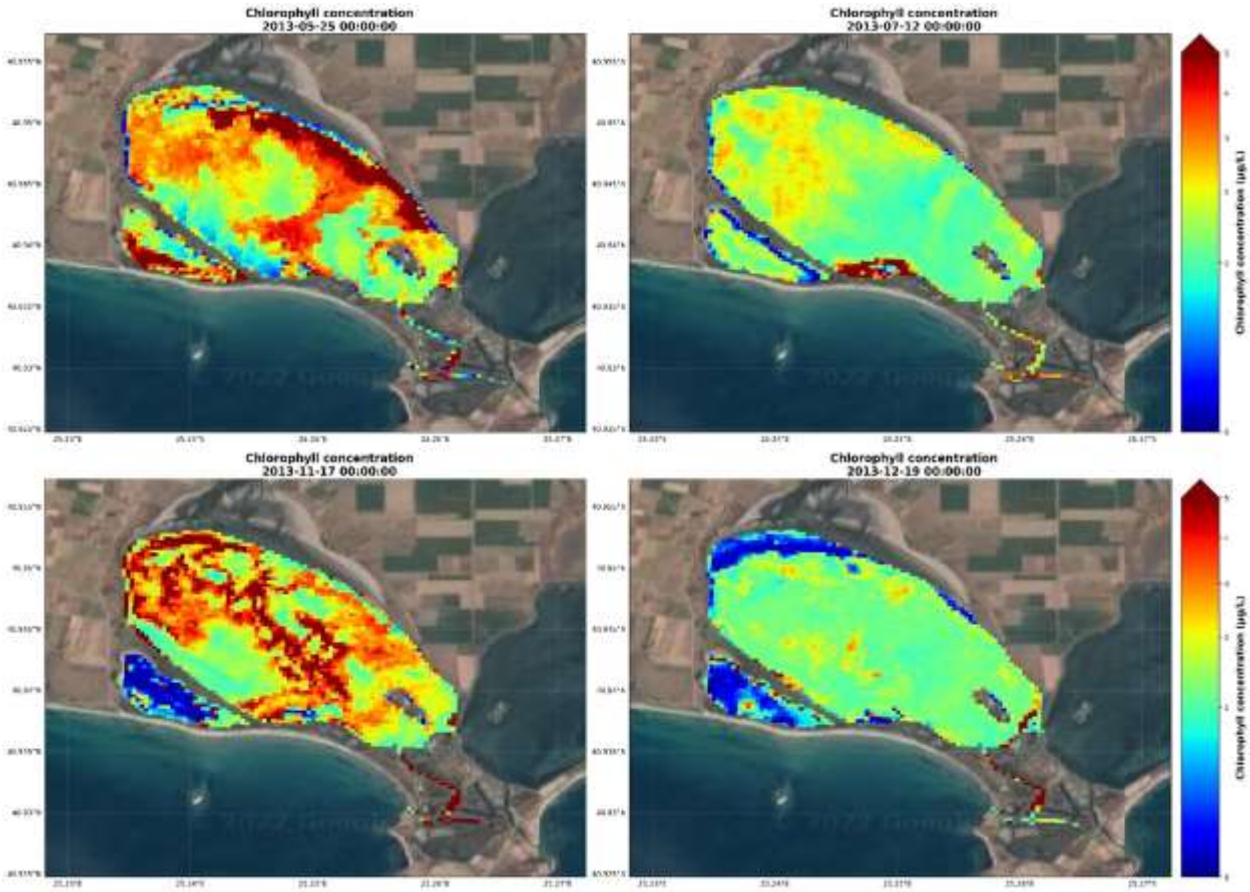

Figure 65. Seasonal evolution of Chl-a concentration in Ptelea lagoon for the year 2013, based on Landsat 8 satellite images.

Figure 66 shows the increase of Chl-a, from low concentrations at the beginning of the year to higher in the summer. Chl-a values range from 1.0 to 3.0 μg/l in late June, with the highest values being detected at the southern parts of the basin. In August, the highest values are found near the northern shores and the north-western shallow parts. In the following months, the high values seem to move towards the center of the lagoon (1.5-2.0 μg/l).

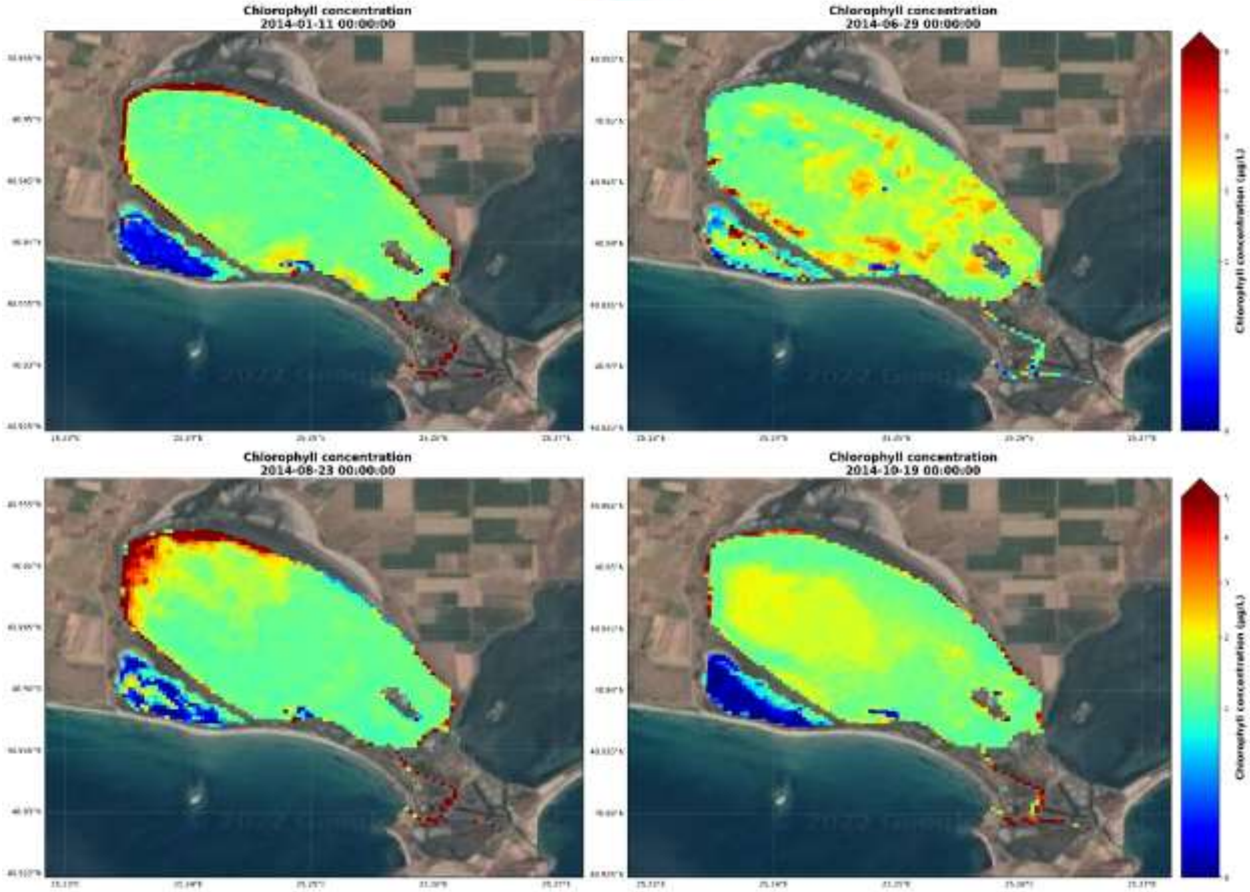

Figure 66. Seasonal evolution of Chl-a concentration in Ptelea lagoon for the year 2014, based on Landsat 8 satellite images.

The first half of 2015 is presented in Figure 67 covered by Landsat 8 and the second half is presented in Figure 68 covered by Sentinel 2. The images selected for the first half of 2015 illustrate that the first peak is reached at the end of spring. In February, Chl-a values range from 0.5 to 1.6 µg/l covering the major parts of the lagoon, with the exception of the northern part, which shows higher values up to 5 µg/l. Increased values spread towards the center of the lagoon in April and covers the whole basin in May.

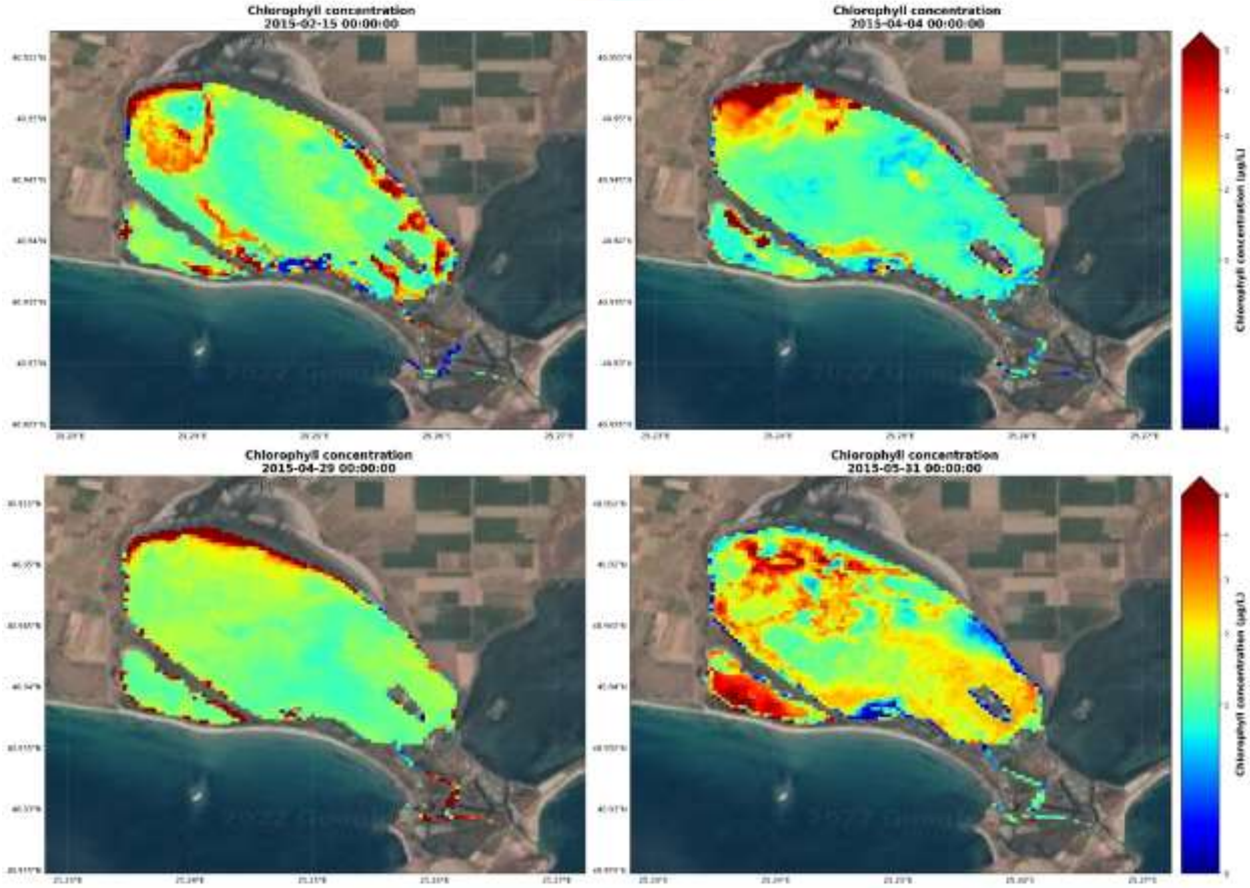

Figure 67. Seasonal evolution of Chl-a concentration in Ptelea lagoon for the year 2015, based on Landsat 8 satellite images.

For the second half of 2015 (Figure 68), higher values are detected at the center of the lagoon during the summer and the first months of autumn (8.0-20.0 μg/l). Another peak is observed in November, where the Chl-a values at the basin range from 8.0 to 15.0 μg/l and higher values are concentrated at the south-eastern part (30 μg/l) of the lagoon.

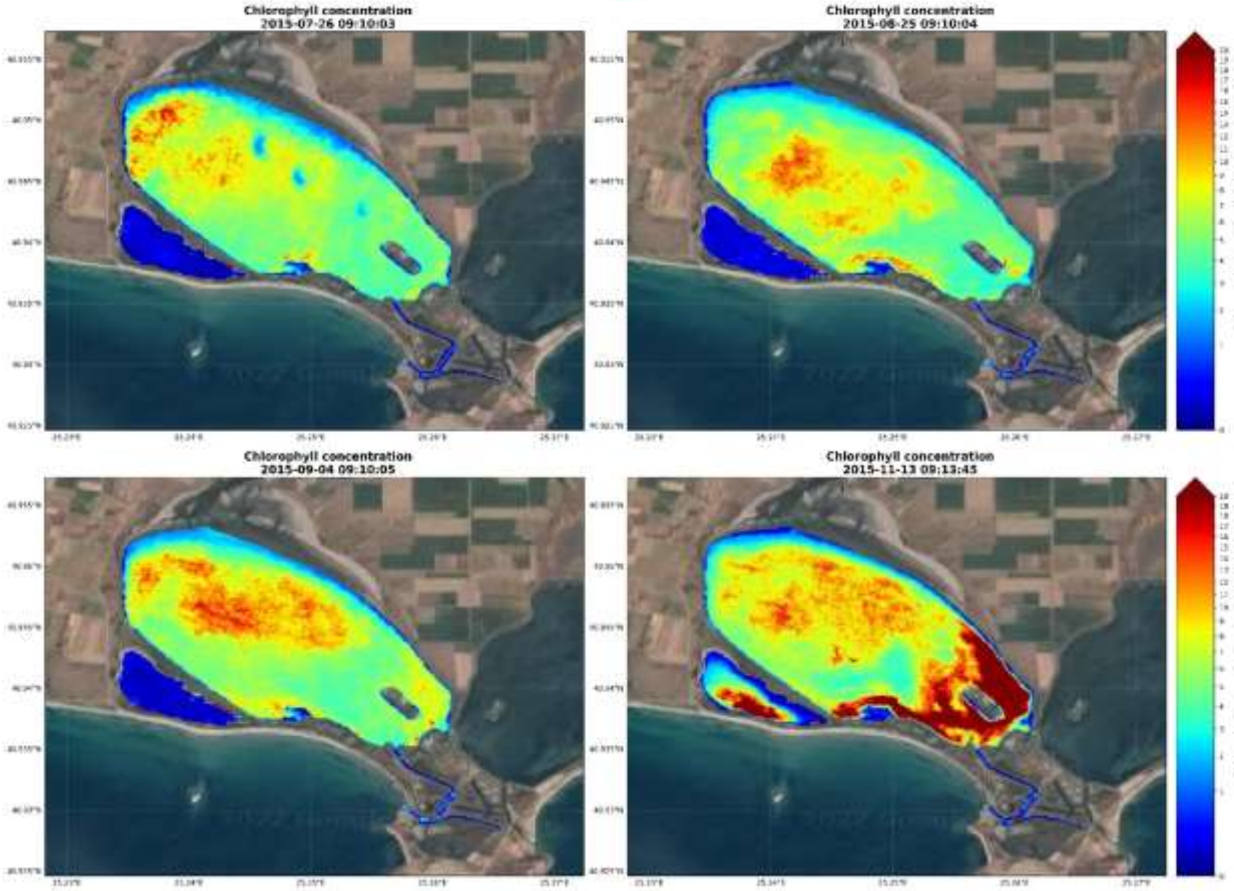

Figure 68. Seasonal evolution of Chl-a concentration in Ptelea lagoon for the year 2015, based on Sentinel 2 satellite images.

For 2016 two images during summer are presented as due to cloudiness these were the only images available for processing (Figure 69). In July, low Chl-a values are observed at the northern part of the lagoon (up to 1.5 µg/l) and higher values on the southern part, reaching 35 µg/l. In August, Chl-a values range around 2 µg/l covering most of the basin, except for the western part where they range from 7.0 to 15.0 µg/l.

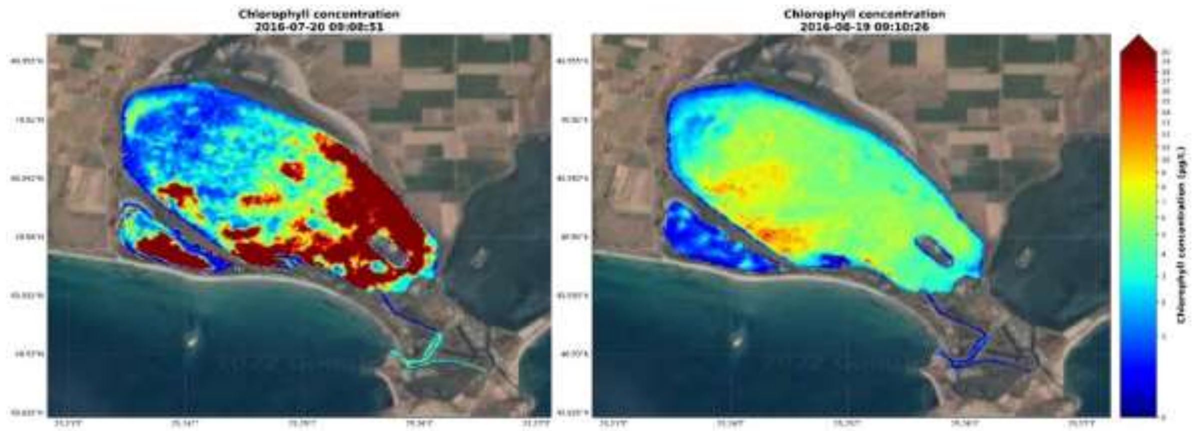

Figure 69. Seasonal evolution of Chl-a concentration in Ptelea lagoon for the year 2016, based on Sentinel 2 satellite images.

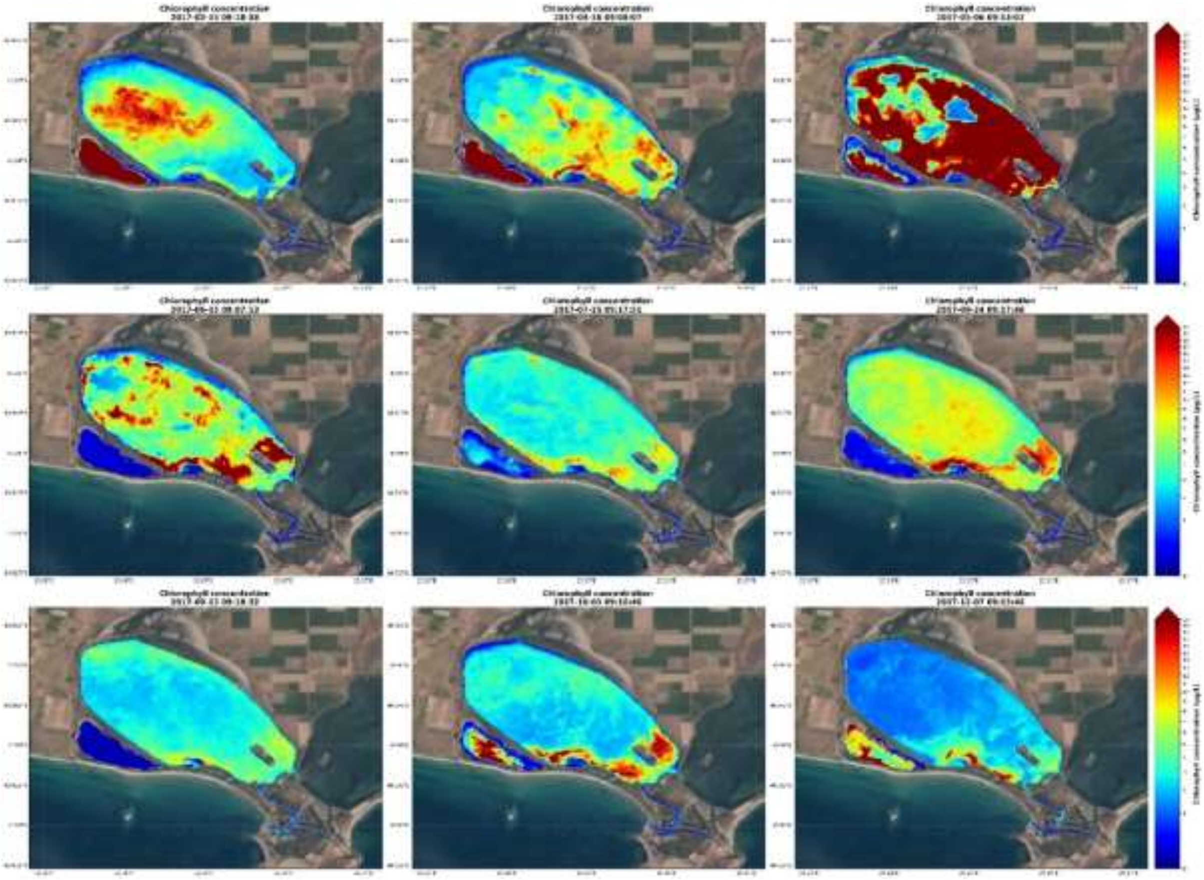

Figure 70. Seasonal evolution of Chl-a concentration in Ptelea lagoon for the year 2017, based on Sentinel 2 satellite images.

During 2017 (Figure 70), higher Chl-a values are observed at the north-western parts of the lagoon (up to 24 µg/l). These increased values are gradually expanded to the southern parts in April, and eventually cover the whole basin in May. The highest Chl-a reached in May is 40 µg/l. In the following months, Chl-a decreases and the next peak is observed in August. In autumn and winter months the Chl-a values decrease, reaching their minimum values in December.

Figure 71 shows the increase of Chl-a values, from low concentrations in January to higher in late May. Almost the whole basin shows high Chl-a values that exceed 30 µg/l. In the following months, Chl-a decreases, until the lowest values are reached, in the beginning of August. A peak is observed in the first days of September, with higher values concentrating at the center and the western shore of the lagoon. In the autumn and winter months, Chl-a values are decreased throughout the basin.

During 2019 (Figure 72), Chl-a starts to increase in late June. The event begins from the eastern shores and the southern parts and ultimately spreads over the basin in November. Chl-a values decrease gradually in December.

The first Chl-a peak in 2020 (Figure 73) is observed in May. Chl-a values start increasing from February and reach their highest values in May (up to 35 µg/l). Then, Chl-a decreases until early September. From mid-September, the Chl-a values increase again starting from the northern and southern parts and spreading to the whole basin by November.

Increased Chl-a values are detected in January 2021 (Figure 74) compared to the previous years, reaching 40 µg/l. In the following months, Chl-a values decrease and then increase again during spring. High values are observed in late September, remaining high until November and confine only to the southern part in December.

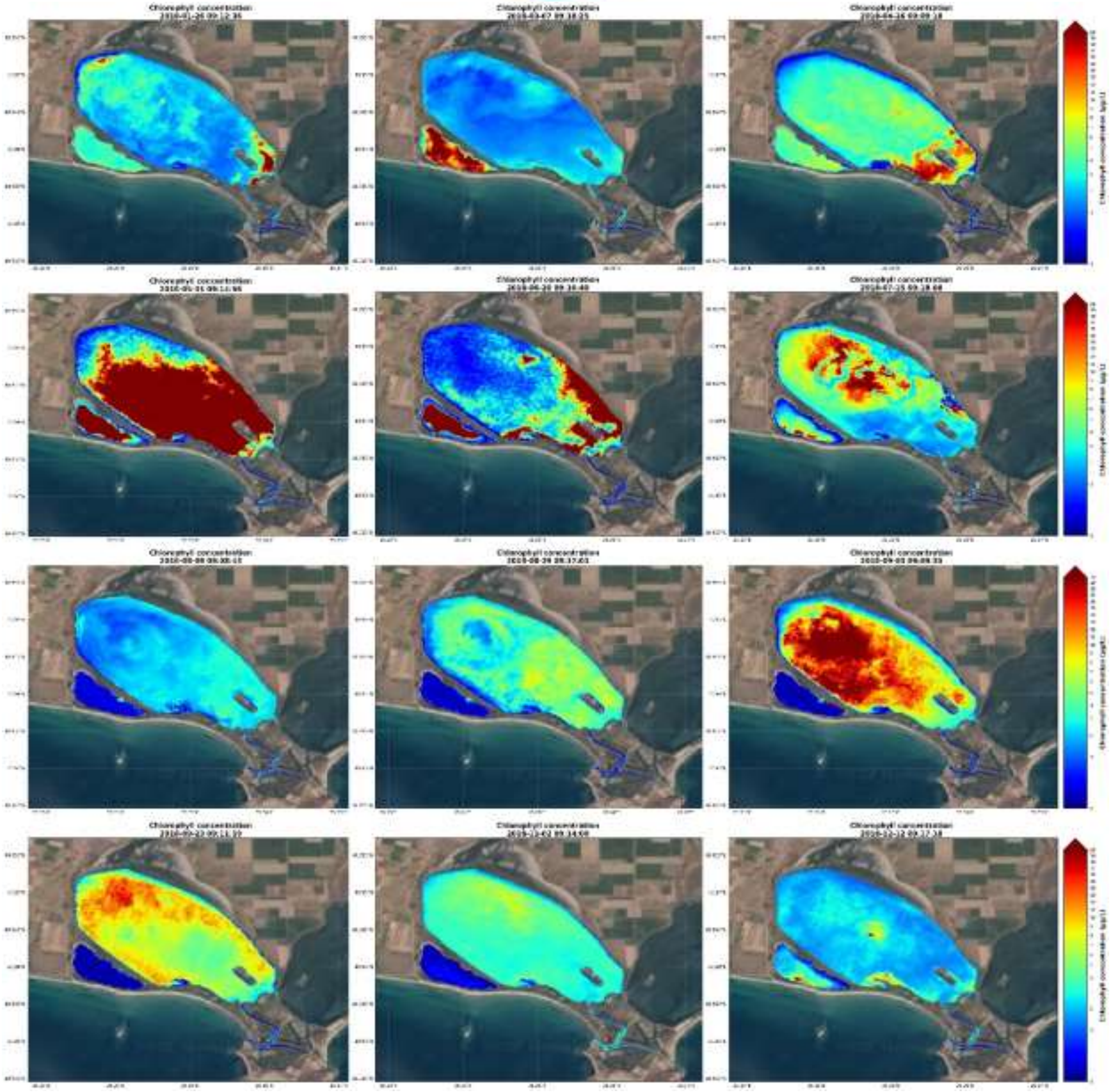

Figure 71. Seasonal evolution of Chl-a concentration in Ptelea lagoon for the year 2018, based on Sentinel 2 satellite images.

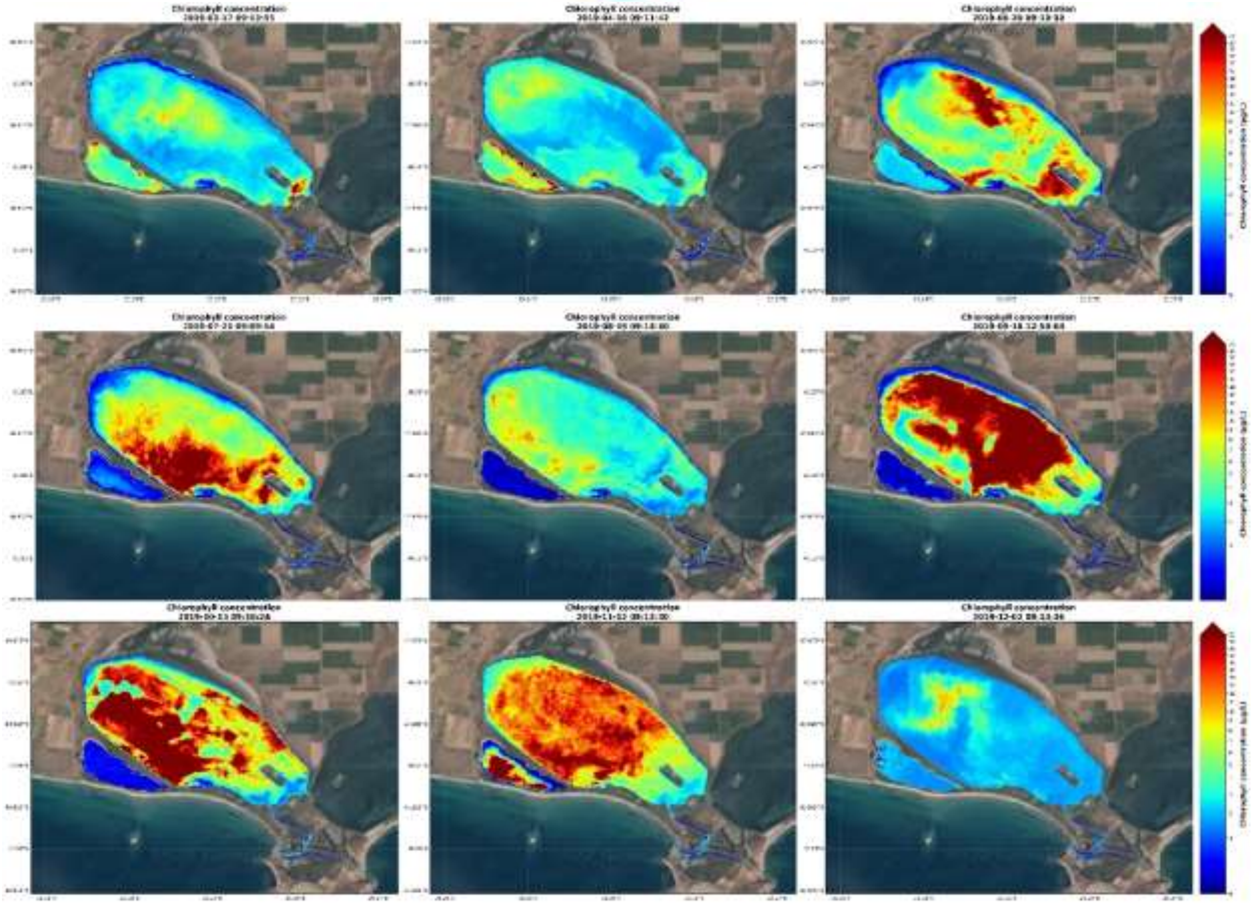

Figure 72. Seasonal evolution of Chl-a concentration in Ptelea lagoon for the year 2019, based on Sentinel 2 satellite images.

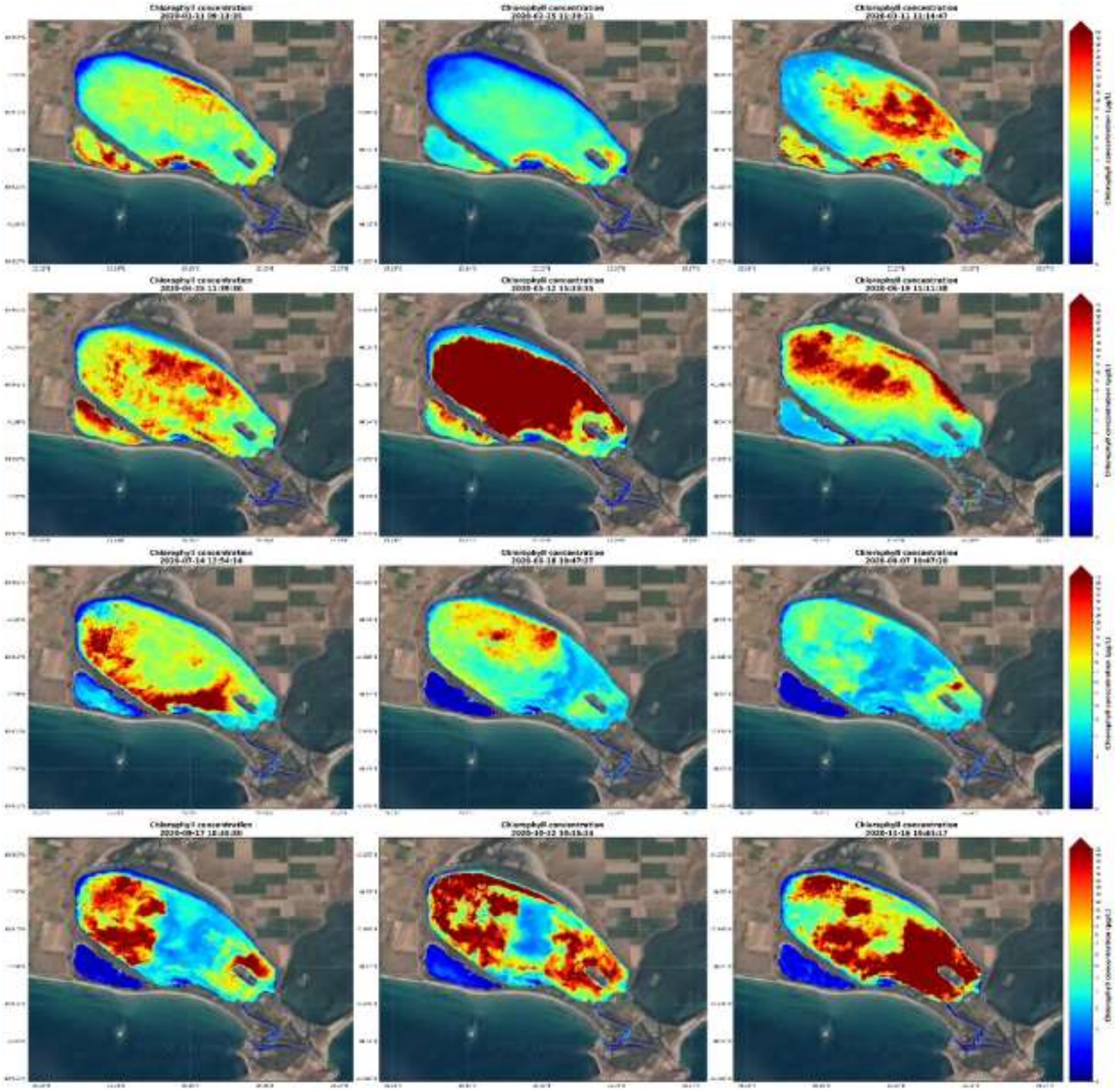

Figure 73. Seasonal evolution of Chl-a concentration in Ptelea lagoon for the year 2020, based on Sentinel 2 satellite images.

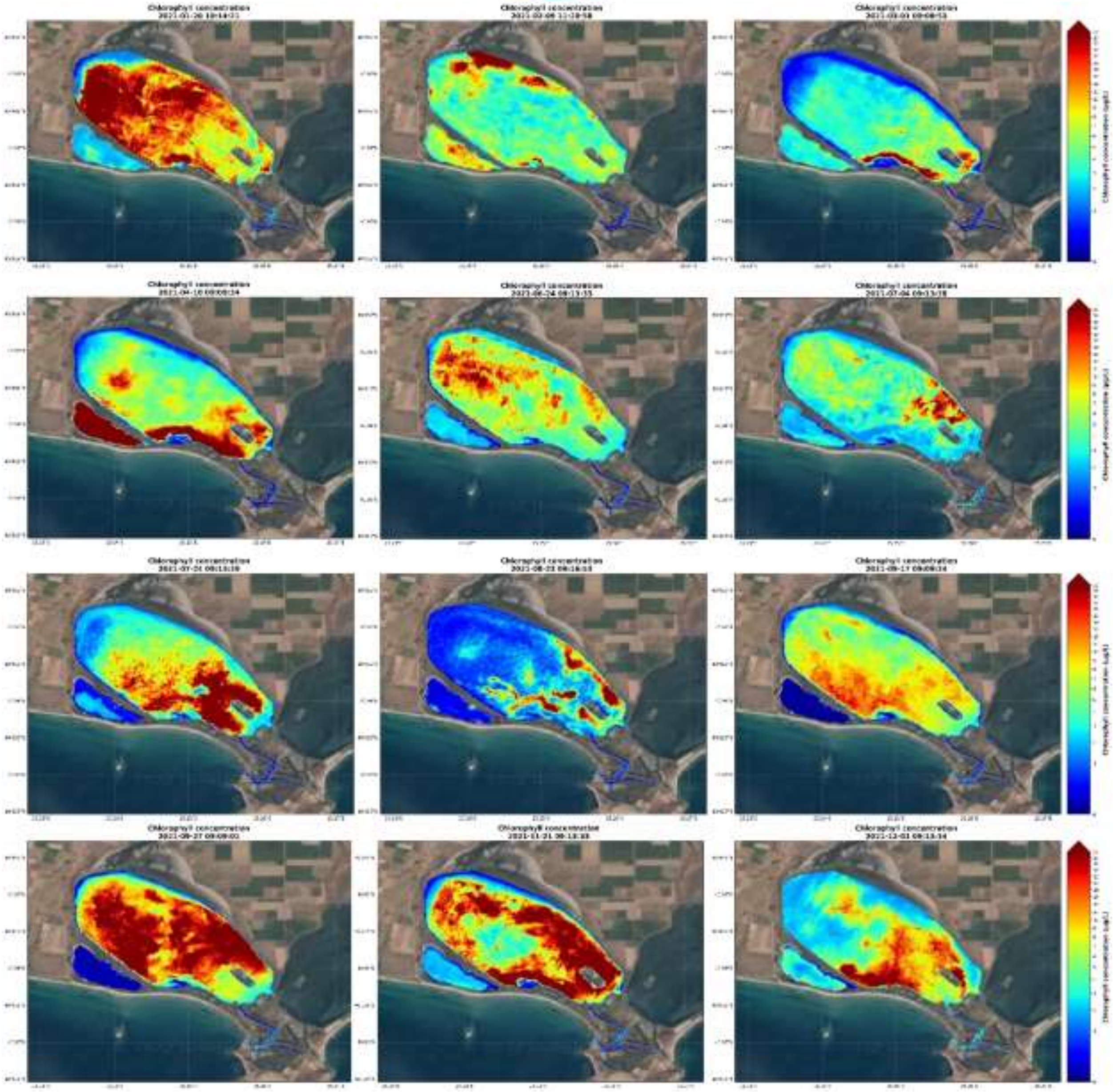

Figure 74. Seasonal evolution of Chl-a concentration in Ptelea lagoon for the year 2021, based on Sentinel 2 satellite images.

3.2 Chlorophyll statistical analysis

Satellite-derived Chlorophyll-a data were extracted from specific points (grid cells), representing the eutrophication conditions at sub-basins of the Nestos and Vistonis coastal lagoons. The analysis was divided in two parts: the analysis on the mean-monthly Landsat data and the analysis on the mean-monthly Sentinel data. Daily Chl-a values were monthly-averaged to smooth out any outliers found in data, as a result of the proximity of the cell to land and the impact of water column shallowness.

Data analysis was performed according to the following steps:

- At each point, statistical measures, like the minimum, maximum, median, mean, standard deviation, skewness and kurtosis were computed.
- An initial assessment of the theoretical probability density function (PDF) fitted on the data was given through the construction of the skewness-kurtosis graph (Cullen and Frey, 1999), in which the Chl-a data distribution were plotted against a series of well-known theoretical distributions (normal, exponential, log-normal, gamma, Weibull). The higher the distance among points, the larger the discrepancy among distributions.
- The best-fit theoretical PDF was determined following the AIC and BIC criteria, and its parameters were computed following the maximum likelihood estimation (MLE) method.
- The probability of exceeding the Chl-a concentration threshold of 2 μg/l was assessed.

3.2.1 Landsat Data

3.2.1.1 Vassova lagoon

The points selected for Chl-a concentration extraction for the eutrophication assessment in Vassova lagoon, are shown in Figure 75. These points cover the typical conditions at all sub-basins of the lagoon and are distributed among various depths.

Figure 75. Points for Chl-a concentration extraction in Vassova lagoon.

Table 8 presents the statistical measures for Chl-a concentration at all points examined in Vassova lagoon.

Table 8. Statistical measures per point for Chl-a concentration at Vassova Lagoon.

Points	Min	Max	Median	Mean	St. deviation	Skewness	Kurtosis
1	0.660	2.721	1.216	1.434	0.560	1.141	3.206
2	0.639	3.755	1.271	1.389	0.581	2.920	13.139
3	0.526	3.684	1.184	1.359	0.611	2.200	9.651
4	0.561	35810.54	288.660	3646.255	7255.685	3.338	16.351
5	0.002	5.068	1.171	1.265	0.867	2.990	15.963
6	0.573	34.604	1.442	4.349	7.470	3.073	12.726
7	0.005	10.812	1.329	1.894	1.902	3.809	20.341

Figures 76 and 77 illustrate the skewness-kurtosis plot of Cullen and Frey for the Landsat extracted Chl-a at all points in Vassova lagoon. Based on these graphs and the AIC and BIC criteria, it occurs that:

a) For Points 1, 2, 3, and 6, the log-normal distribution was found to be the best-fit theoretical distribution;

b) For Points 4, 5 and 7, the gamma distribution was found to be the best-fit theoretical distribution.

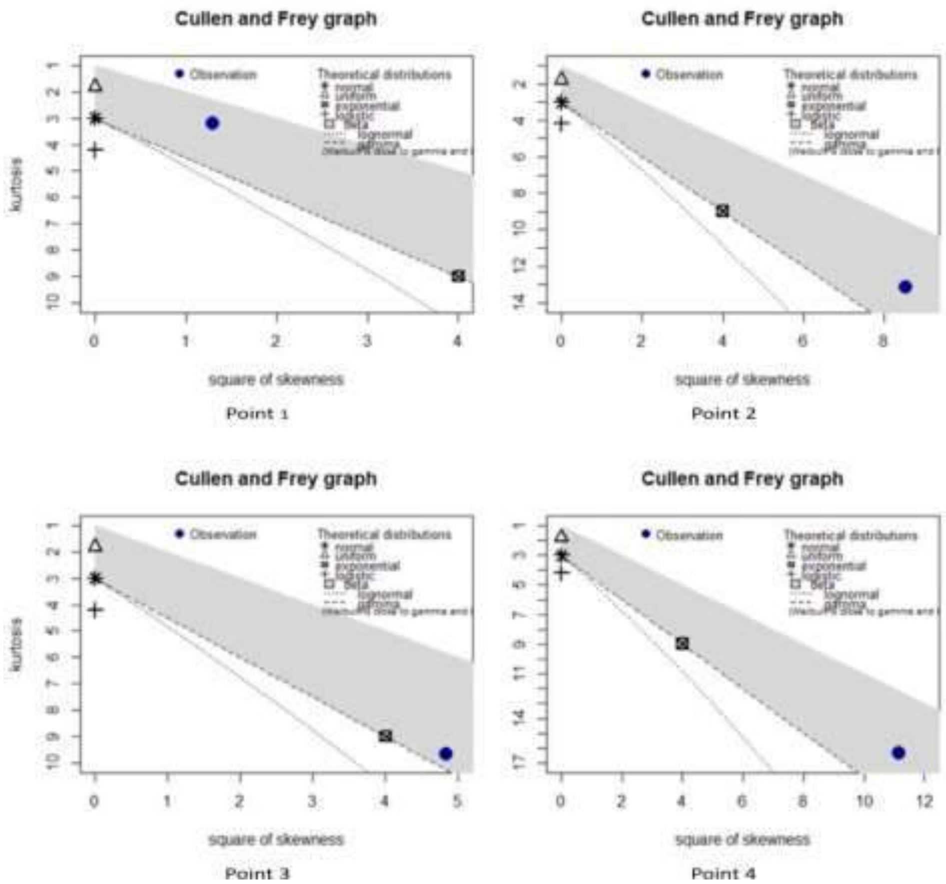

Figure 76. The Cullen and Frey diagrams for the distribution of Chl-a concentration at Points 1 - 4.

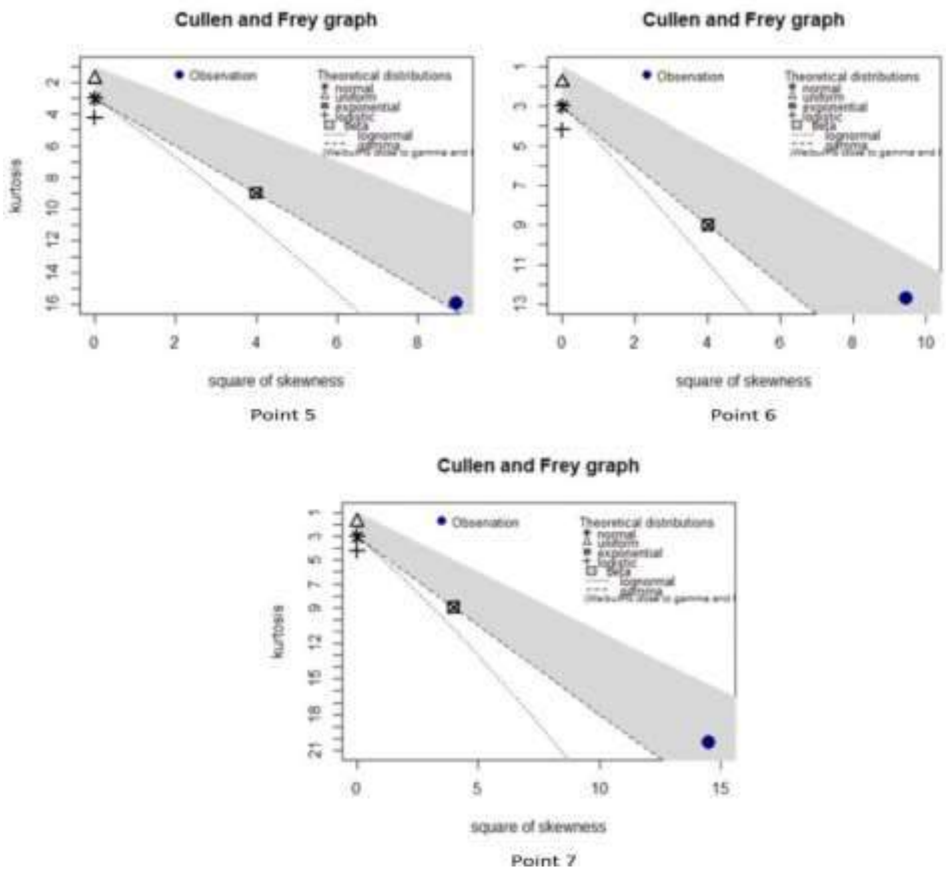

Figure 77. The Cullen and Frey diagrams for the distribution of Chl-a concentration at Points 5 - 7.

Table 9 presents the fitting parameters of the best-fit theoretical probability density function applied on the Chl-a concentration data extracted from Landsat in Vassova lagoon. Mean and standard deviation parameters are given for the normal PDFs, log(mean) and log(sd) parameters for the log-normal distributions and shape and scale for the gamma distributions.

Table 9. Fitting parameters of the best-fit theoretical probability density function.

Points	**1**	**2**	**3**	**4**	**5**	**6**	**7**
Mean							
St Dev							
Log(Mean)	0.296	0.271	0.230			0.764	
Log(St Dev)	0.064	0.058	0.069			0.184	
Shape				0.370	1.467		1.462
Scale							0.215
LogLikelihood	-19.954	-16.154	-20.341	-239.977	-33.887	-65.762	-47.978
AIC	43.908	36.308	44.682	483.954	71.774	135.525	99.956
BIC	46.711	39.110	47.484	486.757	74.576	138.327	102.759

The theoretical probability density functions (PDFs) and the cumulative density functions (CDFs) applied as best-fit on the Chl-a data, together with the relevant Q-to-Q and P-to-P plots are shown in Figures 78 and 79.

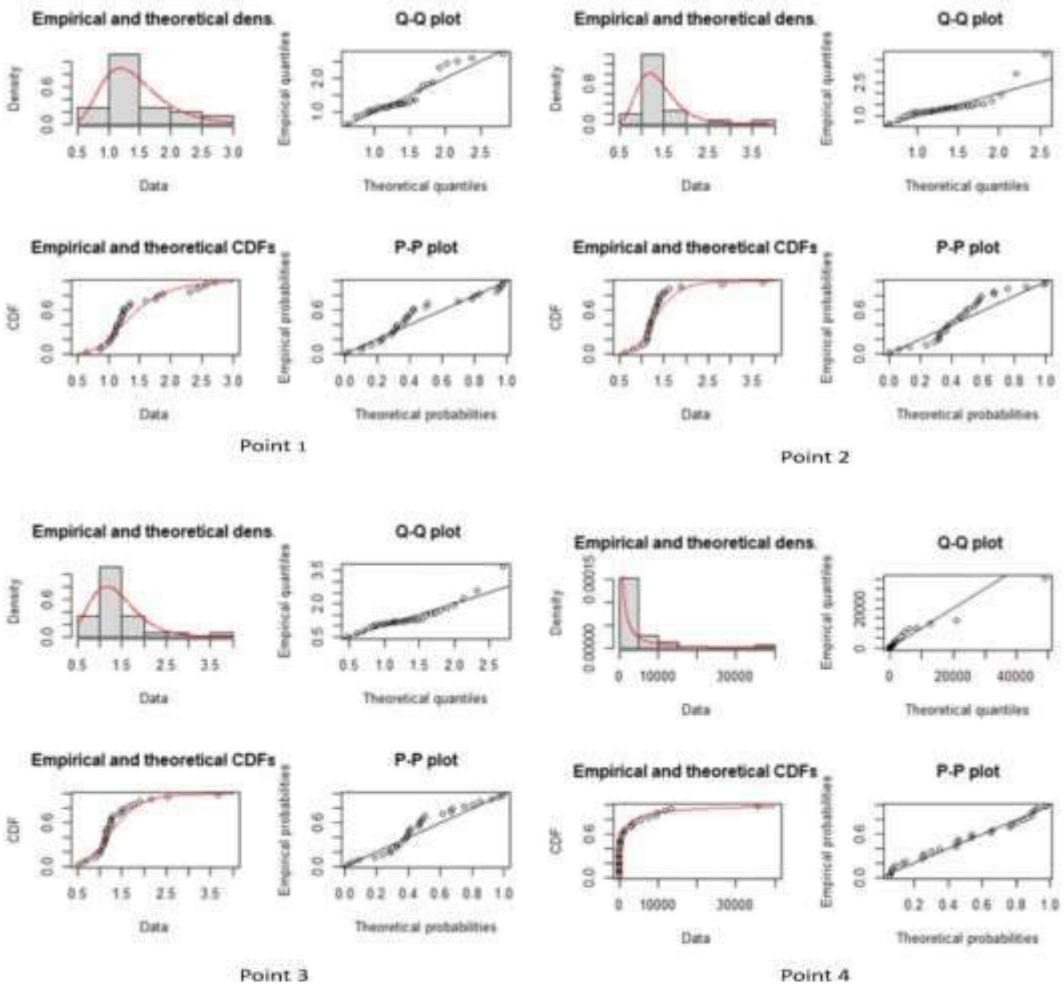

Figure 78. Theoretical probability density functions (PDFs) and the cumulative density functions (CDFs), applied as best-fit on the Chl-a data of points 1 - 4.

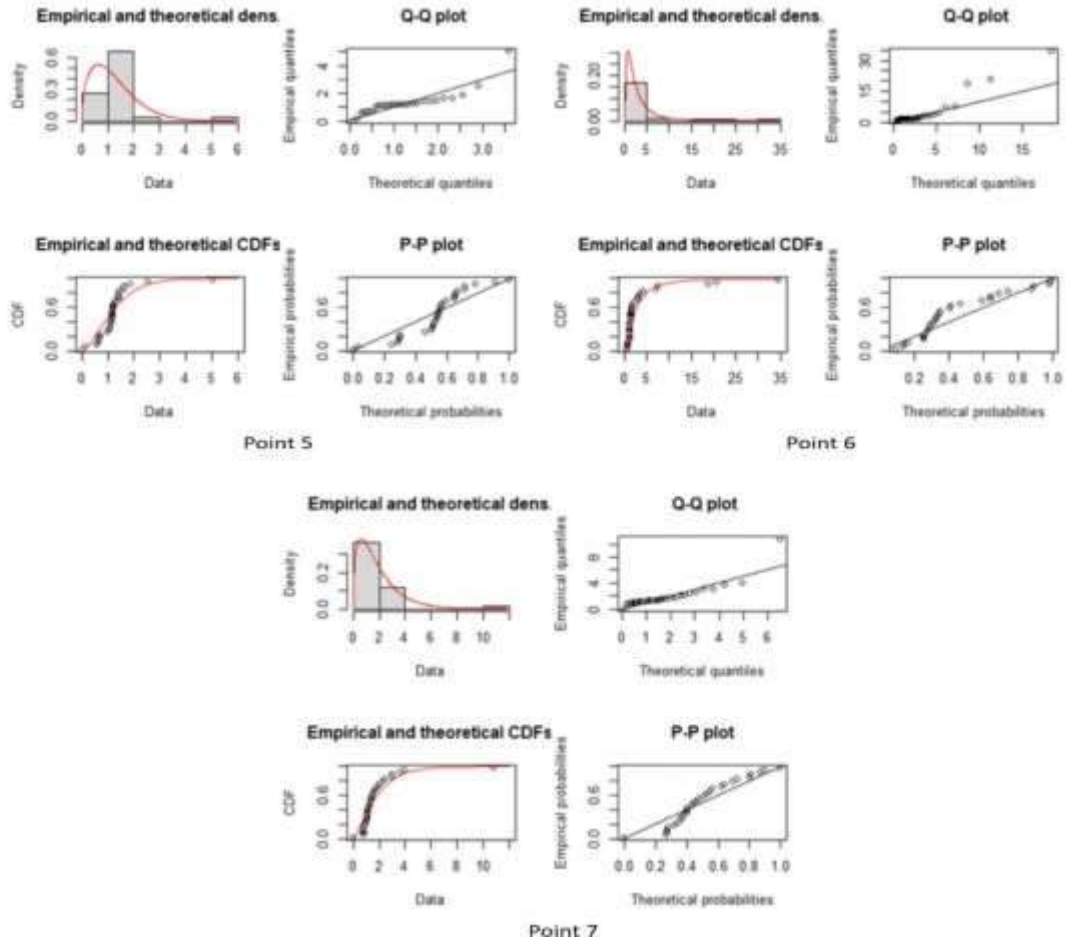

Figure 79. Theoretical probability density functions (PDFs) and the cumulative density functions (CDFs), applied as best-fit on the Chl-a data of points 5 – 7.

Based on the best-fit theoretical CDFs applied on the Chl-a, the probability of exceeding the eutrophication threshold of 2 μg/l was estimated. Probabilities of exceedance for all Vassova lagoon points are summarized in Table 10. Probability is a measure that ranges between 0 and 1, with zero implying that eutrophication is impossible and 1 implying that eutrophication is absolutely certain. Figure 80 illustrates the probability map of exceedance of the eutrophication threshold in Vassova lagoon.

Table 10. Probability of exceedance of the eutrophication threshold in Vassova lagoon.

Points	**Probability of Exceedance**
1	0.128
2	0.091
3	0.111
4	0.907
5	0.178
6	0.528
7	0.849

Based on the above, points 4, 6 and 7 are more vulnerable to eutrophication effects than the rest of the lagoon. Point 4 is located in the wintering canals, point 6 close to the inlet of the lagoon and point 7 in the north part of the lagoon. For point 6, exceedance probability is approximately 0.5, meaning that during half of a typical year eutrophication may exist. For points 4 and 7 exceedance probability is approximately 0.9 meaning almost the whole typical year eutrophication may exist. Based on the available Landsat images, it seems that the eutrophication prone periods are spring and summer. On the contrary, the rest of the points have limited probability for a eutrophication event.

Figure 80. Probability map of exceedance of the eutrophication threshold in Vassova lagoon.

3.2.1.2 Eratino lagoon

The dataset selected for Chl-a concentration extraction in Eratino lagoon has missing data, hence the eutrophication assessment analysis could not be done.

3.2.1.3 Agiasma lagoon

The points selected for Chl-a concentration extraction for the eutrophication assessment in Agiasma lagoon, are shown in Figure 81. These points cover the typical conditions at all sub-basins of the lagoon and are distributed among various depths.

Figure 81. Points for Chl-a concentration extraction in Agiasma lagoon.

Table 11 presents the statistical measures for Chl-a concentration at all points examined in Agiasma lagoon.

Table 11. Statistical measures per point for Chl-a concentration at Agiasma Lagoon.

Points	Min	Max	Median	Mean	St. deviation	Skewness	Kurtosis
1	0.989	4.580	1.439	1.640	0.699	2.823	12.607
2	1.049	1.679	1.281	1.291	0.163	0.656	2.861
3	0.107	2.818	1.162	1.261	0.438	1.502	8.914
4	0.915	2.339	1.378	1.443	0.328	1.032	4.468
5	0.890	72.135	1.610	3.896	11.923	5.839	37.365
6	1.171	3.826	1.909	1.957	0.558	1.515	6.134
7	0.183	5.098	1.398	1.545	0.769	3.320	17.289
8	0.000	4.552	0.364	0.528	0.758	4.679	27.695

Figures 82 and 83 illustrate the skewness-kurtosis plot of Cullen and Frey for the Landsat extracted Chl-a at all points in Agiasma lagoon. Based on these graphs and the AIC and BIC criteria, it occurs that:

a) For Points 2, 3 and 8, the normal distribution was found to be the best-fit theoretical distribution;
b) For Points 1, 4, 5 and 6, the log-normal distribution was found to be the best-fit theoretical distribution;
c) For Point 7, the gamma distribution was found to be the best-fit theoretical distribution.

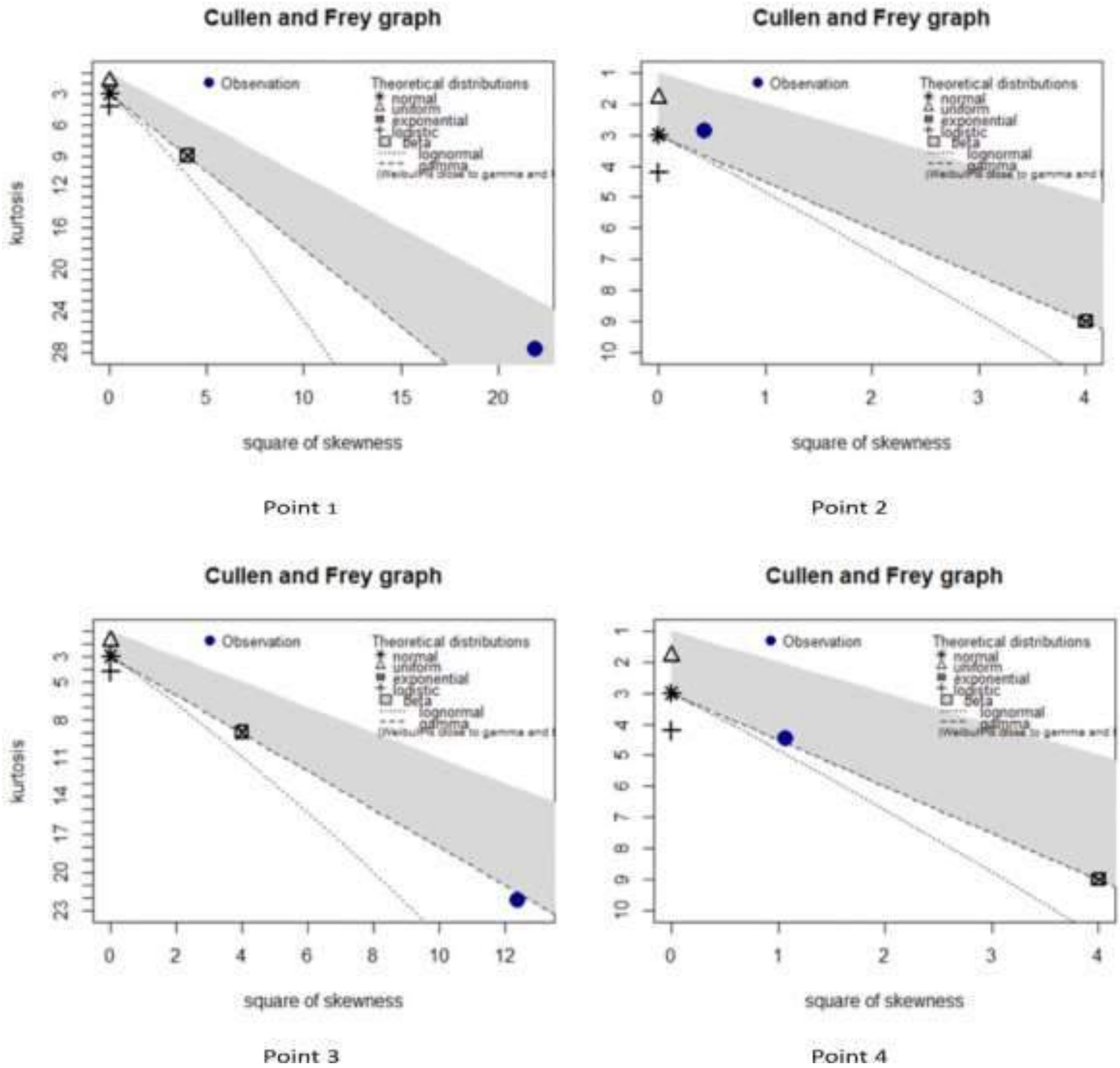

Figure 82. The Cullen and Frey diagrams for the distribution of Chl-a concentration at Points 1 - 4.

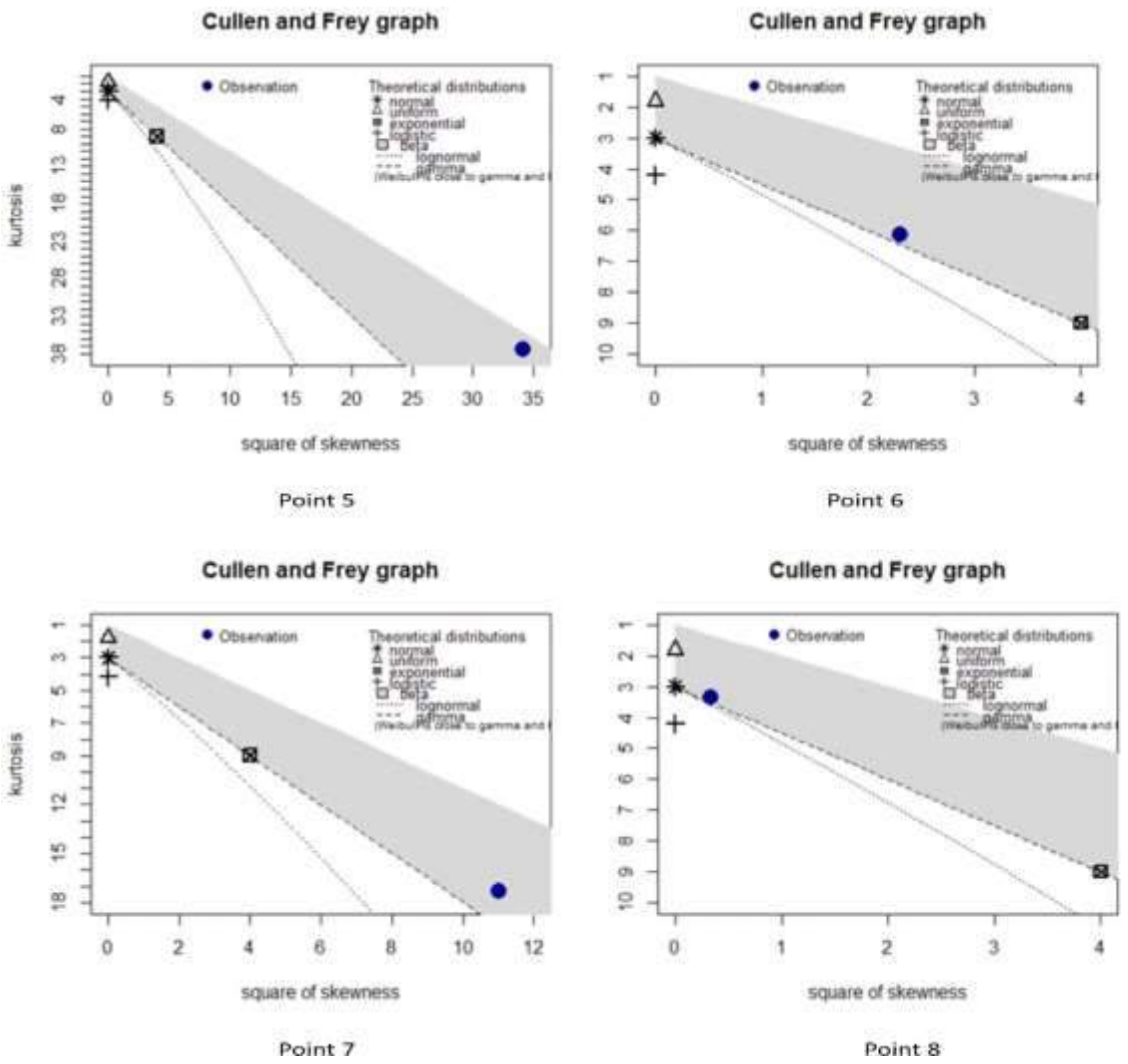

Figure 83. The Cullen and Frey diagrams for the distribution of Chl-a concentration at Points 5 - 8.

Table 12 presents the fitting parameters of the best-fit theoretical probability density function applied on the Chl-a concentration data extracted from Landsat in Agiasma lagoon. Mean and standard deviation parameters are given for the normal PDFs, log(mean) and log(sd) parameters for the log-normal distributions and shape and scale for the gamma distributions.

Table 12. Fitting parameters of the best-fit theoretical probability density function.

Points	1	2	3	4	5	6	7	8
Mean		1.291	1.261					1.272
St Dev		0.161	0.431					0.248
Log(Mean)	0.434			0.343	0.631	0.637		
Log(St Dev)	0.054			0.213	0.759	0.255		

Shape							5.506	
Scale							3.563	
LogLikelihood	-24.941	14.232	-20.264	-7.717	-62.136	-24.169	-32.825	-0.957
AIC	53.883	-24.465	44.529	19.434	128.272	52.339	69.650	5.914
BIC	56.994	-21.354	47.639	22.545	131.382	55.450	72.761	9.025

The theoretical probability density functions (PDFs) and the cumulative density functions (CDFs) applied as best-fit on the Chl-a data, together with the relevant Q-to-Q and P-to-P plots are shown in Figures 84 and 85.

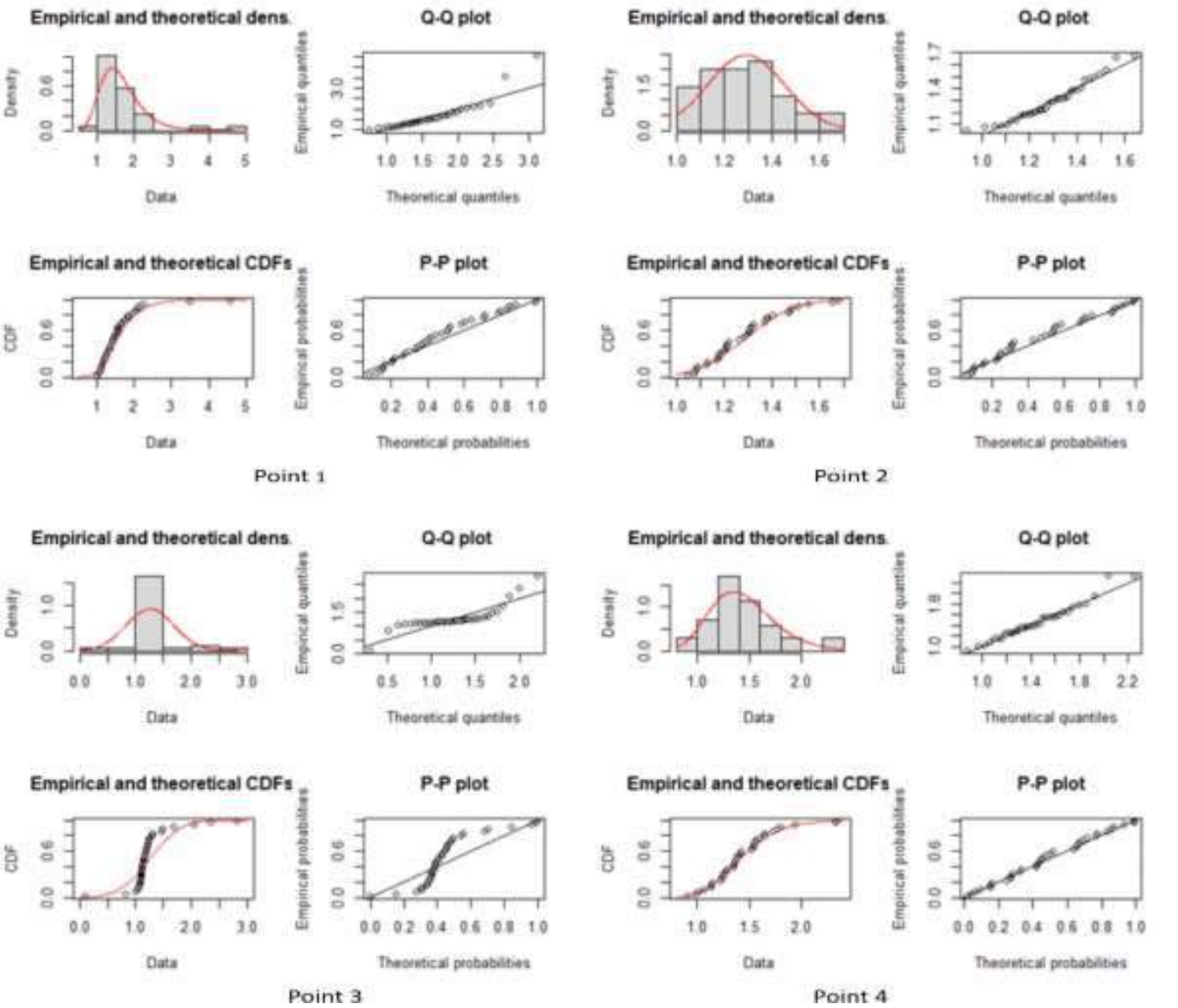

Figure 84. Theoretical probability density functions (PDFs) and the cumulative density functions (CDFs), applied as best-fit on the Chl-a data of points 1 – 4.

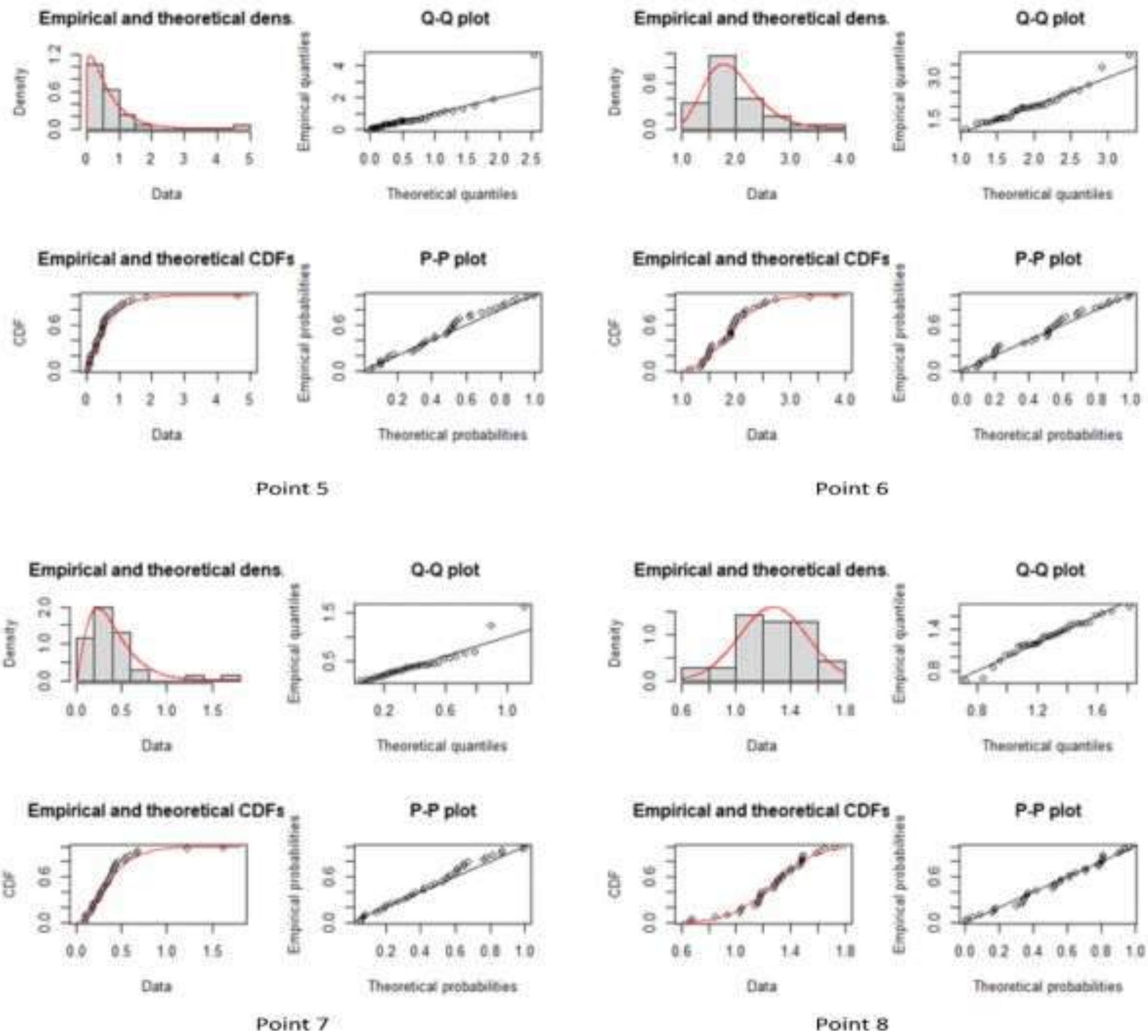

Figure 85. Theoretical probability density functions (PDFs) and the cumulative density functions (CDFs), applied as best-fit on the Chl-a data of points 5 – 8.

Based on the best-fit theoretical CDFs applied on the Chl-a, the probability of exceeding the eutrophication threshold of 2 μg/l was estimated. Probabilities of exceedance for all Agiasma lagoon points are summarized in Table 13. Probability is a measure that ranges between 0 and 1, with zero implying that eutrophication is impossible and 1 implying that eutrophication is absolutely certain. Figure 86 illustrates the probability map of exceedance of the eutrophication threshold in Agiasma lagoon.

Table 13. Probability of exceedance of the eutrophication threshold in Agiasma lagoon.

Points	Probability of Exceedance
1	0.209
2	5.442e-06
3	0.043

4	0.051
5	0.467
6	0.413
7	0.220
8	0.001

Based on the above, points 1, 5 and 6 are more vulnerable to eutrophication effects than the rest of the lagoon. These points are located at the vicinity of the northern inlet of the lagoon and its central basin. Exceedance probability is approx. 0.5, meaning that during half of a typical year eutrophication may exist. Based on the available Landsat images, it seems that the eutrophication prone periods are spring and summer. On the contrary, points located near the southern inlet have limited probability for a eutrophication event.

Figure 86. Probability map of exceedance of the eutrophication threshold in Agiasma lagoon.

3.2.1.4 Porto Lagos lagoon

The points selected for Chl-a concentration extraction for the eutrophication assessment in Porto Lagos lagoon, are shown in Figure 87. These points cover the typical conditions at all sub-basins of the lagoon and are distributed among various depths.

Figure 87. Points for Chl-a concentration extraction in Porto Lagos lagoon.

Table 14 presents the statistical measures for Chl-a concentration at all points examined in Porto Lagos lagoon.

Table 14. Statistical measures per point for Chl-a concentration at Porto Lagos lagoon.

Points	Min	Max	Median	Mean	St. deviation	Skewness	Kurtosis
1	1.036	5.086	1.731	1.939	0.782	2.273	9.929
2	0.080	2.708	1.009	1.042	0.566	0.832	3.793
3	1.108	9.246	4.734	4.748	2.103	0.063	2.209
4	-0.490	1.061	0.294	0.341	0.306	0.176	4.510
5	-0.228	1.245	0.330	0.403	0.314	0.618	3.364
6	1.084	4.403	1.600	1.835	0.698	2.064	7.838
7	0.926	3.802	1.322	1.629	0.680	1.860	5.926
8	1.006	22.340	1.417	2.270	3.554	5.610	35.431
9	0.959	3.591	1.368	1.517	0.506	2.154	10.202
10	1.042	5.002	1.624	1.729	0.724	2.955	14.986
11	0.899	75.929	1.505	3.708	12.578	5.899	37.859
12	0.858	3.974	1.512	1.592	0.508	3.149	17.105
13	0.024	707.430	2.771	64.424	174.313	3.213	12.408

Figures 88, 89 and 90 illustrate the skewness-kurtosis plot of Cullen and Frey for the Landsat extracted Chl-a at all points in Porto Lagos lagoon. Based on these graphs and the AIC and BIC criteria, it occurs that:

a) For Point 3, the gamma distribution was found to be the best-fit theoretical distribution;
b) For all the other points (1-2 and 4-13), the log-normal distribution was found to be the best-fit theoretical distribution.

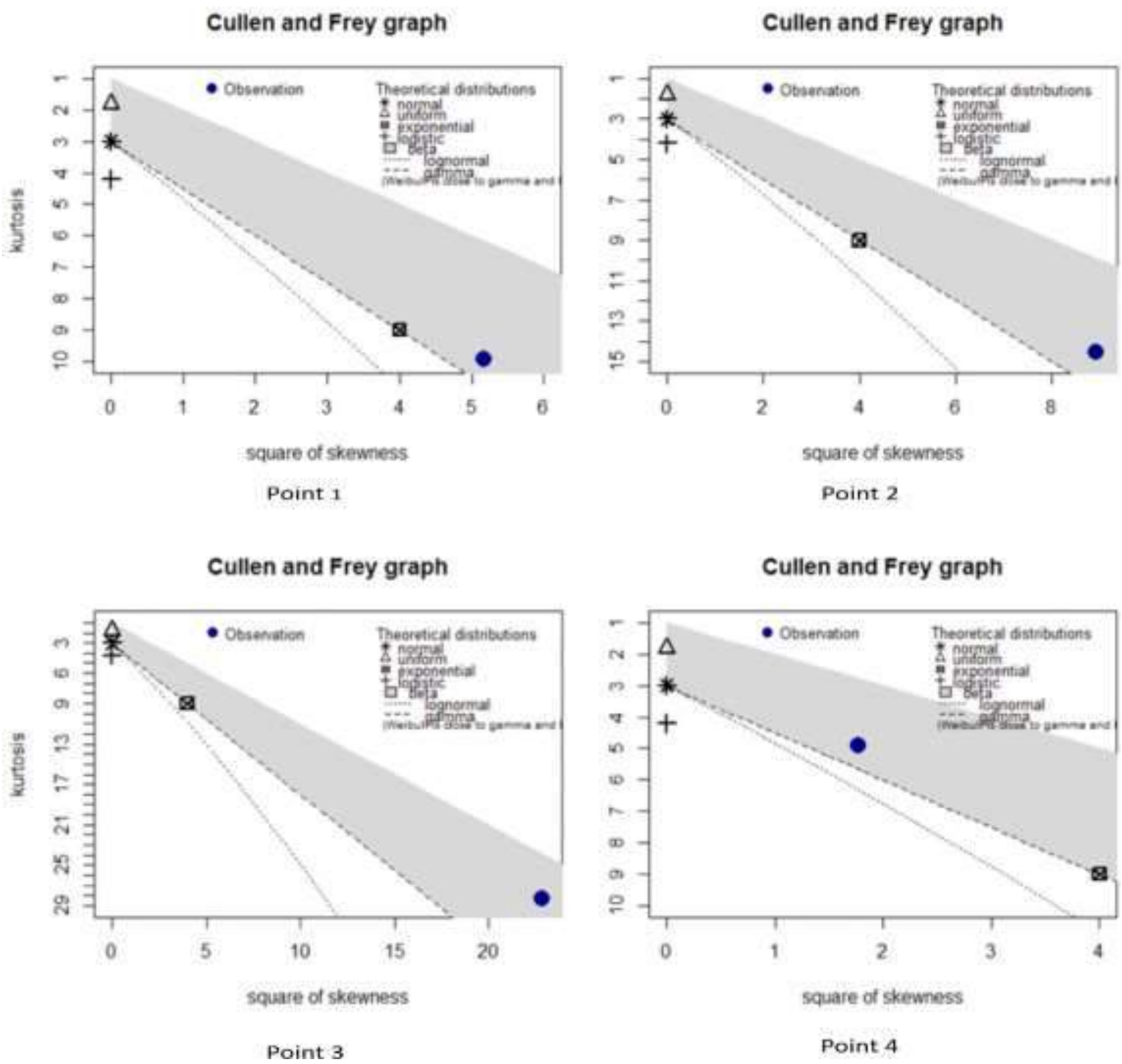

Figure 88. The Cullen and Frey diagrams for the distribution of Chl-a concentration at Points 1 - 4.

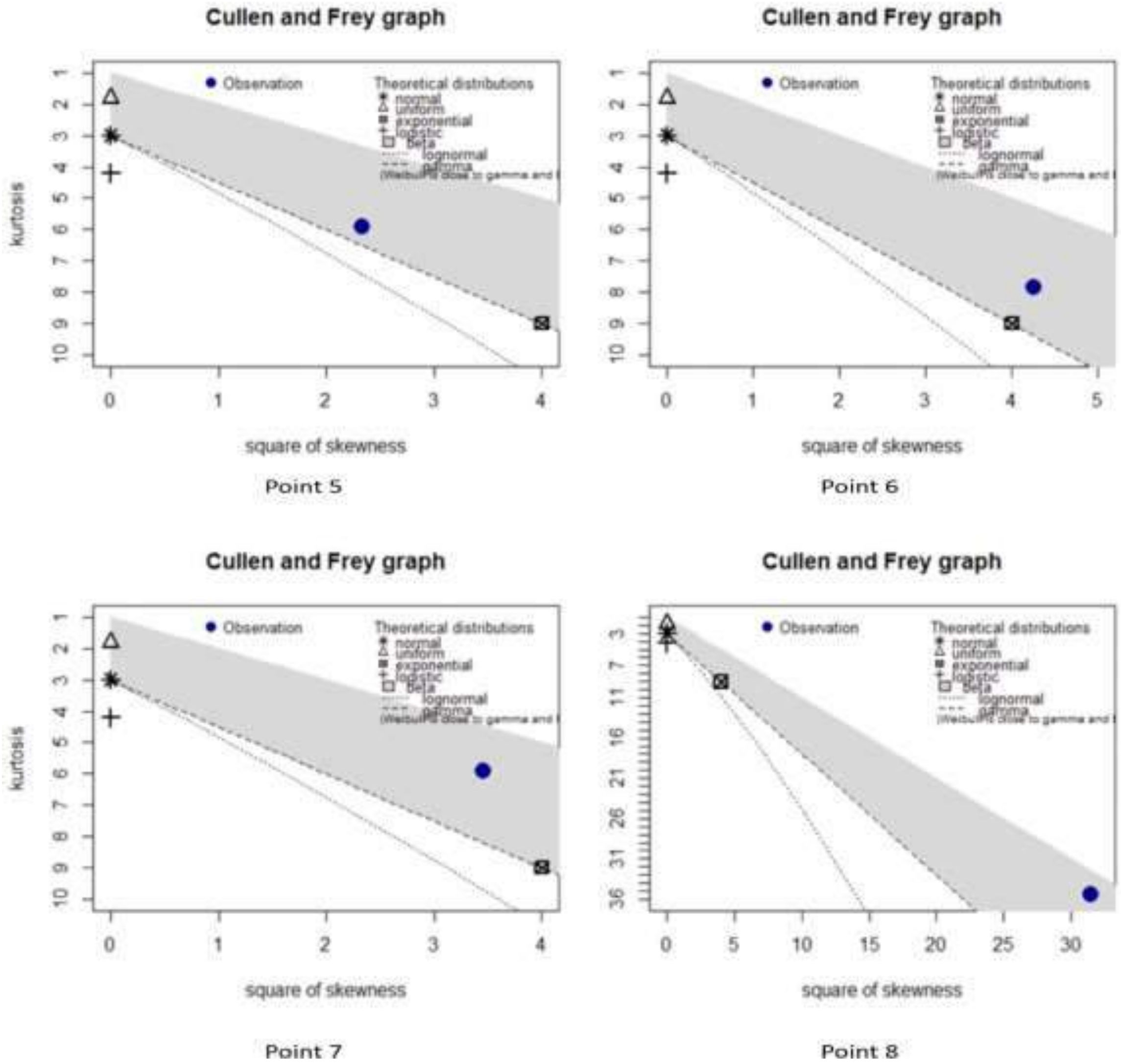

Figure 89. The Cullen and Frey diagrams for the distribution of Chl-a concentration at Points 5 - 8.

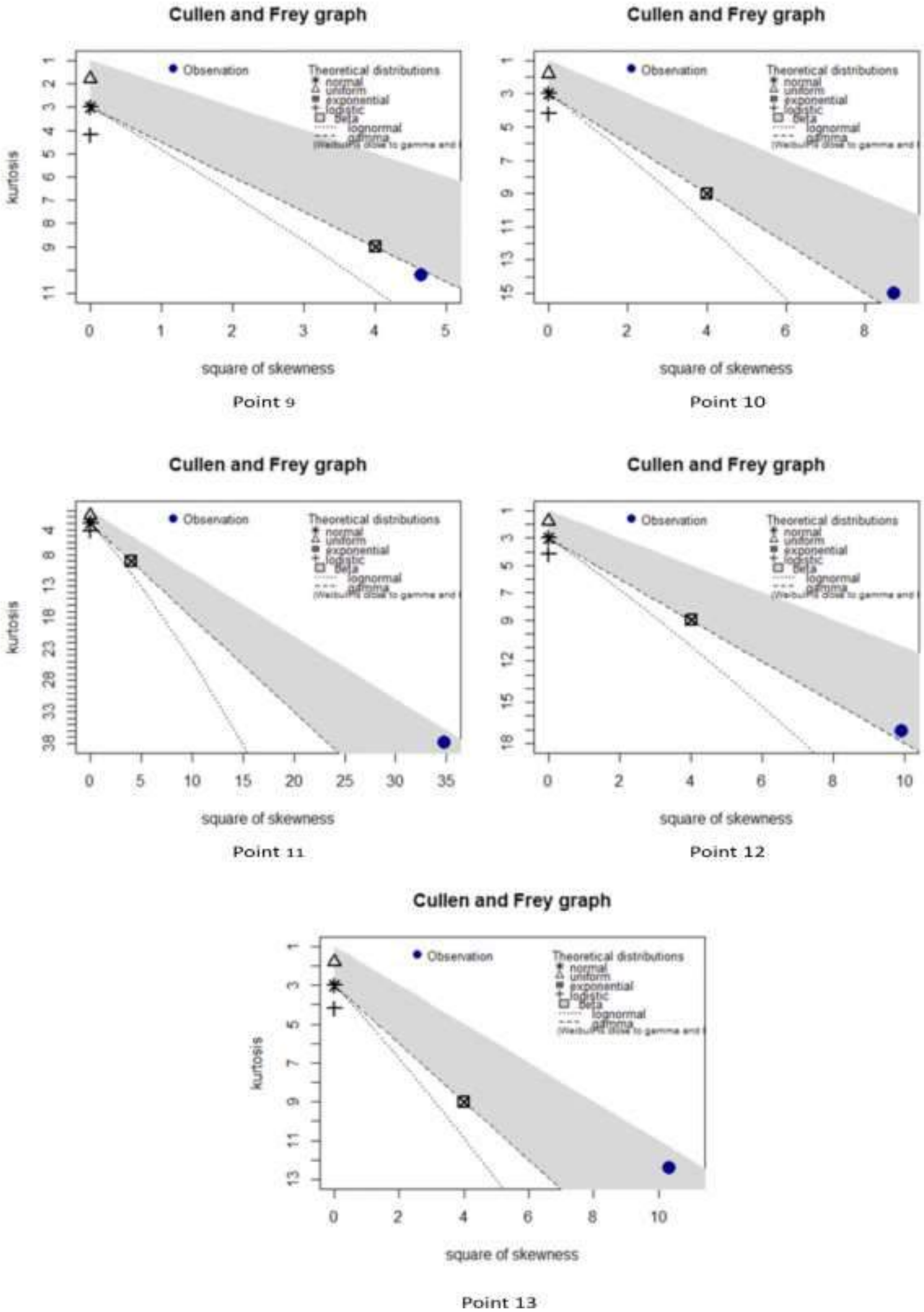

Figure 90. The Cullen and Frey diagrams for the distribution of Chl-a concentration at Points 9 - 13.

Table 15 presents the fitting parameters of the best-fit theoretical probability density function applied on the Chl-a concentration data extracted from Landsat in Porto Lagos lagoon. Mean and standard deviation parameters are given for the normal PDFs, log(mean) and log(sd) parameters for the log-normal distributions and shape and scale for the gamma distributions.

Table 15. Fitting parameters of the best-fit theoretical probability density function.

Points	1	2	3	4	5	6	7
Mean							
St Dev							
Log(Mean)	0.603	1.042		0.341	0.403	0.553	0.424
Log(St Dev)	0.0554	0.094		0.051	0.052	0.052	0.057
Shape			2.928				
Scale			0.862				
LogLikelihood	-31.682	-65.743	-69.323	-19.684	-22.773	-27.962	-26.251
AIC	67.364	135.487	142.646	43.369	49.545	59.925	56.501
BIC	70.474	138.598	145.757	46.480	52.656	63.035	59.612
Points	**8**	**9**	**10**	**11**	**12**	**13**	
Mean							
St Dev							
Log(Mean)	0.534	0.373	0.488	0.531	0.429	1.465	
Log(St Dev)	0.092	0.047	0.054	0.119	0.043	0.373	
Shape							
Scale							
LogLikelihood	-47.296	-18.402	-27.064	-55.879	-16.570	-128.607	
AIC	98.592	40.804	58.128	115.757	37.139	261.213	
BIC	101.703	43.914	61.234	118.868	40.250	264.324	

The theoretical probability density functions (PDFs) and the cumulative density functions (CDFs) applied as best-fit on the Chl-a data, together with the relevant Q-to-Q and P-to-P plots are shown in Figures 91, 92 and 93.

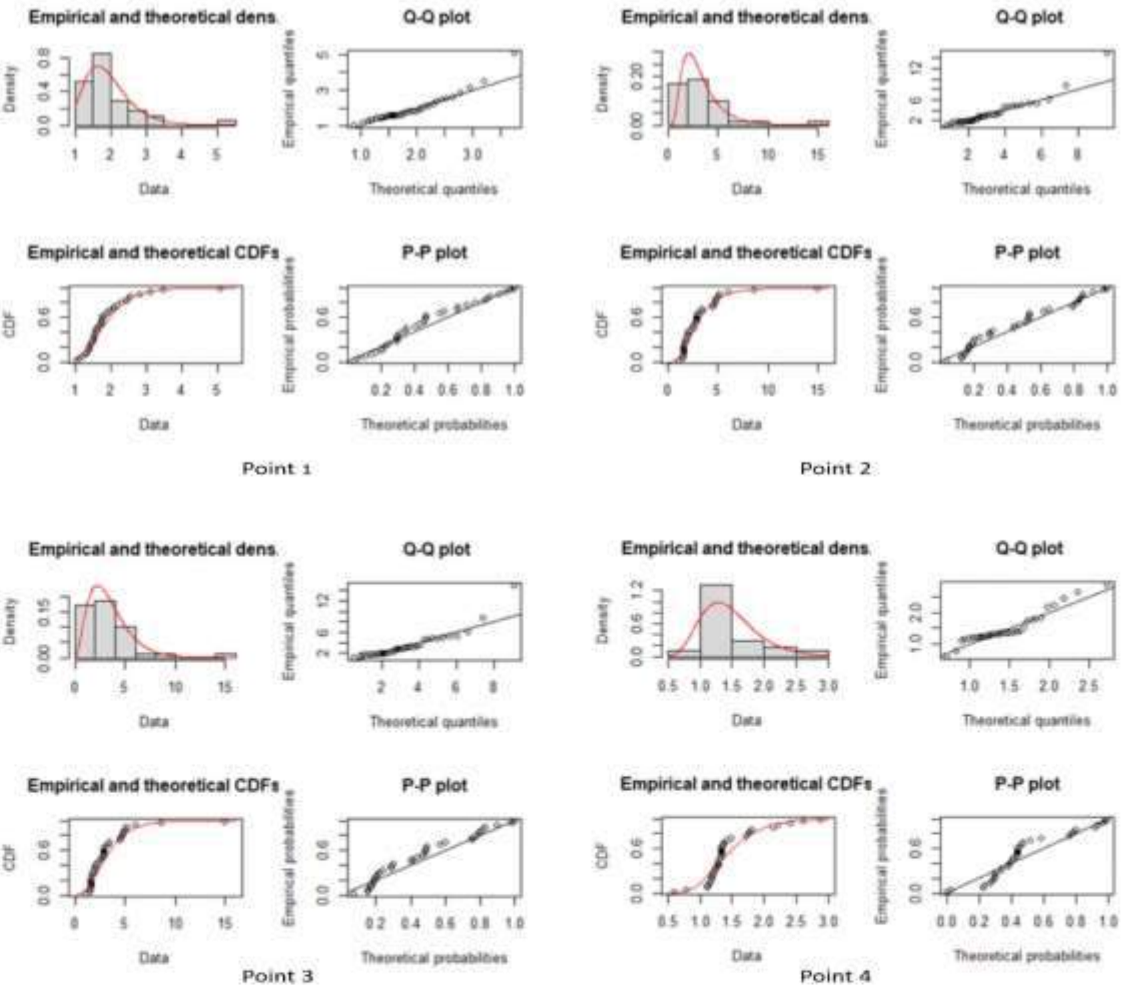

Figure 91. Theoretical probability density functions (PDFs) and the cumulative density functions (CDFs), applied as best-fit on the Chl-a data of points 1 – 4.

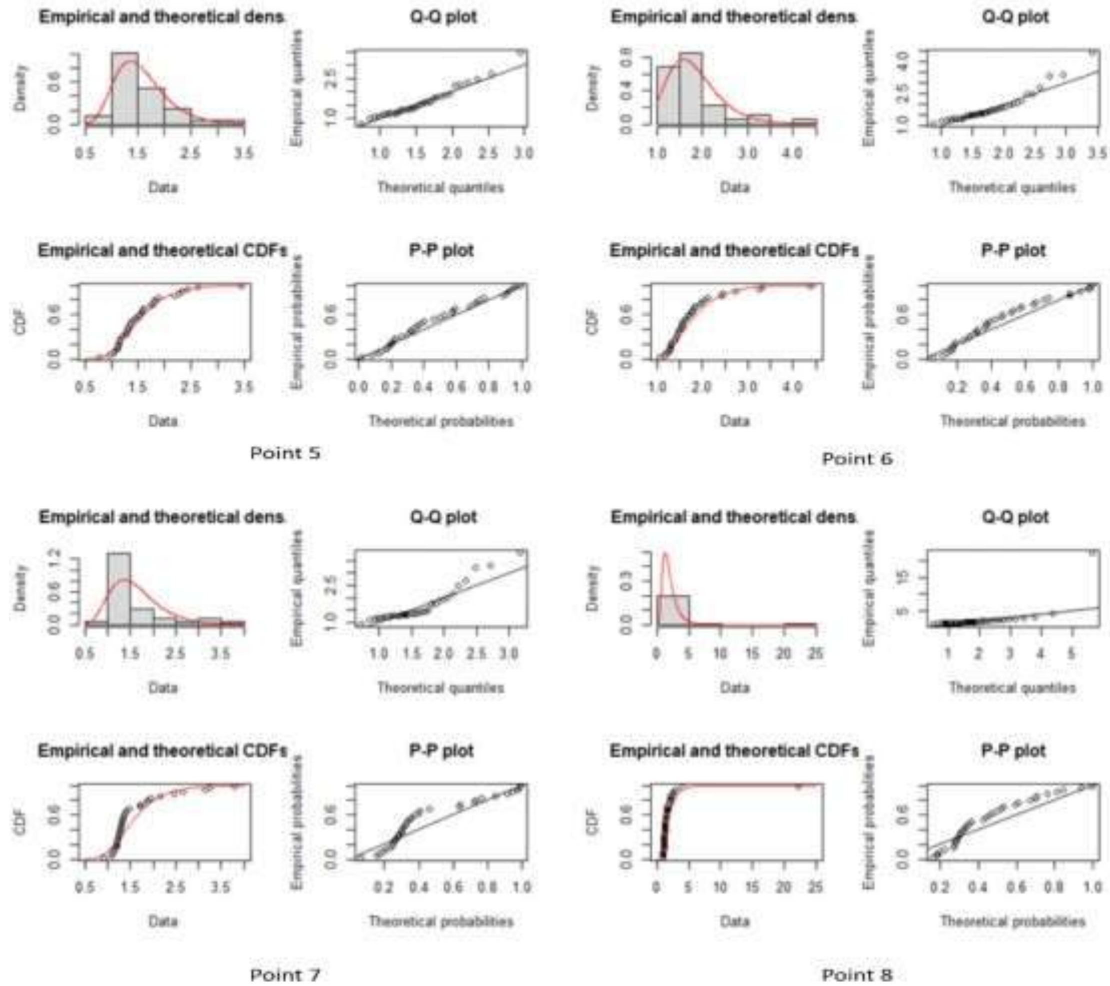

Figure 92. Theoretical probability density functions (PDFs) and the cumulative density functions (CDFs), applied as best-fit on the Chl-a data of points 5 – 8.

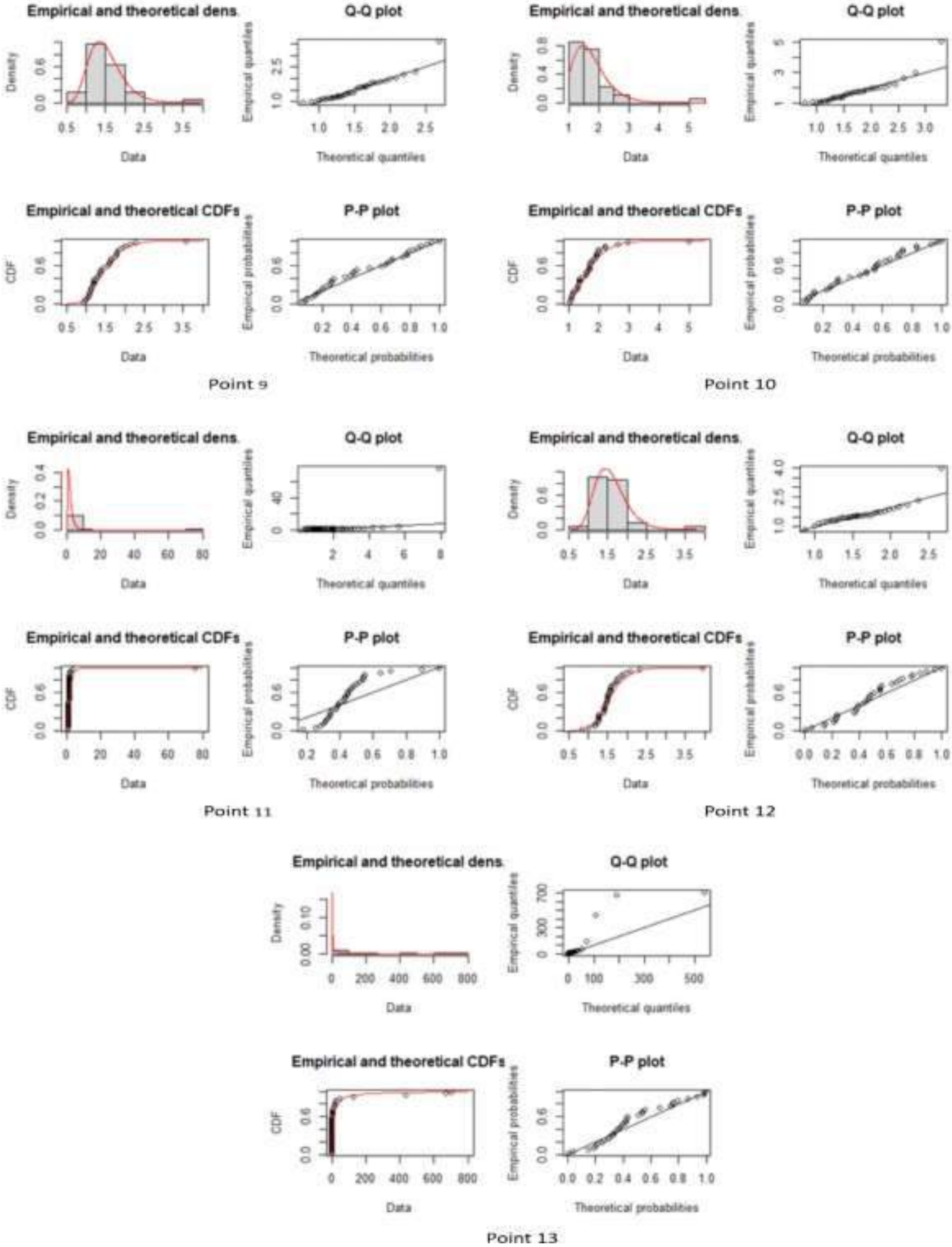

Figure 93. Theoretical probability density functions (PDFs) and the cumulative density functions (CDFs), applied as best-fit on the Chl-a data of points 9 – 13.

Based on the best-fit theoretical CDFs applied on the Chl-a, the probability of exceeding the eutrophication threshold of 2 μg/l was estimated. Probabilities of exceedance for all Porto Lagos lagoon points are summarized in Table 16. Probability is a measure that ranges between 0 and 1, with zero implying that eutrophication is impossible and 1 implying that eutrophication is absolutely certain. Figure 94 illustrates the probability map of exceedance of the eutrophication threshold in Porto Lagos lagoon.

Table 16. Probability of exceedance of the eutrophication threshold in Porto Lagos lagoon.

Points	Probability of Exceedance
1	0.391
2	0.734
3	0.989
4	0.122
5	0.175
6	0.326
7	0.211
8	0.386
9	0.128
10	0.262
11	0.409
12	0.148
13	0.637

Based on the above, points 2, 3 and 13 are more vulnerable to eutrophication effects than the rest of the lagoon. Points 2 and 3 are located in the small canals inside the lagoon connecting the two main sub-basins of the lagoon and 13 close to the inlet of the lagoon. Exceedance probability ranges from 0.6 to almost 1, eutrophication may exist for almost the whole typical year. Based on the available Landsat images, it seems that the eutrophication prone periods are spring and summer. The rest of the points have limited probability for a eutrophication event.

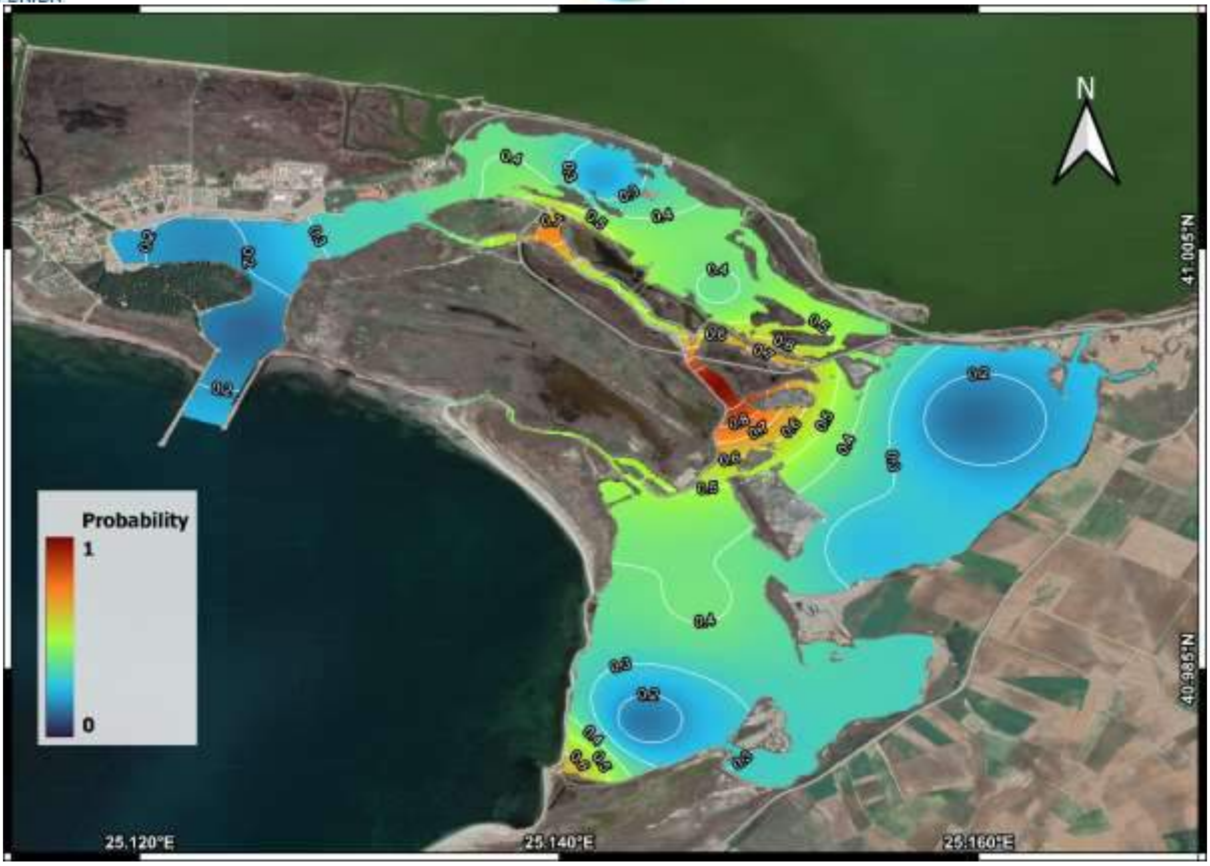

Figure 94. Probability map of exceedance of the eutrophication threshold in Porto Lagos lagoon.

3.2.1.5 Xirolimni

The points selected for Chl-a concentration extraction for the eutrophication assessment in Xirolimni lagoon, are shown in Figure 95. These points cover the typical conditions of the lagoon and are distributed among various depths.

Figure 95. Points for Chl-a concentration extraction in Xirolimni lagoon.

Table 17 presents the statistical measures for Chl-a concentration at all points examined in Xirolimni lagoon.

Table 17. Statistical measures per point for Chl-a concentration at Xirolimni Lagoon.

Points	Min	Max	Median	Mean	St. deviation	Skewness	Kurtosis
1	0.668	11.183	1.415	1.993	1.842	4.680	22.054
2	0.516	3.079	1.290	1.313	0.448	1.706	9.299
3	0.002	1.743	0.394	0.502	0.474	1.099	3.892
4	0.634	3.448	1.311	1464	0.626	1.430	5.056
5	0.560	17.902	1.315	1.793	2.820	5.806	37.113
6	0.402	5.104	1.345	1.587	0.944	2.242	8.888
7	0.448	1.800	1.214	1.216	0.270	-0.596	4.750

Figures 96 and 97 illustrate the skewness-kurtosis plot of Cullen and Frey for the Landsat extracted Chl-a at all points in Xirolimni lagoon. Based on these graphs and the AIC and BIC criteria, it occurs that:

a) For Points 1, 4, 5 and 6, the log-normal distribution was found to be the best-fit theoretical distribution;
b) For Points 2,3 and 7, the gamma distribution was found to be the best-fit theoretical distribution.

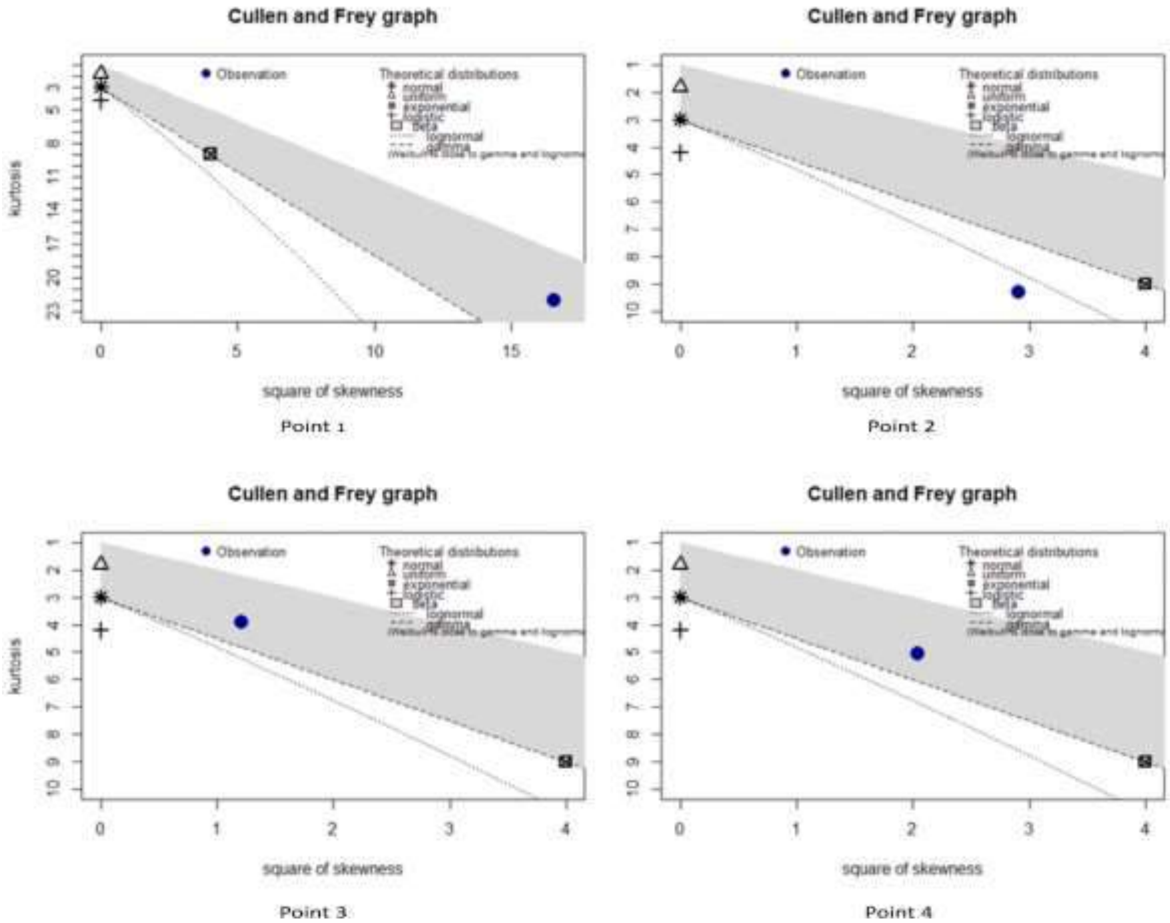

Figure 96. The Cullen and Frey diagrams for the distribution of Chl-a concentration at Points 1 - 4.

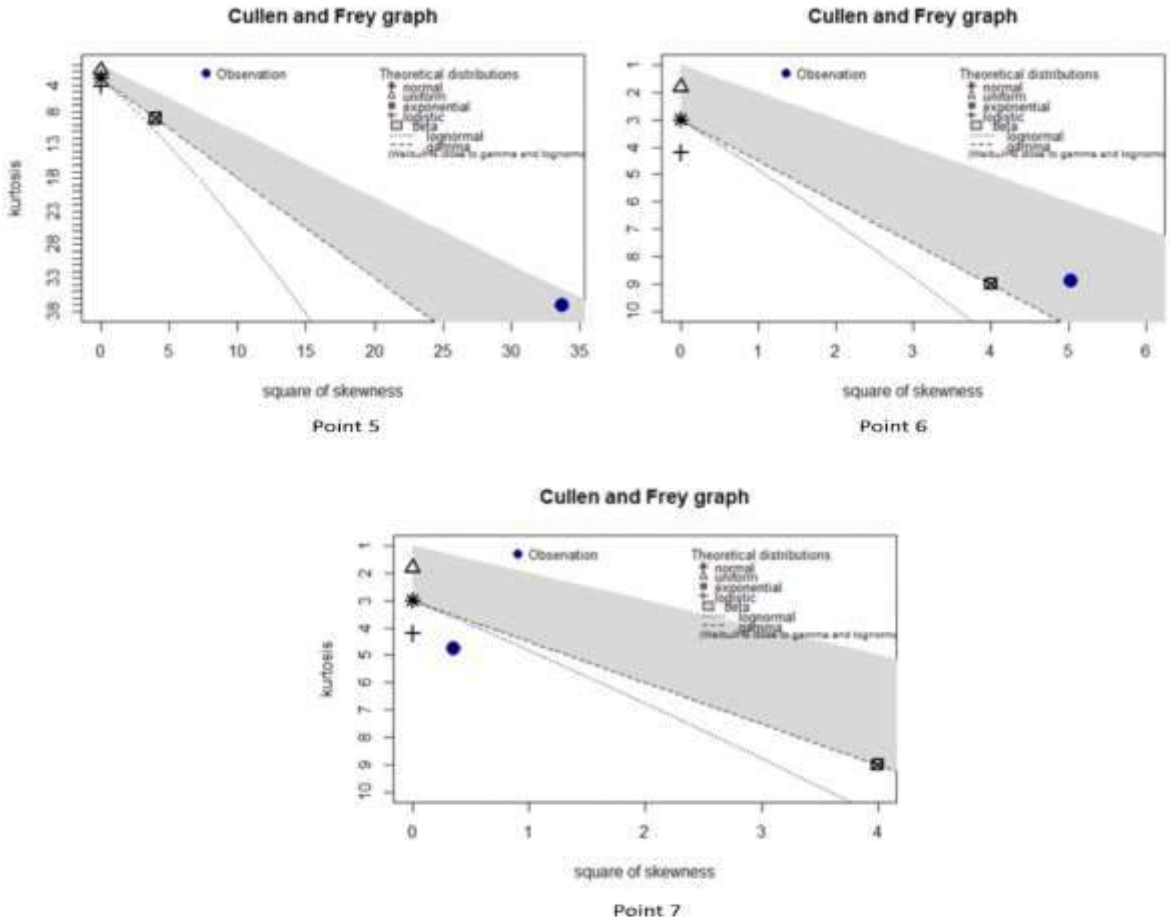

Figure 97. The Cullen and Frey diagrams for the distribution of Chl-a concentration at Points 5 - 7.

Table 18 presents the fitting parameters of the best-fit theoretical probability density function applied on the Chl-a concentration data extracted from Landsat in Xirolimni lagoon. Mean and standard deviation parameters are given for the normal PDFs, log(mean) and log(sd) parameters for the log-normal distributions and shape and scale for the gamma distributions.

Table 18. Fitting parameters of the best-fit theoretical probability density function.

Points	**1**	**2**	**3**	**4**	**5**	**6**	**7**
Mean							
St Dev							
Log(Mean)	0.498			0.305	0.321	0.332	
Log(St Dev)	0.090			0.064	0.086	0.084	
Shape		9.792	0.878				5.247
Scale		7.456	0.474				1.317
LogLikelihood	-45.173	-18.051	-10.414	-26.678	-37.398	-36.608	-2.999
AIC	94.346	40.102	24.828	57.356	78.795	77.216	10.000

BIC	97.456	43.212	27.939	60.466	81.906	80.326	13.108

The theoretical probability density functions (PDFs) and the cumulative density functions (CDFs) applied as best-fit on the Chl-a data, together with the relevant Q-to-Q and P-to-P plots are shown in Figures 98 and 99.

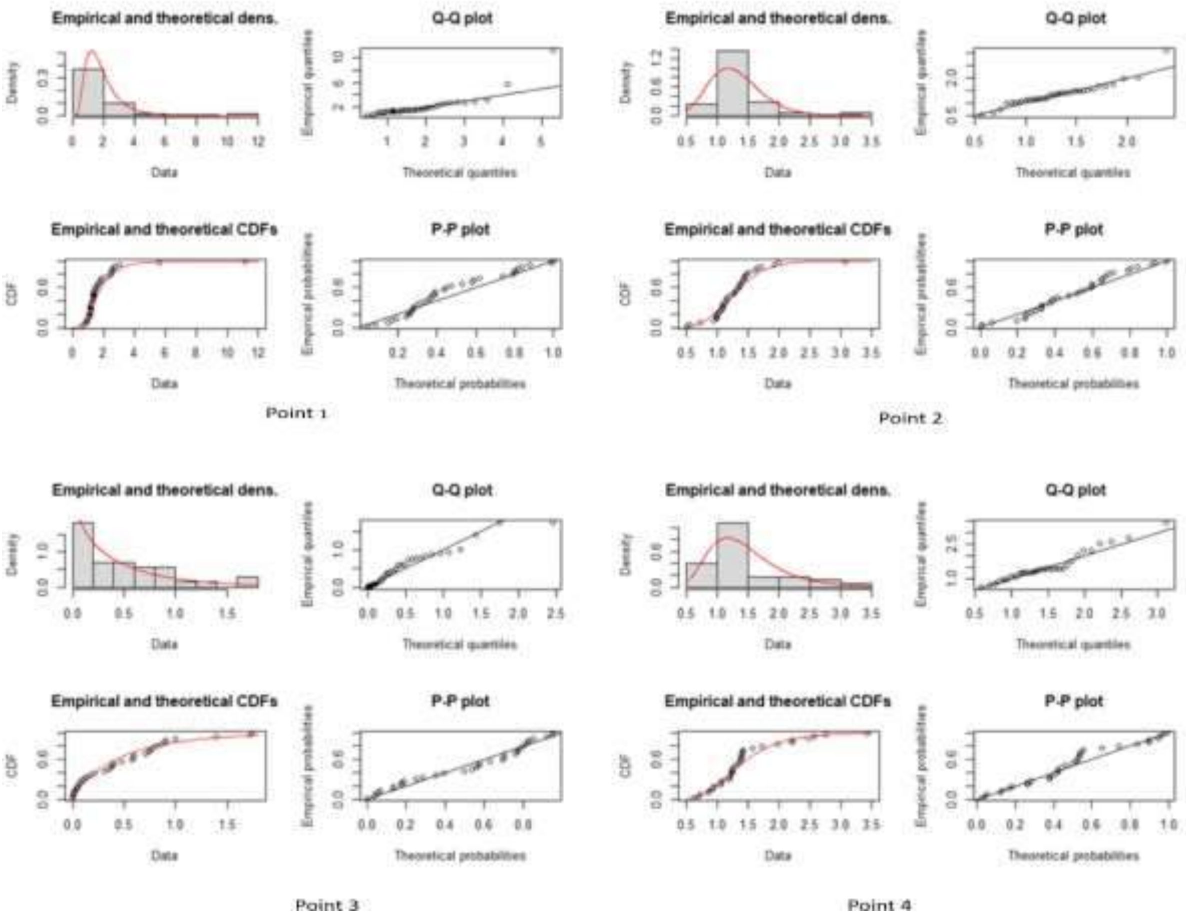

Figure 98. Theoretical probability density functions (PDFs) and the cumulative density functions (CDFs), applied as best-fit on the Chl-a data of points 1 – 4.

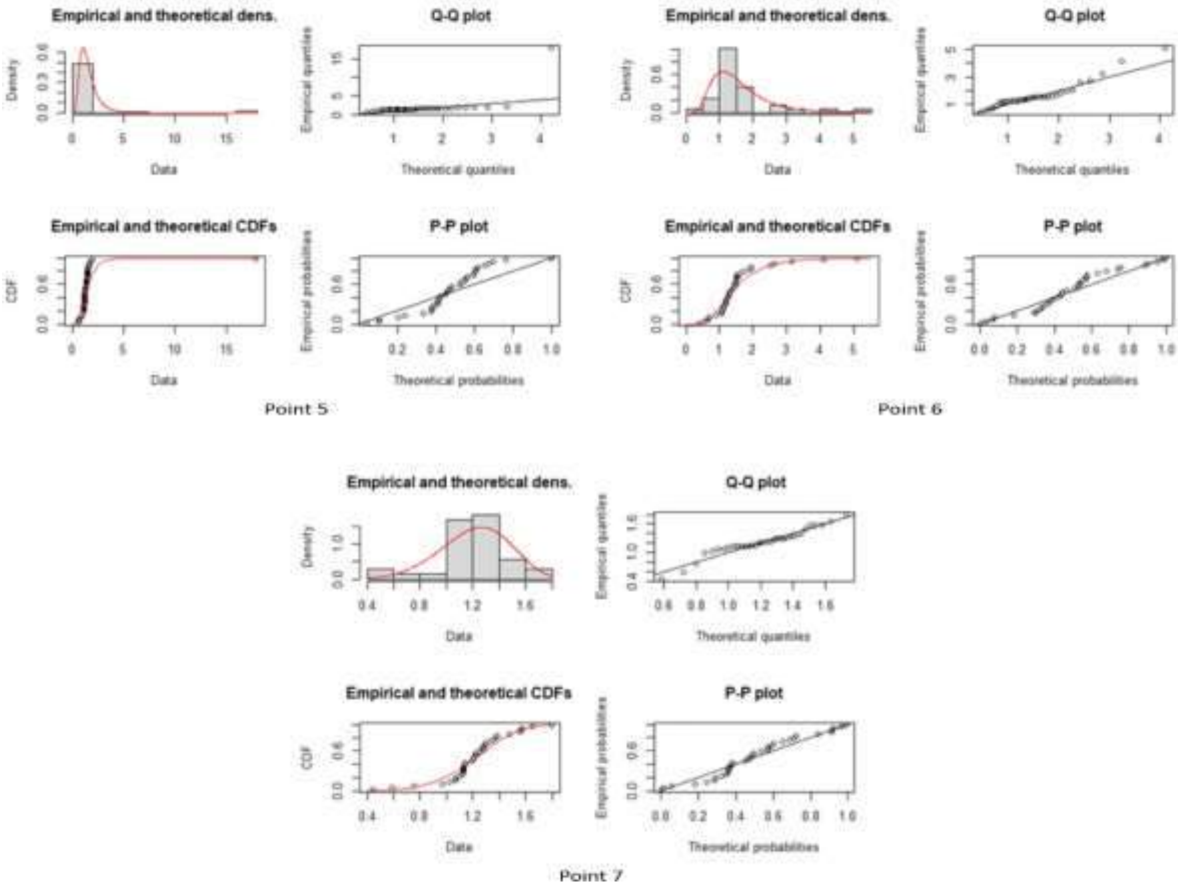

Figure 99. Theoretical probability density functions (PDFs) and the cumulative density functions (CDFs), applied as best-fit on the Chl-a data of points 5 – 7.

Based on the best-fit theoretical CDFs applied on the Chl-a, the probability of exceeding the eutrophication threshold of 2 μg/l was estimated. Probabilities of exceedance for all Xirolimni lagoon points are summarized in Table 19. Probability is a measure that ranges between 0 and 1, with zero implying that eutrophication is impossible and 1 implying that eutrophication is absolutely certain. Figure 100 illustrates the probability map of exceedance of the eutrophication threshold in Xirolimni lagoon.

Table 19. Probability of exceedance of the eutrophication threshold in Xirolimni lagoon.

Points	**Probability of Exceedance**
1	0.358
2	0.073
3	0.030
4	0.155
5	0.233
6	0.232
7	0.000

Based on the above, exceedance probability for all points is below 0.5, meaning they have limited probability for a eutrophication event.

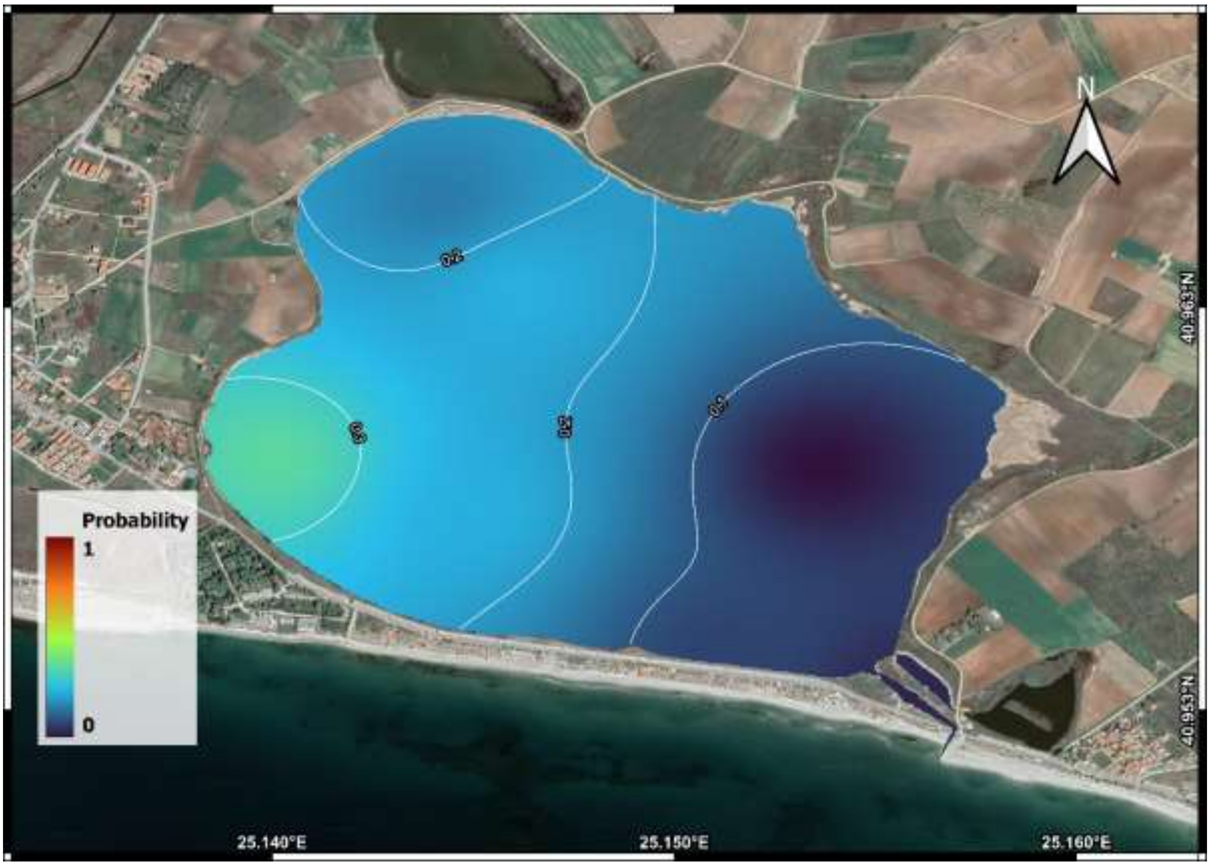

Figure 100. Probability map of exceedance of the eutrophication threshold in Xirolimni lagoon.

3.2.1.6 Ptelea

The points selected for Chl-a concentration extraction for the eutrophication assessment in Ptelea lagoon, are shown in Figure 101. These points cover the typical conditions of the lagoon and are distributed among various depths.

Figure 101. Points for Chl-a concentration extraction in Ptelea lagoon.

Table 20 presents the statistical measures for Chl-a concentration at all points examined in Ptelea lagoon.

Table 20. Statistical measures per point for Chl-a concentration at Ptelea Lagoon.

Points	**Min**	**Max**	**Median**	**Mean**	**St. deviation**	**Skewness**	**Kurtosis**
1	0.009	9.097	1.195	1.380	1.462	4.585	27.131
2	0.043	1238.171	1.192	55.386	231.934	4.611	24.820
4	0.008	124.978	1.550	5.936	21.347	5.456	33.732
5	0.011	19.165	1.206	2.067	3.784	3.991	18.613
6	0.003	2.557	1.257	1.218	0.552	0.126	3.440

Figure 102 illustrates the skewness-kurtosis plot of Cullen and Frey for the Landsat extracted Chl-a at all points in Ptelea lagoon. Based on these graphs and the AIC and BIC criteria, it occurs that:

a) For Point 6, the normal distribution was found to be the best-fit theoretical distribution;
b) For Points 2, 4, and 5, the log-normal distribution was found to be the best-fit theoretical distribution;
c) For Point 1, the gamma distribution was found to be the best-fit theoretical distribution.

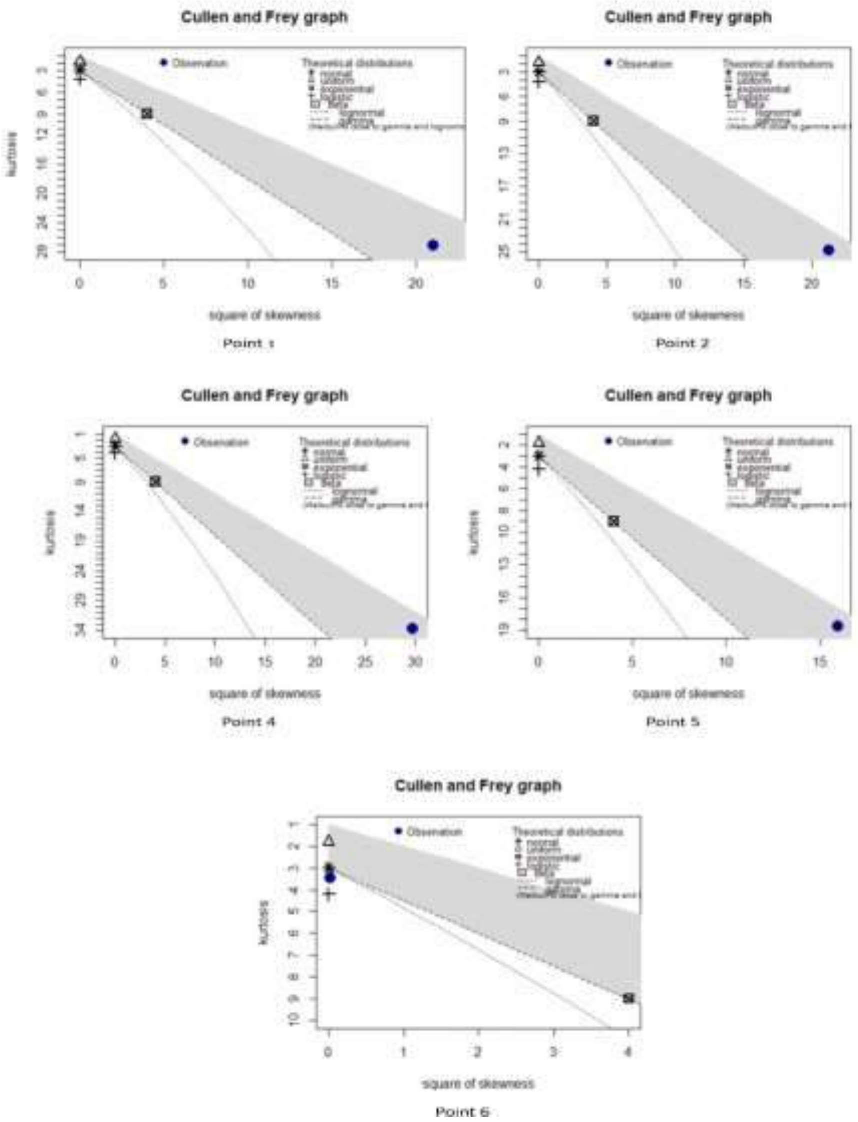

Figure 102. The Cullen and Frey diagrams for the distribution of Chl-a concentration at Points 1 - 6.

Table 21 presents the fitting parameters of the best-fit theoretical probability density function applied on the Chl-a concentration data extracted from Landsat in Ptelea lagoon. Mean and standard deviation parameters are given for the normal PDFs, log(mean) and log(sd) parameters for the log-normal distributions and shape and scale for the gamma distributions.

Table 21. Fitting parameters of the best-fit theoretical probability density function.

Points	**1**	**2**	**4**	**5**	**6**
Mean					1.218
St Dev					0.544
Log(Mean)		0.573	0.429	0.115	

Log(St Dev)		0.300	0.229	0.187	
Shape	1.593				
Scale	1.154				
LogLikelihood	-44.270	-89.803	-75.265	-57.250	-28.368
AIC	92.541	183.606	154.530	118.500	60.735
BIC	95.652	186.717	157.641	121.610	63.846

The theoretical probability density functions (PDFs) and the cumulative density functions (CDFs) applied as best-fit on the Chl-a data, together with the relevant Q-to-Q and P-to-P plots are shown in Figure 103.

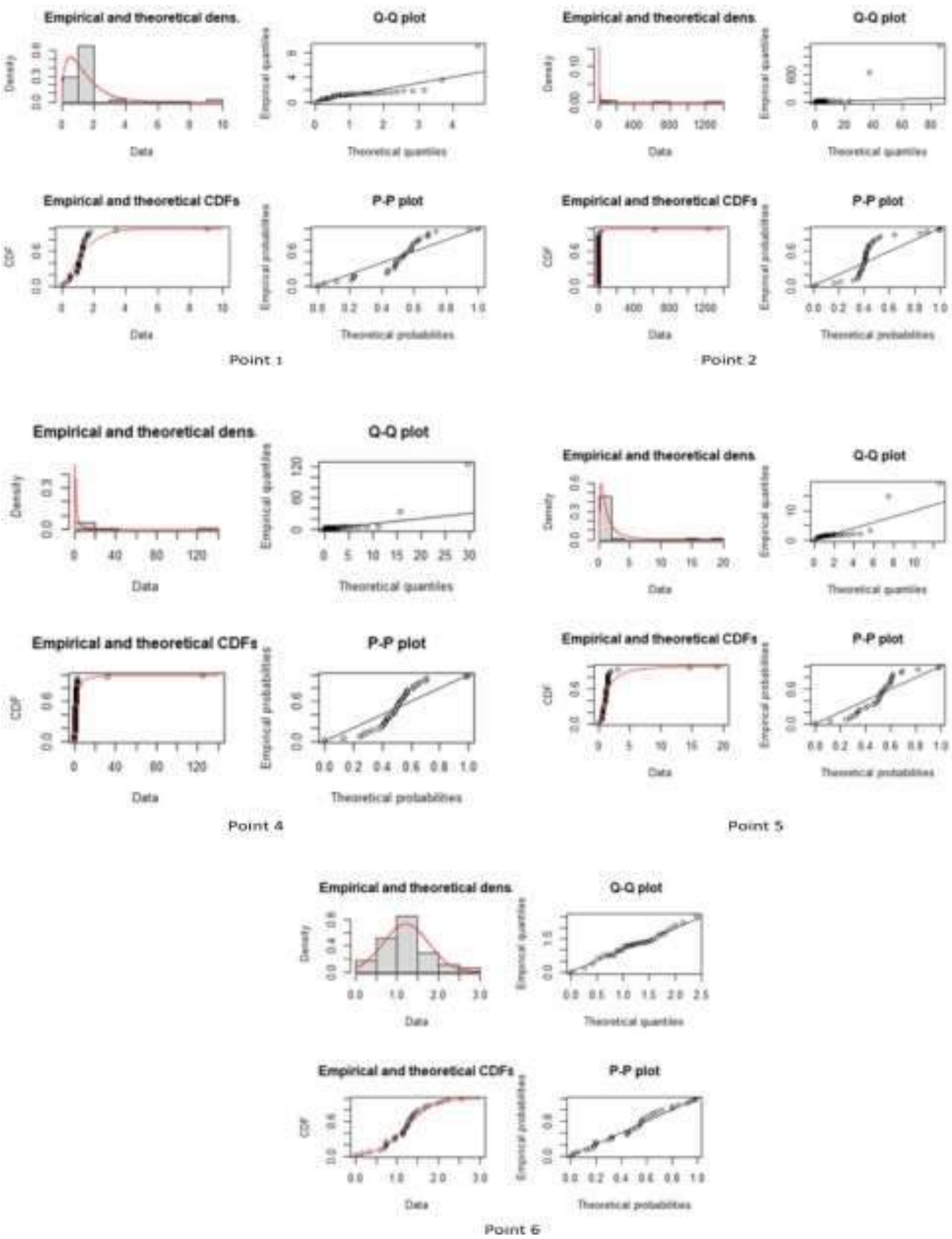

Figure 103. Theoretical probability density functions (PDFs) and the cumulative density functions (CDFs), applied as best-fit on the Chl-a data of points 1 – 6.

Based on the best-fit theoretical CDFs applied on the Chl-a, the probability of exceeding the eutrophication threshold of 2 μg/l was estimated. Probabilities of exceedance for all Ptelea lagoon points are summarized in Table 22 Probability is a measure that ranges between 0 and 1, with zero implying that eutrophication is impossible and 1 implying that eutrophication is absolutely certain.

Table 22. Probability of exceedance of the eutrophication threshold in Ptelea lagoon.

Points	Probability of Exceedance
1	0.645
2	0.473
4	0.423
5	0.301
6	0.075

Based on the above, points 1, 2 and 4 are more vulnerable to eutrophication effects than the rest of the lagoon. Exceedance probability is approx. 0.5, meaning that during half of a typical year eutrophication may exist. Based on the available Landsat images, it seems that the eutrophication prone periods are spring and summer. Point 6 has limited probability for a eutrophication event. Figure 104 illustrates the probability map of exceedance of the eutrophication threshold in Ptelea lagoon.

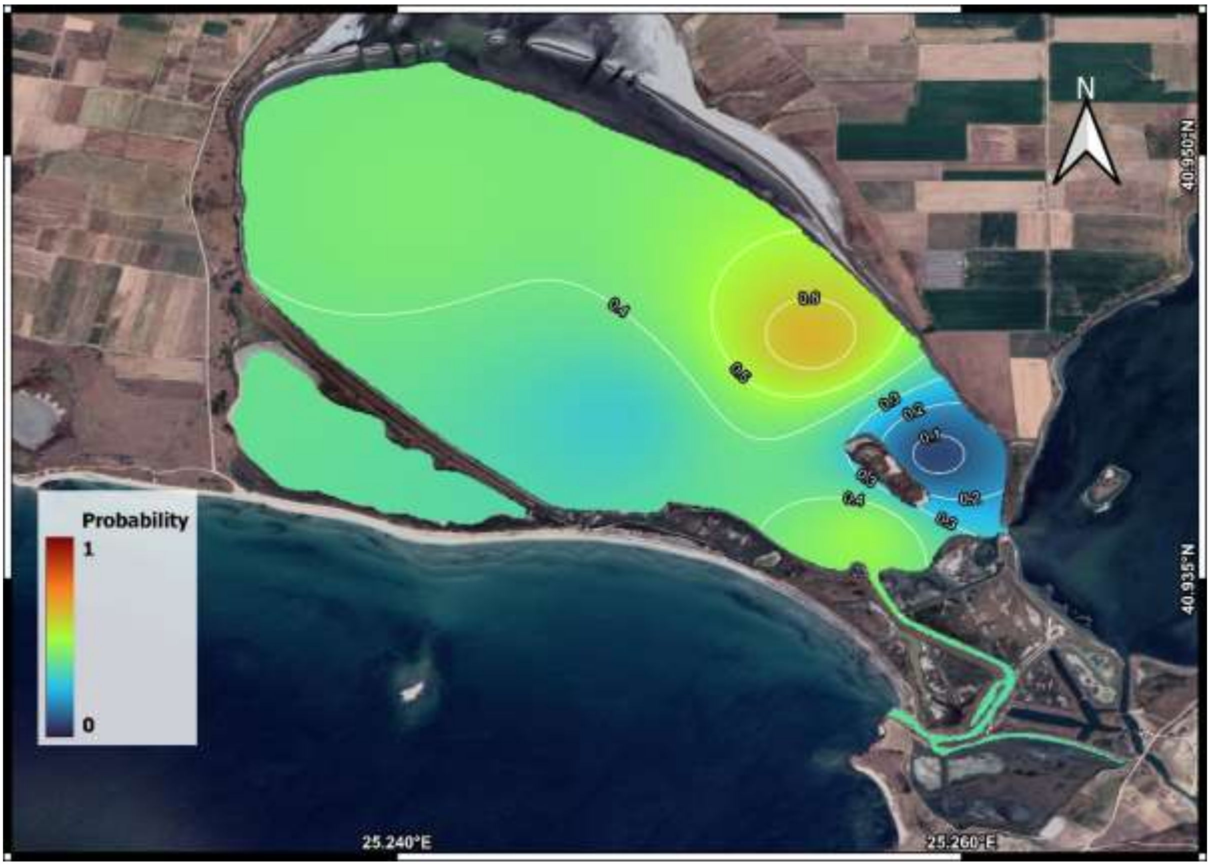

Figure 104. Probability map of exceedance of the eutrophication threshold in Ptelea lagoon.

3.2.2 Sentinel Data

3.2.2.1 Vassova lagoon

The points selected for Chl-a concentration extraction for the eutrophication assessment in Vassova lagoon, are the same as shown in Figure 75.

Table 23 presents the statistical measures for Chl-a concentration derived from Sentinel data at all points examined in Vassova lagoon.

Table 23. Statistical measures per point for Chl-a concentration at Vassova Lagoon.

Points	Min	Max	Median	Mean	St. deviation	Skewness	Kurtosis
1	0.149	37.452	1.802	2.400	4.418	7.918	66.740
2	0.084	5.165	1.912	1.941	0.677	1.448	10.598
3	0.408	4.661	2.189	2.161	0.730	0.500	4.790
4	0.086	7.966	3.322	3.318	1.359	0.367	4.689
5	0.440	241.690	2.116	5.984	29.548	8.052	68.175
6	0.115	3.893	2.125	2.143	0.533	-0.277	6.440
7	0.665	5.305	2.077	2.066	0.652	1.700	11.357

Figures 105 and 106 illustrate the skewness-kurtosis plot of Cullen and Frey for the Sentinel extracted Chl-a at all points in Vassova lagoon. Based on these graphs and the AIC and BIC criteria, it occurs that:

a) For Points 2, 3, 4 and 6, the normal distribution was found to be the best-fit theoretical distribution;
b) For Points 1, and 5, the log-normal distribution was found to be the best-fit theoretical distribution;
c) For Point 7, the gamma distribution was found to be the best-fit theoretical distribution.

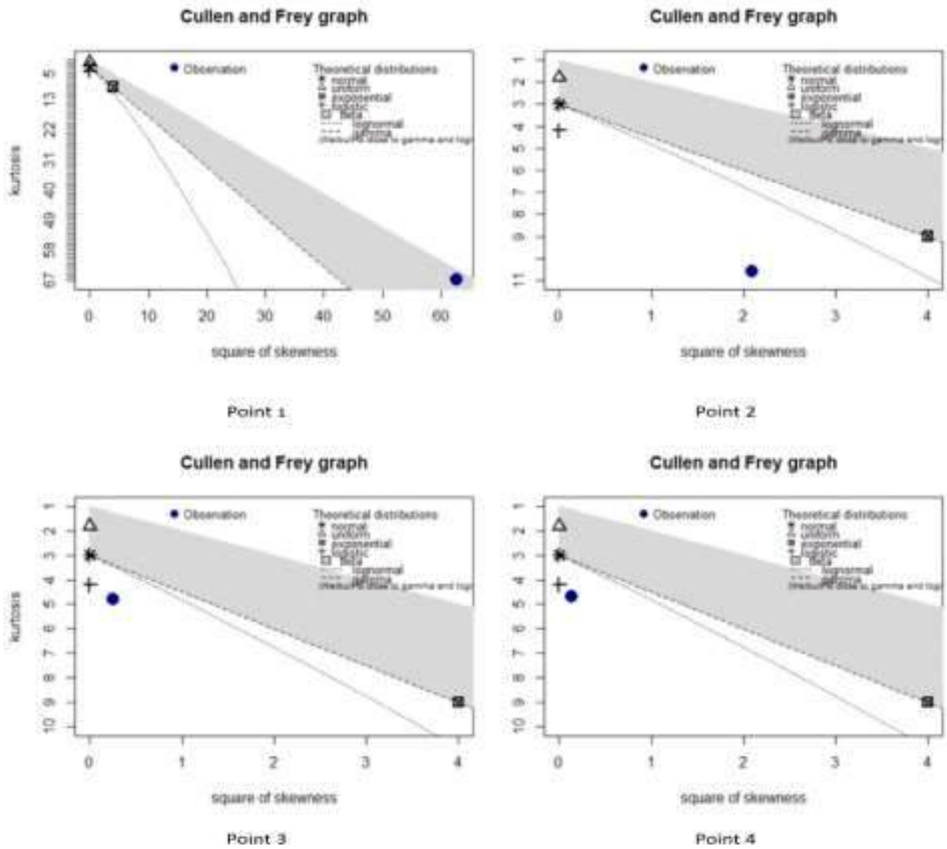

Figure 105. The Cullen and Frey diagrams for the distribution of Chl-a concentration at Points 1 - 4.

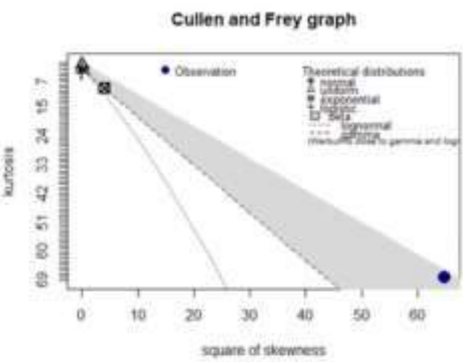

Point 5

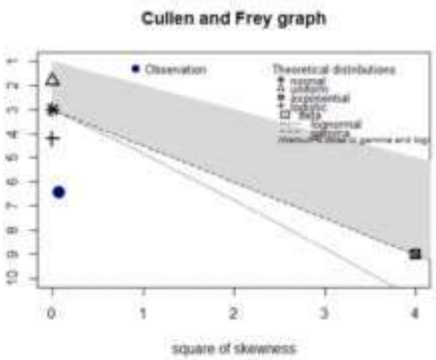

Point 6

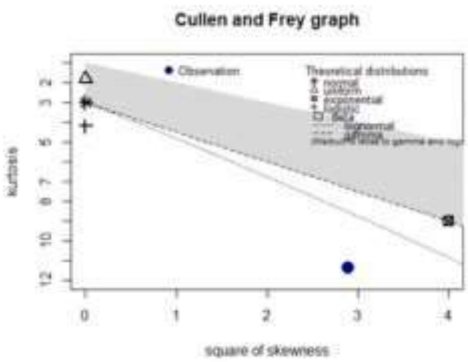

Point 7

Figure 106. The Cullen and Frey diagrams for the distribution of Chl-a concentration at Points 5 - 7.

Table 24 presents the fitting parameters of the best-fit theoretical probability density function applied on the Chl-a concentration data extracted from Sentinel in Vassova lagoon. Mean and standard deviation parameters are given for the normal PDFs, log(mean) and log(sd) parameters for the log-normal distributions and shape and scale for the gamma distributions.

Table 24. Fitting parameters of the best-fit theoretical probability density function.

Points	**1**	**2**	**3**	**4**	**5**	**6**	**7**
Mean		1.941	2.161	3.318		2.143	
St Dev		0.672	0.725	1.349		0.529	
Log(Mean)	0.605				0.793		
Log(St Dev)	0.068				0.089		
Shape							10.929
Scale							5.289
LogLikelihood	-94.750	-67.437	-72.401	-113.410	-124.785	-51.573	-60.575
AIC	193.500	138.873	148.801	230.821	253.569	107.146	125.149
BIC	197.879	143.252	153.181	235.200	257.949	111.525	129.529

The theoretical probability density functions (PDFs) and the cumulative density functions (CDFs) applied as best-fit on the Chl-a data, together with the relevant Q-to-Q and P-to-P plots are shown in Figures 107 and 108.

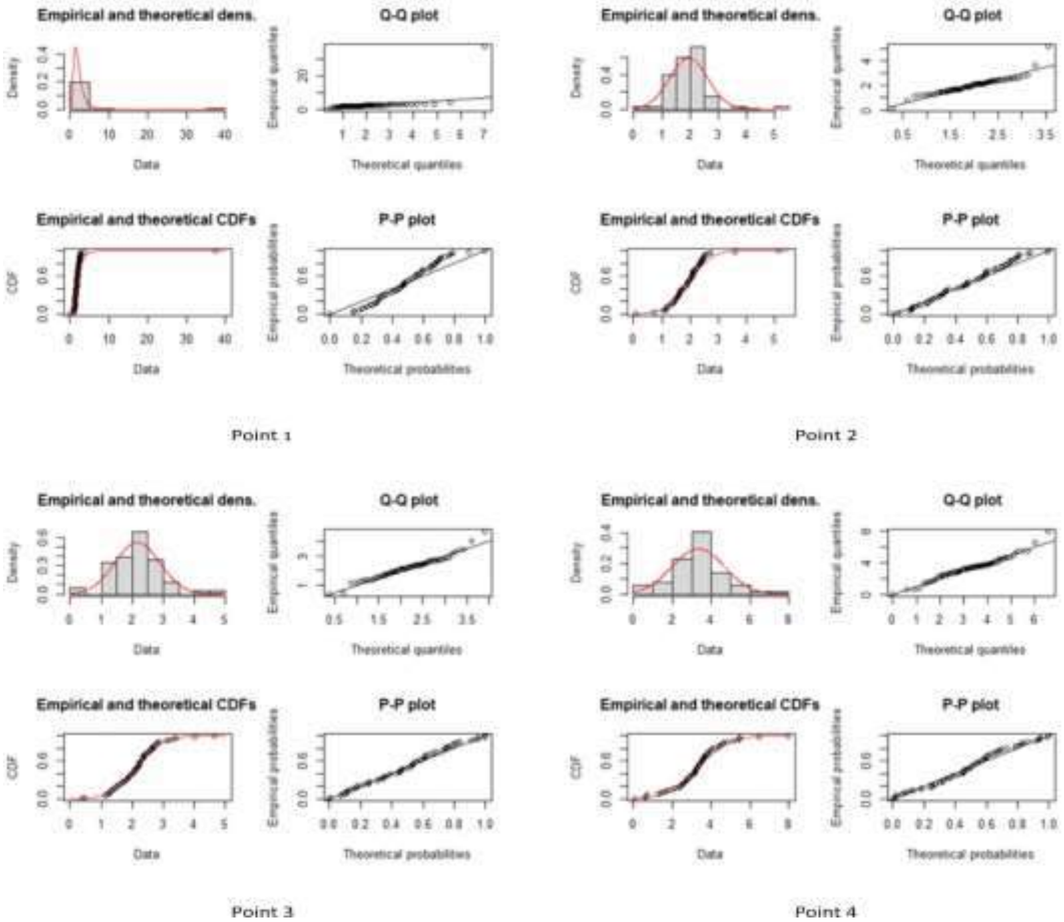

Figure 107. Theoretical probability density functions (PDFs) and the cumulative density functions (CDFs), applied as best-fit on the Chl-a data of points 1 – 4.

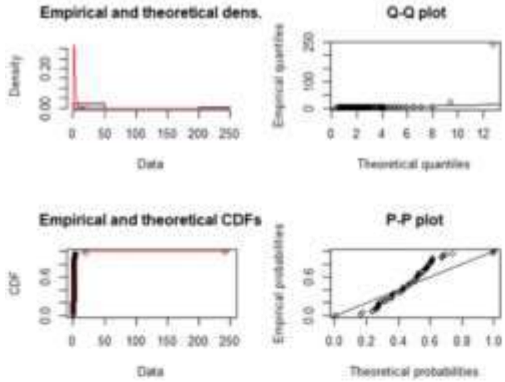

Point 5

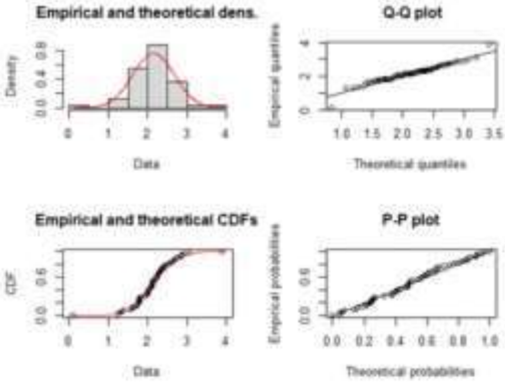

Point 6

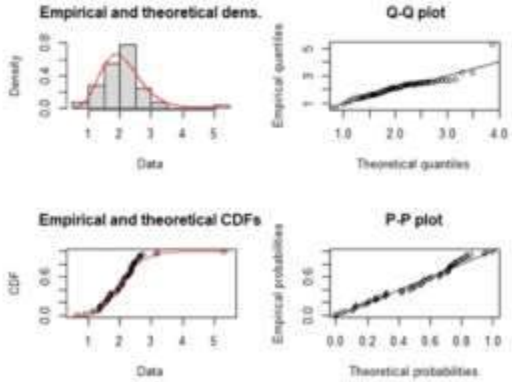

Point 7

Figure 108. Theoretical probability density functions (PDFs) and the cumulative density functions (CDFs), applied as best-fit on the Chl-a data of points 5 – 7.

Based on the best-fit theoretical CDFs applied on the Chl-a, the probability of exceeding the eutrophication threshold of 2 μg/l was estimated. Probabilities of exceedance for all Vassova lagoon points are summarized in Table 25. Probability is a measure that ranges between 0 and 1, with zero implying that eutrophication is impossible and 1 implying that eutrophication is absolutely certain. Figure 109 illustrates the probability map of exceedance of the eutrophication threshold in Vassova lagoon.

Table 25. Probability of exceedance of the eutrophication threshold in Vassova lagoon.

Points	**Probability of Exceedance**
1	0.437
2	0.465
3	0.588
4	0.836
5	0.554
6	0.607
7	0.502

Based on the above, all points are more vulnerable to eutrophication effects. For point 4, exceedance probability is approximately 0.8 meaning that almost ten months of the year eutrophication may exist. Points 1 and 2 show the lower exceedance probability, below 0.5. Based on the available Sentinel images, it seems that the eutrophication prone periods are spring and summer.

Figure 109. Probability map of exceedance of the eutrophication threshold in Vassova lagoon.

3.2.2.2 Eratino lagoon

The points selected for Chl-a concentration extraction for the eutrophication assessment in Eratino lagoon, are shown in Figure 110. These points cover the typical conditions at all sub-basins of the lagoon and are distributed among various depths.

Figure 110. Points for Chl-a concentration extraction in Eratino lagoon.

Table 26 presents the statistical measures for Chl-a concentration at all points examined in Eratino lagoon.

Table 26. Statistical measures per point for Chl-a concentration at Eratino Lagoon.

Points	Min	Max	Median	Mean	St. deviation	Skewness	Kurtosis
1	0.090	3.272	2.070	2.101	0.506	-0.849	5.972
2	0.985	4.875	1.609	1.752	0.640	2.395	11.850
3	0.591	5.110	2.038	2.091	0.613	1.595	11.805
4	1.049	6.015	2.113	2.259	0.855	1.561	7.631
5	0.800	23.254	1.831	2.133	2.789	7.249	58.347
6	0.021	4.011	2.010	1.989	0.620	0.103	6.094
7	0.111	49.525	2.177	2.865	6.006	7.806	64.592
8	0.553	5.243	2.618	2.689	0.819	0.722	4.491
9	0.842	7.833	1.746	1.813	0.910	4.753	34.156

Figures 111 and 112 illustrate the skewness-kurtosis plot of Cullen and Frey for the Sentinel extracted Chl-a at all points in Eratino lagoon. Based on these graphs and the AIC and BIC criteria, it occurs that:

a) For Points 1 and 6, the normal distribution was found to be the best-fit theoretical distribution;
b) For Points 5, 7 and 9, the log-normal distribution was found to be the best-fit theoretical distribution;
c) For Points 3 and 8, the gamma distribution was found to be the best-fit theoretical distribution;
d) For Points 2 and 3, the gumbel distribution was found to be the best-fit theoretical distribution.

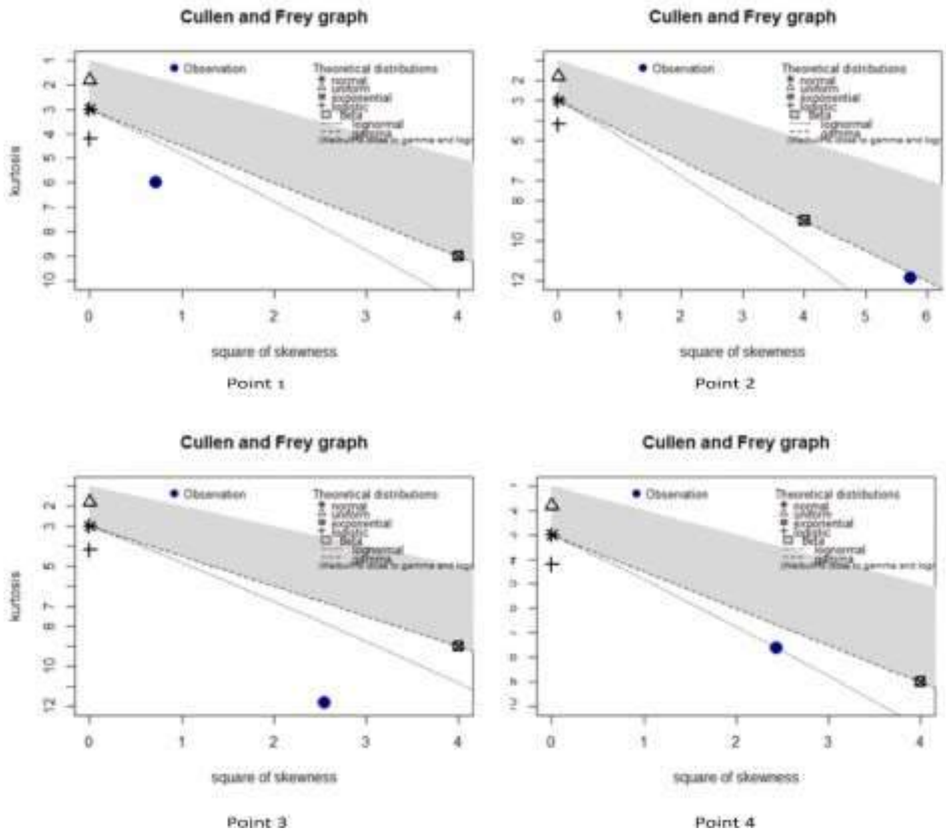

Figure 111. The Cullen and Frey diagrams for the distribution of Chl-a concentration at Points 1 - 4.

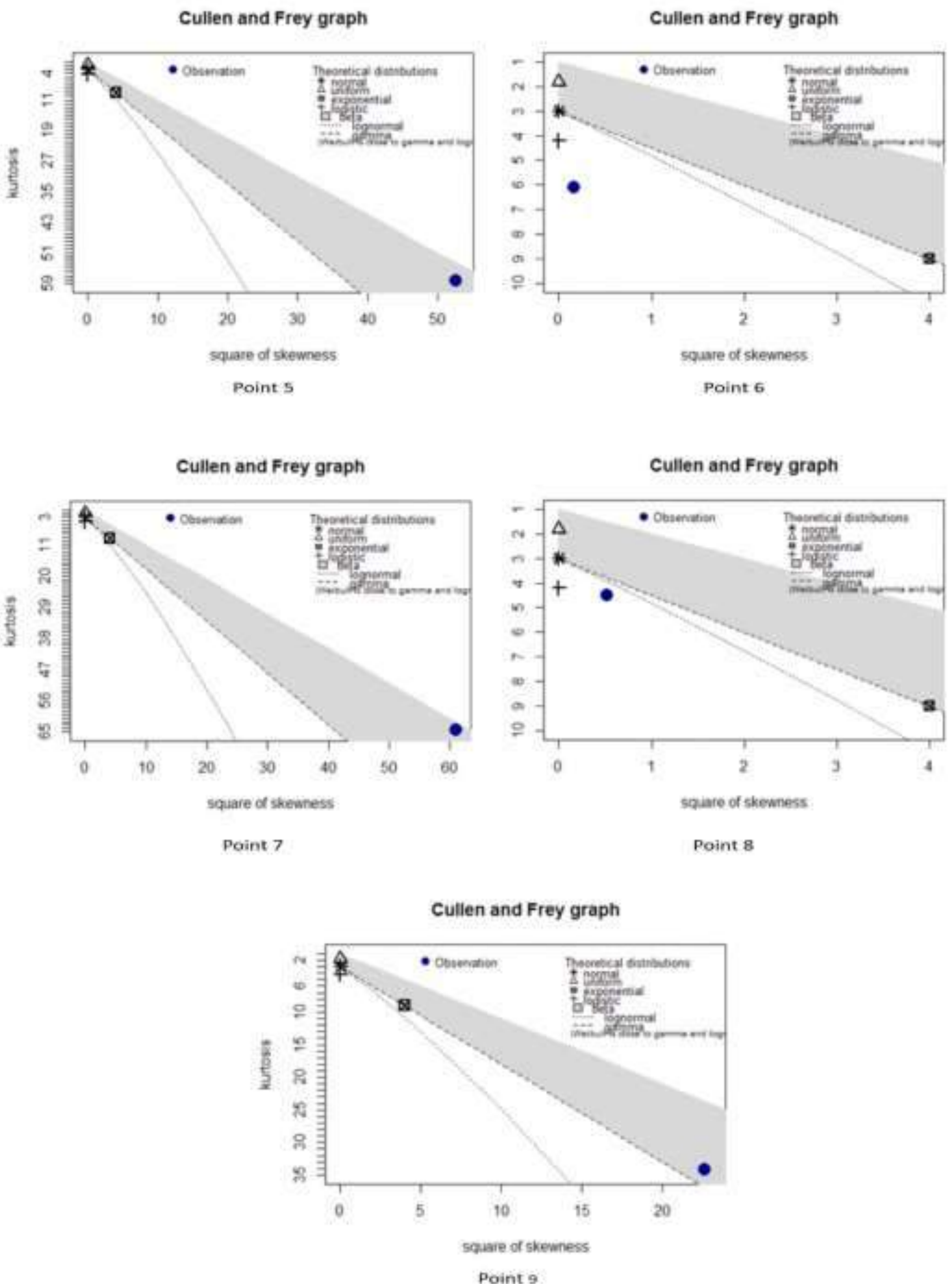

Figure 112. The Cullen and Frey diagrams for the distribution of Chl-a concentration at Points 5 - 9.

Table 27 presents the fitting parameters of the best-fit theoretical probability density function applied on the Chl-a concentration data extracted from Sentinel in Eratino lagoon. Mean and standard deviation parameters are given for the normal PDFs, log(mean) and log(sd) parameters for the log-normal distributions and shape and scale for the gamma distributions.

Table 27. Fitting parameters of the best-fit theoretical probability density function.

Points	**1**	**2**	**3**	**4**	**5**	**6**	**7**	**8**	**9**
Mean	2.101					1.988			
St Dev	0.502					0.615			
Log(Mean)					0.567		0.730		0.522
Log(St Dev)					0.058		0.077		0.045
Shape			12.047					10.316	
Scale			5.761					3.836	
a		1.499		1.890					
b		0.400		0.617					
LogLikelihood	-45.924	-45.074	-55.689	-70.247	-76.641	-58.811	-104.135	-76.120	-56.811
AIC	95.849	94.149	115.378	144.495	157.283	121.623	212.270	156.240	117.621
BIC	100.135	98.435	119.665	148.781	161.569	125.909	216.556	160.526	121.908

The theoretical probability density functions (PDFs) and the cumulative density functions (CDFs) applied as best-fit on the Chl-a data, together with the relevant Q-to-Q and P-to-P plots are shown in Figures 113 and 114.

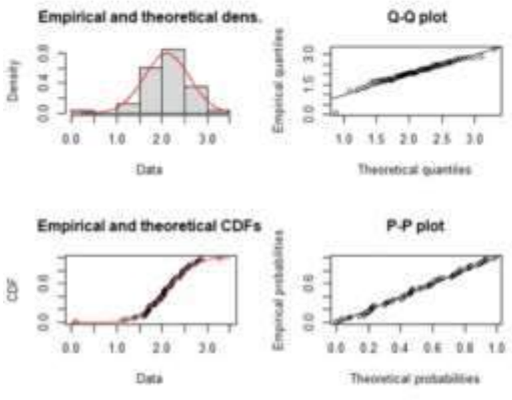

Point 1

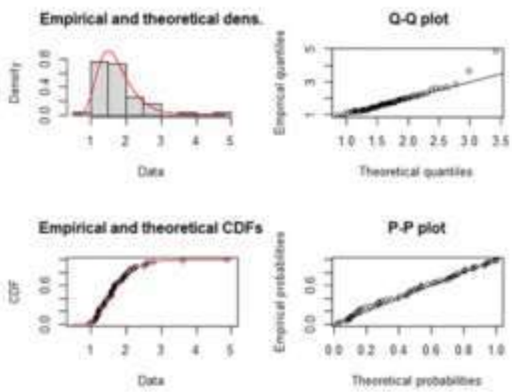

Point 2

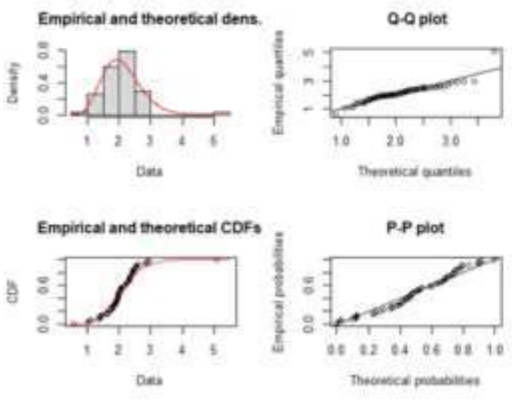

Point 3

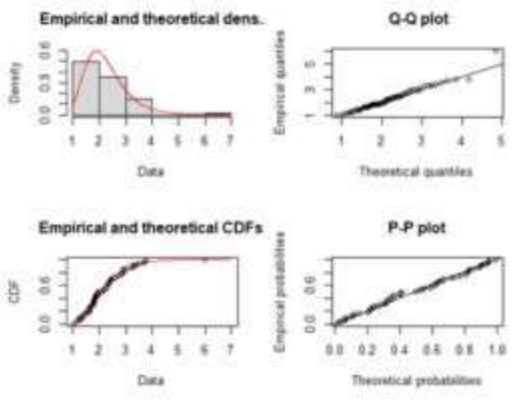

Point 4

Figure 113. Theoretical probability density functions (PDFs) and the cumulative density functions (CDFs), applied as best-fit on the Chl-a data of points 1 – 4.

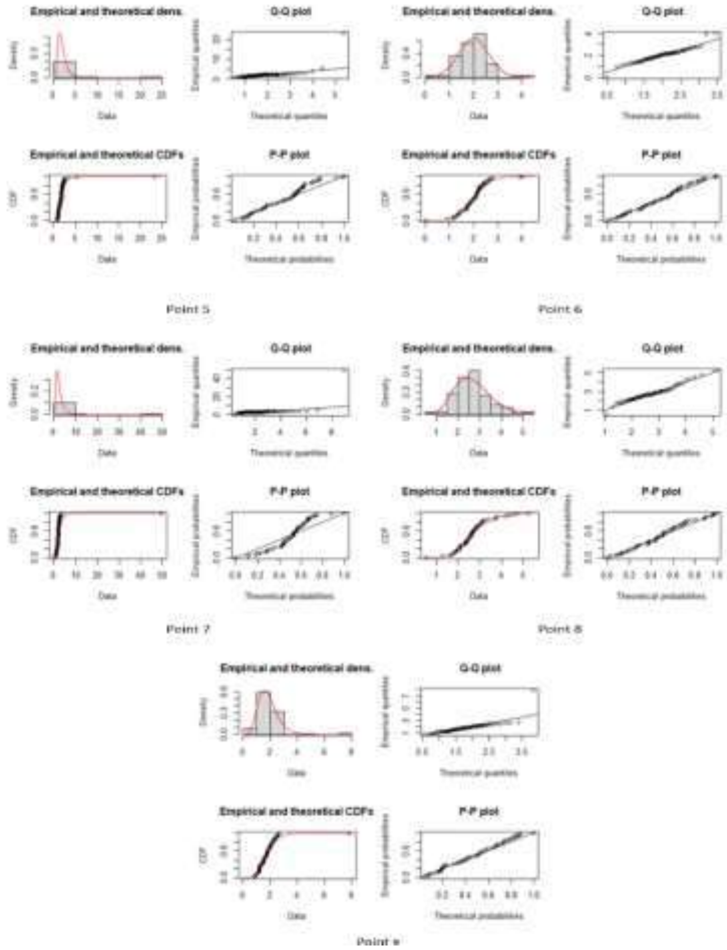

Figure 114. Theoretical probability density functions (PDFs) and the cumulative density functions (CDFs), applied as best-fit on the Chl-a data of points 5 – 9.

Based on the best-fit theoretical CDFs applied on the Chl-a, the probability of exceeding the eutrophication threshold of 2 μg/l was estimated. Probabilities of exceedance for all Eratino lagoon points are summarized in Table 28. Probability is a measure that ranges between 0 and 1, with zero implying that eutrophication is impossible and 1 implying that eutrophication is absolutely certain. Figure 115 illustrates the probability map of exceedance of the eutrophication threshold in Eratino lagoon.

Table 28. Probability of exceedance of the eutrophication threshold in Eratino lagoon.

Points	Probability of Exceedance
1	0.580
2	0.273
3	0.523

4	0.568
5	0.393
6	0.492
7	0.524
8	0.802
9	0.348

Based on the above, points 1, 3, 4, 6, 7 and 8 are more vulnerable to eutrophication effects. Point 1 is close to the inlet of the lagoon, point 4 in the natural channel which supply the lagoon with agricultural runoff, point 3 is in the upper part of the lagoon and points 6, 7 and 8 in the east part of the lagoon. For points 1, 3, 4, 6 and 7, exceedance probability is approximately 0.5 and for point 8 is higher reaching 0.8. Points 2, 5 and 9 have limited probability for a eutrophication event.

Figure 115. Probability map of exceedance of the eutrophication threshold in Eratino lagoon.

3.2.2.3 Agiasma lagoon

The points selected for Chl-a concentration extraction for the eutrophication assessment in Agiasma lagoon, are shown in Figure 81.

Table 29 presents the statistical measures for Chl-a concentration at all points examined in Agiasma lagoon.

Table 29. Statistical measures per point for Chl-a concentration at Agiasma Lagoon.

Points	Min	Max	Median	Mean	St. deviation	Skewness	Kurtosis
1	0.919	6.572	1.753	1.926	0.842	3.107	17.261
2	0.882	5.090	1.939	2.023	0.617	2.034	11.505
3	1.301	7.467	1.990	2.231	0.961	3.547	17.863
4	1.026	5.742	2.240	2.272	0.754	1.837	9.836
5	0.916	5.236	1.933	2.058	0.889	1.947	7.850
6	0.410	222.925	2.078	5.522	26.618	8.250	71.347
7	0.815	13.700	1.668	1.864	1.546	6.783	55.045
8	1.014	15.508	2.461	2.638	1.776	5.773	44.357

Figures 116 and 117 illustrate the skewness-kurtosis plot of Cullen and Frey for the Sentinel extracted Chl-a at all points in Agiasma lagoon. Based on these graphs and the AIC and BIC criteria, it occurs that:

a) For Points 1, 2, 3, 4, 6, 7 and 8, the log-normal distribution was found to be the best-fit theoretical distribution;
b) For Point 5, the gamma distribution was found to be the best-fit theoretical distribution.

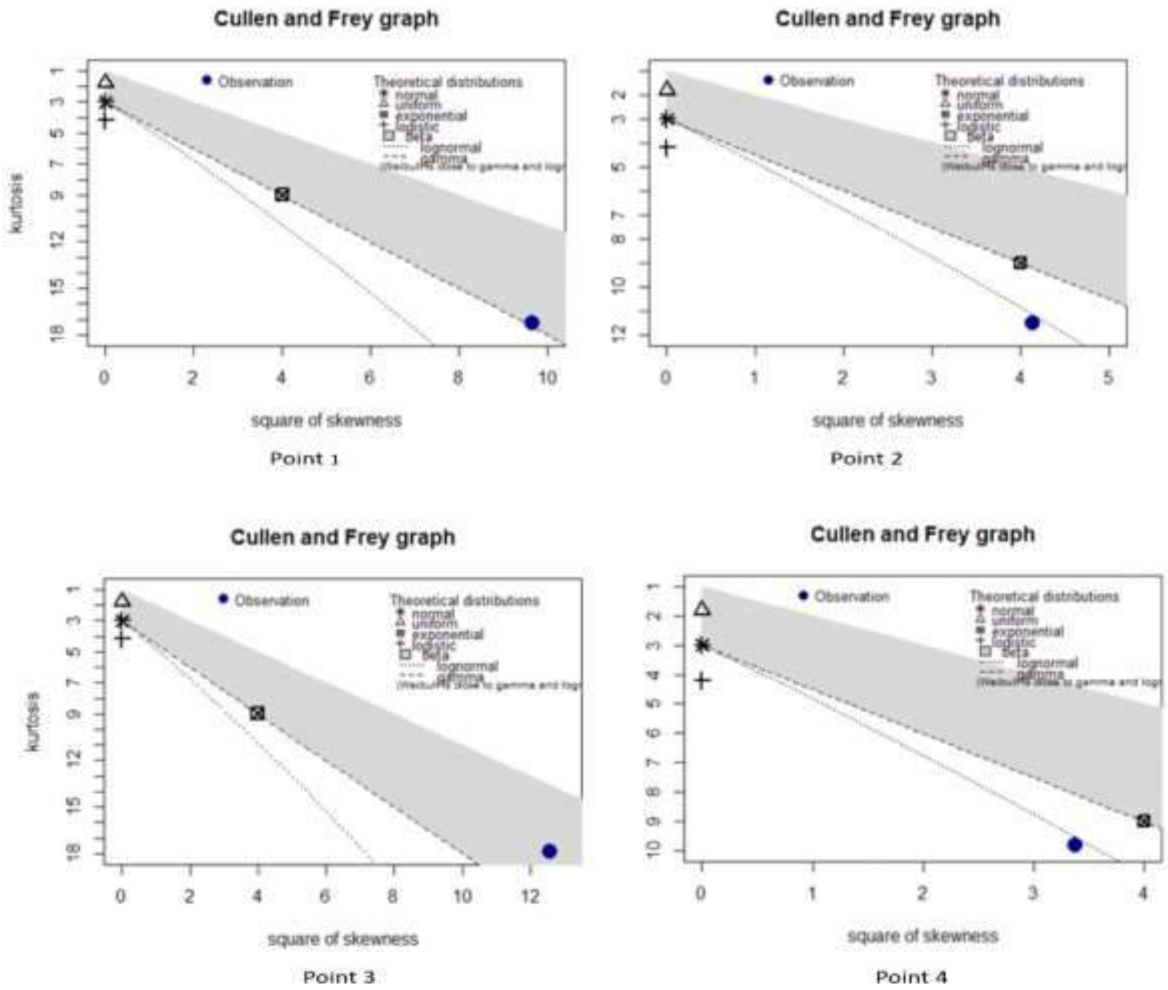

Figure 116. The Cullen and Frey diagrams for the distribution of Chl-a concentration at Points 1 - 4.

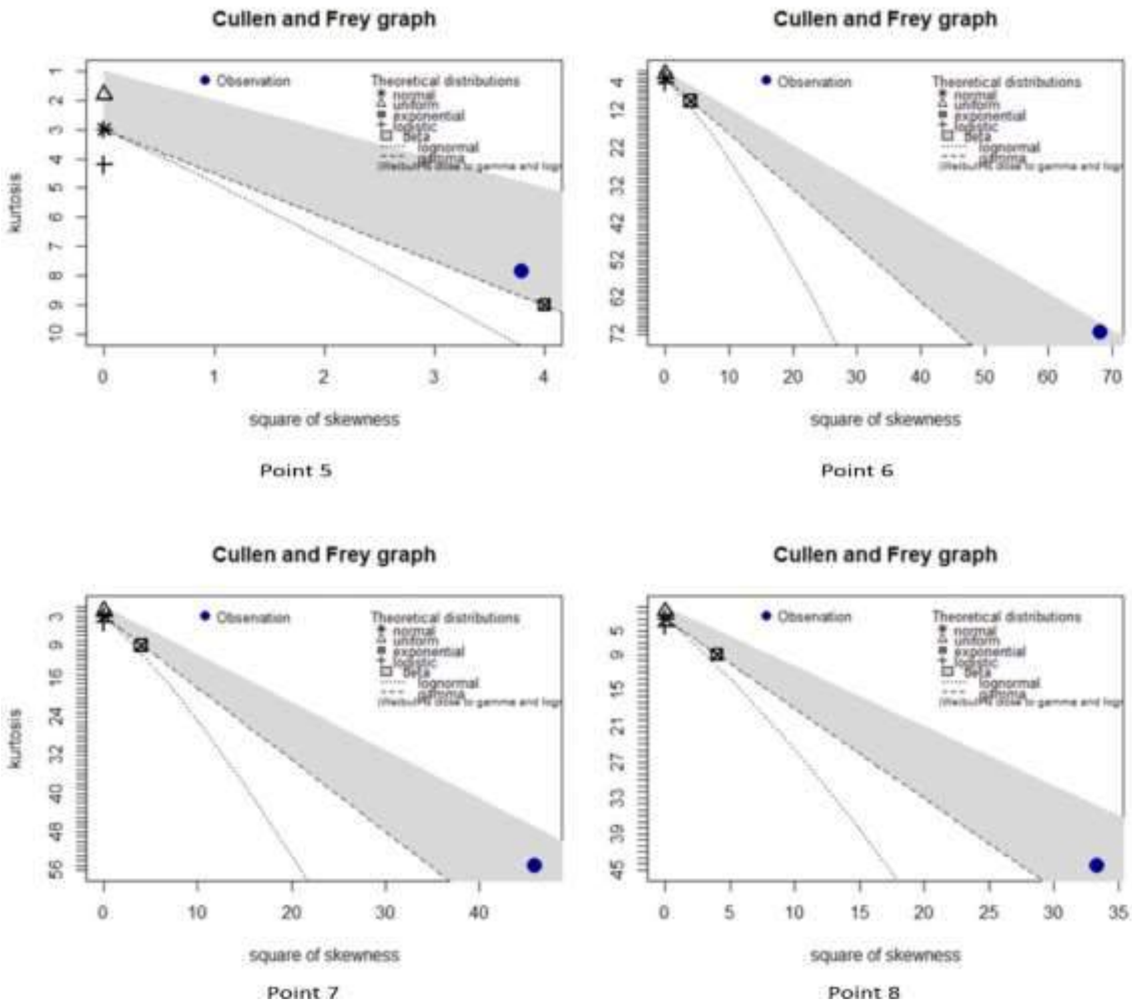

Figure 117. The Cullen and Frey diagrams for the distribution of Chl-a concentration at Points 5 - 8.

Table 30 presents the fitting parameters of the best-fit theoretical probability density function applied on the Chl-a concentration data extracted from Sentinel in Agiasma lagoon. Mean and standard deviation parameters are given for the normal PDFs, log(mean) and log(sd) parameters for the log-normal distributions and shape and scale for the gamma distributions.

Table 30. Fitting parameters of the best-fit theoretical probability density function.

Points	**1**	**2**	**3**	**4**	**5**	**6**	**7**	**8**
Mean								
St Dev								
Log(Mean)	0.590	0.665	0.747	0.773		0.775	0.505	0.866
Log(St Dev)	0.041	0.033	0.036	0.037		0.088	0.049	0.050
Shape					6.925			
Scale					3.365			

LogLikelihood	-64.474	-55.335	-65.869	-69.757	-77.509	-130.029	-70.913	-96.403
AIC	132.949	114.670	135.738	143.514	159.017	264.058	145.826	196.805
BIC	137.417	119.138	140.207	147.982	163.485	268.526	150.294	201.273

The theoretical probability density functions (PDFs) and the cumulative density functions (CDFs) applied as best-fit on the Chl-a data, together with the relevant Q-to-Q and P-to-P plots are shown in Figures 118 and 119.

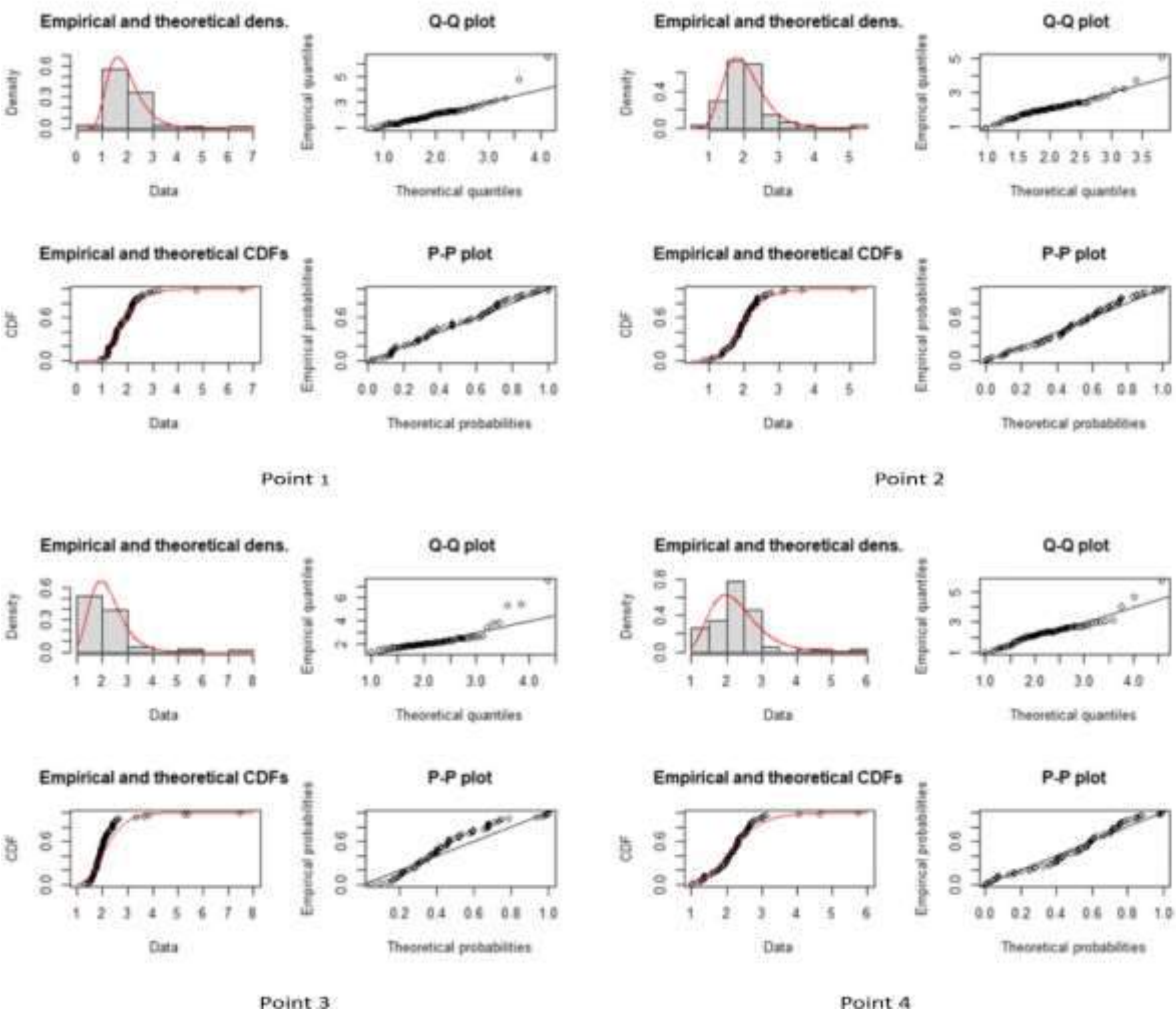

Figure 118. Theoretical probability density functions (PDFs) and the cumulative density functions (CDFs), applied as best-fit on the Chl-a data of points 1 – 4.

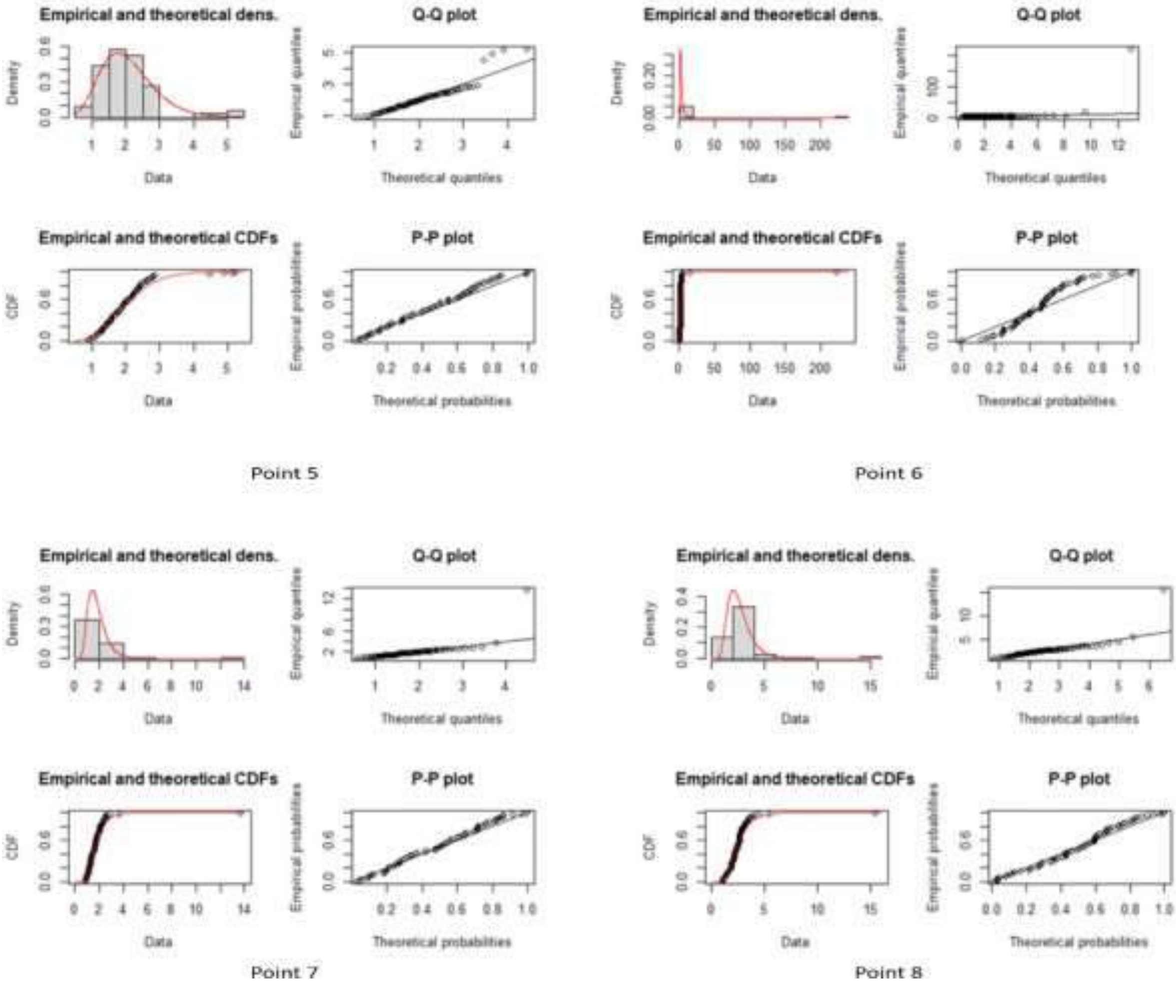

Figure 119. Theoretical probability density functions (PDFs) and the cumulative density functions (CDFs), applied as best-fit on the Chl-a data of points 5 – 8.

Based on the best-fit theoretical CDFs applied on the Chl-a, the probability of exceeding the eutrophication threshold of 2 μg/l was estimated. Probabilities of exceedance for all Agiasma lagoon points are summarized in Table 31. Probability is a measure that ranges between 0 and 1, with zero implying that eutrophication is impossible and 1 implying that eutrophication is absolutely certain. Figure 120 illustrates the probability map of exceedance of the eutrophication threshold in Agiasma lagoon.

Table 31. Probability of exceedance of the eutrophication threshold in Agiasma lagoon.

Points	**Probability of Exceedance**
1	0.381
2	0.460
3	0.572
4	0.602
5	0.479
6	0.544

7	0.322
8	0.662

Based on the above, points 3, 4, 6 and 86 are more vulnerable to eutrophication effects with exceedance probability over 0.5 and points 2 and 5 follows with exceedance probability a little lower than 0.5. Points 2, 3 and 8 are located in the lower part of the lagoon and close to the lagoon inlet. Points 1 and 7 have limited probability for a eutrophication event.

Figure 120. Probability map of exceedance of the eutrophication threshold in Eratino lagoon.

3.2.2.4 Porto Lagos lagoon

The points selected for Chl-a concentration extraction for the eutrophication assessment in Porto Lagos lagoon, are shown in Figure 87.

Table 32 presents the statistical measures for Chl-a concentration at all points examined in Porto Lagos lagoon.

Table 32. Statistical measures per point for Chl-a concentration at Porto Lagos lagoon.

Points	Min	Max	Median	Mean	St. deviation	Skewness	Kurtosis
1	0.913	19.864	1.818	2.180	2.331	6.959	55.819
2	0.854	6.520	2.050	2.076	0.725	3.581	24.236
3	0.894	2.856	1.775	1.789	0.426	0.212	2.453

4	0.323	16.440	1.510	1.915	2.000	6.257	47.292
5	0.567	214.846	1.647	5.802	27.048	7.437	60.297
6	0.697	68.272	1.693	3.275	8.436	7.310	59.390
7	0.691	1094.969	1.783	18.410	134.557	8.124	68.994
8	0.668	831.726	1.610	14.807	102.143	8.114	68.891
9	0.520	84.250	1.468	2.868	10.204	8.047	68.133
10	0.672	14.246	1.409	1.760	1.699	6.396	49.374
11	0.633	68.025	1.430	2.684	8.221	7.962	67.178
12	0.816	4.392	1.440	1.679	0.774	1.620	5.995
13	0.066	4.358	0.789	1.050	0.882	1.344	5.089

Figures 121, 122 and 123 illustrate the skewness-kurtosis plot of Cullen and Frey for the Sentinel extracted Chl-a at all points in Porto Lagos lagoon. Based on these graphs and the AIC and BIC criteria, it occurs that:

a) For Points 1, 5, 6, 7, 8, 9, 10. 11 and 12, the log-normal distribution was found to be the best-fit theoretical distribution;
b) For Point 3 and 13, the gamma distribution was found to be the best-fit theoretical distribution;
c) For Points 2 and 4, the gumbel distribution was found to be the best-fit theoretical distribution.

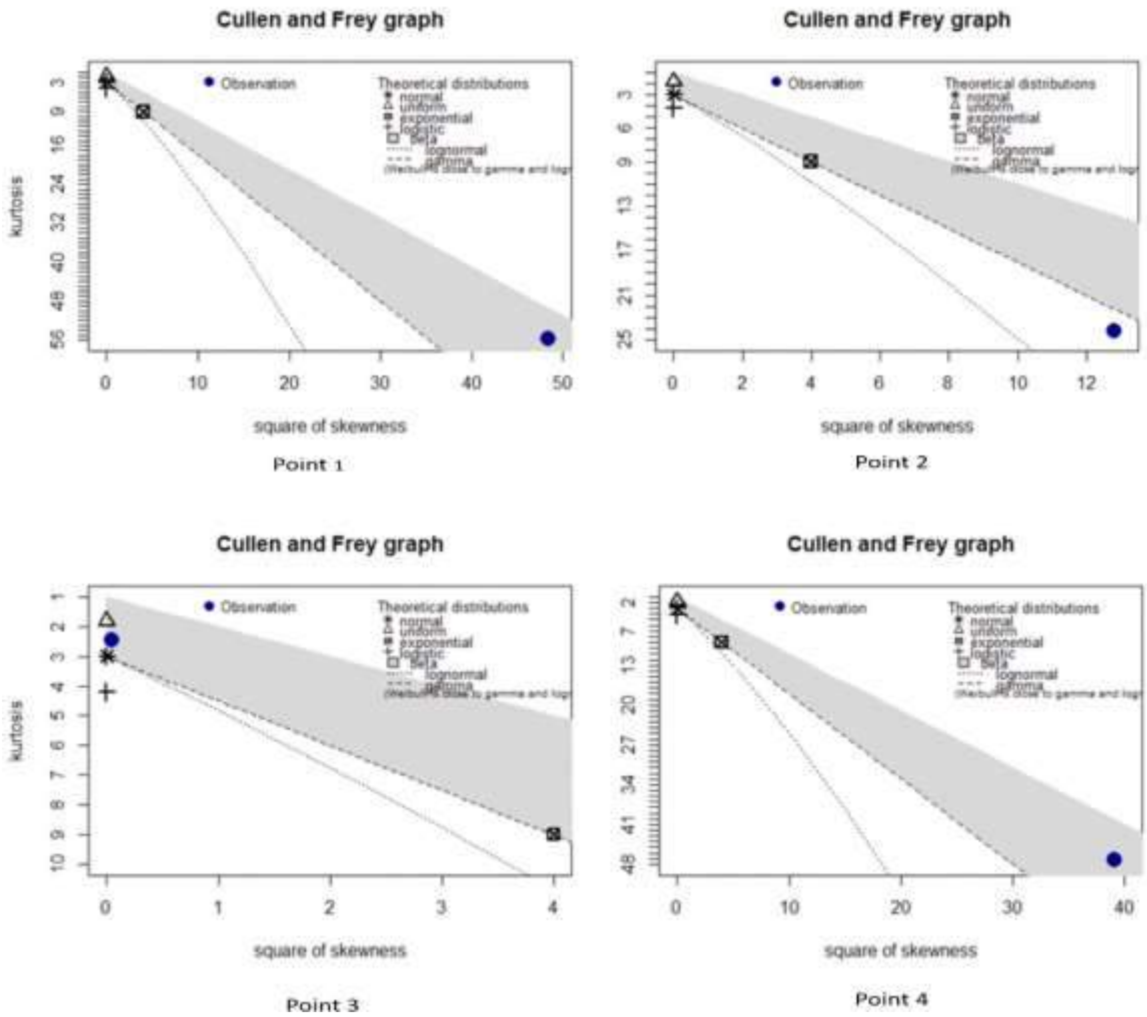

Figure 121. The Cullen and Frey diagrams for the distribution of Chl-a concentration at Points 1 - 4.

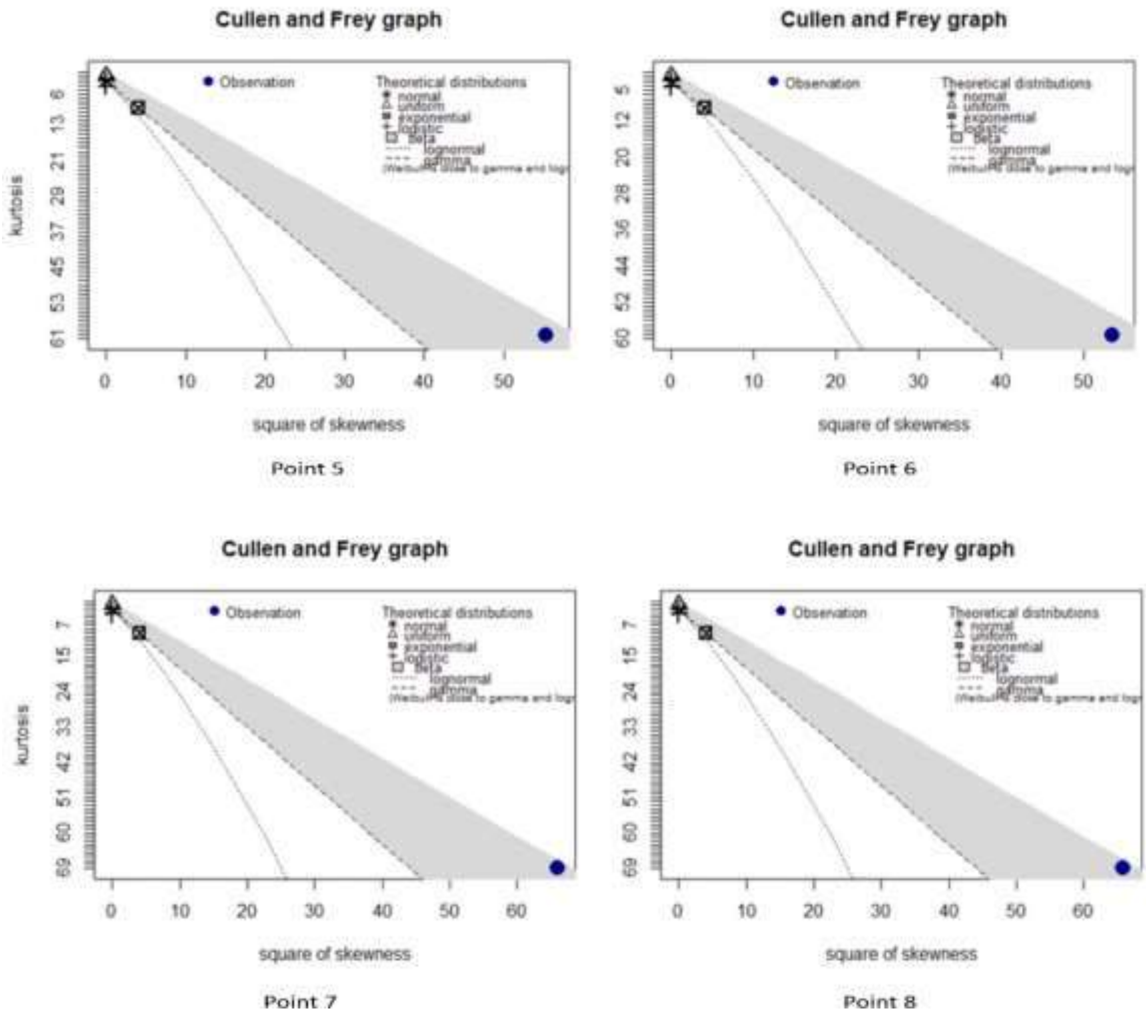

Figure 122. The Cullen and Frey diagrams for the distribution of Chl-a concentration at Points 5 - 8.

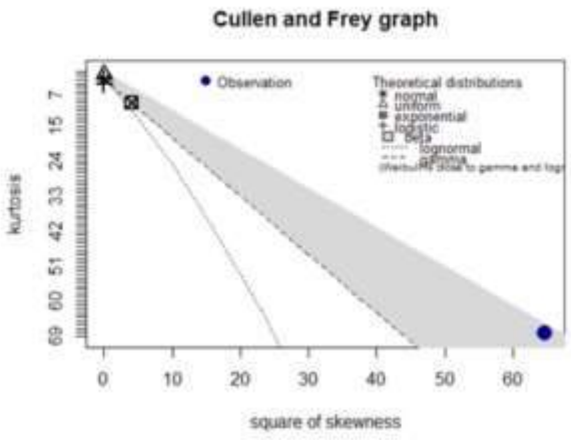

Point 9

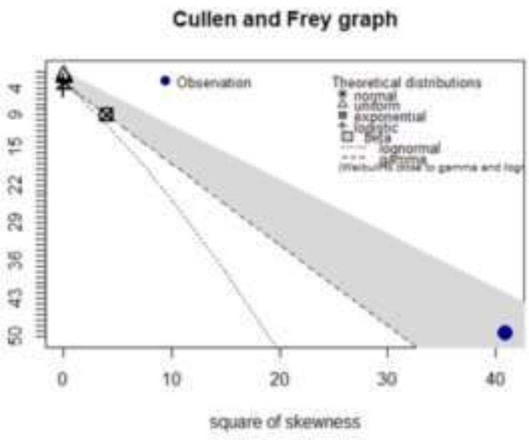

Point 10

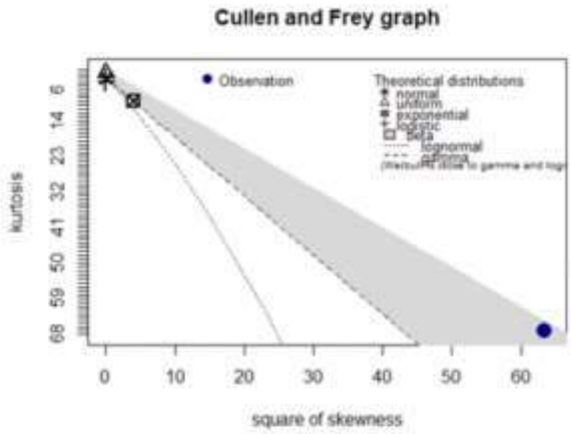

Point 11

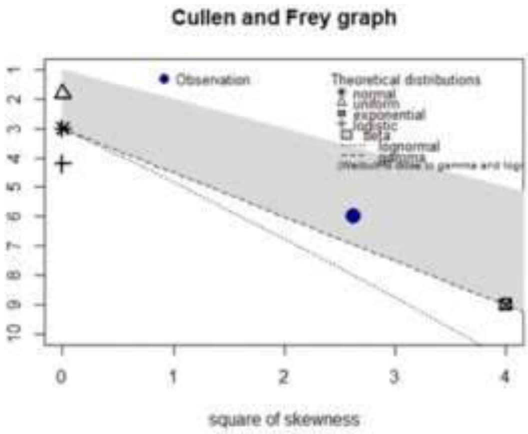

Point 12

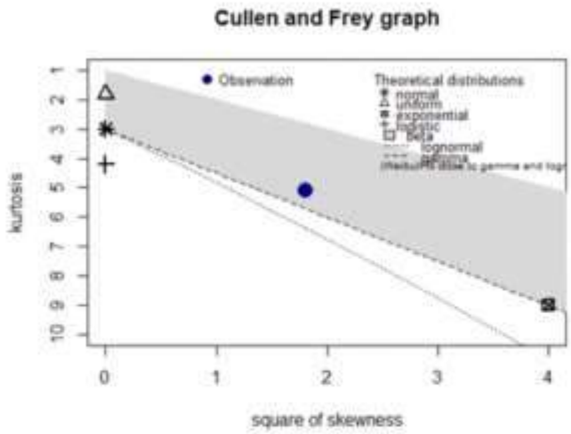

Point 13

Figure 123. The Cullen and Frey diagrams for the distribution of Chl-a concentration at Points 9 - 13.

Table 33 presents the fitting parameters of the best-fit theoretical probability density function applied on the Chl-a concentration data extracted from Landsat in Porto Lagos lagoon. Mean and standard deviation parameters are given for the normal PDFs, log(mean) and log(sd) parameters for the log-normal distributions and shape and scale for the gamma distributions.

Table 33. Fitting parameters of the best-fit theoretical probability density function.

Points	1	2	3	4	5	6	7
Mean							
St Dev							
Log(Mean)	0.621				0.613	0.678	0.622
Log(St Dev)	0.055				0.100	0.084	0.110
Shape			17.465				
Scale			9.760				
a		1.803		1.433			
b		0.475		0.671			
LogLikelihood	-81.529	-54.843	-36.387	-87.002	-119.745	-112.870	-127.103
AIC	167.184	113.686	76.774	178.003	243.489	229.740	258.205
BIC	171.654	118.066	81.153	182.382	247.868	234.119	262.584
Points	**8**	**9**	**10**	**11**	**12**	**13**	
Mean							
St Dev							
Log(Mean)	0.641	0.454	0.414	0.470	0.431		
Log(St Dev)	0.117	0.078	0.556	0.076	0.050		
Shape						1.215	
Scale							
a							
b							
LogLikelihood	-132.631	-93.181	-68.540	-94.151	-62.039	-67.317	
AIC	269.262	190.362	141.079	192.303	128.079	138.632	
BIC	273.641	194.741	145.459	196.682	132.458	143.012	

The theoretical probability density functions (PDFs) and the cumulative density functions (CDFs) applied as best-fit on the Chl-a data, together with the relevant Q-to-Q and P-to-P plots are shown in Figures 124, 125 and 126.

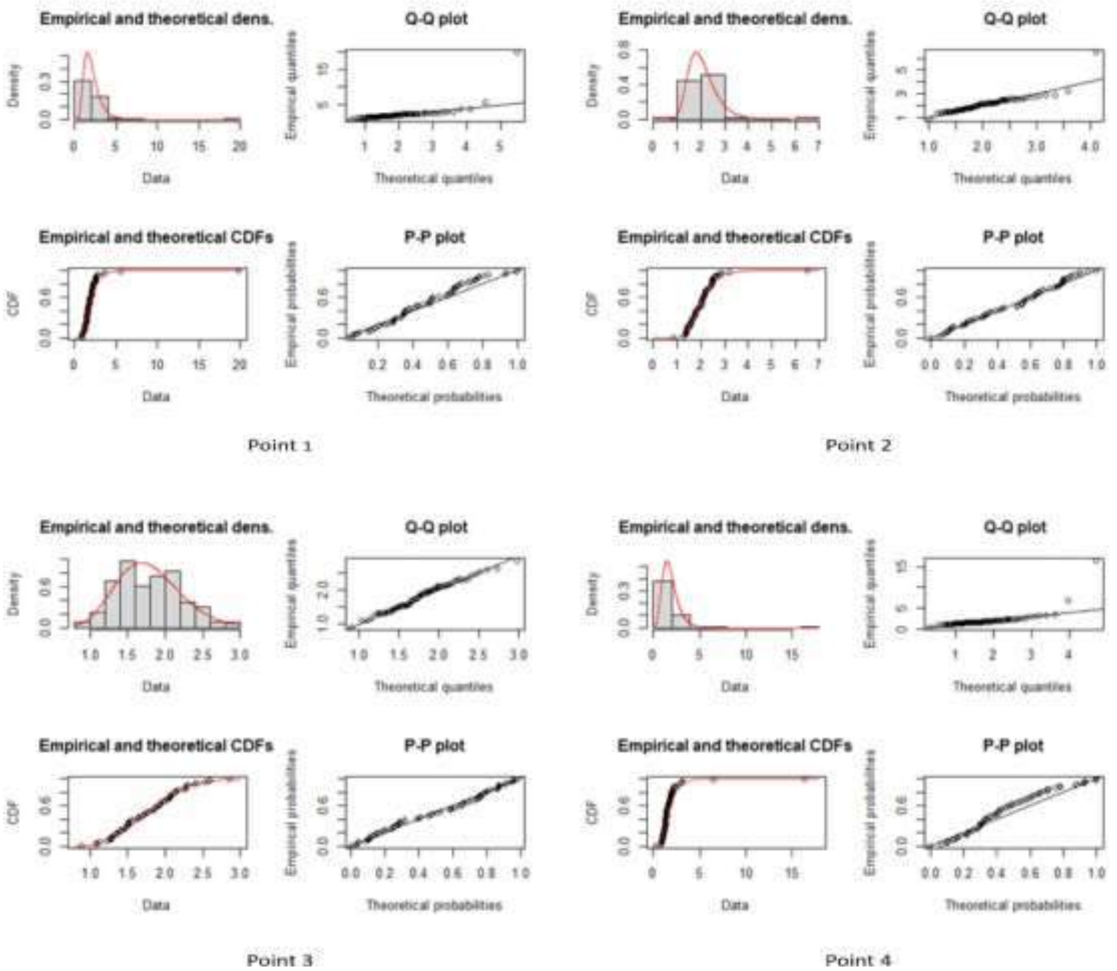

Figure 124. Theoretical probability density functions (PDFs) and the cumulative density functions (CDFs), applied as best-fit on the Chl-a data of points 1 - 4.

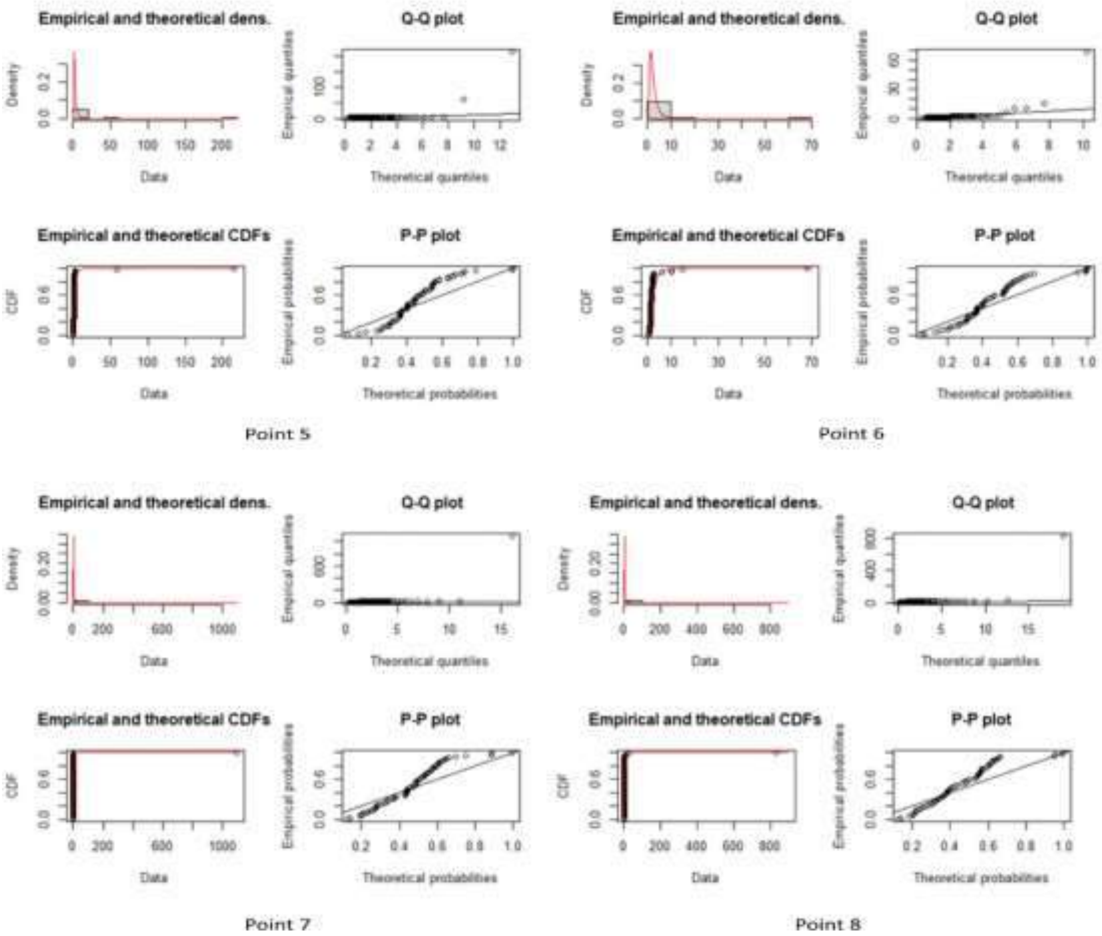

Figure 125. Theoretical probability density functions (PDFs) and the cumulative density functions (CDFs), applied as best-fit on the Chl-a data of points 5 - 8.

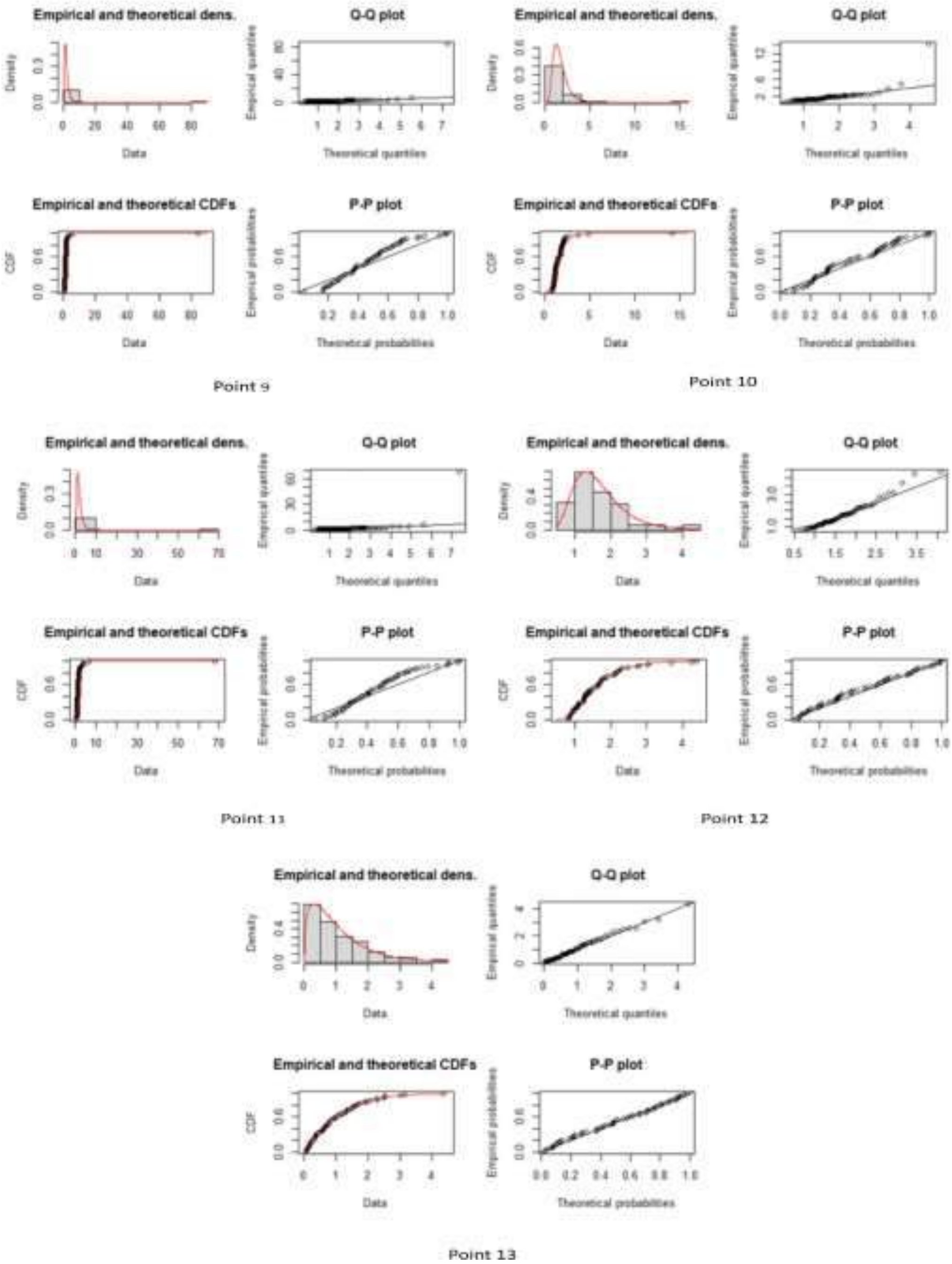

Figure 126. Theoretical probability density functions (PDFs) and the cumulative density functions (CDFs), applied as best-fit on the Chl-a data of points 9 – 13.

Based on the best-fit theoretical CDFs applied on the Chl-a, the probability of exceeding the eutrophication threshold of 2 μg/l was estimated. Probabilities of exceedance for all Porto Lagos lagoon points are summarized in Table 34. Probability is a measure that ranges between 0 and 1, with zero implying that eutrophication is impossible and 1 implying that eutrophication is absolutely certain. Figure 127 illustrates the probability map of exceedance of the eutrophication threshold in Porto Lagos lagoon.

Table 34. Probability of exceedance of the eutrophication threshold in Porto Lagos lagoon.

Points	Probability of Exceedance
1	0.436
2	0.517
3	0.290
4	0.330
5	0.460
6	0.491
7	0.468
8	0.478
9	0.352
10	0.269
11	0.362
12	0.258
13	0.133

Based on the above, points 1, 2, 5, 6, 7 and 8 are more vulnerable to eutrophication effects than the rest of the lagoon. These points are located at the north west basin of the lagoon. Exceedance probability is approx. 0.5, meaning that during half of a typical year eutrophication may exist. Based on the available Sentinel images, it seems that the eutrophication prone periods are spring and summer. On the contrary, points located at the east basin have limited probability for a eutrophication event.

Figure 127. Probability map of exceedance of the eutrophication threshold in Porto Lagos lagoon.

3.2.2.5 *Xirolimni*

The points selected for Chl-a concentration extraction for the eutrophication assessment in Xirolimni lagoon, are shown in Figure 95.

Table 35. Statistical measures per point for Chl-a concentration at Xirolimni Lagoon. presents the statistical measures for Chl-a concentration at all points examined in Xirolimni lagoon.

Table 35. Statistical measures per point for Chl-a concentration at Xirolimni Lagoon.

Points	Min	Max	Median	Mean	St. deviation	Skewness	Kurtosis
1	0.095	208.517	2.386	5.819	25.431	8.032	67.958
2	0.052	5.566	2.089	2.033	0.760	1.319	9.812
3	0.040	49.868	2.318	3.739	6.763	5.748	39.144
4	0.675	53.312	2.610	4.174	6.795	6.226	46.587
5	0.125	10.275	1.780	2.158	1.426	3.427	19.787
6	0.546	270.361	2.181	6.616	33.021	8.082	68.529
7	0.203	44.589	2.080	2.705	5.286	7.884	66.346

Figures 128 and 129 illustrate the skewness-kurtosis plot of Cullen and Frey for the Sentinel extracted Chl-a at all points in Xirolimni lagoon. Based on these graphs and the AIC and BIC criteria, it occurs that:

a) For Point 2, the normal distribution was found to be the best-fit theoretical distribution;
b) For Points 1, 3, 4, 6 and 7, the log-normal distribution was found to be the best-fit theoretical distribution;
c) For Point 5, the gumbel distribution was found to be the best-fit theoretical distribution.

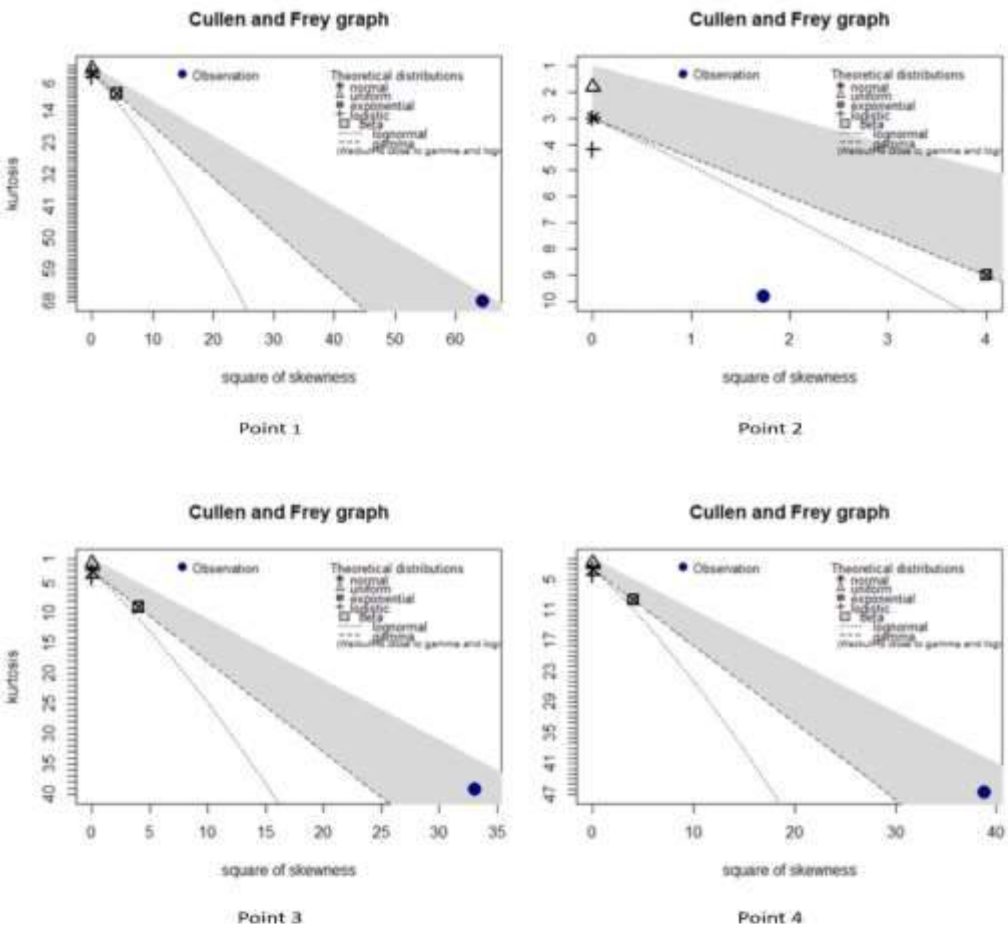

Figure 128. The Cullen and Frey diagrams for the distribution of Chl-a concentration at Points 1 - 4.

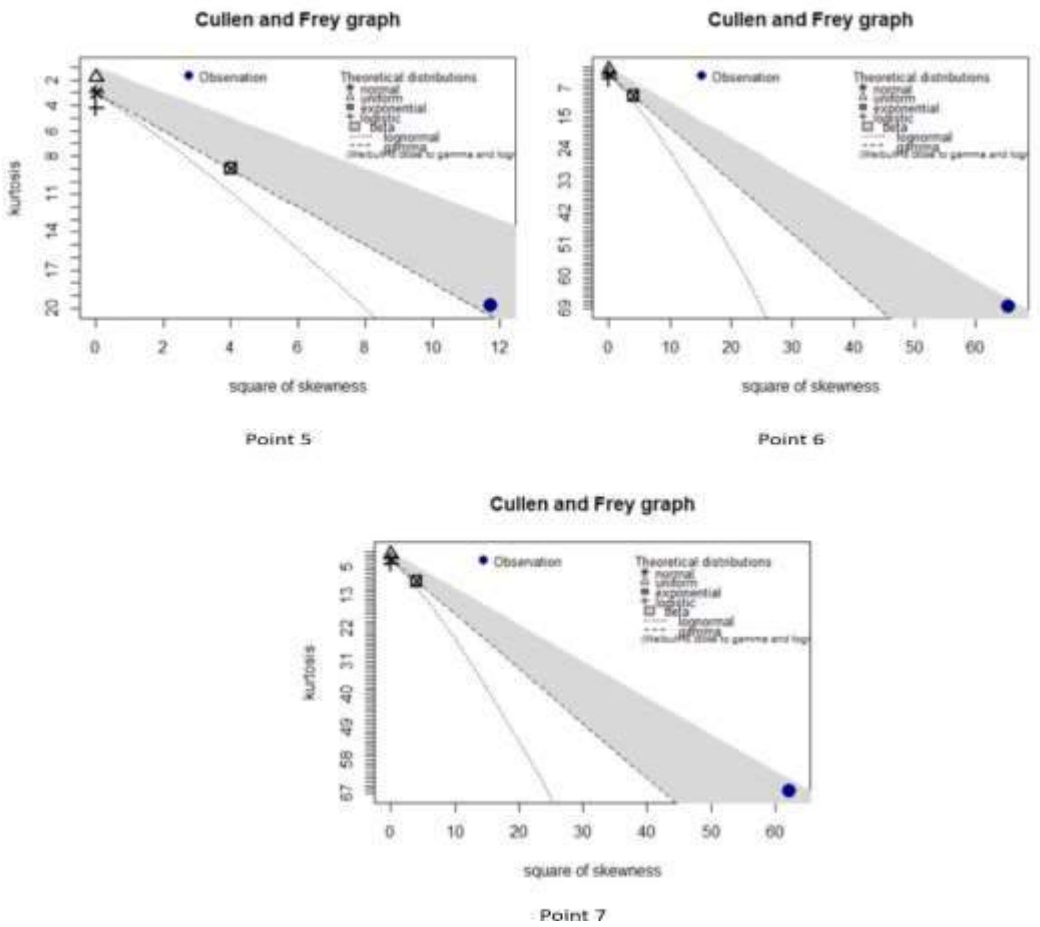

Figure 129. The Cullen and Frey diagrams for the distribution of Chl-a concentration at Points 5 - 7.

Table 36. Fitting parameters of the best-fit theoretical probability density function. presents the fitting parameters of the best-fit theoretical probability density function applied on the Chl-a concentration data extracted from Sentinel in Xirolimni lagoon. Mean and standard deviation parameters are given for the normal PDFs, log(mean) and log(sd) parameters for the log-normal distributions and shape and scale for the gamma distributions.

Table 36. Fitting parameters of the best-fit theoretical probability density function.

Points	**1**	**2**	**3**	**4**	**5**	**6**	**7**
Mean		2.033					
St Dev		0.754					
Log(Mean)	0.884		0.828	1.072		0.866	0.696
Log(St Dev)	0.100		0.115	0.084		0.094	0.071
Shape							
Scale							
a					1.645		
b					0.838		

LogLikelihood	-138.512	-75.002	-143.835	-139.018	-94.729	-133.074	-103.048
AIC	281.023	154.004	291.670	282.037	193.457	270.149	210.096
BIC	285.403	158.383	296.050	286.416	197.836	274.528	214.475

The theoretical probability density functions (PDFs) and the cumulative density functions (CDFs) applied as best-fit on the Chl-a data, together with the relevant Q-to-Q and P-to-P plots are shown in Figures 130 and 131.

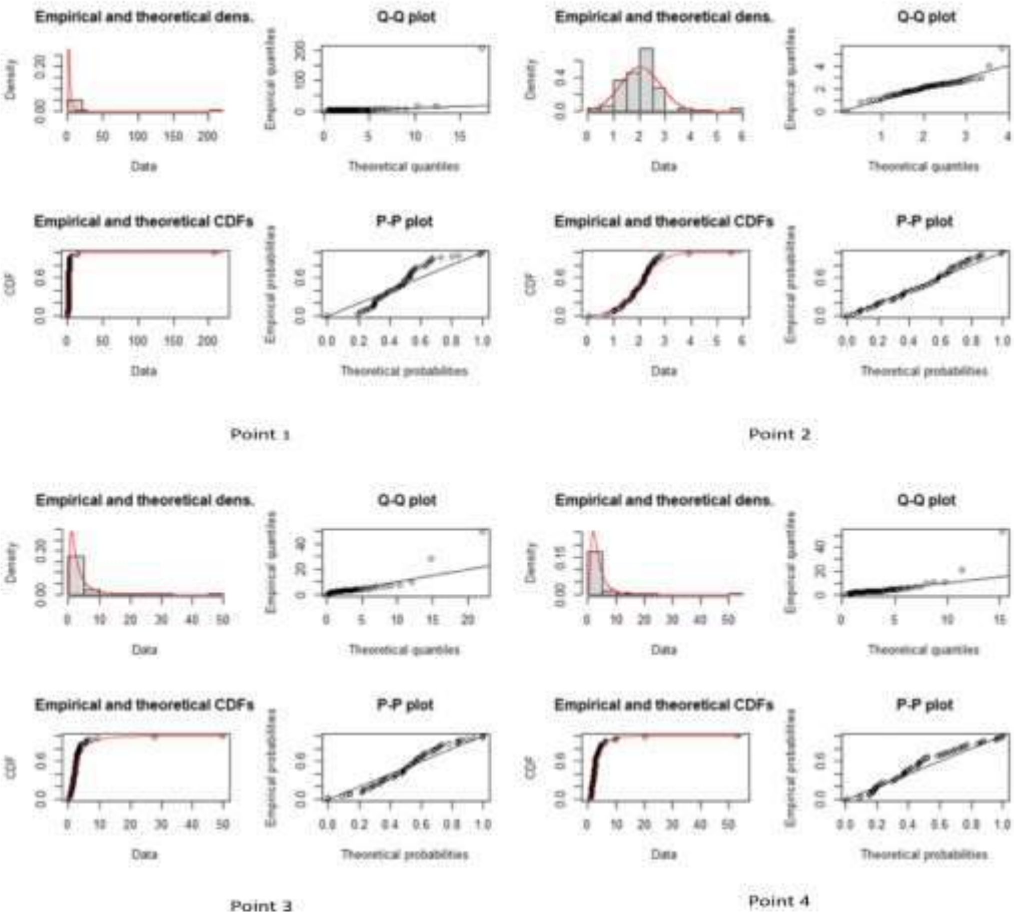

Figure 130. Theoretical probability density functions (PDFs) and the cumulative density functions (CDFs), applied as best-fit on the Chl-a data of points 1 – 4.

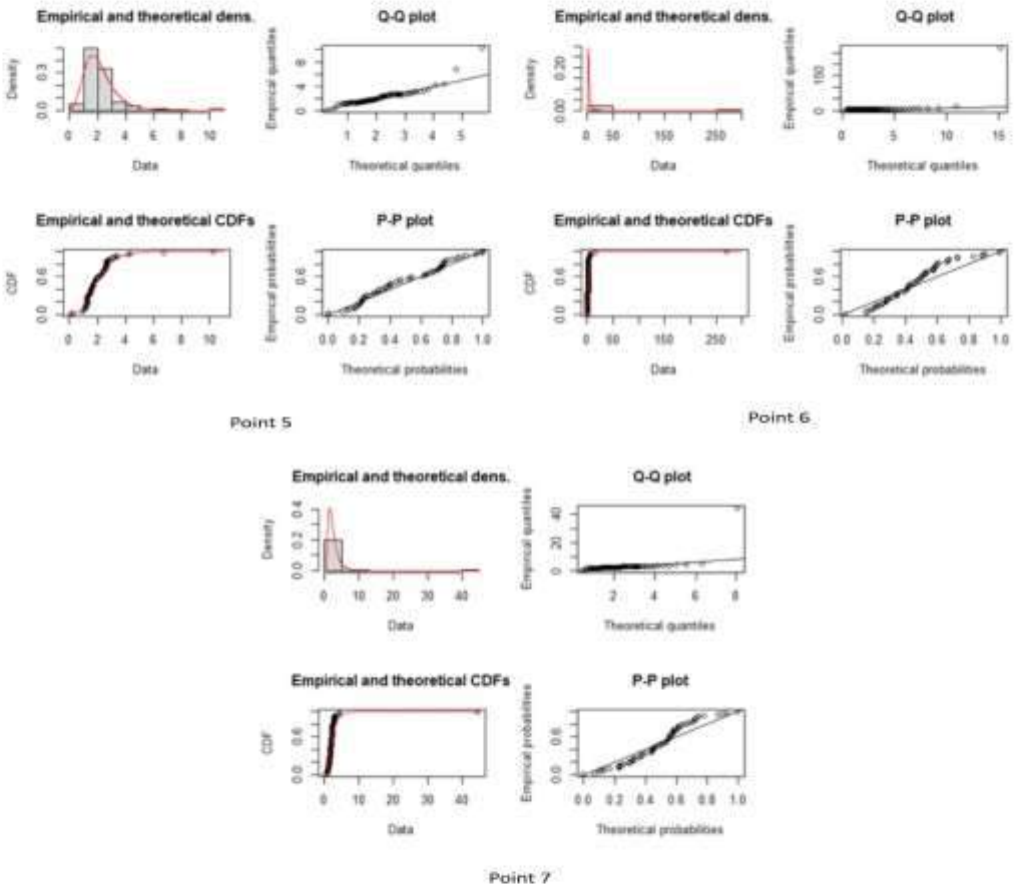

Figure 131. Theoretical probability density functions (PDFs) and the cumulative density functions (CDFs), applied as best-fit on the Chl-a data of points 5 – 7.

Based on the best-fit theoretical CDFs applied on the Chl-a, the probability of exceeding the eutrophication threshold of 2 μg/l was estimated. Probabilities of exceedance for all Xirolimni lagoon points are summarized in Table 37. Probability is a measure that ranges between 0 and 1, with zero implying that eutrophication is impossible and 1 implying that eutrophication is absolutely certain. Figure 132 illustrates the probability map of exceedance of the eutrophication threshold in Xirolimni lagoon.

Table 37. Probability of exceedance of the eutrophication threshold in Xirolimni lagoon.

Points	Probability of Exceedance
1	0.592
2	0.517
3	0.557
4	0.711
5	0.520
6	0.590
7	0.502

Based on the above, all points are vulnerable to eutrophication effects with exceedance probability over 0.5. Point 4, which is located on the southern part of the lagoon, shows the higher exceedance probability around 0.7. Based on the available Sentinel images, it seems that the eutrophication prone periods are spring and summer.

Figure 132. Probability map of exceedance of the eutrophication threshold in Xirolimni lagoon.

3.2.2.6 Ptelea

The points selected for Chl-a concentration extraction for the eutrophication assessment in Ptelea lagoon, are shown in Figure 101.

Table 38 presents the statistical measures for Chl-a concentration at all points examined in Ptelea lagoon.

Table 38. Statistical measures per point for Chl-a concentration at Ptelea Lagoon.

Points	Min	Max	Median	Mean	St. deviation	Skewness	Kurtosis
1	0.597	93.855	5.998	12.938	17.527	2.764	11.892
2	0.010	53.320	6.087	10.710	12.002	2.063	6.722
3	0.085	6.881	1.549	1.689	1.082	1.802	9.787
4	0.340	225.318	5.768	15.535	29.925	5.558	40.297

5	0.083	242.107	5.467	15.358	32.397	5.732	40.858
6	0.535	285.309	9.329	27.705	55.905	3.437	14.903

Figures 133 and 134 illustrate the skewness-kurtosis plot of Cullen and Frey for the Sentinel extracted Chl-a at all points in Ptelea lagoon. Based on these graphs and the AIC and BIC criteria, it occurs that:

a) For Points 1, 4, 5 and 6, the log-normal distribution was found to be the best-fit theoretical distribution;
b) For Point 3, the gamma distribution was found to be the best-fit theoretical distribution;
c) For Point 2, the gumbel distribution was found to be the best-fit theoretical distribution;

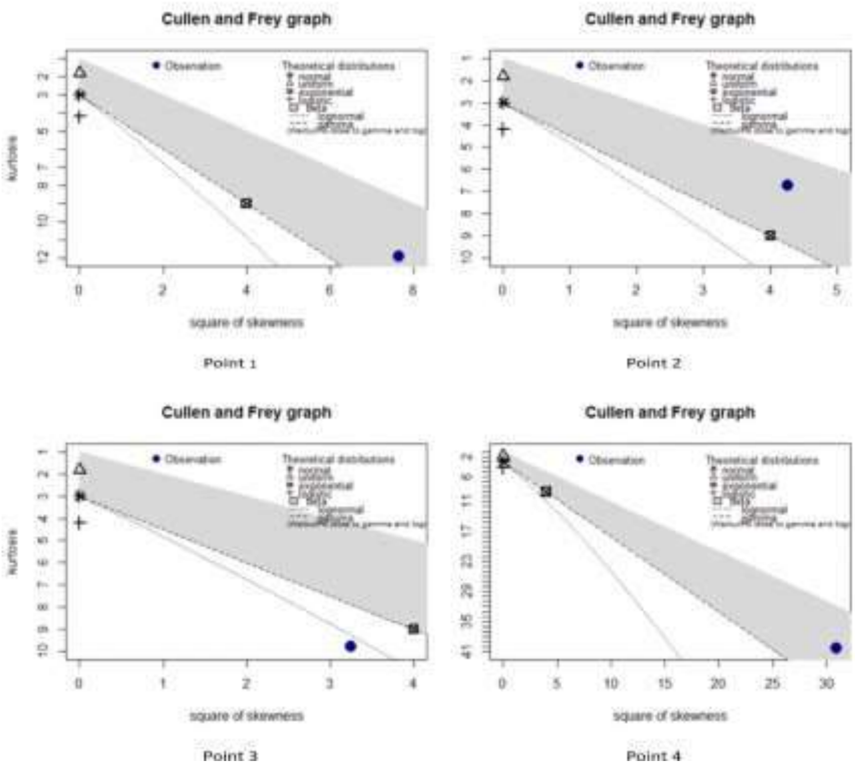

Figure 133. The Cullen and Frey diagrams for the distribution of Chl-a concentration at Points 1 - 4.

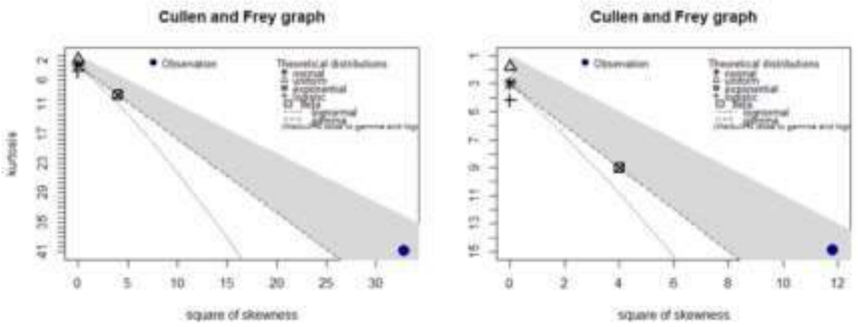

Point 5 Point 6

Figure 134. The Cullen and Frey diagrams for the distribution of Chl-a concentration at Points 5 - 6.

Table 39 presents the fitting parameters of the best-fit theoretical probability density function applied on the Chl-a concentration data extracted from Sentinel in Ptelea lagoon. Mean and standard deviation parameters are given for the normal PDFs, log(mean) and log(sd) parameters for the log-normal distributions and shape and scale for the gamma distributions.

Table 39. Fitting parameters of the best-fit theoretical probability density function.

Points	1	2	3	4	5	6
Mean						
St Dev						
Log(Mean)	1.927			1.964	1.938	2.364
Log(St Dev)	0.135			0.147	0.147	0.150
Shape			1.647			
Scale						
a		6.196				
b		6.292				
LogLikelihood	-230.642	-238.302	-90.760	-239.017	-237.374	-267.301
AIC	465.284	480.605	185.521	482.034	478.747	538.603
BIC	469.694	485.014	189.930	486.443	483.157	543.012

The theoretical probability density functions (PDFs) and the cumulative density functions (CDFs) applied as best-fit on the Chl-a data, together with the relevant Q-to-Q and P-to-P plots are shown in Figures 135 and 136.

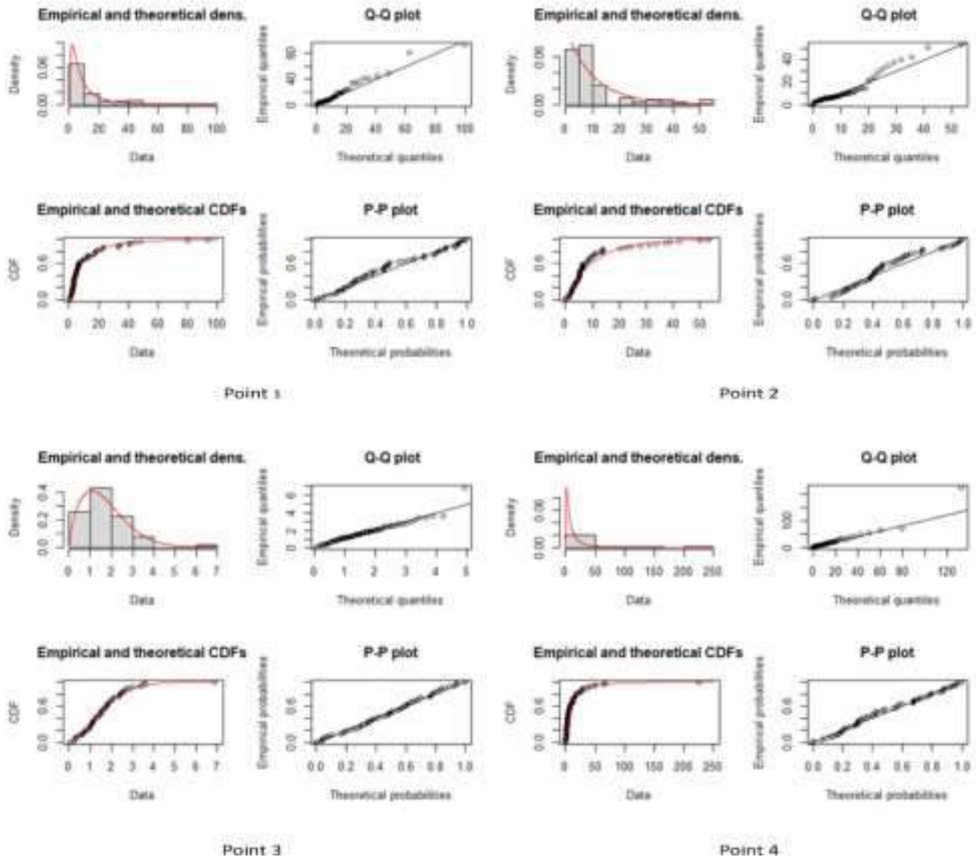

Figure 135. Theoretical probability density functions (PDFs) and the cumulative density functions (CDFs), applied as best-fit on the Chl-a data of points 1 – 4.

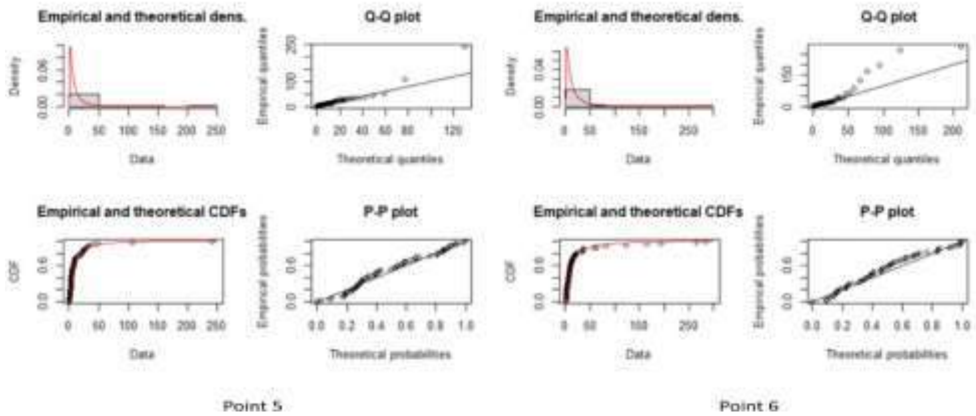

Figure 136. Theoretical probability density functions (PDFs) and the cumulative density functions (CDFs), applied as best-fit on the Chl-a data of points 5 – 6.

Based on the best-fit theoretical CDFs applied on the Chl-a, the probability of exceeding the eutrophication threshold of 2 μg/l was estimated. Probabilities of exceedance for all Ptelea lagoon points are summarized in Table 40. Probability is a measure that ranges between 0 and 1, with zero implying that eutrophication is impossible and 1 implying that eutrophication is absolutely certain. Figure 137 illustrates the probability map of exceedance of the eutrophication threshold in Ptelea lagoon.

Table 40. Probability of exceedance of the eutrophication threshold in Ptelea lagoon.

Points	Probability of Exceedance
1	0.869
2	0.824
3	0.686
4	0.855
5	0.849
6	0.913

Based on the above, all points are vulnerable to eutrophication effects. Exceedance probability varies from 0.7 to 0.9, meaning there is high probability eutrophication may exist during a typical year. Based on the available Sentinel images, it seems that the eutrophication prone periods are spring and summer.

Figure 137. Probability map of exceedance of the eutrophication threshold in Ptelea lagoon.

4 Conclusions

In this work, a neuro-fuzzy model was developed to estimate Chl-a values from Landsat 8 and Sentinel-2 satellite images. The model was trained using in-situ data collected at times coinciding to the crossing of these satellites. The model was implemented at the reflectance data from 6 lagoons of the Nestos and Vistonis complexes in Northern Greece.

The annual evolution of Chl-a in Vassova lagoon registers two maxima. The first one occurs in spring (May-June) and the next one in the summer around August. The center of the lagoon and the north part are the parts that usually show higher Chl-a values than the rest of the basin.

Eratino and Agiasma exhibit three peaks, one in spring (April-May), the second one in summer and the third one in November. In Eratino, higher Chl-a values occur at the center and the southeast parts and in Agiasma at the northern part.

In Porto Lagos, higher Chl-a values occur at the northern part and the southeast basin. Throughout the years studied, a regular peak was recorded around July-August.

In Xirolimni lagoon, the first peak occurs in late spring, and the second one in November and Chl-a was found to be in greater concentration across the shores.

Finally, Ptelea shows higher Chl-a concentration values compared to the other lagoons studied. Chl-a values determined range from 1.0 to 40.0 μg/l, while the values in the other lagoons rarely exceed 5 μg/l.

5 References

Antoine, D., André, J.-M., Morel, A., 1996. Oceanic primary production: 2. Estimation at global scale from satellite (Coastal Zone Color Scanner) chlorophyll. Global Biogeochemical Cycles 10, 57-69.

Brezonik, P., Menken, K.D., Bauer, M., 2005. Landsat-based Remote Sensing of Lake Water Quality Characteristics, Including Chlorophyll and Colored Dissolved Organic Matter (CDOM). Lake and Reservoir Management 21, 373-382.

Bukata, R.P., 2013. Retrospection and introspection on remote sensing of inland water quality:"Like Déjà Vu All Over Again". Journal of Great Lakes Research, 2-5.

Cao, Z., Ma, R., Duan, H., Pahlevan, N., Melack, J., Shen, M., Xue, K., 2020. A machine learning approach to estimate chlorophyll-a from Landsat-8 measurements in inland lakes. Remote Sensing of Environment 248, 111974.

Costanza, R., d'Arge, R., de Groot, R., Farber, S., Grasso, M., Hannon, B., Limburg, K., Naeem, S., O'Neill, R.V., Paruelo, J., Raskin, R.G., Sutton, P., van den Belt, M., 1997. The value of the world's ecosystem services and natural capital. Nature 387, 253-260.

Cullen, A.C., Frey, H.C., 1999. Probabilistic techniques in exposure assessment. Plenum Press, USA, pp. 81-159.

Dall'Olmo, G., Gitelson, A., Rundquist, D., Leavitt, B., Barrow, T., Holz, J., 2005. Assessing the potential of SeaWiFS and MODIS for estimating chlorophyll concentration in turbid productive waters using red and near-infrared bands. Remote Sensing of Environment 96, 176-187.

Devlin, M., Bricker, S., Painting, S., 2011. Comparison of five methods for assessing impacts of nutrient enrichment using estuarine case studies. Biogeochemistry 106, 177-205.

Gholizadeh, M.H., Melesse, A.M., Reddi, L., 2016. A Comprehensive Review on Water Quality Parameters Estimation Using Remote Sensing Techniques. Sensors 16.

Gitelson, A., Dall'Olmo, G., Moses, W., Rundquist, D., Barrow, T., Fisher, T., Gurlin, D., Holz, J., 2008. A Simple semi-analytical model for remote estimation of chlorophyll-a in turbid waters: Validation. Remote Sensing of Environment 112, 3582-3593.

Gurlin, D., Gitelson, A.A., Moses, W.J., 2011. Remote estimation of chl-a concentration in turbid productive waters — Return to a simple two-band NIR-red model? Remote sensing of environment. 115, 3479-3490.

Han, L., 1997. Spectral reflectance with varying suspended sediment concentrations in clear and algae-laden waters. Photogrammetric engineering and remote sensing 63, 701-705.

Han, L., Jordan, K.J., 2005. Estimating and mapping chlorophyll-a concentration in Pensacola Bay, Florida using Landsat ETM+ data. International Journal of Remote Sensing 26, 5245-5254.

Hu, C., Lee, Z., Franz, B., 2012. Chlorophyll aalgorithms for oligotrophic oceans: A novel approach based on three-band reflectance difference. Journal of Geophysical Research: Oceans 117.

Ibelings, B.W., Vonk, M., Los, H.F.J., van der Molen, D.T., Mooij, W.M., 2003. FUZZY MODELING OF CYANOBACTERIAL SURFACE WATERBLOOMS: VALIDATION WITH NOAA-AVHRR SATELLITE IMAGES. Ecological Applications 13, 1456-1472.

Jimeno-Sáez, P., Senent-Aparicio, J., Cecilia, J.M., Pérez-Sánchez, J., 2020. Using Machine-Learning Algorithms for Eutrophication Modeling: Case Study of Mar Menor Lagoon (Spain). 17, 1189.

Jordan, T.E., Correll, D.L., Miklas, J.J., Weller, D.E., 1991. Long-term trends in estuarine nutrients and chlorophyll, and short-term effects of variation in watershed discharge. Marine Ecology Progress Series.

Kadiri, M., Zhang, H., Angeloudis, A., Piggott, M.D., 2021. Evaluating the eutrophication risk of an artificial tidal lagoon. Ocean & Coastal Management 203, 105490.

Karydis, M., 1996. Quantitative assessment of eutrophication: A scoring system for characterising water quality in coastal marine ecosystems. Environmental Monitoring and Assessment 41, 233-246.

Kirk, J.T.O., 1994. Light and photosynthesis in aquatic ecosystems. Cambridge university press.

Kjerfve, B., 1994. Coastal lagoon processes. Elsevier.

Koutrakis, E., Emfietzis, G., Sylaios, G., Zoidou, M., Katsiapi, M., Moustaka-Gouni, M.J.M.M.S., 2016. MASSIVE FISH MORTALITY IN ISMARIDA LAKE, GREECE: IDENTIFICATION OF DRIVERS CONTRIBUTING TO THE FISH KILL EVENT. 17, 280-291.

Koutrakis, E.T., Tsikliras, A.C., Sinis, A.I., 2005. Temporal variability of the ichthyofauna in a Northern Aegean coastal lagoon (Greece). Influence of environmental factors. Hydrobiologia 543, 245-257.

Liu, G., Li, L., Song, K., Li, Y., Lyu, H., Wen, Z., Fang, C., Bi, S., Sun, X., Wang, Z., Cao, Z., Shang, Y., Yu, G., Zheng, Z., Huang, C., Xu, Y., Shi, K., 2020. An OLCI-based algorithm for semi-empirically partitioning absorption coefficient and estimating chlorophyll a concentration in various turbid case-2 waters. Remote Sensing of Environment 239, 111648.

Mobley, C.D., 1995. The optical properties of water. Handbook of optics 1, 43-43.

Morrow, J.H., White, B.N., Chimiente, M., Hubler, S., 2000. A bio-optical approach to reservoir monitoring in Los Angeles, California. Advances in limnology. Stuttgart, 179-191.

O'Reilly, J.E., Maritorena, S., Mitchell, B.G., Siegel, D.A., Carder, K.L., Garver, S.A., Kahru, M., McClain, C., 1998. Ocean color chlorophyll algorithms for SeaWiFS. Journal of Geophysical Research: Oceans 103, 24937-24953.

Ogashawara, I., Moreno-Madriñán, M.J., 2014. Improving inland water quality monitoring through remote sensing techniques. ISPRS International Journal of Geo-Information 3, 1234-1255.

Orfanidis, S., Pinna, M., Sabetta, L., Stamatis, N., Nakou, K., 2008. Variation of structural and functional metrics in macrophyte communities within two habitats of eastern Mediterranean coastal lagoons: natural versus human effects. Aquatic Conservation: Marine and Freshwater Ecosystems 18, S45-S61.

Ouma, Y.O., Noor, K., Herbert, K., 2020. Modelling Reservoir Chlorophyll-<i>a</i>, TSS, and Turbidity Using Sentinel-2A MSI and Landsat-8 OLI Satellite Sensors with Empirical Multivariate Regression. Journal of Sensors 2020, 8858408.

Palmer, S.C.J., Kutser, T., Hunter, P.D., 2015. Remote sensing of inland waters: Challenges, progress and future directions. Elsevier.

Schalles, J.F., 2006. OPTICAL REMOTE SENSING TECHNIQUES TO ESTIMATE PHYTOPLANKTON CHLOROPHYLL a CONCENTRATIONS IN COASTAL, in: Richardson, L.L., LeDrew, E.F. (Eds.), Remote sensing of aquatic coastal ecosystem processes. Springer Netherlands, Dordrecht, pp. 27-79.

Shumway, S.E., 1990. A Review of the Effects of Algal Blooms on Shellfish and Aquaculture. 21, 65-104.

Simboura, N., Panayotidis, P., Papathanassiou, E., 2005. A synthesis of the biological quality elements for the implementation of the European Water Framework Directive in the Mediterranean ecoregion: The case of Saronikos Gulf. Ecological Indicators 5, 253-266.

Sylaios, G., Theocharis, V., 2002. Hydrology and nutrient enrichment at two coastal lagoon systems in Northern Greece. Water Resources Management 16, 171-196.

Sylaios, G.K., Tsihrintzis, V.A., Akratos, C., Haralambidou, K., 2006. Quantification of water, salt and nutrient exchange processes at the mouth of a Mediterranean coastal lagoon. Environmental monitoring and assessment 119, 275-301.

Toming, K., Kutser, T., Laas, A., Sepp, M., Paavel, B., Nõges, T., 2016. First Experiences in Mapping Lake Water Quality Parameters with Sentinel-2 MSI Imagery. 8, 640.

Tsihrintzis, V., Sylaios, G., Sidiropoulou, M., Koutrakis, E., 2007. Hydrodynamic modeling and management alternatives in a Mediterranean, fishery exploited, coastal lagoon. Aquacultural Engineering 36, 310-324.

Yew-Hoong Gin, K., Teck Koh, S., Lin, I.I., Soon Chan, E., 2002. Application of Spectral Signatures and Colour Ratios to Estimate Chlorophyll in Singapore's Coastal Waters. Estuarine, Coastal and Shelf Science 55, 719-728.

Zanchettin, D., Traverso, P., Tomasino, M.J.H., 2007. Observations on future sea level changes in the Venice lagoon. 577, 41-53.